Summer 2010

The Effect of Systematic Error in Forced Oscillation Wind Tunnel Test Apparatuses on Determining Nonlinear Unsteady Aerodynamic Stability Derivatives

Brianne Y. Williams
Old Dominion University

THE EFFECT OF SYSTEMATIC ERROR IN FORCED OSCILLATION WIND TUNNEL TEST APPARATUSES ON DETERMINING NONLINEAR UNSTEADY AERODYNAMIC STABILITY DERIVATIVES

by

Brianne Y. Williams
B.S., May 2004, West Virginia University
M.S., May 2007, Old Dominion University

A Thesis Submitted to the Faculty of
Old Dominion University in Partial Fulfillment of the
Requirement for the Degree of

DOCTOR OF PHILOSOPHY

AEROSPACE ENGINEERING

OLD DOMINION UNIVERSITY
August 2010

Approved by:

Drew Landman (Director)

Colin P. Britcher (Member)

Robert Ash (Member)

Patrick Murphy (Member)

Isaac Flory (Member)

ABSTRACT

THE EFFECT OF SYSTEMATIC ERROR IN FORCED OSCILLATION WIND TUNNEL TEST APPARATUSES ON DETERMINING NONLINEAR UNSTEADY AERODYNAMIC STABILITY DERIVATIVES

Brianne Y. Williams
Old Dominion University, 2010
Director: Dr. Drew Landman

One of the basic problems of flight dynamics is the formulation of aerodynamic forces and moments acting on an aircraft in arbitrary motion. Classically conventional stability derivatives are used for the representation of aerodynamic loads in the aircraft equations of motion. However, for modern aircraft with highly nonlinear and unsteady aerodynamic characteristics undergoing maneuvers at high angle of attack and/or angular rates the conventional stability derivative model is no longer valid. Attempts to formulate aerodynamic model equations with unsteady terms are based on several different wind tunnel techniques: for example, captive, wind tunnel single degree-of-freedom, and wind tunnel free-flying techniques. One of the most common techniques is forced oscillation testing. However, the forced oscillation testing method does not address the systematic and systematic correlation errors from the test apparatus that cause inconsistencies in the measured oscillatory stability derivatives. The primary objective of this study is to identify the possible sources and magnitude of systematic error in representative dynamic test apparatuses. Using a high fidelity simulation of a forced oscillation test rig modeled after the NASA LaRC 12-ft tunnel machine, Design of Experiments and Monte Carlo methods, the sensitivities of the longitudinal stability derivatives to systematic errors are computed. Finally, recommendations are made for

improving the fidelity of wind tunnel test techniques for nonlinear unsteady aerodynamic modeling for longitudinal motion.

This thesis is dedicated to my parents, Alfred Williams Jr. and Gloria Williams, for their endless love, encouragement, devotion, and strength while pursuing a higher education. A very special dedication to my grandmother, Margaret Barclift, for her boundless help and commitment to family to allow me the opportunity to finish this dissertation. I also devote this work to Jamie Forsyth for his steadfast support and unconditional love.

ACKNOWLEDGMENTS

Dr. Drew Landman has been an ideal academic advisor. I would like to thank him for his thoughtfulness, advice, patient encouragement, and endless support in completing this project. His value has been immeasurable and greatly appreciated. I would also like to acknowledge Dr. Patrick Murphy, of NASA Langley Research Center, for his support of the project. Finally, I would like to thank my committee for their critiques for improving the quality of my work.

TABLE OF CONTENTS

Page

LIST OF FIGURES x

LIST OF TABLES xvi

LIST OF SYMBOLS xix

Chapter

1. INTRODUCTION 1
   - 1.1 Background and Motivation 1
   - 1.2 Statement of the Problem 9
   - 1.3 Organization of the Dissertation 10

2. LITERATURE REVIEW 13
   - 2.1 Introduction 13
   - 2.2 Forced Oscillation Dynamic Wind Tunnel Testing 14
     - 2.2.1 Single Degree-of-Freedom Forced Oscillation 14
     - 2.2.2 Multi Degree-of-Freedom Forced Oscillation 15
   - 2.3 Experimental Limitations in Dynamic Wind Tunnel Testing 20
   - 2.4 Determination of Dynamic Stability Derivatives from Wind Tunnel Data 21
   - 2.5 Designed Experiments in Wind Tunnel Testing 22
   - 2.6 Summary 23

3. THEORETICAL DEVELOPMENT. 25
   - 3.1 Introduction 25
   - 3.2 Forced Oscillation Wind Tunnel Testing 25
     - 3.2.1 NASA Langley 12-ft Wind Tunnel Dynamic Test Rig (Representative Model) 25
     - 3.2.2 Determining Stability Derivatives from Experimental Data ... 31
   - 3.3 Three-Phase AC Induction Motor Model 33
     - 3.3.1 Reference Frame 35
     - 3.3.2 Induction Machine Dynamic Model 39
     - 3.3.3 Field Oriented Control of Induction Machines 45
     - 3.3.4 Additional Components 47
   - 3.4 Mechanical Resonance and Compliance 57

3.4.1 Characteristics of Resonance and an Example 57
3.4.2 Equations of Motion for Compliantly-Coupled Drivetrain 63
3.4.3 Geared Drives 67
3.5 Summary 69

4. METHODOLOGY 70
4.1 Introduction 70
4.2 Computer Simulation – A Modular Approach 72
4.2.1 Experimental Aerodynamic Model 73
4.2.2 Three-Phase AC Motor Model.....81
4.2.3 Control System Model.....88
4.2.4 Compliantly-Coupled Drivetrain Model 91
4.2.5 Sources of Instability in Simulation 91
4.2.6 Overall Computer Model 96
4.3 Computer Simulation Model Verification and Validation 98
4.3.1 Simulink Model Verification and Validation 101
4.4 Design of Experiments Approach 107
4.4.1 Statistical Principles.....107
4.4.2 Common Design Problems 108
4.4.3 2^k Factorial Designs 108
4.4.4 2^{k-p} Fractional Factorial Designs 110
4.4.5 Central Composite Designs.....112
4.4.6 Hybrid Designs 113
4.4.7 Statistics and Deterministic Computer Models 116
4.4.8 Fitting and Validating Regression Metamodels.....118
4.5 Monte Carlo Simulation 124
4.6 Summary.....133

5. RESULTS 134
5.1 Results 134
5.1.1 Indirect Monte Carlo Simulation 137
5.1.2 Direct Monte Carlo Simulation.....152
5.2 Discussion.....165

6. CONCLUSION AND FUTURE WORK 173
6.1 Summary.....173
6.2 Recommendations 175
6.3 Future Work.....176

REFERENCES 177

APPENDICES
A. Experimental Tabulated Data for F16-XL Aircraft Forced Oscillation Tunnel Wind Test 189
B. Static and Dynamic Coefficient Responses Matlab Code.....192
C. List of Simulation Modeling Assumptions 198

D. Pitch Oscillation Simulation Block Diagram....200
E. Pitch Oscillation Simulation Matlab Code....202
F. ANOVA Results for Responses....209
G. Monte Carlo Simulations....214

VITA....225

LIST OF FIGURES

Figure Page

1. Demonstration of the range of unknown phenomena in flight dynamics [4] 2
2. Example of forced oscillation testing - blended wing body at NASA Langley 14 x 22 Wind Tunnel [8] 3
3. Dynamic test data with the slippage of duty cycles [10] 4
4. Measured and commanded angle of attack [10] 6
5. Jump distortion in angle of attack in time history [10] 7
6. Saturated input in angle of attack time history [10] 7
7. FOS installed in the 12-Ft Wind Tunnel (roll configuration) [95] 27
8. Schematic of the overall FOS in 12-ft wind tunnel [32] 28
9. Overall FOS block diagram [95] 29
10. Cross-section of FOS assembly (in roll configuration) [32] 29
11. Bent FOS sting assembly [96] 30
12. Idealized circuit model of a 2-pole 3-phase induction machine [99] 34
13. Three-phase coupled circuit representation of an induction motor [99] 35
14. Reference frames in AC machine analysis [99] 36
15. Equivalent circuit dq frame 42
16. Indirect vector control schematic 46
17. Typical 3-phase inverter 47
18. Pulse width modulation (PWM) operation 48
19. Block diagrams for proportional control term 49

Figure Page

20. Block diagrams for integral control term 49
21. Block diagrams for derivative control term 50
22. Parallel PID architecture 50
23. Simple compliantly-coupled motor and load 58
24. Motor/Torque transfer function 60
25. Load/Torque transfer function 61
26. Compliantly-Couple Drive Train 63
27. Reduced compliantly-coupled drive train 64
28. Gearbox representation in compliantly-coupled drivetrain 64
29. Equivalent reduced compliantly-couple drive train model 65
30. Modern backlash model – hysteretic (left side) and classical backlash model (right side) 68
31. Flowchart of overall approach 71
32. Detailed forced oscillation system conceptual block diagram 73
33. Three-view sketch of 10% scaled F16-XL aircraft model (units in metric system) 74
34. Variation of static lift coefficient with angle of attack for 10 % F16-XL aircraft 76
35. Variation of static pitching moment coefficient with angle of attack for 10% F16-XL aircraft 76
36. Variation of in-phase lift coefficient with reduced frequency 78
37. Variation of out-of-phase lift coefficient with reduced frequency 79
38. Variation of in-phase pitching moment coefficient with reduced frequency 79

Figure Page

39. Variation of out-of-phase pitching moment coefficient with reduced frequency 80
40. The complete aerodynamic Simulink model 81
41. The complete induction machine Simulink model 82
42. Line-to-Neutral Conversion Simulink model 83
43. Rotor Angular Position Estimation Simulink model 83
44. Unit Vector Simulink model 84
45. ABC-SYN Conversion Simulink model 85
46. SYN-ABC Conversion Simulink model 86
47. Three-phase AC Induction Machine Dynamic model implementation in Simulink 87
48. Implementation of F_{qs}, see Equation 3.49 87
49. Overall indirect vector control Simulink model 88
50. Vector control block in Simulink 89
51. Command voltage generator block in Simulink 89
52. Pulse-width modulation block in Simulink 90
53. Bode plot of a generic integrator 92
54. Bode plot of a generic PI controller 93
55. RC circuit 93
56. Generic 45 Hz low-pass filter Bode plot 94
57. 11 Hz low-pass filter Bode plot 95
58. 5192 Hz low-pass filter Bode plot 95

Figure Page

59. Overall dynamic oscillation simulation in Simulink 97

60. Simplified verification and validation process [126] 98

61. In-phase lift coefficient validation 103

62. Out-of-phase lift coefficient validation 103

63. In-phase pitching moment coefficient validation 104

64. Out-of-phase pitching moment coefficient validation 104

65. Characteristic behavior of 10 Hp AC motor with specified commanded velocity and load torque (reproduction of article results [118]) 105

66. Commanded and feedback position for different reduced frequencies (k = 0.081 left side and k = 0.135 for right side) 106

67. General example of central composite design for k = 2 and $\alpha = \sqrt{2}$ [134] 112

68. Nested face centered design in two factors [135] 114

69. 'Indirect' Monte Carlo Simulation Procedure 127

70. Uniform distribution for incremental equivalent inertia 128

71. Uniform distribution for incremental equivalent damping 128

72. Normal distribution for incremental backlash 129

73. Normal distribution for incremental input saturation 129

74. 'Direct' Monte Carlo Simulation Procedure 130

75. Uniform distribution for equivalent inertia 131

76. Uniform distribution for equivalent damping 131

77. Normal distribution for backlash 132

78. Normal distribution for input saturation 132

Figure Page

79. Example probabilistically symmetric coverage interval for 95% level of confidence [146] 135
80. Example of normal distribution 136
81. Example of positive skewed distribution 136
82. Example of negatively skewed distribution 137
83. Histogram for in-phase lift coefficient (test case #1) 138
84. Histogram for out-of-phase lift coefficient (test case #1) 139
85. Histogram for in-phase pitching moment coefficient (test case #1) 139
86. Histogram for out-of-phase pitching moment coefficient (test case #1) 140
87. Histogram for in-phase lift coefficient (test case #2) 141
88. Histogram for out-of-phase lift coefficient (test case #2) 142
89. Histogram for in-phase pitching moment coefficient (test case #2) 142
90. Histogram for out-of-phase pitching moment coefficient (test case #2) 143
91. Histogram for in-phase lift coefficient (test case #3) 144
92. Histogram for out-of-phase lift coefficient (test case #3) 145
93. Histogram for in-phase pitching moment coefficient (test case #3) 145
94. Histogram for out-of-phase pitching moment coefficient (test case #3) 146
95. Histogram of in-phase lift coefficient (test case #4) 147
96. Histogram of out-of-phase lift coefficient (test case #4) 148
97. Histogram of in-phase pitching moment coefficient (test case #4) 148
98. Histogram of out-of-phase pitching moment coefficient (test case #4) 149
99. Histogram of in-phase lift coefficient (test case #5) 150

100. Histogram of out-of-phase lift coefficient (test case #5) 151

101. Histogram of in-phase pitching moment coefficient (test case #5) 151

102. Histogram of out-of-phase pitching moment coefficient (test case #5)..... 152

103. Histogram for in-phase lift coefficient (test case #1)..... 153

104. Histograms for out-of-phase lift coefficient (test case #1) 153

105. Histograms for in-phase pitching moment coefficient (test case #1) 154

106. Histograms for out-of-phase pitching moment coefficient (test case #1)..... 154

107. Histogram for in-phase lift coefficient (test case #2)..... 155

108. Histogram of out-of-phase lift coefficient (test case #2) 156

109. Histogram of in-phase pitching moment coefficient (test case #2) 156

110. Histogram for out-of-phase pitching moment coefficient (test case #2) 157

111. Histogram of in-phase lift coefficient (test case #3)..... 158

112. Histogram of out-of-phase lift coefficient (test case #3) 158

113. Histograms of in-phase pitching moment coefficient (test case #3)..... 159

114. Histogram of out-of-phase pitching moment coefficient (test case #3)..... 159

115. Histogram of in-phase lift coefficient (test case #4)..... 160

116. Histograms of out-of-phase lift coefficient (test case #4)..... 161

117. Histogram of in-phase pitching moment coefficient (test case #4) 161

118. Histogram of out-of-phase pitching moment coefficient (test case #4)..... 162

119. Histogram of in-phase lift coefficient (test case #5)..... 163

120. Histogram of out-of-phase lift coefficient (test case #5) 163

121. Histogram of in-phase pitching moment coefficient (test case #5) 164

122. Histogram of out-of-phase pitching moment coefficient (test case #5)..... 164

Figure Page

123. Incomplete sinusoidal waveform of dynamic contribution of lift coefficient 170

124. Larger view of pitch oscillation simulation 201

LIST OF TABLES

Table		Page
1.	Model Characteristics [32]	26
2.	FF-10 Balance Loading Limits	31
3.	Notation of commonly used reference frames [100]	37
4.	Summary of process control problems and implementing the PID controller	52
5.	Description of constants	63
6.	Antiresonant and resonant frequency for a given sting type	66
7.	Analysis Procedure for a 2^k design [133]	109
8.	Symbolic Analysis of Variance for a 2^k Design [133]	110
9.	Factor limits	115
10.	2^{5-1} nested face centered design test matrix (center run is shown as bold)	116
11.	Regression Metamodels	121
12.	Regression metamodel fit summary statistics	121
13.	Point prediction results	123
14.	Factor settings test case #1	138
15.	Summary statistics for test case #1	138
16.	Factor settings (test case #2)	140
17.	Summary statistics for test case #2	141
18.	Factor settings (test case #3)	143
19.	Summary statistics for test case #3	144
20.	Factor settings (test case #4)	146

Table Page

21. Summary statistics for test case #4 147

22. Factor settings (test case #5) 149

23. Summary statistics for test case #5 150

24. Summary statistics for test case #1 152

25. Summary statistics for test case #2 155

26. Summary statistics for test case 3 157

27. Summary statistics for test case #4 160

28. Summary statistics for test case #5 162

29. Summary of 95% confidence intervals for all test cases using the 'indirect' Monte Carlo method 167

30. Summary of 95% confidence intervals for all test cases using the 'direct' Monte Carlo method 168

31. Coded Regression Metamodels 172

32. Variation of static coefficient due to angle of attack for 10% F16-XL aircraft [4] 190

33. In-phase and out-of-phase components of lift coefficient [4] 191

34. In-phase and out-of-phase pitching moment coefficient [4] 191

35. ANOVA table for in-phase lift coefficient 210

36. Model adequacy results for in-phase lift coefficient 210

37. ANOVA table for out-of-phase lift coefficient 211

38. Model adequacy results for out-of-phase lift coefficient 211

39. ANOVA table for in-phase pitching moment coefficient 212

Table Page

40. Model adequacy results for in-phase pitching moment coefficient 212

41. ANOVA table for out-of-phase pitching moment coefficient 213

42. Model adequacy results for out-of-phase pitching moment coefficient 213

LIST OF SYMBOLS

Symbol	Description	Units
a	parameter in indicial function	--
B	damping constant	N*m/(rad/s)
b_1	parameter in indicial function	1/sec
c	parameter in indicial function	--
C	Euler transformation matrix	rad
C	capacitance	Farad
C(k)	Theodorsen's function	--
C_L	lift coefficient	--
C_{L_α}	lift coefficient due to angle of attack	--
$C_{L_{\dot{\alpha}}}$	lift coefficient due to angle of attack rate	--
C_{L_q}	lift coefficient due to pitch rate	--
$C_{L_{\dot{q}}}$	lift coefficient due to pitch acceleration	--
C_{m_α}	moment coefficient due to angle of attack	--
$C_{m_{\dot{\alpha}}}$	moment coefficient due to angle of attack rate	--
C_{m_q}	moment coefficient due to pitch rate	--
$C_{m_{\dot{q}}}$	moment coefficient due pitch acceleration	--
e(t) or E(s)	output (time or Laplace domain, respectively)	--
f	supplied frequency	Hz
$\vec{f}$	generic variable (in motor dynamics section)	depends on variable
g(x)	metamodel	depends on response
$\vec{i}$	current	A
J	moment of inertia	kg*m^2
K_{PID}	PID constant gain	--
K_s	spring constant	N*m/rad
k	reduced frequency	--
$\overline{\overline{K}}$	transformation	depends on variable
L	inductance	Henrys
$\vec{M}$	total moment	N*m
M	number of Monte Carlo simulation	
MS	mean square	
n_c	number of cycles	--
N_r	number of coils on rotor	--
n_s	synchronous speed	rad/sec
N_s	number of coils on stator	--

Symbol	Description	Units
p	number of poles	--
PRESS	measure of model quality	--
$\dot{Q}$ (*or* $\dot{q}$)	pitch angular acceleration	rad/sec^2
Q (or q)	pitch angular velocity	rad/sec
$\vec{r}$	position vector from the origin to the mass	m
R	yaw angular velocity	rad/sec
$\dot{R}$	yaw angular acceleration	rad/sec^2
R	resistance	Ohm
R^2	coefficient of determination	--
r_{high}	high end of coverage interval	--
r_{low}	low end of coverage interval	--
s	Laplace transform	--
SS	sum of squares	--
t	time	sec
T	period	sec
T_e	electromagnetic torque	N*m
T_L	load torque	N*m
T_w	equivalent torque	N*m
U	velocity in the x-axis	m/s
u(t) or U(s)	input (time or Laplace domain, respectively)	--
V	velocity in the y-axis	m/s
V	inertial speed	m/s
$\vec{v}$	voltage	V
X	impedance	Ohm
x_{ij}	regression variable	depends on response
y	response or input/output relationship	depends on response

Greek Symbols:

Δ	increment	--
α	angle of attack	rad
α_A	oscillation angle of attack (amplitude)	rad
β_{ij}	regression constants	--
δ	incremental	--
ε	error	depends on response
λ	flux linkage	Wb-t
θ	pitch angle (in flight dynamics section)	rad
θ	angular displacement (in motor dynamics section)	rad

Symbol	Description	Units
θ	position (in compliance section)	rad
σ	standard deviation	--
τ	time constant	sec
τ_r	rotor time constant	sec
ω	angular velocity	rad/sec
ξ	dummy variable of integration	--

Superscripts:

b	body reference frame
c	center of gravity
i	inertial reference frame
^	unit vector
.	derivative
¯	oscillatory data (in-phase or out-of-phase)

Subscripts:

α	angle of attack
abc	abc reference frame
adj	adjusted
AR	anti-resonance
c	control surface
D	derivative
dq	arbitrary reference frame
dyn	Dynamic contribution
e	base (in motor dynamics section)
I	integral
L	load
l	leakage
m	magnetizing
n	neutral line
o	nominal
P	proportional
pred	predicted
q	pitch angular velocity
R	resonance
r	rotor
s	stator
static	static contribution
V	velocity

CHAPTER 1

INTRODUCTION

1.1 Background and Motivation

In classical flight mechanics theory an aircraft is represented as a rigid body with six degrees of freedom. The flight mechanics equations of motion are founded on the conventional stability derivative approach, developed by Bryan in 1911, which estimated the change in a force or moment acting on a vehicle due to a change in perturbation variables [1]. Nelson described perturbation variables as the instantaneous changes from the reference conditions of the airflow angles (i.e. angle of attack and sideslip), translational velocities, angular velocities, control deflection, and their derivatives [2]. With this assumption, the aerodynamic forces and moments can be expressed by a first order Taylor series expansion of the perturbation variables about the reference equilibrium condition.

However, with the increasing need for high maneuverability capabilities in modern combat aircraft there are significant shortcomings in using the conventional stability derivative modeling approach. Figure 1 illustrates the current difficulties in predicting flight dynamics over certain flight regimes. Current prediction methods work adequately over low to moderate angles of attack for a given angular rate (see the green region of Figure 1). On the other hand, at high angles of attack and/or high angular rates, nonlinear unsteady aerodynamic phenomena are more pronounced (see the red region of Figure 1). In this region the aerodynamic characteristics are based on shock waves,

separated flows, vortical flows, movement of separation points, and variation of vortex breakdown locations over the surface [3]. Because of these complex nonlinear aerodynamic phenomena, conventional modeling is limited in prediction capability. These models do not admit time-dependent effects, no 'memory' of past states, and there are strong frequency effects.

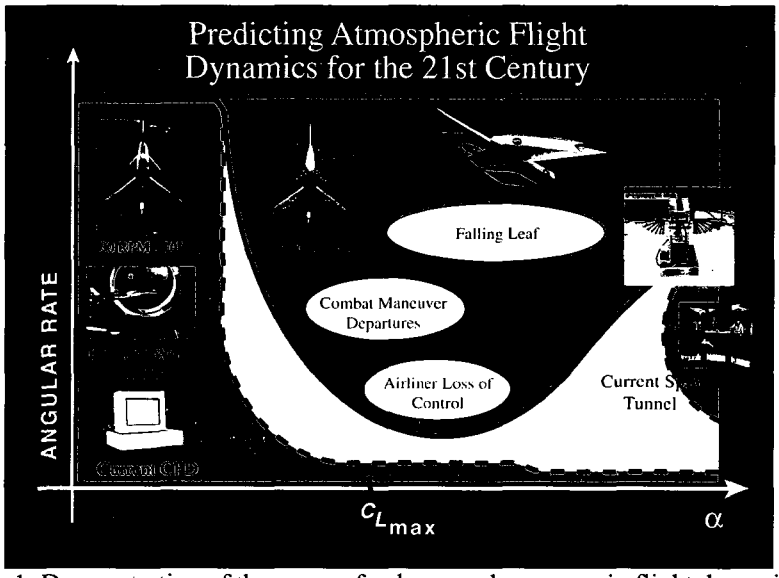

Figure 1: Demonstration of the range of unknown phenomena in flight dynamics [4]

Researchers have devoted significant effort to formulating nonlinear aerodynamic modeling techniques that include the time history. Two primary approaches are taken – analytical techniques and experimental techniques. Current analytical approaches to modeling the unsteady aerodynamic characteristics of an aircraft vary greatly, and there is no standard methodology. The various analytical techniques used have been reviewed extensively by Kyle et al. and Greenwell [3, 5]. Dynamic test techniques range from captive, wind tunnel single degree-of-freedom and free-flying, and outside free-flying. Additional wind tunnel dynamic test techniques have been reviewed by Owens et al. and

Tomek et al. [6, 7]. The most commonly used method is captive testing, of which two methods dominate – forced oscillation and rotary balance testing.

Forced oscillation tests involve a rigidly mounted model on a support system. The support system is then actuated to impart motion to the model. Forces and moments acting on the model are measured. Motion shapes are typically sinusoidal at a single frequency and prescribed amplitude. Other motion shapes include frequency sweeps, ramps, and others designed to optimize model identification. An example of forced oscillation testing is illustrated in Figure 2.

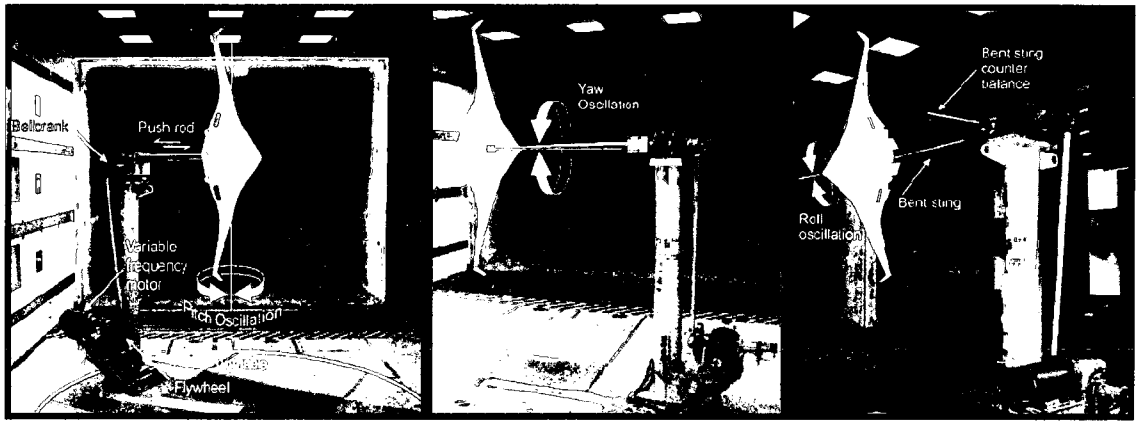

Figure 2: Example of forced oscillation testing - blended wing body at NASA Langley 14 x 22 Wind Tunnel [8]

There are several limitations in forced oscillation testing. The apparatus used for forced oscillation normally takes up more space in the vicinity of the model, causing support interference concerns. Other issues lie in accuracy of the force and moment measurements caused by bias and random errors from instrumentation, calibrations and tare interpolation, structural dynamics, vortex shedding, and wind tunnel fan beat frequencies. Heim examined the effects of error in data acquisition systems and

developed a gradient-based method to determine the number of required oscillation cycles to effectively reduce the error from acquisition systems [9].

Kim, on the other hand, attempted to indicate levels of uncertainty in output measurements that can arise from experimental setup and calibration procedures [10]. That study looked at single-frequency, forced-oscillation tests of an F16-XL 10% scale model aircraft tested at NASA Langley Research Center's 12-ft Wind Tunnel in 1996 and 2000. The study did not examine effects of wind tunnel turbulence, scale effects, structural responses, or the dynamics of the test rig. One issue identified by Kim was the presence of timing signal effects. Since experimental tests are often run using real-time software, there appear to be delays (from multitasking) in the duty cycle leading to uneven sample time intervals. The duty cycle appears to affect the input (i.e. angle of attack), as shown in Figure 3. It was discovered that duty cycle is not a dominant feature affecting the sensitivity of the output measurements. The solution is to simply use more cycles to average out this error, as was suggested.

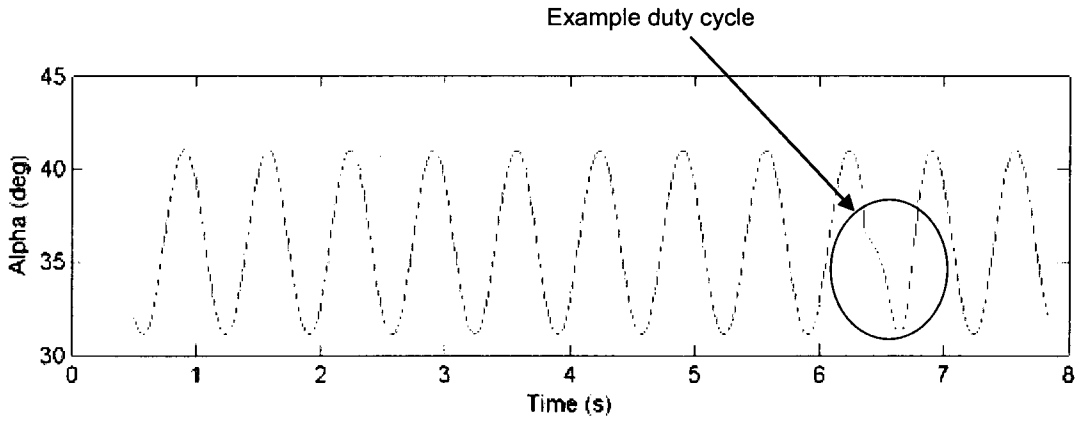

Figure 3: Dynamic test data with the slippage of duty cycles [10]

Kim compared the commanded input to the measured input without including the dynamic test rig effects. It is, of course, desirable that the commanded and measured input is the same; however, the study discovered significant bias amplitudes that vary from peak to peak oscillation (see Figure 4 for example). The method used to improve the calibration was to fit a third-order polynomial that describes the relationship between degrees and voltage and vice-versa on the digital/analog converter and analog/digital converter. Adjusting the bias error and scaling the amplitude input corrected the problem.

Despite resolution of these issues, input measurement errors still existed. The next concern was whether the dynamic test rig was introducing errors. Random jump distortion and input saturation were discovered; examples are illustrated in Figures 5 and 6, respectively. However, the sources of these errors were unknown at the time of the study.

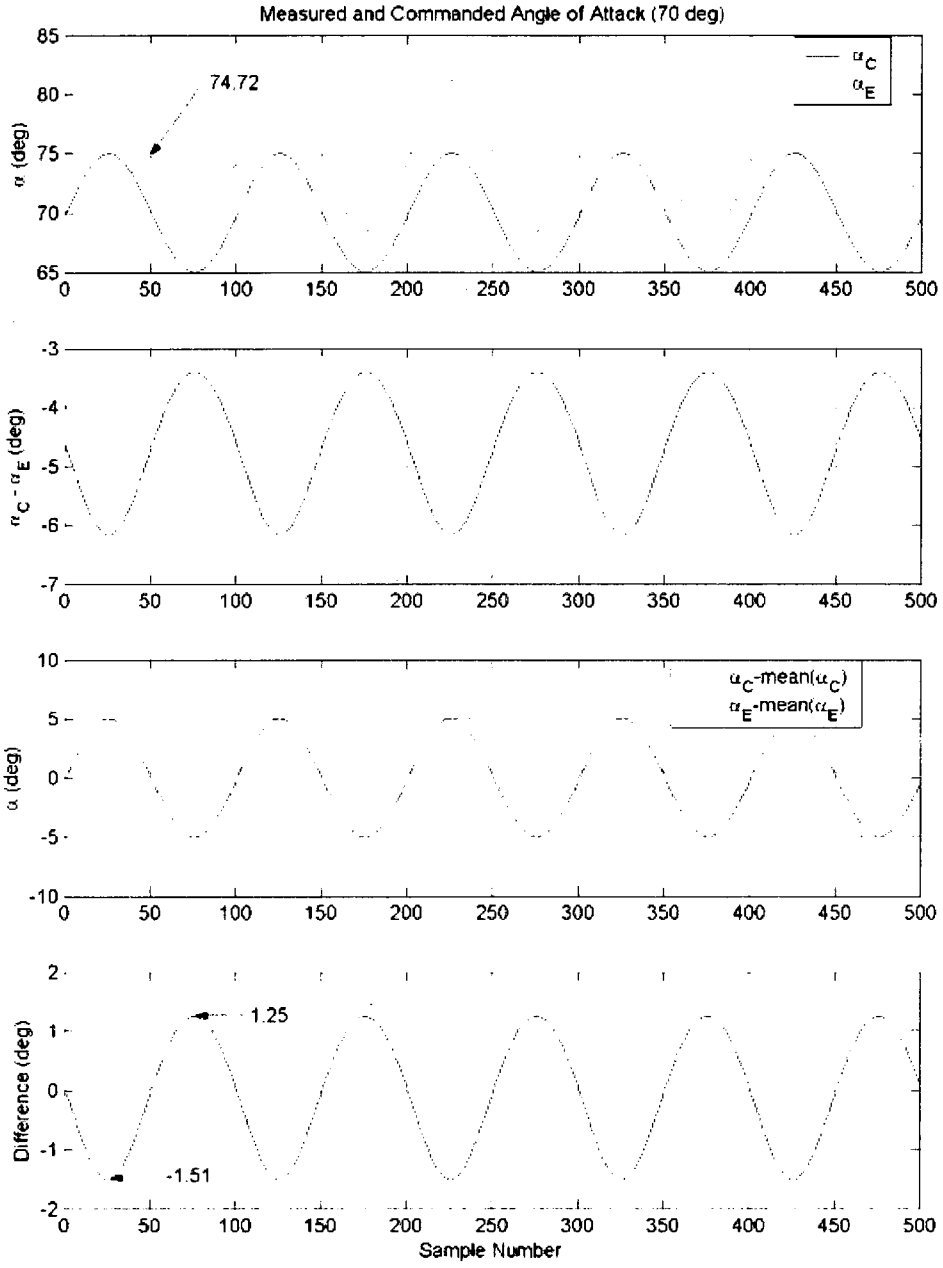

Figure 4: Measured and commanded angle of attack [10]

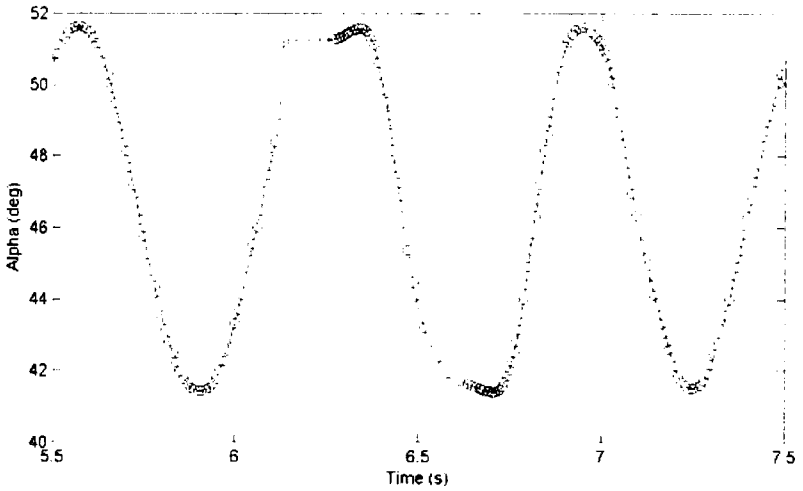

Figure 5: Jump distortion in angle of attack in time history [10]

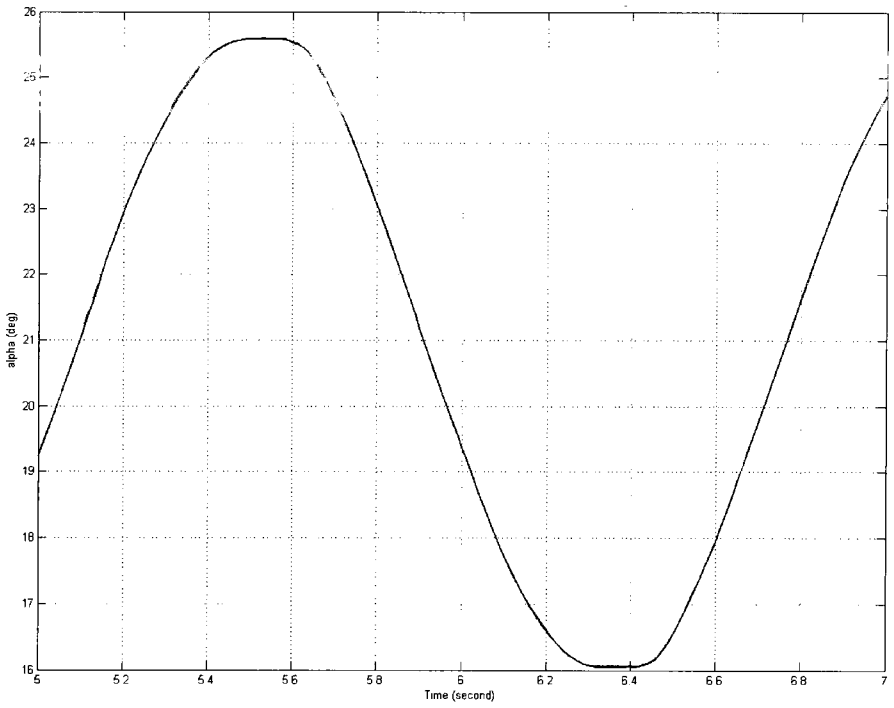

Figure 6: Saturated input in angle of attack time history [10]

Although the Kim and Heim studies clearly demonstrated the need for proper calibration techniques and the need for adequate data sampling; both studies assumed that

systematic errors could be removed by calibration alone. Neither study looked at the dynamic effects of test apparatuses interfering with the aerodynamic measurements.

Understanding the dynamics of a test rig is important because of the design process used and its possible effects. Typically, dynamic test rigs are designed using a sequential approach. For example, the mechanical and structural components are designed first, followed by electrical and electronic components development of selection subsequent interconnection of mechanical and electrical components next, and then selection of a computer to be interfaced with the system. Consequently, when the various elements are not designed as a system several problems arise [11]:

1. When two independently designed components are interconnected, the original characteristics and operating conditions of the two will change due to loading or dynamic interactions.
2. Perfect matching of two independently designed and developed components is practically impossible. As a result, a component can be considerably underutilized or overloaded in the interconnected system, and both conditions are inefficient and undesirable.
3. Some of the external variables in the components will become internal and "hidden" due to interconnection, which can result in potential problems that cannot be explicitly monitored through sensing nor can they be directly controlled.

The interactions between the mechanical components, transmission components, electrical components, and component interconnections introduce systematic errors that can affect the aerodynamic measurement. Common mechanical components are: load

bearing and structural components, fasteners, dynamic isolation components, mechanical actuators, and mechanical controllers. The most common transmission component is the gearbox, which can exhibit backlash. Electronic and electrical components include pulse width modulation inverter, motor controllers, AC motors, digital data acquisition cards, computer hardware and software, etc. Component interconnections may exhibit behavior significantly different from individual performance. Variations result from (electrical) loading effects caused by improper impedance matching between sensors, transducers, control boards, process (plant) equipment, and signal-conditioning hardware [11].

Studying the dynamics of test rigs is important due to nonlinear behavior exhibited by the components. Nonlinearities appear in two forms – static manifestation and dynamic manifestation. Examples of static manifestation are saturation, hysteresis, and offset. Examples of dynamic manifestation are jump phenomenon, limit cycles, and frequency creation. Nonlinearities are present in any physical device to varying levels. If the level of nonlinearities in a system can be neglected without exceeding the error tolerance then the system can be assumed linear. However, this assumption is not valid if system nonlinearities are seen to interact with the aerodynamic loads, which pose a problem for accurately obtaining the nonlinear unsteady stability derivatives that are used to develop aircraft control laws and flight dynamics studies.

1.2 Statement of the Problem

When conducting forced oscillation experiments at small amplitudes (i.e. <5°) and single frequencies ranging from 0.1 to 10 Hz, concerns arise as to the overall accuracy of the measurement. The precision errors of forced oscillation systems have been researched extensively by Heim [9]. Accuracy is determined by the sum of bias and

precision errors. As previously discussed, the accuracy can be affected by dynamics of the test apparatuses interacting with the aerodynamic loads. This study examines the systematic error on nonlinear unsteady stability derivatives caused by mechanical and transmission components in forced oscillation test apparatuses using a high fidelity computer simulation of a dynamic test rig. The goals of the study are to:

1. Identify any possible sources of systematic errors.
2. Identify the magnitude of the systematic errors.
3. Determine the sensitivities of the computed stability derivatives to the systematic errors.
4. Finally, to make recommendations for improving the fidelity of forced oscillation wind tunnel testing.

The study is limited to longitudinal motion only. The study also assumes that mechanical vibrations are minimal and aeroelastic effects are not important.

1.3 Organization of the Dissertation

Chapter 2

Chapter 2 surveys past and current forced oscillation testing techniques. The chapter outlines the several limitations in using the testing, such as experimental limitations and dynamic test rig limitations. A review of current techniques used to determine dynamic stability derivatives from experimental data is provided. Finally, the chapter concludes with a survey of design of experiment studies used in aerodynamic testing.

Chapter 3

Chapter 3 details the mathematical modeling required for development of a high fidelity computer simulation. A representative wind tunnel was used for building the simulation. An aerodynamic model based on experimental F16-XL results was developed. The chapter describes the overall operation of a NASA Langley 12-ft Wind Tunnel forced oscillation facility. The specific components used in forced oscillation, such as a three-phase AC induction motor, are then described mathematically. The dynamic model that describes the three-phase AC induction motor is an open-loop system. To build a closed-loop system the control system model (i.e. field oriented control) is developed and additional components needed in the system, such as PID controllers and a pulse-width modulation inverter, are described. The chapter concludes with a discussion of characteristic behavior of mechanical resonance and compliance. The equations of motion for the compliantly-coupled drivetrain system are then developed, and a description of geared drives and their behavior in a system is presented.

Chapter 4

The chapter details the construction of the computer simulation. The computer model is then validated and verified. Chapter 4 outlines the methodology used for the designed experiments and Monte Carlo simulation in conjunction with the computer simulation.

Chapter 5

Chapter 5 features a discussion of the results from the computer experiment, design experiment, and Monte Carlo simulation. The chapter also details the failure and success in using computer experimentation techniques. It will note statistical limitations in using designed experiments with a computer.

Chapter 6

Chapter 6 concludes the study and makes recommendations for improvement in the fidelity of forced oscillation wind tunnel testing. Recommendations for future work are itemized.

CHAPTER 2

LITERATURE REVIEW

2.1 Introduction

The need for forced oscillation wind tunnel testing is evident by the call for control algorithms at high angle of attack and/or angular rates. Current computational methods are limited at high angles of attack due to flow separation and other complex unsteady aerodynamic phenomena. Researchers around the world have used forced oscillation wind tunnel testing for performance damping characteristic studies and analyses and prediction of stability characteristics.

This chapter serves as a literature survey of past and current forced oscillation wind tunnel test capabilities. It begins with a discussion of the most popular testing method – single degree-of-freedom (DOF) forced oscillation. Limitations in single-DOF testing have caused some researchers to develop multi-DOF forced oscillation testing in order to attempt improved estimates of full flight envelope stability parameters. Experimental limitations in testing are discussed. Several experimental issues such as interference, dynamic similitude, and flow quality continue to plague dynamic wind tunnel testing. The most popular current methods for determining stability parameters from wind tunnel test data are discussed. The chapter concludes with a survey of designed experiments being implemented and used for efficient wind tunnel testing. To date the author has found no designed experiments used in forced oscillation testing.

2.2 Forced Oscillation Dynamic Wind Tunnel Testing

2.2.1 Single Degree-of-Freedom Forced Oscillation

Single degree-of-freedom forced oscillation wind tunnel testing dates back to the 1960s and 1970s. NASA Langley Full Scale Tunnel was one of the first facilities used [12]. At the time, the wind tunnel operated at Mach numbers below 0.1 [13]. Force and moment coefficients due to pitching, yawing, or rolling about a fixed axis were measured at angles of attack up to 110° [14]. The system operated at a range of 0.5 to 1.5 Hz for frequency oscillation with oscillation amplitudes ranging from ±30°. Tests included jet transports [15, 16] and variable sweep fighter configurations [17, 18]. The French Aerospace Lab (ONERA) at Chalais-Meudon developed a similar test rig of the NASA Langley Full Scale Tunnel. However, derivatives were measured using their rig at angles of attack up to 30°, angles of sideslip up to 12°, and in the frequency range of 1 to 2 Hz [19].

A few high speed tunnels at NASA Langley have also been used for forced oscillation testing. Boyden describes the test rig apparatus (for roll) in both the 7 × 10 Foot High Speed Wind Tunnel ($0.2 < M < 0.85$) and the 8 Foot Transonic Pressure Tunnel ($0.2 < M < 1.2$) [20]. At the time, the apparatus was operated at angles of attack (or angles of sideslip) up to 22°.

Arnold Engineering Development Center (AEDC) has developed forced oscillation test rigs for low speed and high speed testing. The von Karman Gas Dynamics Facility (VKF) implemented a forced oscillation system using a cross-flexure pivot. Their system operated at small amplitudes, ±3°, and over an oscillation frequency range of 2 to 56 Hz for either pitch or yaw oscillation. For roll oscillation the system

operated at the same small amplitude, but the oscillation frequency ranged from 2 to 20 Hz. See Burt for more details [21]. For high speed testing, the AEDC used their 4 Foot, and 16 Foot Transonic Tunnels as well as their 16 Foot Supersonic Tunnel [22]. That device was mainly used for cross and cross-coupling derivative measurements operating at angles of attack up to 50°. The systems were updated in the 1980s to include high balance force tolerance [23].

The German Research and Development Institute for Air & Space Travel (DFVLR) developed a model mounted on a moving head supported by a vertical strut with oscillatory motion in pitch, yaw, roll or heave induced by a mobile oscillatory balance [24]. The maximum amplitude for all angular motions is 5°. Plunging motion ranges over 30 mm. The frequency range is 0.2 to 3 Hz with angles of attack up to 15°.

The National Aeronautical Establishment (NAE) is given credit for developing the first fully direct measurement of damping and cross and cross-coupling moment derivatives due to pitching or yawing in 1973 [25]. However, it should be noted that the research group assumed that any secondary motion was negligible.

Other single DOF forced oscillation testing capabilities include work done at universities and overseas: University of Bristol [26], Cambridge University [27], the Middle East Technical University [28], German-Dutch Wind Tunnel (DNW) [29], and National Aerospace Laboratories in India [30].

Over time several wind tunnels have been updated to improve measurement fidelity, resuming testing after long periods of hibernation, or implemented a new system design altogether. When the NASA Langley Full Scale Tunnel was discontinued, the forced oscillation test rig was modified for use in the 14 by 22 Foot Subsonic Wind

Tunnel [6]. Recent research has examined a blended wing body (BWB) under forced oscillation testing at the 14 × 22 Foot Subsonic Wind Tunnel although no results have been published to date [8]. The 12 Foot Low Speed Tunnel was used extensively for dynamic testing in 1996 and 2000 [31, 10]. Several upgrades have been made to the test equipment and are still on-going [32].

NASA Langley high speed tunnels have also been updated due to the increased need for accurate modeling of dynamic derivatives. A mobile system has been used in the Transonic Dynamics Tunnel (TDT), National Transonic Facility (NTF), and Unitary Plan Wind Tunnel (UPWT). That system uses a special oscillating balance where the model is oscillated in a single DOF at the natural frequency of the model/balance system during testing [7].

At DNW-NWB the mobile oscillatory balance has been resurrected from DFLVR research after being stored for two decades [29]. The system was upgraded with modern equipment and brought online primarily for civil transport aircraft studies. The test model is mounted on a belly sting which is attached to a movable hexapod platform. Although the system allows for 6-DOF, to the author's knowledge it has only been used for single DOF tests, due to challenges in stiffness and precision. The system currently is operating at a maximum of: 10° for pitch, 6° for roll, 5° for yaw, 80 mm of travel for heave, and 80 mm of travel for lateral oscillations.

The TsAGI T-38 wind tunnel in Russia has been outfitted with a simple single DOF forced oscillation test rig [33]. That rig was developed for missile testing. It operates over angle of attack ranging from -5° to 45° and Mach numbers ranging from 0.2 to 0.6.

There are a few limitations to using single DOF forced oscillation testing. One particular stand out limitation is, between all the wind tunnels discussed, the lack of agreement between the actual amplitude measured on the model and the generated amplitude from the test rig. Differences ranging from 1% to 5% were found depending on the wind tunnel. This value may seem small; however, it can have significant impact when trying to quantify measurements that are small themselves. Researchers at the University of Bristol have demonstrated interesting nonlinearities in the form of limit cycles in amplitude and stability and bifurcations in a single DOF test rig[34]. Other studies have shown limited motion capabilities [35, 36, 37, 30, 38, and 39]. These limitations alone justify further examination of the test rig dynamics for forced oscillation systems.

High mechanical complexities [40, 41, 42, and 43] and extensive setup and/or running costs [44] are other limitations. The use of active feedback control is a limitation particularly when an unassisted response motion would be ideal [45]. Probably the most inhibitive of these limitations is cost. Consequently, researchers have been developing multi DOF forced oscillation dynamic test rigs with the goal of developing a single system that is efficient, cost-effective, and capable of obtaining the majority of stability derivatives over a flight envelope. However, it is argued that designed experiment approaches can alleviate this problem.

2.2.2 Multi Degree-of-Freedom Forced Oscillation

The concept of multi DOF dynamic testing is not new. It also has its roots in developments dating back to the 60s and 70s. During this time, a model was often suspended elastically in such a way that it could oscillate with several degrees-of-

freedom. One such model was used at the Royal Aircraft Establishment (RAE) at Bedford, England but is no longer operational [46, 47]. Another method used during that time was to elastically suspend the model from cables. The model was allowed to translate laterally and vertically as well as rotate about all three axes. This method allowed up to 5-DOF in oscillation and was implemented at the NASA Langley Transonic Dynamics Tunnel [48].

Contemporary new multi- DOF test rigs include an interesting system called the Pendulum Support Rig (PSR) [49]. In that system, the model is suspended on a gimbaled pendulum support strut. The forced oscillation motion is initiated from the control surfaces on the model rather than through the support mechanism. There are several advantages of using this type of system:

1. Multiple degrees-of-freedom,
2. Reduced interference effects,
3. Incorporation of suitable sensors can allow real-time feedback control systems both to develop and evaluate control laws,
4. Reduced mass models which reduce fabrication costs.

There are several difficulties with using this type of rig. The motion is not totally arbitrary. The only practical solution to all the limitations of existing dynamic test rigs is to account for all 6-DOF. The biggest issue is that it is evident that the dynamics of the aircraft model and of the pendulum strut can couple to create behaviors that are not purely aerodynamic in nature. Again, the fidelity of the aerodynamic measurement comes under question because the rig dynamics may have a significant impact on the aerodynamics. As always, strut interference remains an issue. Lowenberg and Kyle also

pointed out that the sensors in their system are adding friction and the actuators, which rely on cables passing through the gimbals, exacerbate these effects. Finally, their control system also introduced dead bands, lags, and severe stability and control issues.

The PSR system was independently tested by Gatto at Brunel University [50]. He asserted that technique predicted well for longitudinal stability and control derivatives but was fraught with difficulties. The results were sensitive from variations in upstream flow conditions, mechanical vibrations, and asymmetric nonlinear aerodynamic/structural coupling.

A different type of test rig, using the same principle as the PSR, was set up at the University of Bristol. The rig was 3-DOF gimbal mounted on a vertical support strut fixed to the wind tunnel floor [51]. The model was actuated using its control surfaces. The work showed divergent behavior in the coefficients for dynamic testing in the form of bifurcations and limit cycles. Difficulties were also present in attaining sufficient rotation.

Following the work at University of Bristol, researchers at ITT Kanpur in India developed a 5-DOF dynamic rig called the H-model [52]. The group pointed out that the PSR test rig could generate unwanted model velocity oscillations, especially under longitudinal maneuvers. Although the study improved tracking, compared to the original PSR, by employing a PID controller, it still exhibited test rig dynamics affecting their results. There are future plans for developing arbitrary motion paths with multi- DOF test rigs for the NASA Langley 14×22 Foot Subsonic Wind Tunnel [6].

2.3 Experimental Limitations in Dynamic Wind Tunnel Testing

Limitations in the dynamics of test rigs affecting the fidelity of stability parameters has been demonstrated and discussed. It is, however, worth mentioning the experimental limitations discovered in all types of dynamic testing. Wind tunnel experiments are not without sources of error, and the challenge increases for high angle of attack experiments where the flowfield is unsteady [53]. Examples of errors that influence the aerodynamic data include: dynamic support interference [54, 55], unsteady wall interference [56], test facility interference [57, 58], Reynolds number effects [59], freestream turbulence [60], and dynamic scaling issues [3]. For forced oscillation dynamic testing in particular, support interference and dynamic scaling errors are the most problematic.

Support interference is present for any dynamic test; however, proper corrections can alleviate the problem [61]. Interference can be minimized by not using asymmetric sting or sting strut supports or by using a half-model [62]. Slender symmetric stings have been shown to cause little support interference at moderate to high angle of attack tests [54 and 64].

Full-scale predictions rely on satisfying similitude requirements. Besides the usual requirements of Reynolds number and Mach number, other important parameters unique to dynamic testing are: reduced angular velocity, Strouhal number, and Froude number. Reduced angular velocity is a measure of the angular rate of the aircraft. Meeting the similitude requirements ensures that distributions of flow angles across the test model are the same [6]. Strouhal number, also called reduced oscillatory frequency, accounts for the unsteady aerodynamic effects caused by flow oscillation [6]. Froude

number maintains the ratio of inertia and gravitational effects between the test model and the full-scale vehicle [6].

2.4 Determination of Dynamic Stability Derivatives from Wind Tunnel Data

There appear to be no standard methods for determining dynamic stability derivatives from wind tunnel data. A brief review of the most popular techniques will be summarized here. Significant contributions for estimating aerodynamic parameters theoretically have been made by Tobak, Tobak and Schiff, and Goman [64-68 and 69]. However, limited attempts have been made to estimate aerodynamic parameters from experimental data.

The traditional method is to split the response of the forced oscillation test into in-phase and out-of-phase components [70]. The out-of-phase component provides the damping derivatives while the in-phase component provides the stiffness derivatives.

The small amplitude method measures the response to a small amplitude oscillation about a given axis and integrates the output to obtain the in-phase and out-of-phase components [71]. This method is most popular and has been used a great deal at NASA Langley [31] and by other researchers internationally [72].

Klein and Noderer have implemented the indicial response function as a method for determining unsteady aerodynamic parameters from experimental data [73, 74]. Their method assumes a generic 1st-order form of an indicial response. For example,

$$C_{L_\alpha}(t) = a\left(1 - e^{-b_1 t}\right) + c \ . \tag{2.1}$$

The parameters a, b_1, and c are identified from the experimental data. An extensive body of work detailing this method has been provided by Klein and colleagues [31, 75, 76, and 77].

2.5 Designed Experiments in Wind Tunnel Testing

Experimental design has been particularly beneficial in wind tunnel testing to identify interactions, bias errors, and random errors among many other things. Formal statistical experimental design has its origins in agriculture and life sciences, dating back to the 1920s and 1930s. Other design techniques have been used extensively in industrial settings [78] and for quality improvements during the 1970s [79-81]. The approach has been used by engineers in the manufacturing, chemical processing, and semiconductor industries for decades. More recently engineers have been using designed experiments in aerodynamic wind tunnel testing. It has become popular because the approach is nearly insensitive to the type of test, type of model being used, and is independent of complexities in the wind tunnel. It is arguably more efficient to use designed experiments over one-factor-at-time (OFAT) testing because of reduced cost [82, 83], avoiding wasteful data collection. Using designed experiments is beneficial because of the increased productivity with minimal resources.

Several studies have used designed experiments in various applications of aerodynamic wind tunnel testing. DeLoach was one of the first to use design of experiments (DOE) in a wind tunnel, performing stability configuration testing at the ViGYAN Low Speed Wind Tunnel [84]. Obviously, configuration studies implement several aircraft configuration changes. The end result is a very large test matrix. The study showed substantial systematic errors that would not be present during OFAT testing. Similarly, other configuration studies have used fractional factorial design in order to reduce the amount of data taken [85, 86]. The studies showed that using

blocking, randomization, and replication were particularly beneficial in cryogenic wind tunnels where temperature effects vary greatly.

Several bodies of work have focused on internal and external balance calibration using designed experiments [87, 88]. With the ever increasing demands on high performance aircraft, detailed studies are needed over the entire flight regime. Again, designed experiments are beneficial in studies of high performance aircraft because the entire flight regime can be investigated with minimal resources. For example, Landman et al. studied the X-31 aircraft and performed a characterization study of the blended wing body (BWB) demonstrating the benefits of the approach [88, 89].

2.6 Summary

In conclusion, the literature review surveyed past and current forced oscillation wind tunnel techniques. The chapter discussed single DOF forced oscillation used to capture the unsteady aerodynamic phenomena at high angle of attack. Due to difficulties in obtaining the stability derivatives for the full flight spectrum some researchers have developed multi-DOF forced oscillation. When either testing technique was used, all researchers have shown differences between commanded amplitude and actual motion generated by the test rig. It will be shown that the difference does affect the dynamic stability parameters computed from experimental data. Those differences can either over-predict or under-predict the final result. Besides difficulties in performing forced oscillation testing due to test rig dynamics and aerodynamic/structure interactions other experimental limitations have been discussed. The limitations affect virtually all wind tunnel experiments including, for example, dynamic scaling issues and support interference effects. The chapter also provided a brief overview of popular techniques for

determining stability derivatives from wind tunnel data and concluded with a brief discussion of design experiments being used in wind tunnel experiments. This section supports the use of designed experiments as being of great benefit for aerodynamic test engineers.

CHAPTER 3

THEORETICAL DEVELOPMENT

3.1 Introduction

This chapter details the theoretical development necessary for understanding the pitch forced oscillation simulation. The NASA Langley 12-ft Wind Tunnel dynamic test rig has been chosen as a representative system. A basic dynamic model and test rig is described for this system in order to establish realistic performance data. The test rig is characterized by an AC motor that powers the system and the compliantly-coupled drivetrain. In addition to the motor and drivetrain dynamics, there are several important components such as, PID controllers, current and velocity limiters, gearboxes, pulse-width modulation, filters, and feedback devices. The dynamic behaviors of these components are also discussed, as well as possible problems with their implementation. The dynamic derivatives are determined from experimental data for an F16-XL aircraft that has been used to represent the aerodynamics.

3.2 Forced Oscillation Wind Tunnel Testing

3.2.1 NASA Langley 12-ft Wind Tunnel Dynamic Test Rig (Representative Model)

- *12-foot Low Speed Wind Tunnel*

As a representative wind tunnel, this study examines the forced oscillation dynamic test rig developed at the NASA Langley 12-ft Low-Speed Wind Tunnel. A new forced oscillation system (FOS) was designed to improve operational efficiencies. The new FOS design goals included the ability and flexibility to oscillate a model in

sinusoidal as well as non-sinusoidal motion profiles [32]. There are two baseline fighter model configuration characteristics used at NASA Langley; they are characterized in Table 2 [32].

Table 1: Model Characteristics [32]

Model Class	"90-lb"	"200-lb"
Length, L	1.83 m	3.05 m
Wing Span, b	1.22 m	2.83 m
Mass, M	40.8 kg	90.7 kg
Roll Inertia, I_x	1.36 kg m^2	5.69 kg m^2
Pitch Inertia, I_y	10.71 kg m^2	40.00 kg m^2
Yaw Inertia, I_z	11.39 kg m^2	42.44 kg m^2

For a selected constant reduced frequency and model class the dynamic freestream velocity is usually limited to low speed dynamic pressures [94]. Consequently, the 12-ft wind tunnel was selected as the primary facility for the FOS. The tunnel can operate at dynamic pressures up to 7 psf (U_∞ = 77 ft/sec at sea-level conditions) which corresponds to a unit Reynolds number of approximately 492,000 per foot. The test section has a turbulence level of about 0.6 percent [32]. The test section airflow is produced by a 15.8-ft diameter, 6 blade drive fan powered by a 280 HP, 600 V, 600 rpm DC motor controlled by a 500 Hp AC motor [32].

- *System Description*

Figure 7 shows the FOS installation in the 12-ft wind tunnel. The figure shows a high performance aircraft in the rolled position. The system is capable of both static and dynamic testing. It is also capable of independent α and β combinations. For pitch oscillation testing, the system has an angle of attack range from -5° to 85°. The

maximum pitch capability of the test rig is 260 °/sec pitch rate and 2290 °/sec^2 pitch acceleration. For roll oscillation testing, the system has a range of displacements from ±170 degrees with a maximum capability of 190 °/sec roll rate and 12,750 °/sec^2 roll acceleration.

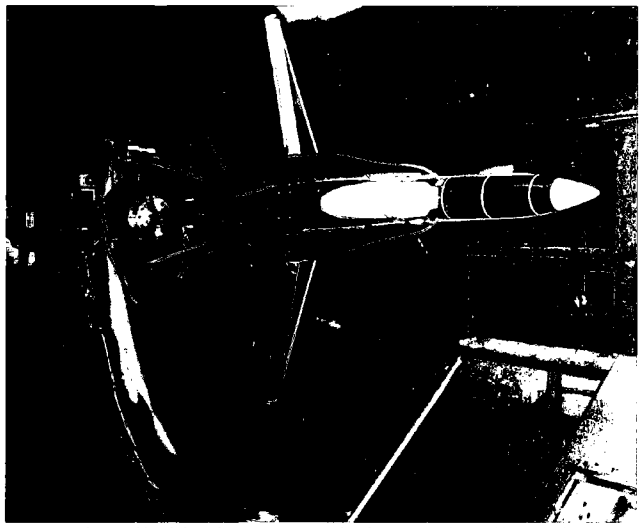

Figure 7: FOS installed in the 12-Ft Wind Tunnel (roll configuration) [95]

Figure 8 shows a schematic of the overall system implemented in the tunnel. The system can be controlled from either the test section or from the control room. Custom software using a LabVIEW-based PXI real-time controller (RTC) was developed to manage the system. Management includes system safety, communication, operations, position motion control, and system feedback. Additional information about the design process and analysis used for the FOS system is contained in [32].

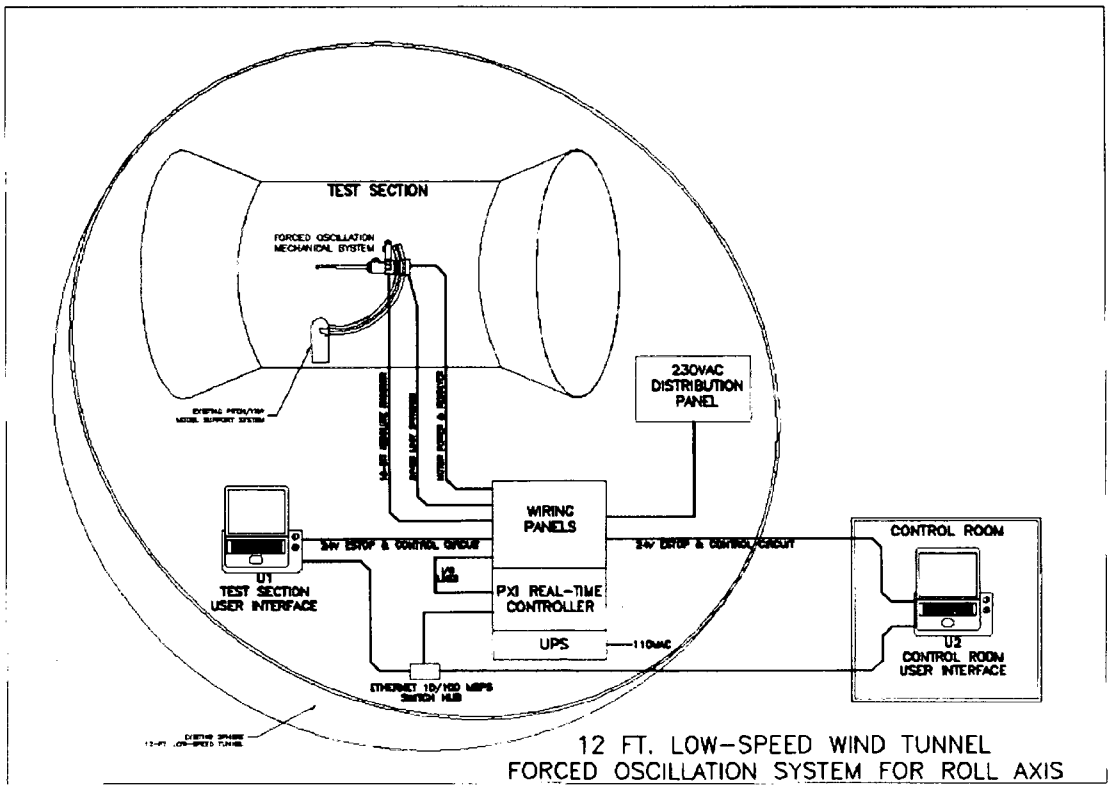

Figure 8: Schematic of the overall FOS in 12-ft wind tunnel [32]

- *Forced Oscillation System Mechanical Subsystem*

Figure 9 illustrates the overall FOS mechanical subsystem. The user prescribes the position motion, and the control algorithm executes a positional, closed-loop algorithm for tracking. The velocity control loop is managed internally using a BDS4 amplifier. The amplifier powers the motor which imparts the desired test article motion via the drive system components.

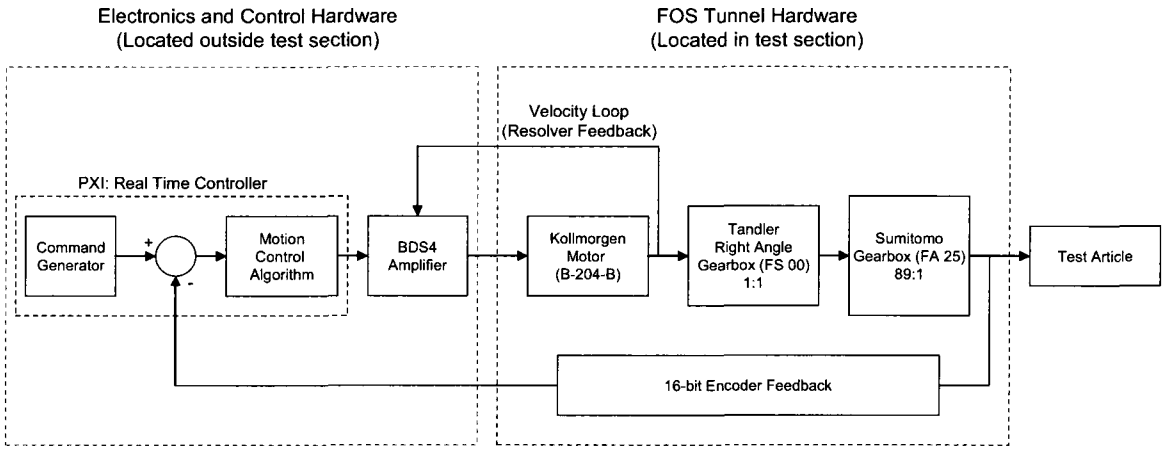

Figure 9: Overall FOS block diagram [95]

Figure 10 shows a cross-section of the FOS mechanical system. This particular configuration is setup for roll dynamic testing. The sting is replaced with a bent sting, as shown in Figure 11, for the pitch dynamic testing configuration. The Kollmorgen B-204-B motor has a maximum speed of 3600 rpm with a peak torque of 13.8 N-m and a continuous stall torque of 4.7 N-m.

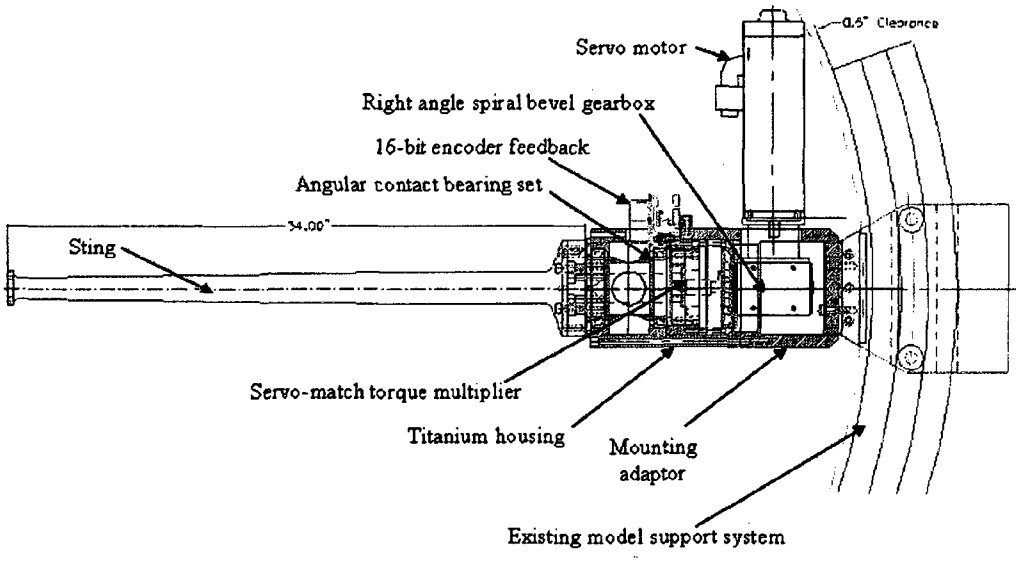

Figure 10: Cross-section of FOS assembly (in roll configuration) [32]

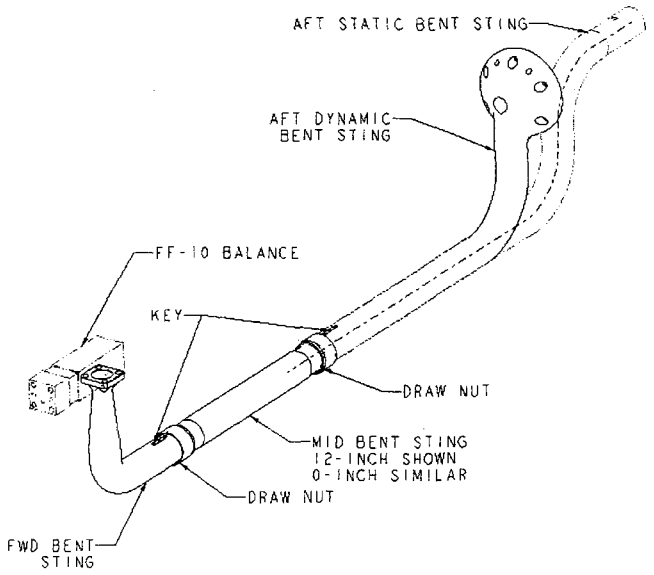

Figure 11: Bent FOS sting assembly [96]

The drive train consists of a Tandler right angle gearbox, Sumitomo servo-match gearbox, sting, and FF-10 balance. The right angle drive is a spiral bevel, which is a bevel gear with helical teeth. It provides a 1:1 gear ratio with low backlash. The right angle gearbox drives the low Sumitomo precision cycloid torque multiplier gearbox. That gearbox provides an 89:1 gearing ratio. The Sumitomo gearbox is attached to the machine drive shaft. The sting shaft, depicted on Figure 14, is used for rolling motion. As mentioned previously, the shaft is replaced with a bent sting for pitching motions – the focus of this study. The shaft is supported by a pair of matched angular contact ball bearings [32]. The ball bearings are used to reduce rotational friction and support radial and axial loads. A 16-bit encoder is attached to the drive shaft to measure the sting angular position and is used for closed-loop motion control. Finally, the FF-10 balance is

used to measure forces and moments during testing. Table 3 lists the balance loading limits.

Table 2: FF-10 Balance Loading Limits

	FF-10 Balance
Normal Force	1780 N (400 lbf)
Axial Force	890 N (200 lbf)
Side Force	890 N (200 lbf)
Roll Moment	141 N-m (1248 in-lbf)
Pitch Moment	226 N-m (2000 in-lbf)
Yaw Moment	226 N-m (2000 in-lbf)

3.2.2 Determining Stability Derivatives from Experimental Data

During a forced oscillation wind tunnel test, the model is constrained to follow a specified position time history. For the longitudinal case, the pitch angle is the same as the angle of attack. Pitch angle and angle of attack are physically the same in the wind tunnel. However, in flight the aircraft is not constrained so that the pitch angle and angle of attack can change independently. This means that in flight the pitch angle, θ, and its rate of change, q, can be very different than the angle of attack, α, and its rate of change $\dot{\alpha}$. Consequently, because the angle of attack and pitch rate are physically the same during a forced oscillation test it is not possible to separate the components associated with pitch rate and $\dot{\alpha}$. Therefore, the stability derivatives, discussed earlier, cannot be measured directly. The stability derivatives will take the form of a combination; for example, $C_{m_\alpha} + C_{m_q}$.

The aerodynamic coefficients are assumed to be linear functions of the angle of attack, pitching velocity, and their associated rates. The increment in the lift coefficient with respect to its mean value is formulated as:

$$\Delta C_L = C_{L_\alpha}\Delta\alpha + \frac{l}{V}C_{L_{\dot\alpha}}\dot\alpha + \frac{l}{V}C_{L_q}q + \left(\frac{l}{V}\right)^2 C_{L_{\dot q}}\dot q . \tag{3.1}$$

For harmonic motion,

$$\begin{aligned} \Delta\alpha &= \alpha_A \sin\omega t \\ \dot\alpha = q &= \omega\alpha_A \cos\omega t \\ \ddot\alpha = \dot q &= -\omega^2\alpha_A \sin\omega t \end{aligned} \tag{3.2}$$

After substituting Equation 3.2 into 3.1,

$$\begin{aligned} \Delta C_L &= \alpha_A\left(C_{L_\alpha} - k^2 C_{L_{\dot q}}\right)\sin\omega t + \alpha_A k\left(C_{L_{\dot\alpha}} + C_{L_q}\right)\cos\omega t \\ &= \alpha_A\left(\overline{C}_{L_\alpha}\sin\omega t + k\overline{C}_{L_q}\cos\omega t\right) \end{aligned} \tag{3.3}$$

where the in-phase and out-of-phase components of lift coefficient have been identified as $\overline{C}_{L_\alpha}$ and $\overline{C}_{L_q}$, respectively. Using the same approach for pitching moment, the in-phase and out-of-phase pitching moment coefficients are, respectively,

$$\begin{aligned} \overline{C}_{m_\alpha} &= C_{m_\alpha} - k^2 C_{m_{\dot q}} \\ \overline{C}_{m_q} &= C_{m_q} + C_{m_{\dot\alpha}} \end{aligned} \tag{3.4}$$

The in-phase and out-of-phase components of lift coefficient are found by integrating the time histories of ΔC_L over a given number of cycles as:

$$\begin{aligned} \overline{C}_{L_\alpha} &= \frac{2}{\alpha_A n_c T}\int_0^{n_c T}\Delta C_L(t)\sin\omega t\, dt \\ \overline{C}_{L_q} &= \frac{2}{\alpha_A n_c k T}\int_0^{n_c T}\Delta C_L(t)\cos\omega t\, dt \end{aligned} \tag{3.5}$$

where $T = 2\pi/\omega$ is the period. The same approach is used to compute the in-phase and out-of-phase components for pitching moment, so that:

$$\overline{C}_{m_\alpha} = \frac{2}{\alpha_A n_c T} \int_0^{n_c T} \Delta C_m(t) \sin \omega t \; dt$$
$$\overline{C}_{m_q} = \frac{2}{\alpha_A n_c k T} \int_0^{n_c T} \Delta C_m(t) \cos \omega t \; dt \qquad (3.6)$$

Equations 3.5 and 3.6 have assumed that the sine waveform is of high fidelity.

3.3 Three-Phase AC Induction Motor Model

The induction motor is one of the most common types of motors in existence. It is widely used because of its good self-starting capability, simple and rugged structure, low cost, and reliability [97]. A Kollmorgen B-204-B, three-phase induction motor is currently being used by the NASA LaRC 12-ft wind tunnel to actuate the forced oscillation motion. An idealized model of that motor is illustrated in Figure 12.

The primary working principle of an induction motor is quite simple. The revolving magnetic fields in the stator cause the rotor to turn, providing the necessary torque. The rotating fields create out-of-phase voltages in the stator windings. The three applied voltages are 120-degrees out-of-phase with each other; this produces the three phases, typically called a, b, and c phases. Also, the number of poles determines how many times the magnetic field in the stator revolves for any given generated frequency. For example, a general induction motor, with 4-poles and 60 Hz supplied frequency, will typically have a stator rotating field speed of 1,800 rpm, where the synchronous speed of the motor is computed in terms of supplied frequency, f [Hz], and the number of poles as,

$$n_s = \frac{120 \cdot f}{p} \; . \qquad (3.7)$$

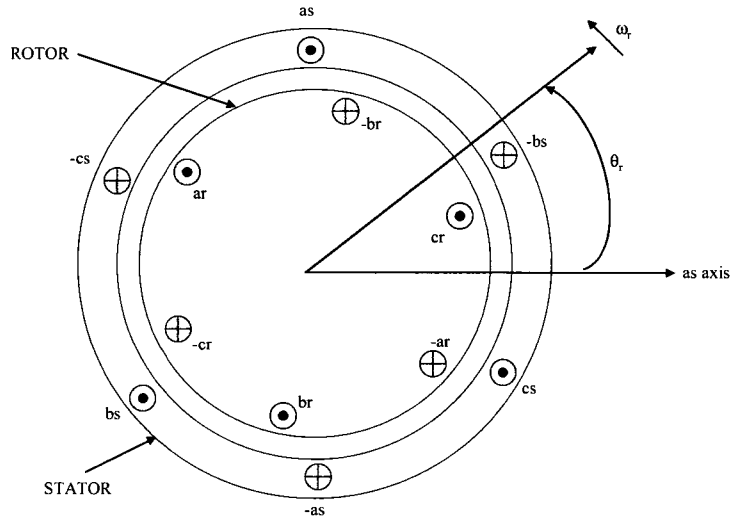

Figure 12: Idealized circuit model of a 2-pole 3-phase induction machine [99]

The following assumptions were made about the FOS motor [98]:

1. Squirrel cage type – The cage winding always reacts by producing the rotor field having the same number of poles as the inducing stator field. It also assumes the rotor voltages are zero.
2. Symmetrical – The stator windings are identical, sinusoidally distributed, and displaced 120°, with n_s equivalent turns and stator resistance r_s. Similarly, the rotor windings or bars are considered as three identical, sinusoidally distributed, displaced 120°, with n_r equivalent turns and rotor resistance r_r.
3. Wye-connected – Assumes that the motor has the following circuitry illustrated in Figure 13.

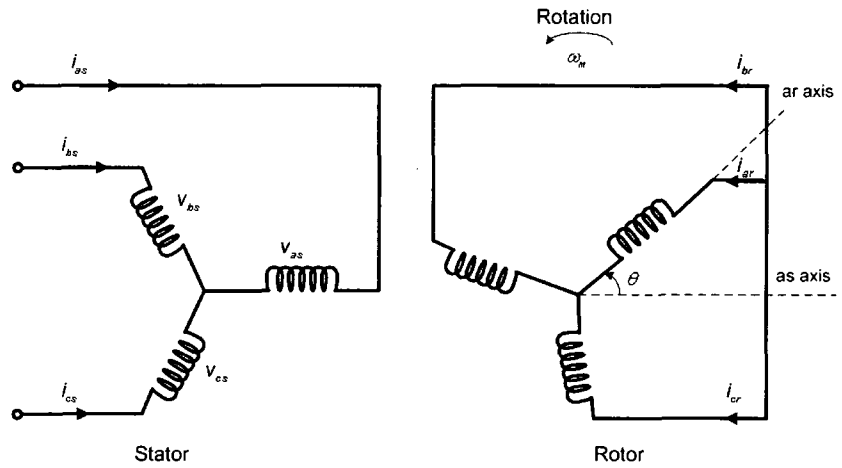

Figure 13: Three-phase coupled circuit representation of an induction motor [99]

4. Balanced – Assumes that a balanced 3-phase set is generally defined as a set of equal-amplitude sinusoidal quantities which are displaced by 120°. In mathematical terms $f_{as} + f_{bs} + f_{cs} = 0$; therefore, $f_{0s} = 0$ where f is an arbitrary variable that can represent either voltage or current depending on the type of inverter used for the motor.
5. Uniform air gap – Assumes that the air gap between the rotor and stator is uniform.
6. Stationary stator frame – Assumes that the stator is fixed ($\omega_s = 0$).

These assumptions represent an oversimplification which cannot describe the behavior of induction machines in all modes of operation. However, for this application its behavior can be adequately predicted using this simplified representation.

3.3.1 Reference Frame

The goal of the reference frame theory is related primarily to a change of variables used in the analysis of AC machines to eliminate time-varying variables. This method was introduced by R.H. Park in the late 1920s [100]. He formulated a change of

variables which, in effect, replaced the variables (voltages, currents, and flux linkages) associated with the stator windings of synchronous machines with variables associated with fictitious windings rotating with the rotor. In other words, the stator variables are transformed to a frame of reference fixed in the rotor; this is called Park's transformation. The transformation has the unique property of eliminating all time-varying inductances from the voltage equations of the synchronous machine which occur due to:

1. Electric circuits in relative motion and
2. Electric circuits with varying magnetic reluctance.

Additional transformations have been developed by Stanley, Kron, Brereton, and Clark for specific applications such as an induction machine with a fixed stator [100]. However, each transformation is based on Park's transformation. Other types of transformations are illustrated in Figure 14.

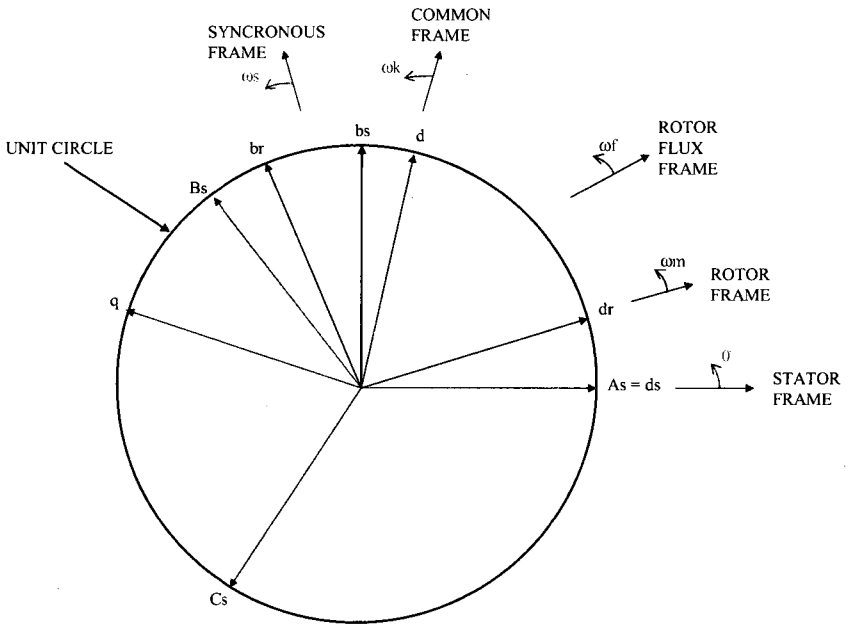

Figure 14: Reference frames in AC machine analysis [99]

After the transformation(s), the reference frame is typically called the arbitrary reference frame or d-q reference frame. Table 3 provides a list of commonly used reference frames in the analysis of AC machines; namely, the arbitrary, stationary, rotor, and synchronous reference frames and their associated notation.

Table 3: Notation of commonly used reference frames [100]

		Notation	
Reference Frame of Speed	Interpretation	Variables	Transformation
ω (unspecified)	Stationary circuit variables referred to the arbitrary reference frame.	$\vec{f}_{qd0s}$	$\overline{\overline{K}}_s$
0	Stationary circuit variables referred to the stationary reference frame.	$\vec{f}^{\,s}_{qd0s}$	$\overline{\overline{K}}^{s}_{s}$
ω_r	Stationary circuit variables referred to a reference frame fixed in the rotor.	$\vec{f}^{\,r}_{qd0s}$	$\overline{\overline{K}}^{r}_{s}$
ω_e	Stationary circuit variables referred to the synchronously rotating reference frame.	$\vec{f}^{\,e}_{qd0s}$	$\overline{\overline{K}}^{e}_{s}$

The transformation of the 3-phase stator variables into the arbitrary frame is:

$$\vec{f}_{dq0s} = \overline{\overline{K}}_s \vec{f}_{abcs} \tag{3.8}$$

where

$$\left(\vec{f}_{qd0s}\right)^T = \begin{bmatrix} f_{qs} & f_{ds} & f_{0s} \end{bmatrix} \tag{3.9}$$

$$\left(\vec{f}_{abcs}\right)^T = \begin{bmatrix} f_{as} & f_{bs} & f_{cs} \end{bmatrix}, \tag{3.10}$$

and

$$\overline{\overline{K}}_s = \frac{2}{3}\begin{bmatrix} \cos\theta & \cos\left(\theta - \frac{2\pi}{3}\right) & \cos\left(\theta + \frac{2\pi}{3}\right) \\ \sin\theta & \sin\left(\theta - \frac{2\pi}{3}\right) & \sin\left(\theta + \frac{2\pi}{3}\right) \\ \frac{1}{2} & \frac{1}{2} & \frac{1}{2} \end{bmatrix}. \tag{3.11}$$

$$\theta = \int_0^t \omega(\xi) \cdot d\xi + \theta(0) \tag{3.12}$$

where ξ is a dummy variable of integration. In the above equations, f can represent voltage, current, flux linkage, or electric charge. The superscript, T, denotes the transpose of a matrix. The s subscript indicates the variables, parameters, and transformation associated with stationary circuits. The angular displacement, θ, must be continuous in time. However, the angular velocity associated with the change of variables is unspecified. The frame of reference may rotate at any constant or varying angular velocity or it may remain stationary. The arbitrary connotation stems from the fact that the angular velocity of the transformation is unspecified and can be selected arbitrarily in order to expedite the solution of system equations or to satisfy the system constraints. The change of variables may be applied to variables for any waveform and time sequence; however, the transformation is typically appropriate for an *abc* sequence [100]. For completeness the other transformations in Table 4 are provided.

$$\overline{\overline{K_s^s}} = \frac{2}{3}\begin{bmatrix} 1 & -1/2 & -1/2 \\ 0 & \sqrt{3}/2 & -\sqrt{3}/2 \\ 1/2 & 1/2 & 1/2 \end{bmatrix} \tag{3.13}$$

This equation assumes that $\omega = 0$ ($\theta = 0$). Since the motor is assumed to be balanced (i.e. $f_{as} + f_{bs} + f_{cs} = 0$, *so* $f_{0s} = 0$), it reduces to the Clark transformation,

$$\overline{\overline{K_s^s}} = \frac{2}{3}\begin{bmatrix} 1 & -1/2 & -1/2 \\ 0 & \sqrt{3}/2 & -\sqrt{3}/2 \end{bmatrix}. \tag{3.14}$$

If $\omega = \omega_e$ ($\theta = \theta_e$), the transformation becomes:

$$\overline{\overline{K_s^e}} = \frac{2}{3}\begin{bmatrix} \cos\theta_e & \cos(\theta_e - 2\pi/3) & \cos(\theta_e + 2\pi/3) \\ -\sin\theta_e & -\sin(\theta_e - 2\pi/3) & -\sin(\theta_e + 2\pi/3) \\ 1/2 & 1/2 & 1/2 \end{bmatrix}. \tag{3.15}$$

Again, when the motor is balanced that equation becomes,

$$\overline{\overline{K_s^e}} = \frac{2}{3}\begin{bmatrix} \cos\theta_e & \cos(\theta_e - 2\pi/3) & \cos(\theta_e + 2\pi/3) \\ -\sin\theta_e & -\sin(\theta_e - 2\pi/3) & -\sin(\theta_e + 2\pi/3) \end{bmatrix}. \tag{3.16}$$

The matrix $\overline{\overline{K_s^r}}$ is similar to Equations 3.66 and 3.67; however, $\omega = \omega_r$ ($\theta = \theta_r$) instead.

3.3.2 Induction Machine Dynamic Model

Traditionally, the equations of motion for an AC motor have been defined in the *abc* reference frame. The voltage equations are expressed in machine variables (i.e. current, voltage, and flux linkage). In the following equations, the s subscript denotes variables and parameters associated with the stator circuits, and the r-subscript denotes variables and parameters associated with the rotor circuits. Both $\mathbf{r}_s$ and $\mathbf{r}_r$ are diagonal matrices, each with equal nonzero elements [100].

$$\vec{v}_{abcs} = \vec{r}_s \vec{i}_{abcs} + \frac{d\vec{\lambda}}{dt} \tag{3.17}$$

$$\vec{v}_{abcr} = \vec{r}_r \vec{i}_{abcr} + \frac{d\vec{\lambda}}{dt} \tag{3.18}$$

For a magnetically linear system, the flux linkages are expressed as

$$\begin{bmatrix} \vec{\lambda}_{abcs} \\ \vec{\lambda}_{abcr} \end{bmatrix} = \begin{bmatrix} \overline{\overline{L}}_s & \overline{\overline{L}}_{sr} \\ \left(\overline{\overline{L}}_{sr}\right)^T & \overline{\overline{L}}_r \end{bmatrix} \begin{bmatrix} \vec{i}_{abcs} \\ \vec{i}_{abcr} \end{bmatrix}. \tag{3.19}$$

Then, the winding inductances are defined as follows:

$$\overline{\overline{L}}_s = \begin{bmatrix} L_{ls}+L_{ms} & -\frac{1}{2}L_{ms} & -\frac{1}{2}L_{ms} \\ -\frac{1}{2}L_{ms} & L_{ls}+L_{ms} & -\frac{1}{2}L_{ms} \\ -\frac{1}{2}L_{ms} & -\frac{1}{2}L_{ms} & L_{ls}+L_{ms} \end{bmatrix} \tag{3.20}$$

$$\overline{\overline{L}}_r = \begin{bmatrix} L_{lr}+L_{mr} & -\frac{1}{2}L_{mr} & -\frac{1}{2}L_{mr} \\ -\frac{1}{2}L_{mr} & L_{lr}+L_{mr} & -\frac{1}{2}L_{mr} \\ -\frac{1}{2}L_{mr} & -\frac{1}{2}L_{mr} & L_{lr}+L_{mr} \end{bmatrix} \tag{3.21}$$

$$\overline{\overline{L}}_{sr} = L_{sr}\begin{bmatrix} \cos\theta_r & \cos(\theta_r+2\pi/3) & \cos(\theta_r-2\pi/3) \\ \cos(\theta_r-2\pi/3) & \cos\theta_r & \cos(\theta_r+2\pi/3) \\ \cos(\theta_r+2\pi/3) & \cos(\theta_r-2\pi/3) & \cos\theta_r \end{bmatrix}. \tag{3.22}$$

Here, L_{ls} and L_{ms} are the leakage and magnetizing inductance of the stator and windings, respectively. Also, L_{lr} and L_{mr} are for the rotor windings. The inductance L_{sr} is the amplitude of the mutual inductances between the stator and rotor windings. It is more convenient to refer all rotor variables to the stator windings by appropriate turn ratios [100].

$$\vec{i}'_{abcr} = \frac{N_r}{N_s}\vec{i}_{abcr} \tag{3.23}$$

$$\vec{v}'_{abcr} = \frac{N_s}{N_r}\vec{v}_{abcr} \tag{3.24}$$

$$\vec{\lambda}'_{abcr} = \frac{N_s}{N_r}\vec{\lambda}_{abcr} \tag{3.25}$$

The magnetizing and mutual inductances are set as

$$L_{ms} = \frac{N_s}{N_r}L_{sr} \tag{3.26}$$

$$\overline{\overline{L'}}_{sr} = \frac{N_s}{N_r}\overline{\overline{L}}_{sr} = L_{ms}\begin{bmatrix} \cos\theta_r & \cos(\theta_r + 2\pi/3) & \cos(\theta_r - 2\pi/3) \\ \cos(\theta_r - 2\pi/3) & \cos\theta_r & \cos(\theta_r + 2\pi/3) \\ \cos(\theta_r + 2\pi/3) & \cos(\theta_r - 2\pi/3) & \cos\theta_r \end{bmatrix} \tag{3.27}$$

$$L_{mr} = \left(\frac{N_r}{N_s}\right)^2 L_{ms}. \tag{3.28}$$

Finally we let

$$\overline{\overline{L'}}_r = \left(\frac{N_s}{N_r}\right)^2 \overline{\overline{L}}_r. \tag{3.29}$$

Then,

$$\overline{\overline{L'_r}} = \begin{bmatrix} L'_{lr} + L_{ms} & -\frac{1}{2}L_{ms} & -\frac{1}{2}L_{ms} \\ -\frac{1}{2}L_{ms} & L'_{lr} + L_{ms} & -\frac{1}{2}L_{ms} \\ -\frac{1}{2}L_{ms} & -\frac{1}{2}L_{ms} & L'_{lr} + L_{ms} \end{bmatrix} \tag{3.30}$$

where

$$L'_{lr} = \left(\frac{N_s}{N_r}\right)^2 L_{lr}. \tag{3.31}$$

The flux linkages can be expressed as

$$\begin{bmatrix} \vec{\lambda}_{abcs} \\ \vec{\lambda}'_{abcr} \end{bmatrix} = \begin{bmatrix} \overline{\overline{L}}_s & \overline{\overline{L'_{sr}}} \\ \left(\overline{\overline{L'_{sr}}}\right)^T & \overline{\overline{L'_r}} \end{bmatrix} \begin{bmatrix} \vec{i}_{abcs} \\ \vec{i}_{abcr} \end{bmatrix}. \tag{3.32}$$

Finally, the voltage equations are expressed in terms of machine variables referred to the stator windings as,

$$\begin{bmatrix} \vec{v}_{abcs} \\ \vec{v}_{abcr} \end{bmatrix} = \begin{bmatrix} \vec{r}_s + \frac{d\overline{\overline{L}}_s}{dt} & \frac{d\overline{\overline{L'_{sr}}}}{dt} \\ \frac{d\left(\overline{\overline{L'_{sr}}}\right)^T}{dt} & \vec{r}'_r + \frac{d\overline{\overline{L'_r}}}{dt} \end{bmatrix} \tag{3.33}$$

where

$$\vec{r}_r' = \left(\frac{N_s}{N_r}\right)^2 \vec{r}_r . \tag{3.34}$$

Following the steps outlined by Krause [100], the torque equation, in terms of machine variables, is written:

$$T_e = \left(\frac{P}{2}\right)\left(\vec{i}_{abcs}\right)^T \frac{\partial}{\partial \theta_r}\left[\overline{\overline{L_{sr}'}}\right]\cdot \vec{i}_{abcr}' . \tag{3.35}$$

Also note that the torque and rotor speed are related by

$$T_e = J\left(\frac{2}{P}\right)\frac{d\omega_r}{dt} + T_L . \tag{3.36}$$

The previous section has outlined the use of the so-called arbitrary reference frame transformation and its application to stationary circuits. The equivalent circuit for an AC motor in the dq frame is shown schematically in Figure 15. Note that in Figure 15, F_{ij} is the same as λ_{ij}.

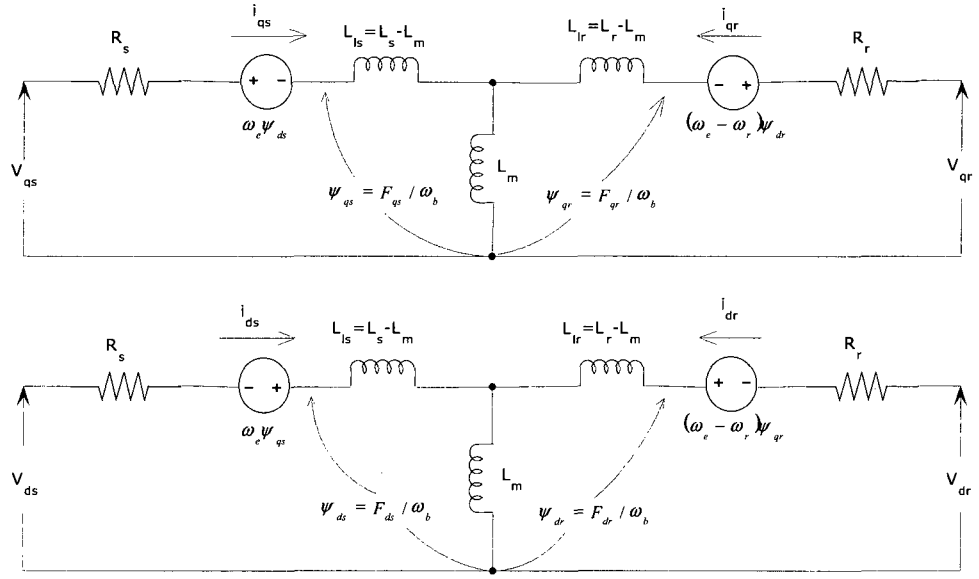

Figure 15: Equivalent circuit dq frame

Applying the same approach and rewriting the equations of motion for an AC motor in terms of reactances rather than inductances, the equations of motion become Equations 3.37 to 3.42. It should be noted that the zero phase terms have been dropped since the motor is assumed to be balanced.

$$\frac{d\lambda_{qs}}{dt} = \omega_b\left[v_{qs} - \frac{\omega_e}{\omega_b}\lambda_{ds} + \frac{R_s}{X_{ls}}\left(\lambda_{mq} + \lambda_{qs}\right)\right] \tag{3.37}$$

$$\frac{d\lambda_{ds}}{dt} = \omega_b\left[v_{ds} + \frac{\omega_e}{\omega_b}\lambda_{qs} + \frac{R_s}{X_{ls}}\left(\lambda_{md} + \lambda_{ds}\right)\right] \tag{3.38}$$

$$\frac{d\lambda_{qr}}{dt} = \omega_b\left[v_{qr} - \frac{\left(\omega_e - \omega_r\right)}{\omega_b}\lambda_{dr} + \frac{R_r}{X_{lr}}\left(\lambda_{mq} - \lambda_{qr}\right)\right] \tag{3.39}$$

$$\frac{d\lambda_{dr}}{dt} = \omega_b\left[v_{dr} + \frac{\left(\omega_e - \omega_r\right)}{\omega_b}\lambda_{qr} + \frac{R_r}{X_{lr}}\left(\lambda_{md} - \lambda_{dr}\right)\right] \tag{3.40}$$

$$\lambda_{mq} = X_{ml}^{*}\left[\frac{\lambda_{qs}}{X_{ls}} + \frac{\lambda_{qr}}{X_{lr}}\right] \tag{3.41}$$

$$\lambda_{md} = X_{ls}^{*}\left[\frac{\lambda_{ds}}{X_{ls}} + \frac{\lambda_{dr}}{X_{lr}}\right] \tag{3.42}$$

Then, the current and torque equations can be written:

$$i_{qs} = \frac{1}{X_{ls}}\left(\lambda_{qs} - \lambda_{mq}\right) \tag{3.43}$$

$$i_{ds} = \frac{1}{X_{ls}}\left(\lambda_{ds} - \lambda_{md}\right) \tag{3.44}$$

$$i_{qr} = \frac{1}{X_{lr}}\left(\lambda_{qr} - \lambda_{mq}\right) \tag{3.45}$$

$$i_{dr} = \frac{1}{X_{lr}}(\lambda_{dr} - \lambda_{md}) \tag{3.46}$$

$$T_e = \frac{3}{2}\left(\frac{p}{2}\right)\frac{1}{\omega_b}\left(\lambda_{ds} i_{qs} - \lambda_{qs} i_{ds}\right) \tag{3.47}$$

$$T_e - T_L = J\left(\frac{2}{p}\right)\frac{d\omega_r}{dt}. \tag{3.48}$$

The flux linkage rate equations have been derived in detail by Krause [100]. Assuming the motor is a squirrel cage induction machine, the rotor voltages, v_{qr} and v_{dr}, in Equations (3.39) and (3.40) are set to zero. Next, these equations have been recast into state-space form.

State-space form is obtained by substituting Equations (3.41) and (3.42) into (3.37 – 3.42) and collecting similar terms. The state vector is $x = \left[\lambda_{qs} \quad \lambda_{ds} \quad \lambda_{qr} \quad \lambda_{dr} \quad \omega_r\right]^T$. Also note that $\lambda_{ij} = \psi_{ij} \cdot \omega_b$, where λ_{ij} is the flux linkage (where i = q or d and j = s or r), and ψ_{ij} is the flux. Then, the model equations are as follows:

$$\frac{d\lambda_{qs}}{dt} = \omega_b\left[v_{qs} - \frac{\omega_e}{\omega_b}\lambda_{ds} + \frac{R_s}{X_{ls}}\left(\frac{X^*_{ml}}{X_{lr}}\lambda_{qr} + \left(\frac{X^*_{ml}}{X_{lr}} - 1\right)\lambda_{qs}\right)\right] \tag{3.49}$$

$$\frac{d\lambda_{ds}}{dt} = \omega_b\left[v_{ds} + \frac{\omega_e}{\omega_b}F_{qs} + \frac{R_s}{X_{ls}}\left(\frac{X^*_{ml}}{X_{lr}}\lambda_{dr} + \left(\frac{X^*_{ml}}{X_{lr}} - 1\right)\lambda_{ds}\right)\right] \tag{3.50}$$

$$\frac{d\lambda_{qr}}{dt} = \omega_b\left[-\frac{(\omega_e - \omega_r)}{\omega_b}\lambda_{dr} + \frac{R_r}{X_{lr}}\left(\frac{X^*_{ml}}{X_{ls}}\lambda_{qs} + \left(\frac{X^*_{ml}}{X_{lr}} - 1\right)\lambda_{qr}\right)\right] \tag{3.51}$$

$$\frac{d\lambda_{dr}}{dt} = \omega_b\left[\frac{(\omega_e - \omega_r)}{\omega_b}\lambda_{qr} + \frac{R_r}{X_{lr}}\left(\frac{X^*_{ml}}{X_{ls}}\lambda_{ds} + \left(\frac{X^*_{ml}}{X_{lr}} - 1\right)\lambda_{dr}\right)\right] \tag{3.52}$$

$$\frac{d\omega_r}{dt} = \left(\frac{p}{2J}\right)(T_e - T_L) \; . \tag{3.53}$$

3.3.3 Field Oriented Control of Induction Machines

The main objective of vector control, also called field orientation control, is to independently control the generated torque and flux like a direct-current (DC) motor using separately excited states [101]. The transformation matrix, discussed previously, is used mainly to transform the physical *abc* variables into the *dq* variables. In the *dq* frame, all balanced sinusoidal variables can be viewed as DC quantities. Also, in vector control schemes the synchronous rotation rotor flux angle is a required instantaneous variable because it is used to transform the *abc* frame into the synchronously rotating *dq* frame. There are two main approaches to obtain this angle: direct and indirect schemes.

In the direct scheme, a flux sensor (i.e. Hall sensor) is employed directly to compute the rotating rotor flux angle. However, it may not be practical to implement this scheme due to the difficult installation of the flux sensor in the air gap inside the induction machine [102]. In the indirect scheme, slip must be computed by the controller and a speed sensor is required. With this information, the rotating rotor flux angle can be computed indirectly. In other words, the slip relation must appear in the indirect scheme [102]. For this study, the simulation uses the indirect scheme for vector control. Figure 16 is a schematic showing this implementation of indirect vector control.

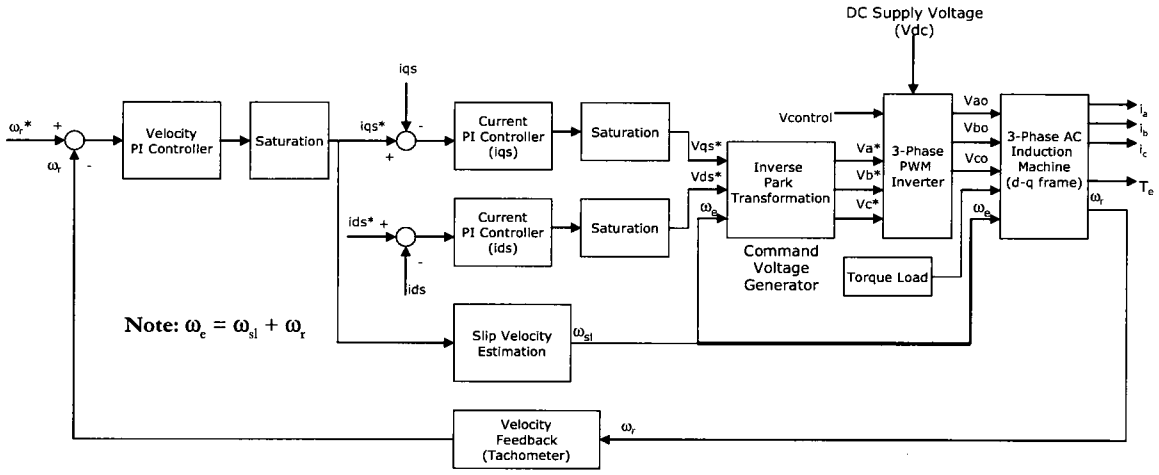

Figure 16: Indirect vector control schematic

The slip is estimated by

$$\omega_{sl} = s = \frac{\omega_e - \omega_r}{\omega_e} = \frac{L_m}{\tau_r}\frac{i_{qs}^e}{\lambda_{dr}^e} \tag{3.54}$$

where, $\tau_r = L_r / r_r$ is called the rotor time constant.

The benefit of using vector control over frequency or phase control techniques is that those techniques are primarily steady-state. Steady-state solutions are not appropriate for predicting dynamic performance of the motor. The vector control technique allows one to model transients.

Figure 20 includes additional components that have not yet been discussed. One element is a pulse width modulation inverter (PWM). The others are cascaded PID controllers and velocity and current limiter components. The limiters are represented as saturation components. Each component will be discussed to conclude the chapter. Smaller components, not shown in Figure 16, include filters, encoders, and tachometers which will also be discussed.

3.3.4 Additional Components

- *Pulse Width Modulation*

AC motors are often powered by inverters. The inverter converts DC power to AC power at the required frequency and amplitude. A typical 3-phase inverter is illustrated in Figure 17.

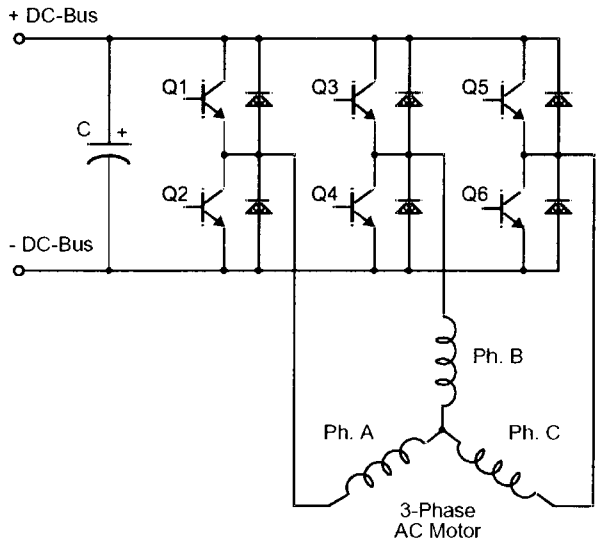

Figure 17: Typical 3-phase inverter

The inverter consists of three half-bridge units where the upper and lower switches are linked to operate as polar opposites, meaning that when the upper switch is turned on, the lower switch must be turned off and vice versa. Since the power device off time is longer than its on time, some dead time must be utilized between the time one transistor of the half-bridge is deactivated and its complementary device is activated. The output voltage is created primarily by a pulse width modulation technique, where an isosceles triangle carrier wave is compared with a fundamental-frequency sine modulating wave. The natural points of intersection determine the switching points of the

power devices of a half-bridge inverter. This technique is shown in Figure 18. The 3-phase voltage waves are shifted 120° with respect to one another; thus, a 3-phase motor can be powered.

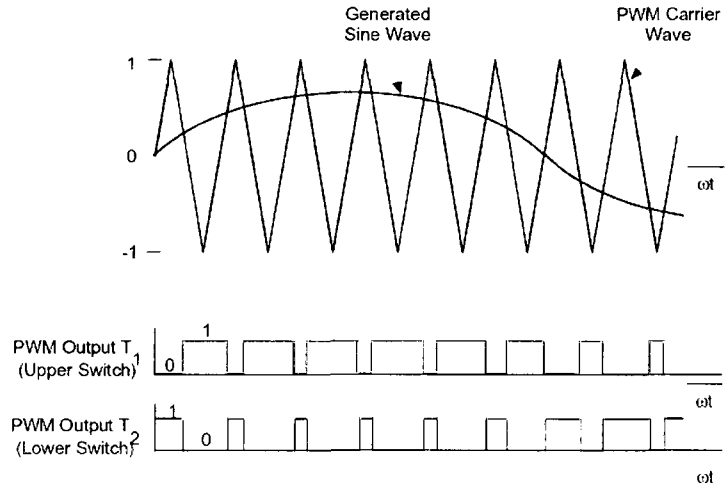

Figure 18: Pulse width modulation (PWM) operation

PWM has a significant problem associated with generating harmonics. The harmonics look like a sine wave with harmonic content. Generally, for a three-phase AC induction motor neither the 3rd-order harmonic components nor multiples of 3 are produced. Traditionally, these "triplen" harmonics cause distortion and heating effects. This causes motor losses and affects overall performance [103].

- *Three-term Controllers and Multi-loop Feedback Control*

Proportional, Integral, Derivative (PID) controllers were first developed by Callender et al. in 1936 [104]. The technology was based primarily on experimental work and simple linearized approximations of systems [105]. Over time, PID controllers have become one of the most popular controllers for three reasons: (1) their past record of success, (2) their wide availability, and (3) their simplicity in use [106].

The proportional term, also called the gain, adjusts the output proportional with the error value. That gain is denoted with the constant, K_p. The representation of proportional control is given in the time and Laplace domains.

$$\begin{aligned} &\textit{Time Domain}: && u_c(t) = K_P e(t) \\ &\textit{Laplace Domain}: && U_c(s) = K_P E(s) \end{aligned} \tag{3.55}$$

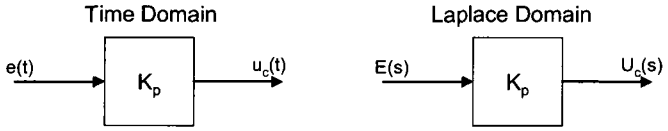

Figure 19: Block diagrams for proportional control term

The integral term, sometimes called reset, is used to correct for any steady-state offset from a constant reference signal value. The time and Laplace domains representations for integral control are given as:

$$\begin{aligned} &\textit{Time Domain}: && u_c(t) = K_I \int^{t} e(\tau) d\tau \\ &\textit{Laplace Domain}: && U_c(s) = \left[\frac{K_I}{s}\right] E(s) \end{aligned} \tag{3.56}$$

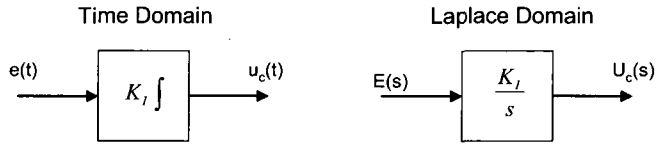

Figure 20: Block diagrams for integral control term

Finally, the derivative term, sometimes called the rate, is used to control the rate of change of the error signal. The time and Laplace domains for derivative control are given as:

$$\begin{aligned} &\textit{Time Domain}: \quad u_c(t) = K_D \frac{de}{dt} \\ &\textit{Laplace Domain}: \; U_c(s) = [K_D s] E(s) \end{aligned} \quad . \tag{3.57}$$

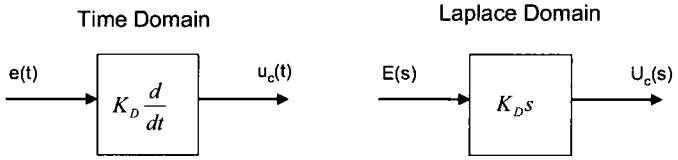

Figure 21: Block diagrams for derivative control term

The basic Laplace domain representation for a parallel PID controller, also known as a decoupled PID, is given in Equation 3.109. This form is the classical textbook case because it lacks any modifications that can be present in a real system. For example, the derivative term is usually not implemented due to adverse noise amplification properties [106]. The general architecture for the parallel PID controller is represented in Figure 22.

$$U_c(s) = \left[K_p + K_I \frac{1}{s} + K_D s \right] E(s) \tag{3.58}$$

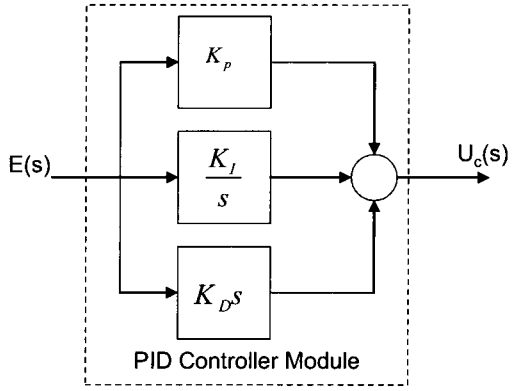

Figure 22: Parallel PID architecture

- *PID Controller Tuning*

Tuning a single PID controller is quite simple. Several methods exist such as manual method, Ziegler-Nichols method, and loop optimization software [106]. For this study the manual method was used for simplicity and because the system could not be tuned using a standard step response input.

The manual process for tuning a PID controller is to first set all the gains to zero, adjusting subsequently the proportional gain until the system is responsive to input changes without overshoot or divergence. Next, the integral gain is increased until the errors disappear. Finally, the differential gain is increased in order to accelerate the system response.

Re-examining Figure 22, it is clear that the PID controllers have been implemented in different loops for cascaded control. There are two reasons for this type of control system [106]:

1. To use the inner measure to attenuate the effect of supply disturbances or any internal process disturbance on the outer process in the sequence.
2. To use the outer process measurement to control the process final output quality.

Tuning cascaded PID controllers becomes more complex when the system is sensitive to instabilities as is the present case. The inner loop is tuned first by adjusting the proportional gain for speed of response or, if that is inadequate, tuned for proportional and integral gains to remove low-frequency supply disturbance signals [106]. After the inner loop is tuned, it functions like a low-pass filter within the outer loop [107]. Note that each loop operates over a different frequency range, so once the inner loop is tuned there is little need to return to it. Finally, the outer loop is tuned. Each loop needs to be

as responsive as possible because it becomes a barrier to the next higher outer loop [107]. Typically, cascade control structures often take the form of PI/P or PI/PI [106]. Derivative gain is usually avoided due to the presence of a significant measurement of noise.

- *PID Control Issues*

There are several common problems in the implementation of a PID controller. Table 5 summarizes the common process control problems and the appropriate PID implementation [106]. It should be noted that some of these problems are not applicable to a simulation study; however, they can possibly occur in real applications. As a result, it is useful to discuss these aspects for improving the fidelity of actual forced oscillation wind tunnel test techniques. Since modification is required for the parallel PID controller to operate effectively consideration is given to some common modifications: bandwidth-limited derivative control, proportional and derivative kick modifications, anti-windup circuit design, and reverse acting control [106]. Each modification will be discussed in a qualitative sense. The mathematical development of the modifications can be reviewed in [106] and are summarized in Table 4.

Table 4: Summary of process control problems and implementing the PID controller [Taken from 106]

Process Control Problem	PID Controller Solution
Measurement Noise	
▪ Significant measurement noise on process variable in the feedback loop ▪ Noise amplified by the pure derivative term ▪ Noise signals look like high frequency signals	▪ Replace the pure derivative term by a bandwidth limited derivative term ▪ This prevents measurement noise amplification
Proportional and Derivative Kick	
▪ P- and D-terms used in the forward path ▪ Step references causing rapid changes and spikes in the control signal ▪ Control signals are causing problems or outages with actuator unit.	▪ Move the proportional and derivative terms into feedback path ▪ This leads to the different forms of PID controllers

Nonlinear Effects ▪ Saturation characteristics present in actuators ▪ Leads to integral windup and causes excessive overshoot	▪ Use anti-windup circuits in the integral term of the PID controller ▪ These circuits are often present and used without the installer being aware of their use
Negative Process Gain ▪ A positive step change produces a negative response ▪ Negative feedback with such a process gives a closed-loop unstable process	▪ Use the option of a reverse acting PID controller structure

When a measured process contains excessive noise, the noise is modeled as a high frequency phenomenon. The noise is then amplified through the derivative term in the controller. Since this is highly undesirable, a low-pass filter is often placed in the derivative term to remedy the problem.

Another problem is *proportional kick* which occurs because of rapid changes in the reference signal when the PID controller is in a parallel structure format. The solution is simply to restructure the controller by placing the proportional term into the feedback path. The derivative kick is similar to the proportional kick problem.

There are many sources of nonlinearity that can affect the performance of the PID controller. One common source is that the process plant is nonlinear. Consequently, there are different operating conditions with different dynamics. The typical remedy is gain or controller scheduling. Another issue is actuator saturation and windup. All actuators have physical limitations; for example, a motor has limited velocity, which can have severe consequences. The integral term goes into windup, an unstable mode [109]. The feedback loop cannot function, and the actuator saturates; the process will revert to open-loop control. Open-loop control can be dangerous if the system is unstable. The process can also exhibit excessive overshoot in the process output. Also, the integrator

windup will delay the control action until the controller returns to an unsaturated state. The solution to the problem is to effectively switch off the integral module when the system saturates. The integral term is then recovered when the controller reenters its linear operating region. Anti-windup circuitry is used to achieve this goal [109].

Some processes have very complex dynamics and can produce inverse responses. This occurs when a positive step change at the input causes the output response to go negative and then recover to finish positive [106]. That process behavior usually has a physical origin where two competing effects, a fast dynamic effect and a slow dynamic effect, conspire to produce the negative start [109]. The remedy is quite simple. An additional gain of [-1] is placed at the output of the controller to maintain a negative feedback loop.

- *Controller Saturation*

As mentioned previously, all actuators have physical limitations. Consequently, engineers who design controllers for motors have included position limiters, velocity limiters and current limiters within the control loops. Position controllers are designed to hold the position commanded from an external source at the desired position. Velocity limiters avoid reaching excessive motor speeds. The velocity limiter is placed after the output of the velocity PID controller. If the motor stalls, the generated current can become dangerously high. Current limiters are added to the output of the current PID controllers in order to stay within the current rating for the motor and drive system. Current controllers are also used to eliminate the effects of induced voltage from the motor armatures that complicate velocity control and torque control [110, 111]. The velocity and current limiters are represented as saturation elements in Figure 16.

- *Filters*

The overall system simulation neglects filters for practical reasons that will be discussed in Chapter 4. However, filters have a practical use in a control system and are present in the actual FOS. Typically, they are found throughout the controller system, the feedback devices, and the power converter [107]. Filters are used for three primary reasons: (1) to reduce noise, (2) to eliminate aliasing, and (3) to attenuate resonance.

The most common filter is the low-pass filter. Low-pass filters are used to remove high-frequency noise from a variety of sources, including electrical interconnections, resolution limitations, and noise sources in feedback devices. Filters can also be used to remove resonance. Ellis [107] states that "electrical resonance commonly occurs in current and voltage controllers; inductances and capacitances, either from components or from parasitic effects, combine to form L-C circuits that have little resistive damping." A resonant circuit exhibits ringing and can generate higher voltages and currents than its input. Low-pass filters are also applied to the command or feedback signals or to elements of the control law (for example, the derivative term in a PID controller). One primary issue with using low-pass filters is that they can cause instability by causing phase lag at the gain crossover frequency.

- *Feedback Devices*

Feedback devices are typically sensors that sense position and/or velocity. Encoders, resolvers, and tachometers are a few commonly used sensors. The position feedback sensor is usually either an encoder or a resolver coupled with a resolver-to-digital converter. Encoders are generally more accurate than resolvers. However, resolvers are more reliable. Encoders often generate more electrical noise when the cable

between motor and encoder is long [107]. Resolvers, on the other hand, contain more position error.

One major error with encoders and resolvers is cyclic error. Cyclic error is a low frequency error that repeats with each revolution of the feedback device [107]. It causes low frequency torque ripple on the motor shaft. Unlike high frequency perturbations, cyclic errors cannot be filtered out when they are low enough to be at or below the velocity loop bandwidth. Ellis provided an example of a motor operating at 60 rpm with a 2/rev cyclic error which generated a 2 Hz ripple [107]. Cyclic error is believed to result from imperfections in the feedback device and from mounting issues. Ellis pointed out that the total cyclic error from a feedback device can be in excess of 40 min^{-1}, 15-20 min^{-1} for resolvers and 1-10 min^{-1} for encoders [107]. The values may sound small but can generate a surprisingly large amount of torque ripple.

Velocity ripple is a type of error produced directly from position error. Its presence is evident when the motor speed is held constant. One way to remove velocity ripple is to add torque ripple that induces ripple in the actual speed. The feedback signal is improved, but the actual velocity performance is worse. If the bandwidth is high enough compared to the ripple frequency, it can induce severe torque ripple while only canceling an error that exists in the feedback signal. On the other hand, if the ripple frequency is higher than the bandwidth, the motor speed is relatively smooth, but the feedback signal indicated has ripple.

A tachometer is a sensor that measures the rotation speed of a shaft. Typically, it is encased within the motor. The biggest problem with tachometers is misalignment. If the tachometer is not aligned with the motor shaft, it can cause a cyclic false-speed

signal. The output then consists of a DC voltage proportional to the average speed over a revolution plus a superimposed high frequency, low amplitude cyclic voltage.

3.4 Mechanical Resonance and Compliance

Motor drives are used in a wide range of applications. Typically, command response and dynamic stiffness are the two key rating factors for high performance applications. In order to achieve high performance, designers often use closed loop controllers such as proportional-integral (PI) velocity loops in servo systems [107]. As such, the controllers must have high gains in order for the system to obtain high performance.

The down side of high performance is mechanical resonance. Mechanical resonance is caused by compliance between two or more components in the mechanical transmission chain. The resonance is typically the compliance between the motor and load. Another example of resonance is from the motor and feedback. Compliance is defined as a "manifestation of elasticity in solid, flexible bodies" [112]. Compliance can come from within the load, where the load can be thought of as multiple inertias connected together by compliant couplings [106]. Also, resonance can be caused by a compliant motor mount. In other words, the motor frame oscillates within the machine frame.

3.4.1 Characteristics of Resonance and an Example

To demonstrate the characteristics of resonance, a simple example is provided of a compliant coupling between a motor and a load and is depicted in Figure 23. Further examples have been discussed by Craig [113]. Figure 23 contains the following parameters: the rotor inertia of a motor, J_M, the driven-load inertia, J_L, the elasticity of

coupling, K_S, the viscous damping of coupling, B_{ML}, the viscous damping between ground and motor rotor, B_M, the viscous damping between ground and load inertia, B_L, and the electromagnetic torque applied to the motor rotor, T. The elasticity of the coupling, K_S, can be neglected in low-power systems; however, modeling it in high-power systems is critical.

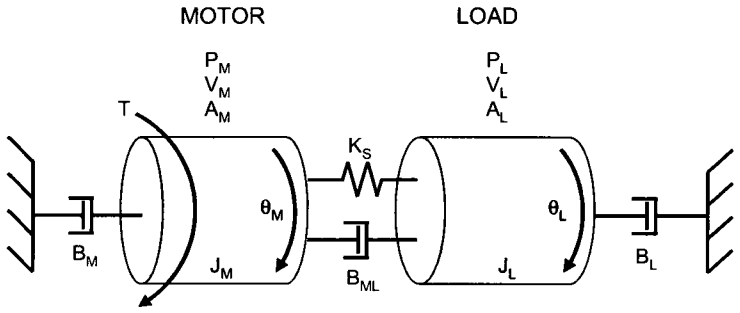

Figure 23: Simple compliantly-coupled motor and load

The following assumptions were made before the equations of motion were derived for Figure 23. First, the viscous damping of the coupling, B_{ML}, is small since transmission materials provide little damping. Second, B_M and B_L are neglected in the following analysis because they exert small influences on resonance. They are, however, included for completeness. Finally, Coulomb friction ("stiction") has been neglected. Coulomb friction has little effect on stability when the motor is moving. On the other hand, when the motor is at rest, the impact of stiction on resonance is more complex. Stiction can be thought of as increasing the load inertia when the motor is at rest. The resonance equations of motion are:

$$T - B_M\dot{\theta}_M - B_{ML}\left(\dot{\theta}_M - \dot{\theta}_L\right) - K_S\left(\theta_M - \theta_L\right) = J_M\ddot{\theta}_M \tag{3.59}$$

$$-B_L\dot{\theta}_L + B_{ML}(\dot{\theta}_M - \dot{\theta}_L) + K_S(\theta_M - \theta_L) = J_L\ddot{\theta}_L. \tag{3.60}$$

Applying Laplace transforms and writing Equations 3.60 and 3.61 in matrix form results in the following:

$$\begin{bmatrix} J_M s^2 + (B_{ML} + B_M)s + K_S & -(B_{ML}s + K_S) \\ -(B_{ML}s + K_S) & J_L s^2 + (B_{ML} + B_L)s + K_S \end{bmatrix} \begin{bmatrix} \Theta_M(s) \\ \Theta_L(s) \end{bmatrix} = \begin{bmatrix} T(s) \\ 0 \end{bmatrix}. \tag{3.61}$$

Assuming that $B_L = B_M = 0$, the following transfer functions are obtained:

$$\frac{\Theta_M}{T}(s) = \left[\frac{1}{(J_M + J_L)s^2}\right]\left[\frac{J_L s^2 + B_{ML} + K_S}{\frac{J_L J_M}{J_L + J_M}s^2 + B_{ML}s + K_S}\right] \tag{3.62}$$

$$\frac{\Theta_L}{T}(s) = \left[\frac{1}{(J_M + J_L)s^2}\right]\left[\frac{B_{ML}s + K_S}{\frac{J_L J_M}{J_L + J_M}s^2 + B_{ML}s + K_S}\right]. \tag{3.63}$$

Values used for the examples that follow are: $J_L = 0.002$ kg-m^2, $J_M = 0.002$ kg-m^2, $K_S = 200$ N-m/rad and $B_{ML} = 0.01$ N-m-s/rad. The resulting compliantly coupled motor and load has the characteristics depicted in Figure 24 and Figure 25. The frequency where the gain is at the bottom of the trough is called the antiresonant frequency, ω_{AR}. Mathematically that is where the numerator has its minimum value. The antiresonant frequency is the natural frequency of oscillation of the load and the spring. Note that the motor inertia is not a factor. For this example, the antiresonant frequency is 316 rad/s (50.3 Hz). The antiresonant frequency can be calculated by [107],

$$\omega_{AR} = \sqrt{\frac{K_S}{J_L}}. \tag{3.64}$$

The resonant frequency, ω_R, is the frequency where the gain reaches a peak. Mathematically, at this frequency the denominator is minimized. Also for this example, the resonant frequency is 447 rad/s (71.2 Hz). That resonant frequency can be calculated by [107],

$$\omega_R = \sqrt{\frac{K_S(J_M + J_L)}{J_M J_L}}. \tag{3.65}$$

It should be noted that the antiresonance frequency is always less than the resonance frequency, but that is if and only if the motor inertia is greater than zero. When the motor and load frequencies are less than the antiresonance frequency, a rigidly-coupled motor and load are observed. When the motor and load frequencies are greater than the resonance frequency a compliantly-coupled motor and load are observed.

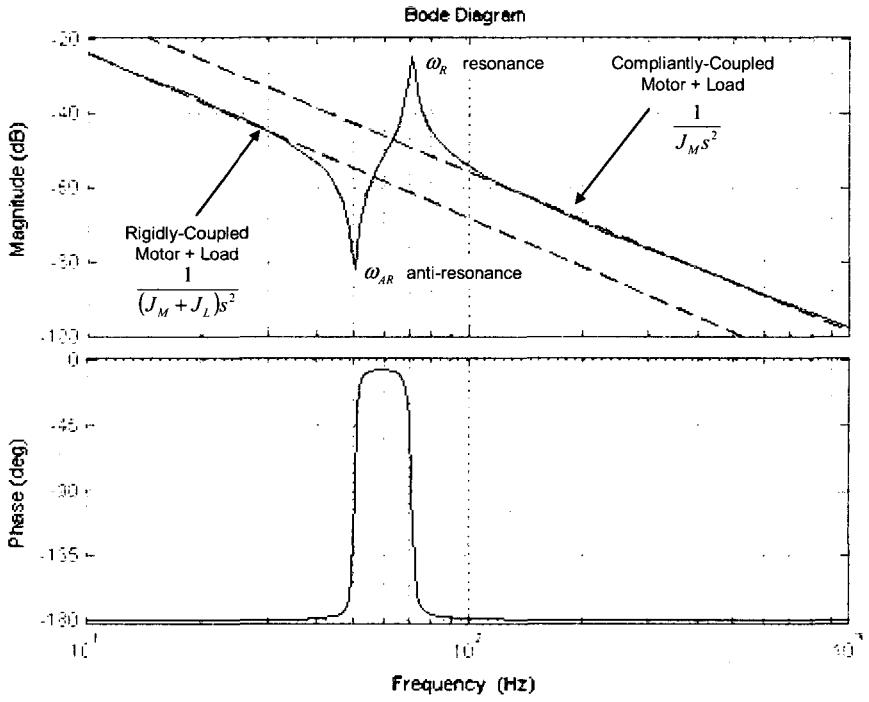

Figure 24: Motor/Torque transfer function

The load transfer function exhibits similar behavior to the motor transfer function except there is no antiresonant frequency. There is 90° more phase lag at high frequency due to the loss of the s^2 term in the numerator. When comparing transfer functions of the motor and load, the system will be in-phase if the system frequency is below the antiresonant frequency, and the system will be out-of-phase if the system frequency is above the antiresonant frequency.

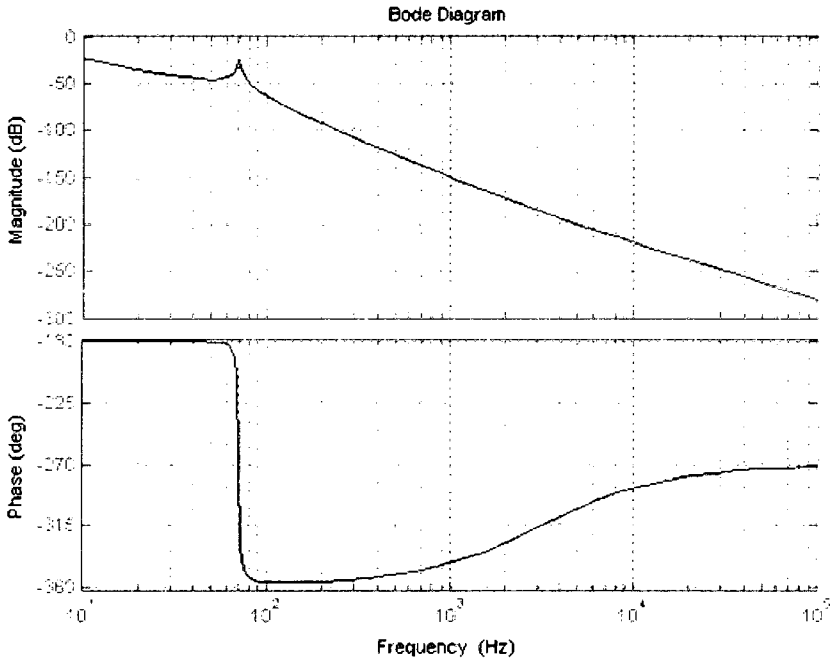

Figure 25: Load/Torque transfer function

Mechanical resonance can cause instability in two ways: tuned resonance and inertial-reduction instability [114]. Although there are important distinctions between the two, both problems can be understood as resulting from the variation of effective inertia with frequency [107]. At the resonant frequency, the system becomes unstable causing the motor and load to oscillate at that frequency, moving in opposite directions as energy

is exchanged between the motor and load [107]. At this frequency, the system is easily excited behaving as if the inertia were very small [107]. This is called *tuned resonance.*

If the system exhibits inertial-reduction instability it becomes unstable above the motor-load resonant frequency. Systems with instability due to inertial reduction behave much as if the load inertia were removed, at least near the frequency of instability [107]. According to Ellis, inertial-reduction instability is most commonly experienced in actual applications. Also, Ellis cautions that some resonance problems are combinations of the two phenomena [107]. In such cases, the frequency of oscillation will be above, but still near, the natural frequency of the motor and load [107].

There are several mechanical and electrical cures for resonances; the reader can refer to [114]. The most common methods are: (1) to increase the motor inertia/load inertia ratio (J_L/J_M), (2) stiffen the transmission, (3) increase damping, and (4) apply filters. At a low J_L/J_M ratio, the resonance and antiresonance frequencies are close together at a high frequency. As J_L/J_M increases, both the antiresonance and resonance frequencies decrease, with the antiresonance frequency decreasing more rapidly.

Increasing the damping between the motor and load coupling increases both the antiresonance and resonance frequencies. This method is used primarily for tuned resonance. Finally, adding low-pass filters to the system is the primary electrical approach. A filter is placed in the control loop to compensate for the change in gain represented by the compliant load [107]. By reducing the gain in the vicinity of the resonant frequency, the resonance can be reduced or eliminated. The disadvantage of using filters is their inherent phase lag. As a general guideline, to avoid instability

problems the desired closed-loop bandwidth should be kept well below the system resonance frequency. Also, the J_L/J_M ratio should be less than 5.

3.4.2 Equations of Motion for Compliantly-Coupled Drivetrain

For the oscillation system in the 12-Ft wind tunnel, the nominal compliance model is depicted in Figure 26. Table 5 describes the inertia constants and torsional damping and spring constants used in Figure 26.

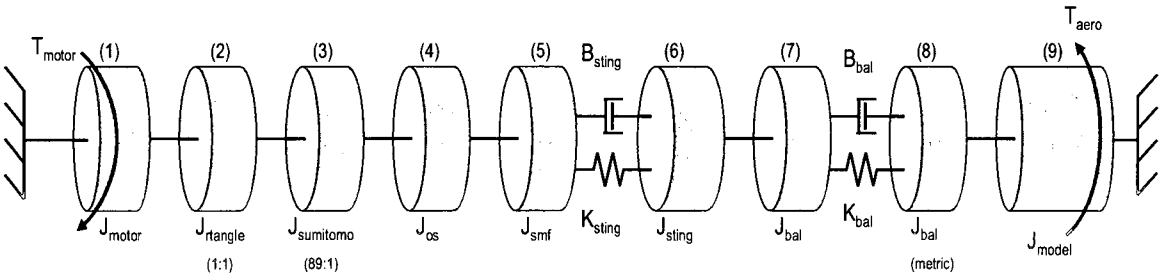

Figure 26: Compliantly-Couple Drive Train

Table 5: Description of constants

Inertia Constants	
Name	Description [kg*m^2]
J_{motor}	Motor rotor inertia
$J_{rtangle}$	1:1 right angle reducer inertia
$J_{sumitomo}$	89:1 torque reducer inertia
J_{os}	Output shaft inertia
J_{smf}	Sting mount flange inertia
J_{sting}	Sting roll inertia
J_{bal}	Balance roll inertia
$J_{bal\ (metric)}$	Metric side balance roll inertia
J_{model}	Model inertia
Torsional Damping Constants	
B_{sting}	Sting viscous damping
B_{bal}	Balance viscous damping
Torsional Spring Constants	
K_{sting}	Sting spring constant
K_{bal}	Balance spring constant

Assuming that the transmission sections that are connected with solid lines are rigid, the inertias simply add. This allows the compliantly-coupled drivetrain model to be reduced to Figure 27.

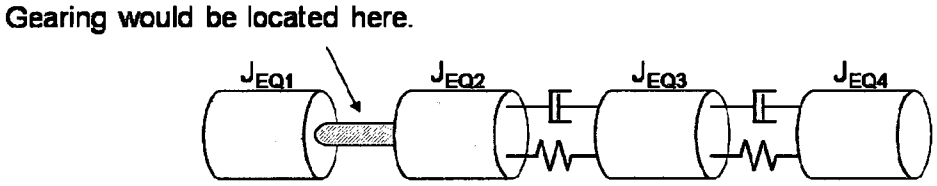

Figure 27: Reduced compliantly-coupled drive train

The following summed inertias are employed:

$$\begin{aligned} J_{EQ1} &= J_{motor} + J_{rt\,angle} + J_{gearbox} \\ J_{EQ2} &= J_{os} + J_{smf} \\ J_{EQ3} &= J_{sting} + J_{bal} \\ J_{EQ4} &= J_{bal(metric)} + J_{model} \end{aligned} \tag{3.66}$$

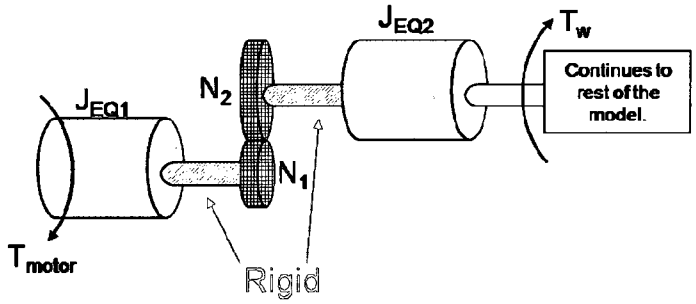

Figure 28: Gearbox representation in compliantly-coupled drivetrain

The gearbox is located between the equivalent inertias, J_{EQ1} and J_{EQ2}, thus producing the equivalent inertia and torque given by:

$$T_{motor} = \left[J_{EQ1} + \left(\frac{N_1}{N_2} \right)^2 J_{EQ2} \right] \ddot{\theta}_1 + \left(\frac{N_1}{N_2} \right) \cdot T_w \tag{3.67}$$

$$J_{EQ} = J_{EQ1} + \left[\left(\frac{N_1}{N_2} \right)^2 \cdot J_{EQ2} \right]. \tag{3.68}$$

Note that

$$T_{EQ} = \left(\frac{N_1}{N_2} \right) \cdot T_w . \tag{3.69}$$

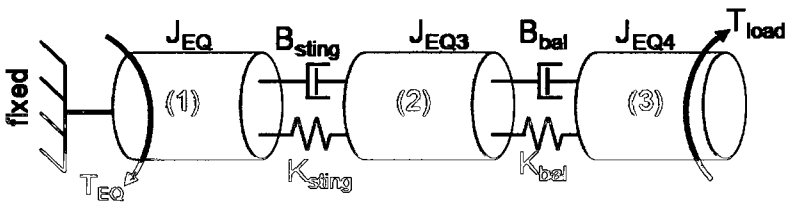

Figure 29: Equivalent reduced compliantly-couple drive train model

Referring to Figure 29, the equations of motion for an equivalent reduced compliantly-coupled drive train can be written as follows,

$$\begin{aligned} &\sum T = J\ddot{\theta} \\ &J_{EQ}\ddot{\theta}_1 = T_{EQ} + B_{sting}\left(\dot{\theta}_2 - \dot{\theta}_1\right) + K_{sting}\left(\theta_2 - \theta_1\right) \\ &J_{EQ3} = B_{bal}\left(\dot{\theta}_3 - \dot{\theta}_2\right) + K_{bal}\left(\theta_3 - \theta_2\right) - B_{sting}\left(\dot{\theta}_2 - \dot{\theta}_1\right) - K_{sting}\left(\theta_2 - \theta_1\right) \\ &J_{EQ4} = T_{load} - B_{bal}\left(\dot{\theta}_3 - \dot{\theta}_2\right) - K_{bal}\left(\theta_3 - \theta_2\right) \end{aligned} \tag{3.70}$$

The resonant and anti-resonant frequencies were estimated between the motor and the load and then between the load and model (i.e. aerodynamic torque). The load inertia depends on the type of oscillation test and the type of sting being employed. During pitch oscillation testing, the 'bent' sting is employed; it has a higher inertia than the 'straight' sting which is typically used for roll oscillation testing. The antiresonant

and resonant frequencies for both a straight sting and bent sting are listed in the table below. The frequencies are also provided between the motor and the load and the load and the model.

Table 6: Antiresonant and resonant frequency for a given sting type

	Straight Sting		Bent Sting	
	Motor + Load	Load + Model	Motor + Load	Load + Model
F_{AR} [Hz]	523	282	76.6	41.6
F_R [Hz]	2293	286	2234	51.9

The resonant frequencies are about the same for the straight and the bent sting. However, for the bent sting the antiresonant frequency is much smaller than the straight sting case. This is because of the increased inertia that causes the antiresonance and resonance frequencies to decrease. As mentioned previously, the antiresonance frequency decreases more rapidly than the resonance frequency. On the other hand, when examining the antiresonance and resonance frequencies between the load and model, the inertia ratio of the load and model is smaller. The smaller inertia ratio causes the resonance and antiresonance frequencies to be close to each other at a high frequency.

These resonant frequencies are important because instability can occur if the oscillation test is operating near resonant frequencies. However, for this study the oscillation test frequencies are between 0.1 and 10 Hz. Therefore, instability issues from the compliance model are not expected. Also, since the spring constants between the motor and load and the load and model are very large (~10^4 Hz), both the antiresonance and resonance will increase. Consequently, the rigid body assumption can be applied to the model, and the motor torque equation becomes

$$T_{motor} = \left(\frac{N_1}{N_2}\right)^2 (B_{bal} + B_{sting}) + \left(\frac{N_1}{N_2}\right) \cdot T_{load} \,. \tag{3.71}$$

The simplified model does not include spring constants. Also, T_{load} represents the aerodynamic load from the test article.

3.4.3 Geared Drives

Electrical motors produce their maximum power at maximum speed (power = torque x angular velocity). Consequently, it becomes necessary to use gearing in order for these systems to drive large loads (requiring large torques) at low speeds [115].

Geared drives are beneficial because of their ability to produce rotational motion in heavy loads. However, gears introduce significant nonlinear characteristics that affect the performance of the driven mechanical system. Undesired effects are:

1. Torsional vibrations,
2. Cyclic rotational disturbances, and
3. Backlash.

These effects cannot be studied independently because they amplify each other and interact. Torsional vibration is a high frequency, very lightly damped oscillation. It is not sensitive to frequency changes in the drive systems. It is primarily generated from three main causes: (1) roll moment of inertia mismatches (of the motor's shaft) which is usually large compared to the combined motor, tachometer, and gearbox moment inertia [116]; (2) the jackshaft is usually long compared to the other shafts, and its couplings create a "springiness" effect in the system; (3) the tachometer is typically coupled to the motor or to the gear high-speed shaft.

Load disturbances are generally caused by a bent or misaligned motor shaft and mechanical misalignments [116]. The misalignments can cause either continuous or random error. Continuous error is caused by cyclic torque disturbances while random error is a type of "one-shot" error.

Backlash is the most complex effect to analyze. Backlash is essentially "a lost motion in a gear train and the system reaction when such parts come back into contact" [112]. It is present in all mechanical systems that employ geared drives. It is a highly nonlinear phenomenon. Figure 30 illustrates the common backlash models. The right sketch represents the classical model, where backlash produces no torque output over a range of rotation angles and is represented as a piecewise-linear stiffness. The left sketch represents the hysteric effect of backlash.

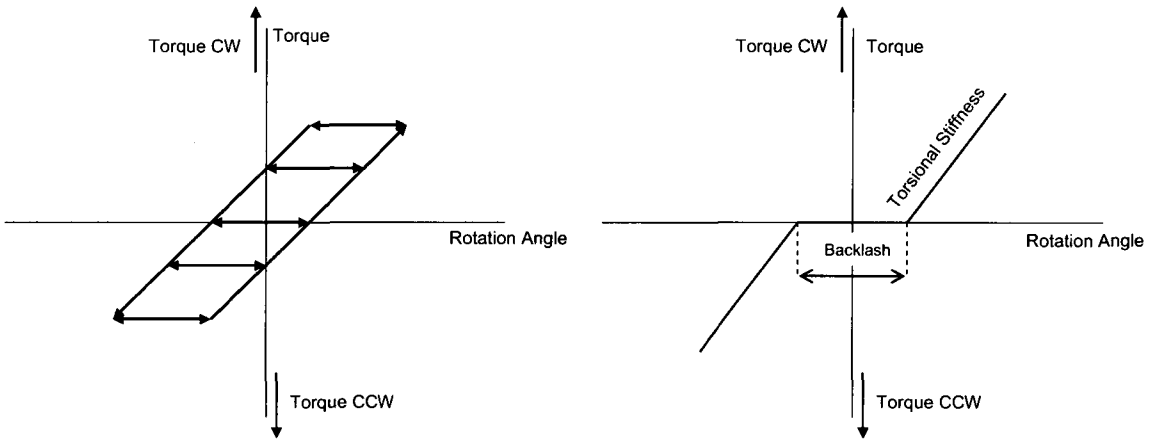

Figure 30: Modern backlash model – hysteretic (left side) and classical backlash model (right side)

There are several challenges resulting from backlash. Backlash causes decoupling of all inertial elements from the drive system. Consequently, the system is only under control on the motor side of the gear drive. On the load side of the gear drive, the system is not being driven. The decoupling effect causes rapid torque transients and can excite

nonlinear torsional vibration [117]. Backlash can generate chaotic vibration depending on the system parameters and initial conditions [117]. Backlash can also interfere with speed regulators. It ruins the effectiveness of the controller and is recognized by torque changes in sign [116]. Backlash is multiplied by multiple gear reduction units.

3.5 Summary

In conclusion, this chapter was devoted to the theoretical developments required for understanding and modeling a forced oscillation wind tunnel testing system. The chapter developed the mathematical equations of motion for an aircraft under longitudinal motion. The classical stability derivatives were derived, and a few specific stability derivatives in pitch were discussed in detail. The important stability derivatives for forced oscillation are the in-phase and out-of-phase lift and pitching moment coefficients. The NASA Langley 12-ft Low Speed Wind Tunnel and its dynamic test rig were used as a representative wind tunnel for forced oscillation testing. The chapter detailed the system description and outlined how stability derivatives are determined from a wind tunnel experiment. The chapter concludes with an examination of the electrical components of the system. The equations of motion for a three-phase AC induction machine were developed. The motor's controller, field oriented control, and mathematical equations were defined and discussed. Specific details were given related to pulse width modulation, PID controllers and controller issues, filters, feedback devices, and controller actuator saturation. Finally, the chapter concludes with the discussion of mechanical resonance and compliance. Equations of motion are derived for the mechanical compliance model. A discussion of geared drives and their impact on dynamic systems was also provided.

CHAPTER 4

METHODOLOGY

4.1 Introduction

This chapter describes how the data were generated using a Simulink computer model and how it was analyzed. The first phase of the chapter details the modular approach used to develop the computer model. The computer model was constructed in sections: aerodynamic model, motor model, control system, and the compliantly-coupled drivetrain system. The second phase of the chapter discusses how the computer simulation was verified and validated. Finally, the chapter concludes with a discussion of the design of experiments approach to analyzing the computer results.

A flowchart of the methodology used for the overall approach is shown in Figure 31. The conception phase consisted of defining the research objectives and constructing a conceptual model of the overall system. The conceptual model was validated by input from knowledgeable experts. The implementation section consisted of constructing a Simulink computer model based on the conceptual model, and an iterative process was then used to verify and validate the computer model. Finally, statistical testing was performed using the computer model along with design of experiments and Monte Carlo simulation.

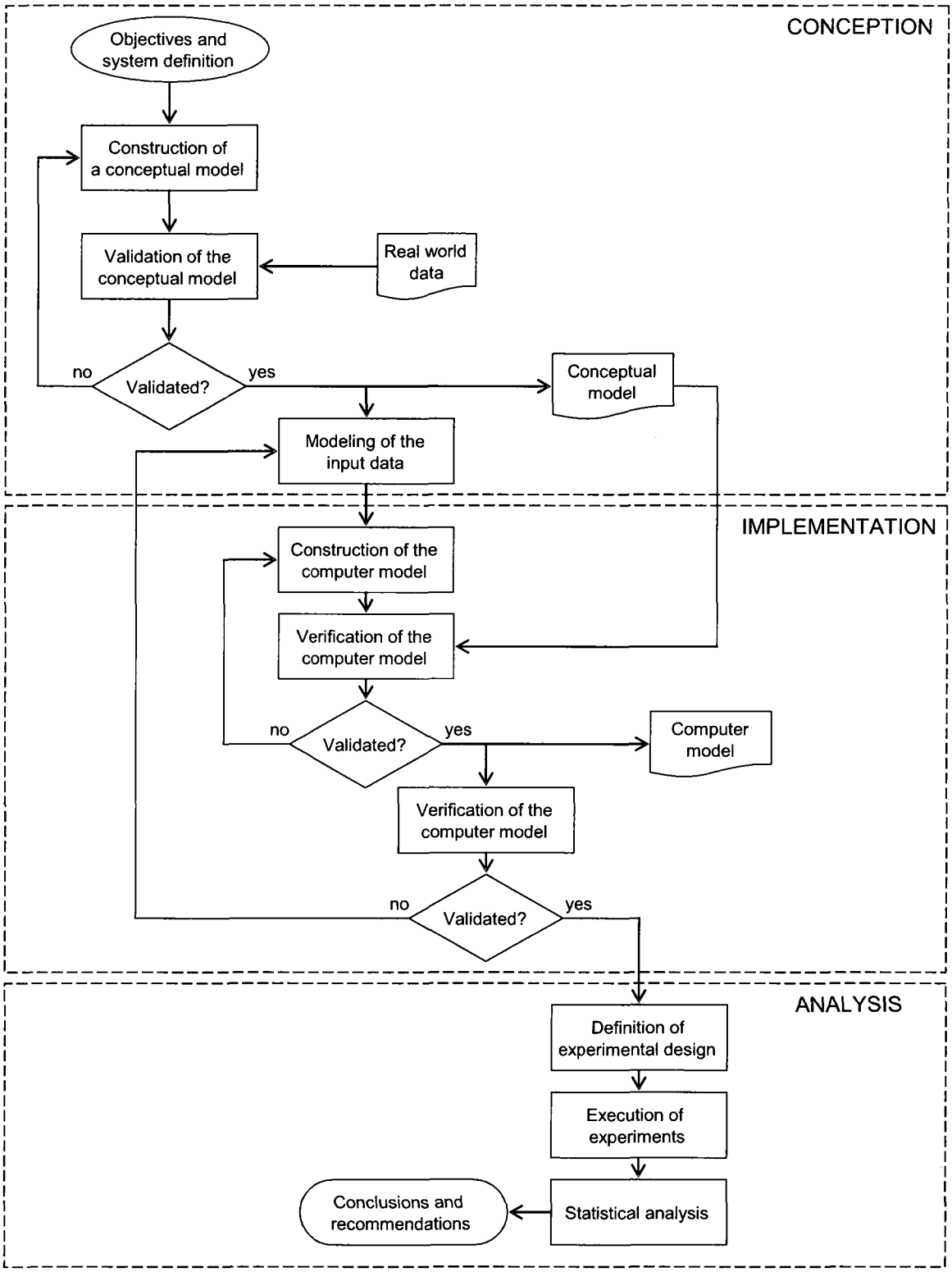

Figure 31: Flowchart of overall approach

Five factors were used in the design of experiments study: equivalent inertia, equivalent damping, reduced frequency, backlash, and input saturation. Equivalent inertia was determined to be the total inertia between the motor and the load. The low factor limit represents the straight sting, and the high factor limit represents the bent sting. The equivalent damping factor limits were determined to be zero damping for the low factor limit. At the high factor limit, equivalent damping was determined to be the sum of the damping for bent sting and the balance. Reduced frequency factor limits were set by the operational limitations of the simulation. The backlash factor limits were reported by the manufacturer (Sumitomo). Finally, input saturation factor limits were estimated from NASA experimental data by examining angle of attack time histories for saturation levels. The low limit assumes no saturation was present. The high limit assumes saturation was present. Values are provided later in the chapter.

4.2 Computer Simulation – A Modular Approach

A modular Simulink implementation of a forced pitch oscillation system is described in a step-by-step approach based on the detailed conceptual block diagram (shown in Figure 32, and the mathematical development in Chapter 3).

Simulink was chosen over other modeling packages because of the ease in modeling transients of electrical machines, implementing other components (i.e. aerodynamics), modeling mechanical drives, and developing drive controls.

There are three specific pitfalls for using a computer simulation with electrical motor models [118]. The first tip is not to use derivative blocks, since some signals have discontinuities and/or ripple that result in infinite solutions when differentiated. Integral and basic arithmetic elements should be used instead. The second pitfall is algebraic

loops. Algebraic loops typically appear in a system that has feedback loops. Simulink attempts to solve the algebraic loop, and if it cannot find a solution, the simulation terminates. Adding a memory block can break up the algebraic loop. It delays the input signal by one sampling time step; however, this can affect the operation of the system, so algebraic loops should be avoided. The final pitfall is to avoid large sampling times. A rule of thumb is that the sampling time should be no larger than 1/10 of the smallest time constant in the model. For a system with an induction motor and drive, the smallest time constant is typically selected based on the switching frequency of the associated pulse width modulation.

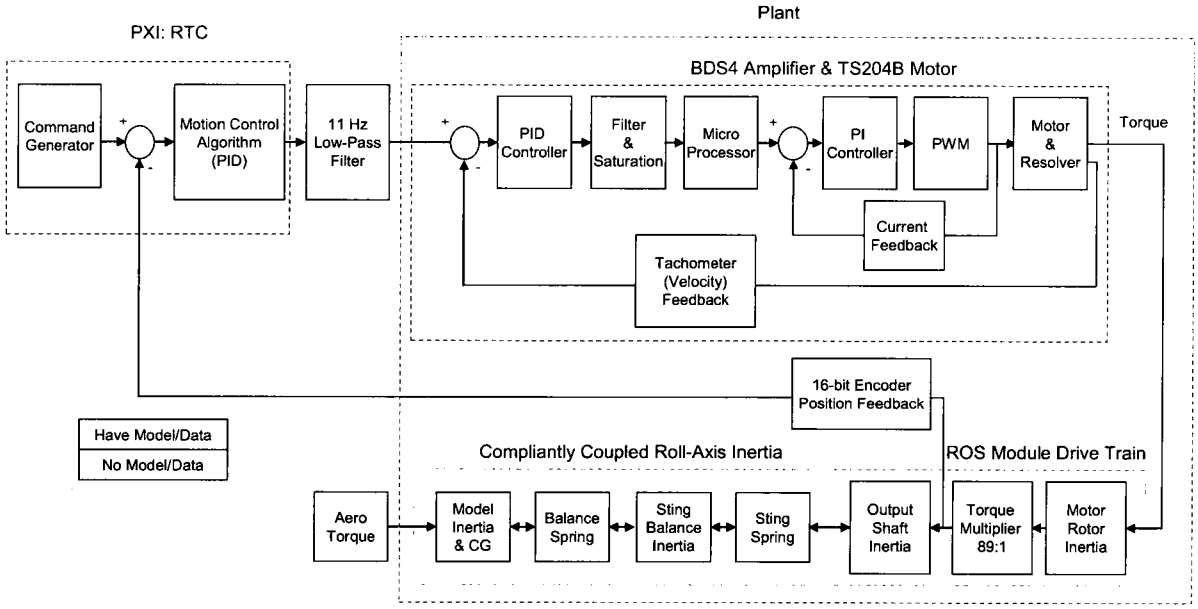

Figure 32: Detailed forced oscillation system conceptual block diagram

4.2.1 Experimental Aerodynamic Model

Initially, two aerodynamic models were developed following the work of Katz [119]; however, neither model had the required fidelity needed to represent the

experimental data because of incomplete physics such as separation effects [119]. An unsteady vortex lattice code and a simplified slender pitching delta wing were tried but were found inadequate.

Due to the lack of viable CFD codes for predicting high angle of attack and unsteady aerodynamic effects for an entire aircraft, this study implemented an experimental model data set. Experimental data were obtained from NASA LaRC 12-ft Low Speed Wind Tunnel experiments during the 1990s [76]. The model, depicted in Figure 33, was a 10% scale model of an F16-XL aircraft. Data were collected for longitudinal static tests, oscillatory tests, and ramp tests and was provided by Murphy [4]. A regression based computer model was developed using the experimental data.

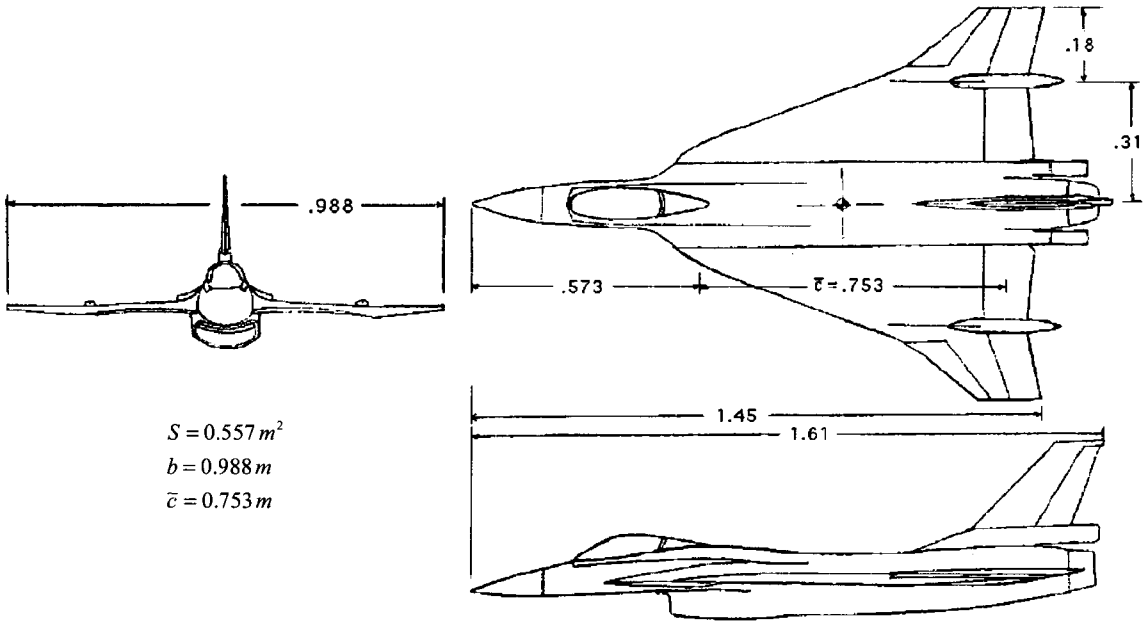

Figure 33: Three-view sketch of 10% scaled F16-XL aircraft model (units in metric system)

The total lift and pitching moment coefficients are based on the sum of the contributions from the static and dynamic parts of lift and pitching moment coefficients such that

$$\begin{aligned} C_{L_{total}} &= C_{L_{static}} + C_{L_{dyn}} \\ C_{m_{total}} &= C_{m_{static}} + C_{m_{dyn}} \end{aligned} \quad . \tag{4.1}$$

The static contributions were obtained from the tabulated data, represented graphically in Figures 34 and 35. The tabulated static coefficient data is contained in Appendix A. The figures were generated using the computational code in Appendix B. If necessary, linear interpolation could be used to obtain values for the coefficients for angles of attack not listed in the table. The static data were implemented in Simulink using a "look-up table" block. The block performs a 1-D, linear interpolation of input values using a specified table. The block was limited so that it could not perform extrapolations outside the boundaries of the table.

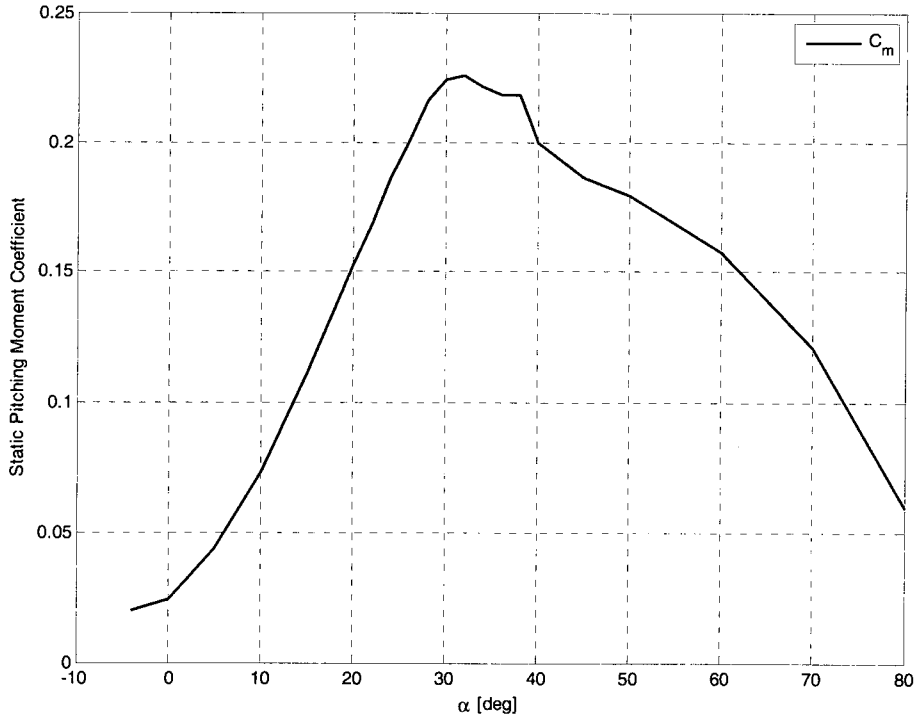

Figure 35: Variation of static pitching moment coefficient with angle of attack for 10% F16-XL aircraft

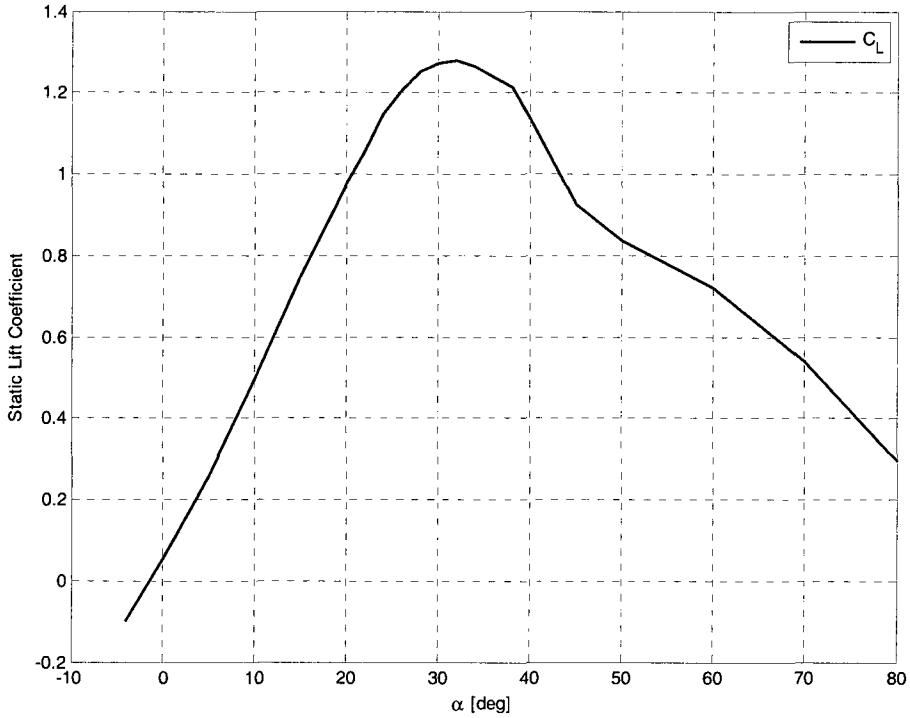

Figure 34: Variation of static lift coefficient with angle of attack for 10 % F16-XL aircraft

Noting that the incremental lift coefficient is the dynamic lift coefficient contribution, Equation 3.3 can be rewritten:

$$C_{L_{dyn}} = \alpha_A \left(\overline{C}_{L_\alpha} \sin \omega t + k \overline{C}_{L_q} \cos \omega t \right) . \tag{4.2}$$

Similarly, Equation 4.2 can be written:

$$C_{L_{dyn}} = \overline{C}_{L_\alpha} \alpha_A \sin \omega t + \overline{C}_{L_q} \alpha_A \left(\frac{\overline{c}\,\omega}{2V} \right) \cos \omega t . \tag{4.3}$$

Assuming the forcing function is based on harmonic motion where

$$\begin{aligned} \theta &= \alpha_A \sin \omega t \\ \dot{\theta} &= \alpha_A \omega \cos \omega t \end{aligned} . \tag{4.4}$$

Substituting these relations into equation 4.3 results in

$$C_{L_{dyn}} = \overline{C}_{L_\alpha} \theta + \left(\frac{\overline{c}}{2V} \right) \overline{C}_{L_q} \dot{\theta} . \tag{4.5}$$

Following the same procedure, the dynamic contribution for pitching moment coefficient is

$$C_{m_{dyn}} = \overline{C}_{m_\alpha} \theta + \left(\frac{\overline{c}}{2V} \right) \overline{C}_{m_q} \dot{\theta} . \tag{4.6}$$

The dynamic stability derivatives are obtained from experimental data. Those data are also tabulated in Appendix A. For this study, the dynamic stability derivatives were obtained at an angle of attack of 30.8°, using a linear regression model fit, as represented in Figures 36-39. The linear regression model fits utilized the method of least squares. Linear in this case means that the regression coefficients are constant. The coefficient of determination, R^2, was used to determine the 'goodness' of the fit [140]. The in-phase and out-of-phase lift and pitching moment coefficient regression models are:

$$\overline{C}_{L_\alpha} = 82.2k^3 - 75.4k^2 + 23.3k - 0.387 \tag{4.7}$$

$$\overline{C}_{L_q} = -1128k^3 + 1005k^2 - 298k + 31.6 \tag{4.8}$$

$$\overline{C}_{m_\alpha} = 6.82k^3 - 8.17k^2 + 3.19k - 0.0191 \tag{4.9}$$

and

$$\overline{C}_{m_q} = -274k^3 + 228k^2 - 62.9k + 5.48\ . \tag{4.10}$$

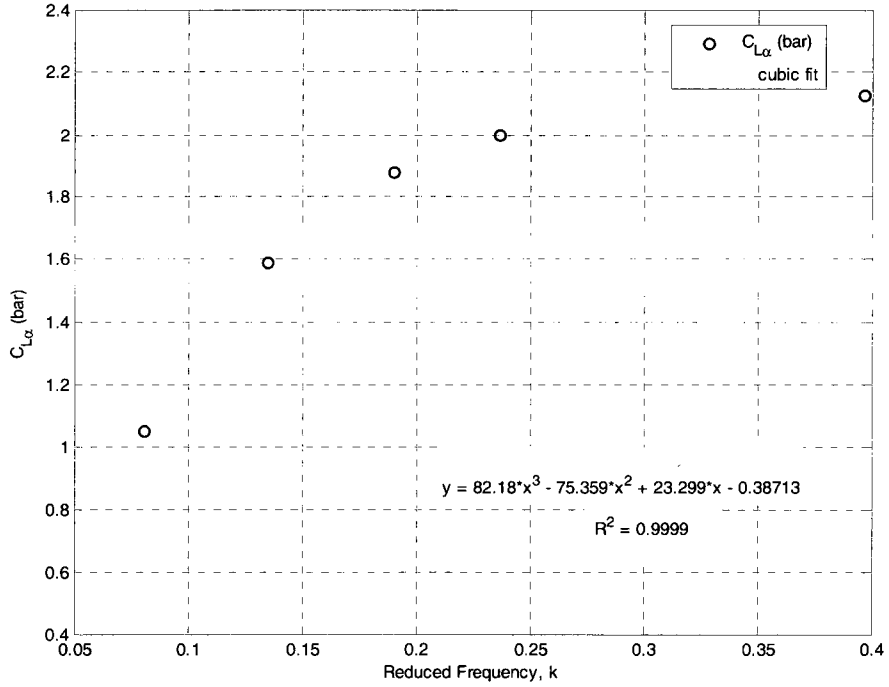

Figure 36: Variation of in-phase lift coefficient with reduced frequency

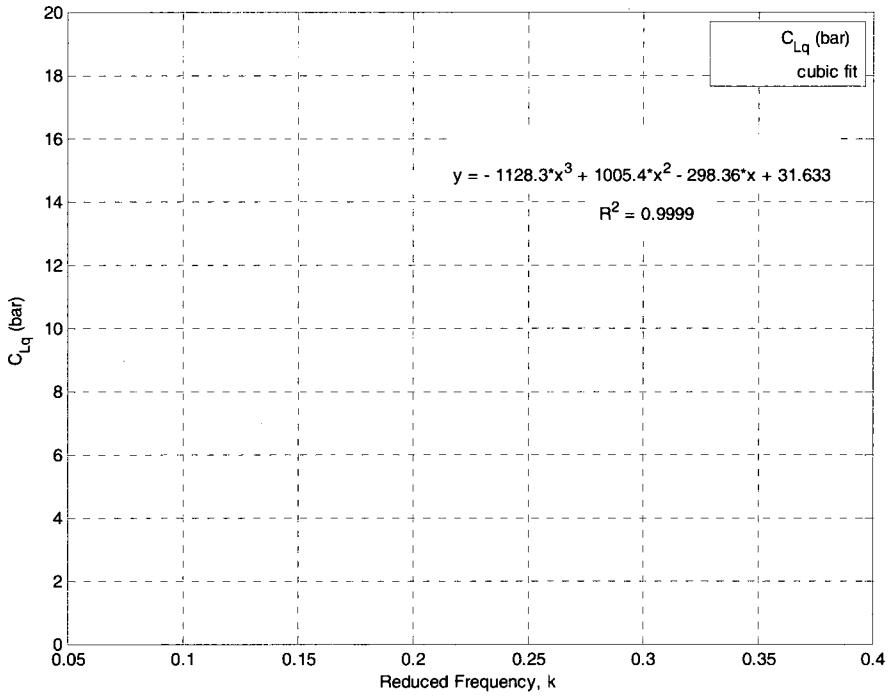

Figure 37: Variation of out-of-phase lift coefficient with reduced frequency

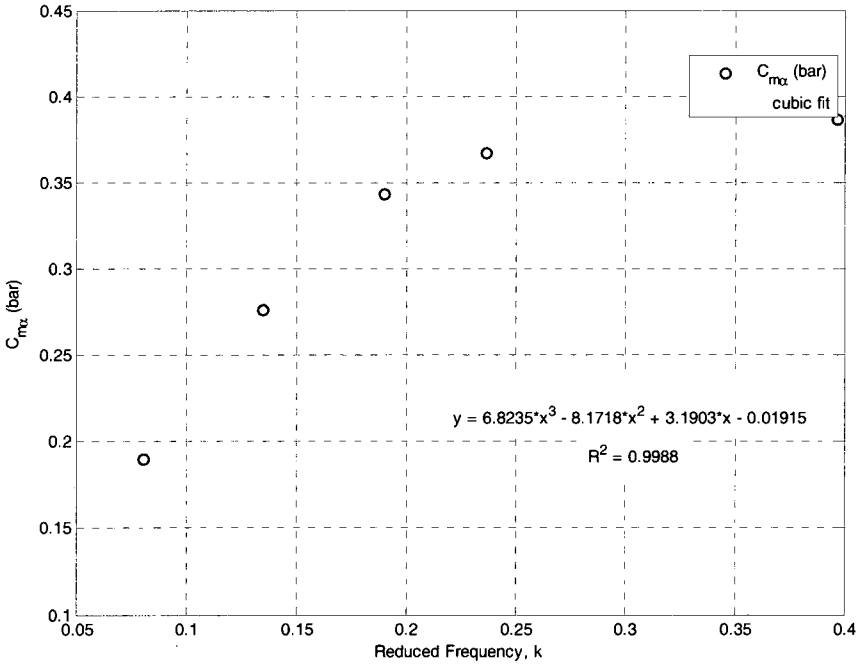

Figure 38: Variation of in-phase pitching moment coefficient with reduced frequency

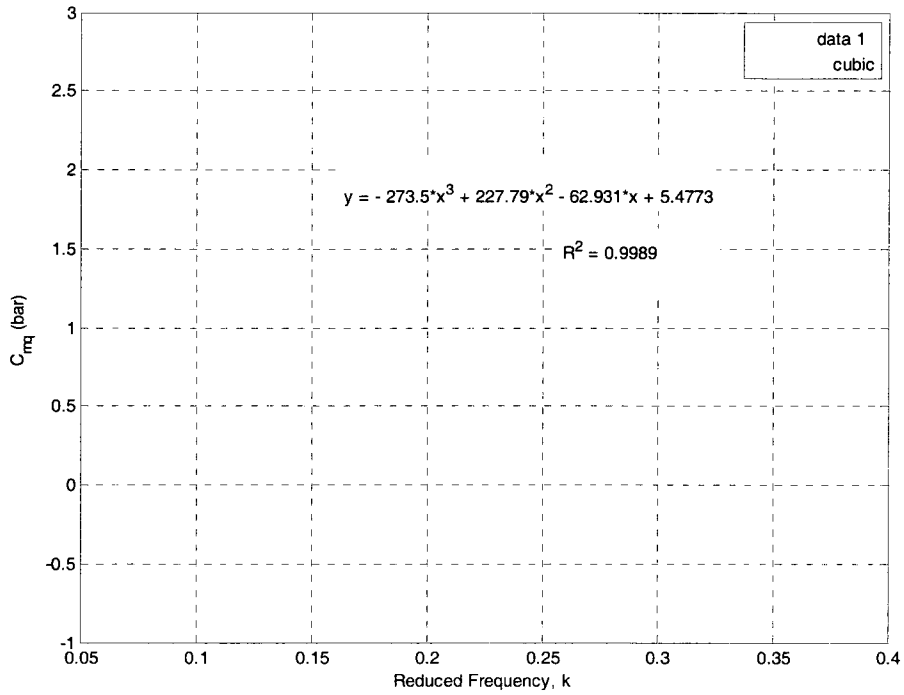

Figure 39: Variation of out-of-phase pitching moment coefficient with reduced frequency

Finally, the total lift and pitching moment coefficients are determined by summing the static and dynamic contributions of the coefficients. Next, the static contributions of lift and pitching moment coefficients are subtracted from the total lift and pitching moment coefficient. This results in the dynamic contribution of the coefficients. The dynamic part is then integrated using the procedure outlined in the previous section to obtain the in-phase and out-of-phase lift and pitching moment coefficients.

The implementation of the Simulink model is represented in Figure 40. The inputs are the static angle of attack, reduced frequency, angular position, and angular velocity. The outputs of the aerodynamic model are the total lift coefficient and total

pitching moment coefficient. The block in Figure 40, titled Dynamic Part, is a user-defined function. It simply contains Equations 4.7-4.10 that represent the dynamic contribution of the coefficients.

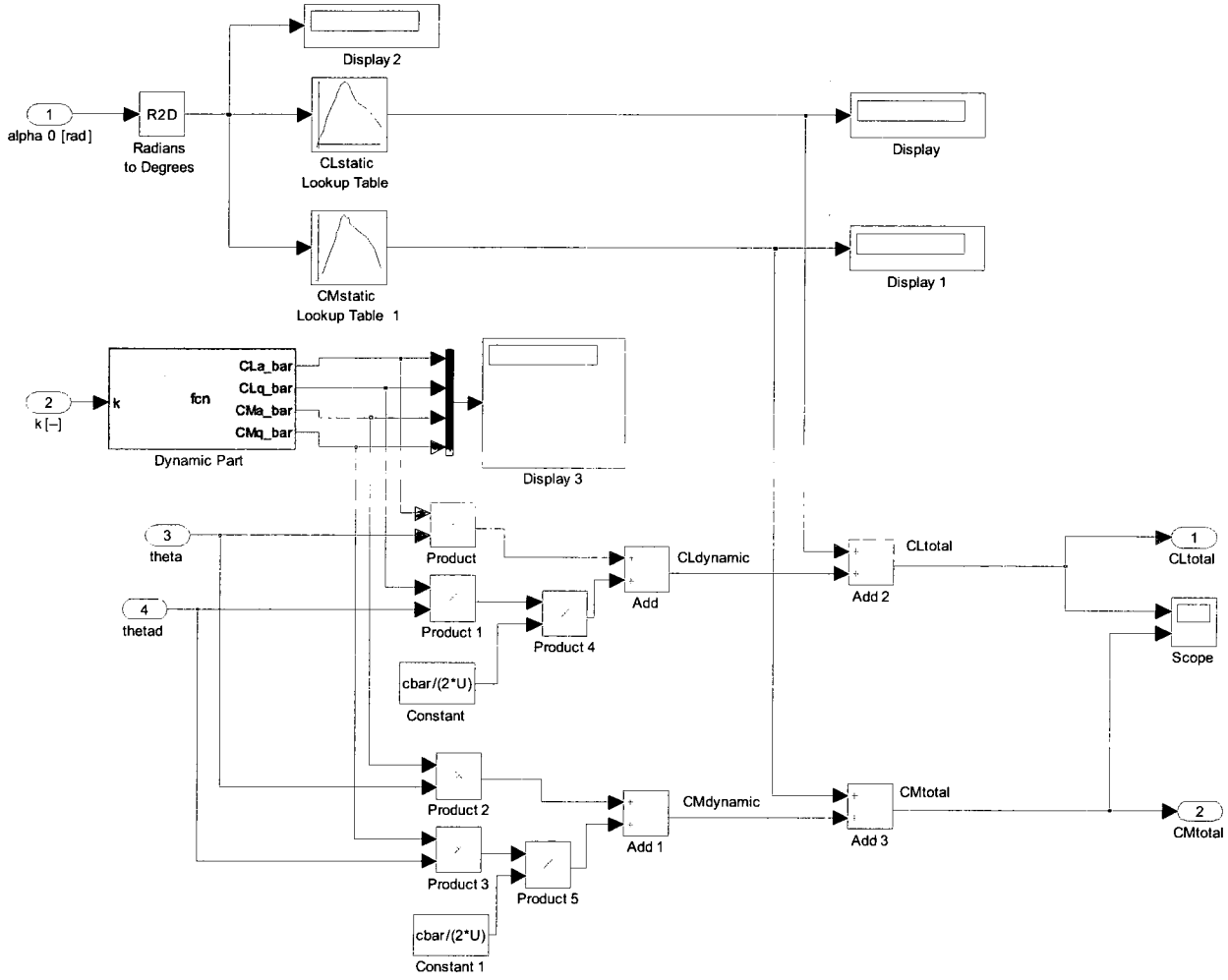

Figure 40: The complete aerodynamic Simulink model

4.2.2 Three-Phase AC Motor Model

The mathematical theory for this section was developed in the previous chapter. The equations of motion for a squirrel cage induction motor in state-space were

developed for the d-q reference frame. This section of the implementation follows the work of Ozpineci and Tolbert [118].

The motor model is an open-loop system. The inputs are: three-phase voltages, their fundamental frequency, and the load torque. The outputs are: three-phase currents, the electrical torque, and the rotor speed.

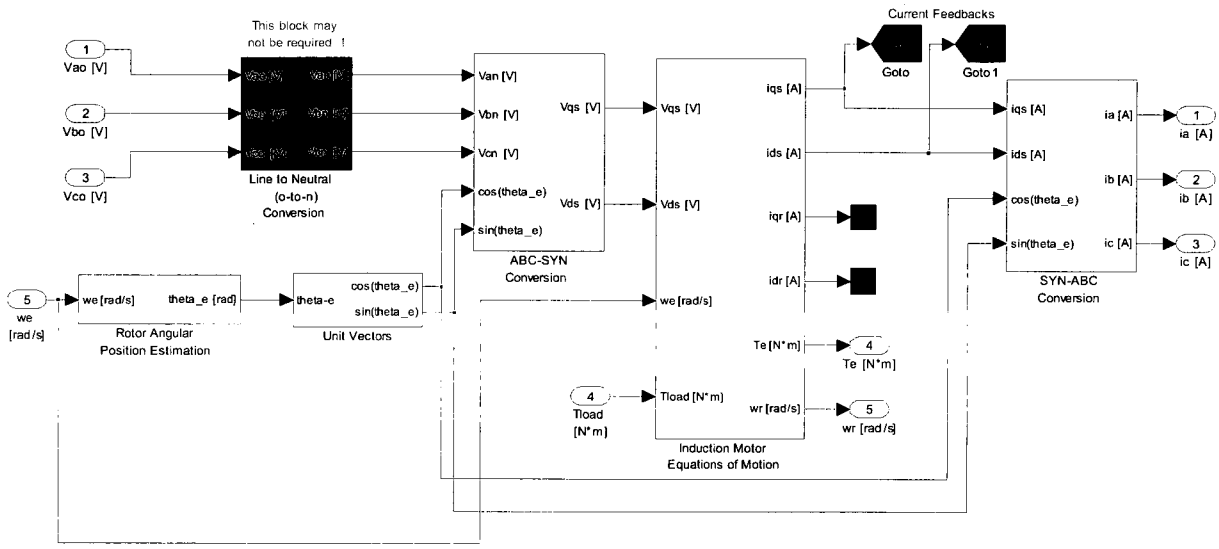

Figure 41: The complete induction machine Simulink model

The line to the neutral conversion block is required for an isolated neutral system; otherwise, it can be bypassed [118]. The transformation is given by Equation 4.11 and is represented by the Simulink matrix gain block, shown in Figure 42.

$$\begin{bmatrix} v_{an} \\ v_{bn} \\ v_{cn} \end{bmatrix} = \begin{bmatrix} +2/3 & -1/3 & -1/3 \\ -1/3 & +2/3 & -1/3 \\ -1/3 & -1/3 & +2/3 \end{bmatrix} \begin{bmatrix} v_{ao} \\ v_{bo} \\ v_{co} \end{bmatrix} \tag{4.11}$$

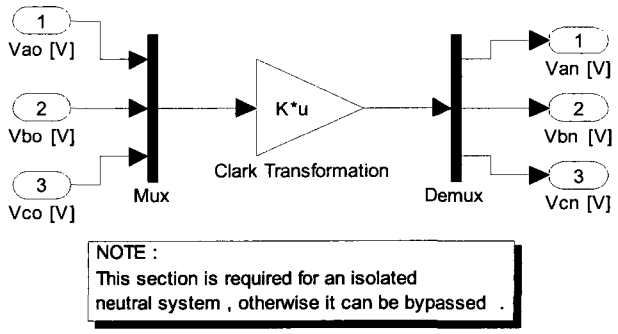

Figure 42: Line-to-Neutral Conversion Simulink model

The next block is the Rotor Angular Position Estimation. The rotor angular position is computed directly by integrating the frequency of the three-phase voltages input, ω_e. Subsequently, the unit vectors are computed by simply taking the sine and cosine of θ_e.

$$\theta_e = \int \omega_e \, dt \tag{4.12}$$

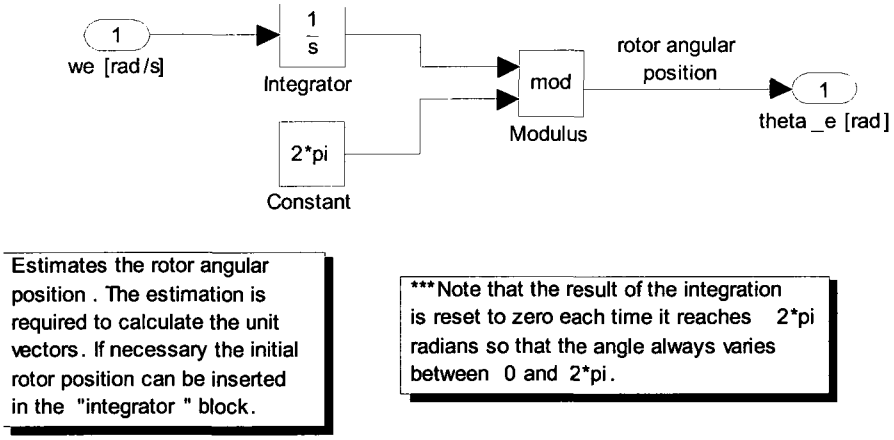

Figure 43: Rotor Angular Position Estimation Simulink model

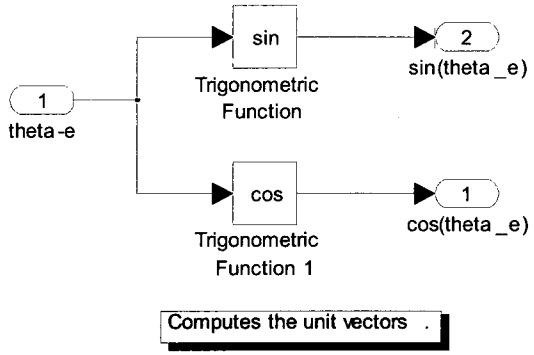

Figure 44: Unit Vector Simulink model

The ABC-SYN conversion block converts the three-phase voltages to the two-phase synchronously rotating frame. Using subscript s to refer to the stationary frame, the three-phase voltages are converted to the two-phase stationary frame using:

$$\begin{bmatrix} v_{qs}^{s} \\ v_{ds}^{s} \end{bmatrix} = \begin{bmatrix} 1 & 0 & 0 \\ 0 & \frac{-1}{\sqrt{3}} & \frac{1}{\sqrt{3}} \end{bmatrix} \begin{bmatrix} v_{an} \\ v_{bn} \\ v_{cn} \end{bmatrix} \tag{4.13}$$

$$\begin{aligned} v_{qs} &= v_{qs}^{s} \cos\theta_e - v_{ds}^{s} \sin\theta_e \\ v_{ds} &= v_{qs}^{s} \sin\theta_e + v_{ds}^{s} \cos\theta_e \end{aligned} \tag{4.14}$$

The equations are implemented into Simulink using a simple matrix gain and sum and product blocks.

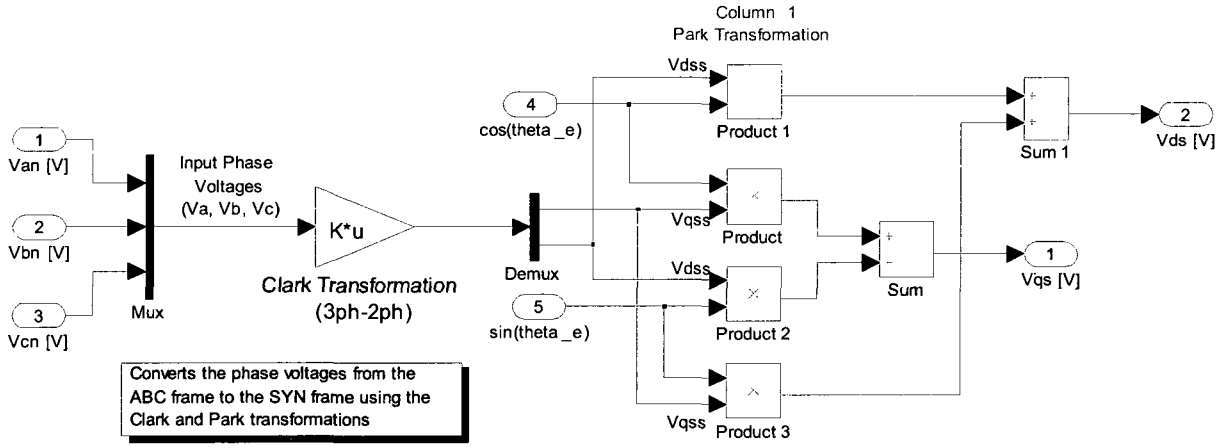

Figure 45: ABC-SYN Conversion Simulink model

The SYN-ABC Conversion block is similar to the ABC-SYN Conversion block. The block converts the current in the synchronous rotating frame to the stationary frame.

$$\begin{aligned} i_{qs}^{s} &= i_{qs}\cos\theta_e + i_{ds}\sin\theta_e \\ i_{ds}^{s} &= -i_{qs}\sin\theta_e + i_{ds}\cos\theta_e \end{aligned} \tag{4.15}$$

$$\begin{bmatrix} i_a \\ i_b \\ i_c \end{bmatrix} = \begin{bmatrix} 1 & 0 \\ \frac{-1}{2} & \frac{-\sqrt{3}}{2} \\ \frac{-1}{2} & \frac{\sqrt{3}}{2} \end{bmatrix} \begin{bmatrix} i_{qs}^{s} \\ i_{ds}^{s} \end{bmatrix} \tag{4.16}$$

Then the currents are converted from the stationary frame to the three-phase current using Equation 4.16. The Simulink model is similar to Figure 45 (see Figure 46).

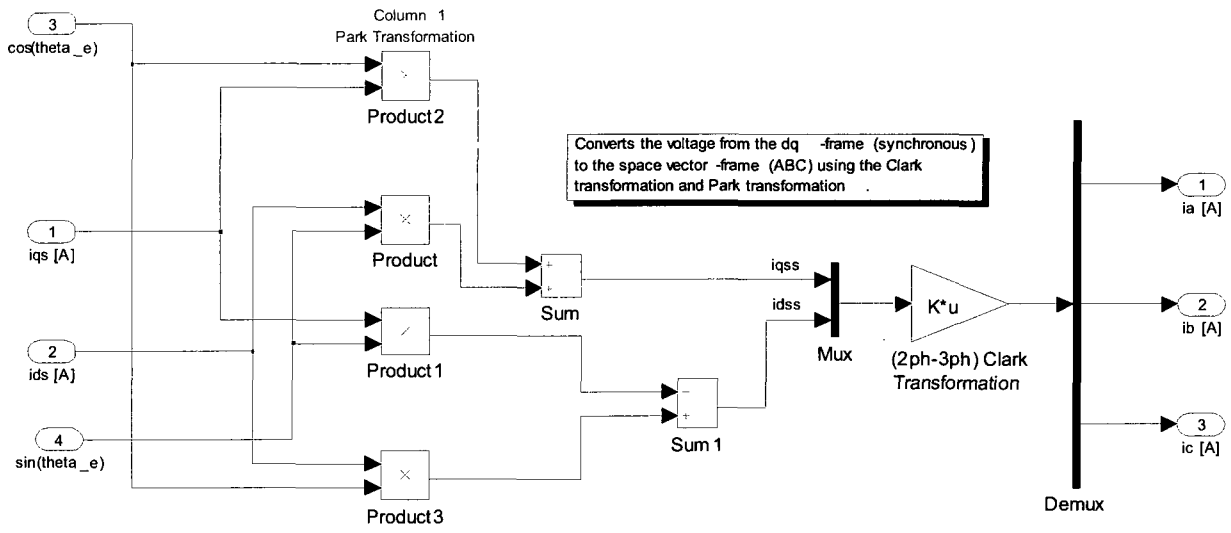

Figure 46: SYN-ABC Conversion Simulink model

The state-space equations derived in the previous chapter are implemented using discrete blocks as represented in Figure 47. The flux linkages in the Simulink model are represented by Equations 3.100-3.103 under column 1 in the figure. Column 2 implements the magnetizing flux linkages using Equations 3.92 and 3.93. Column 3 implements Equations 3.94-3.97 to compute the currents. Finally, column 4 and column 5 implement the electrical torque and rotor angular velocity computations using Equations 3.98 and 3.99.

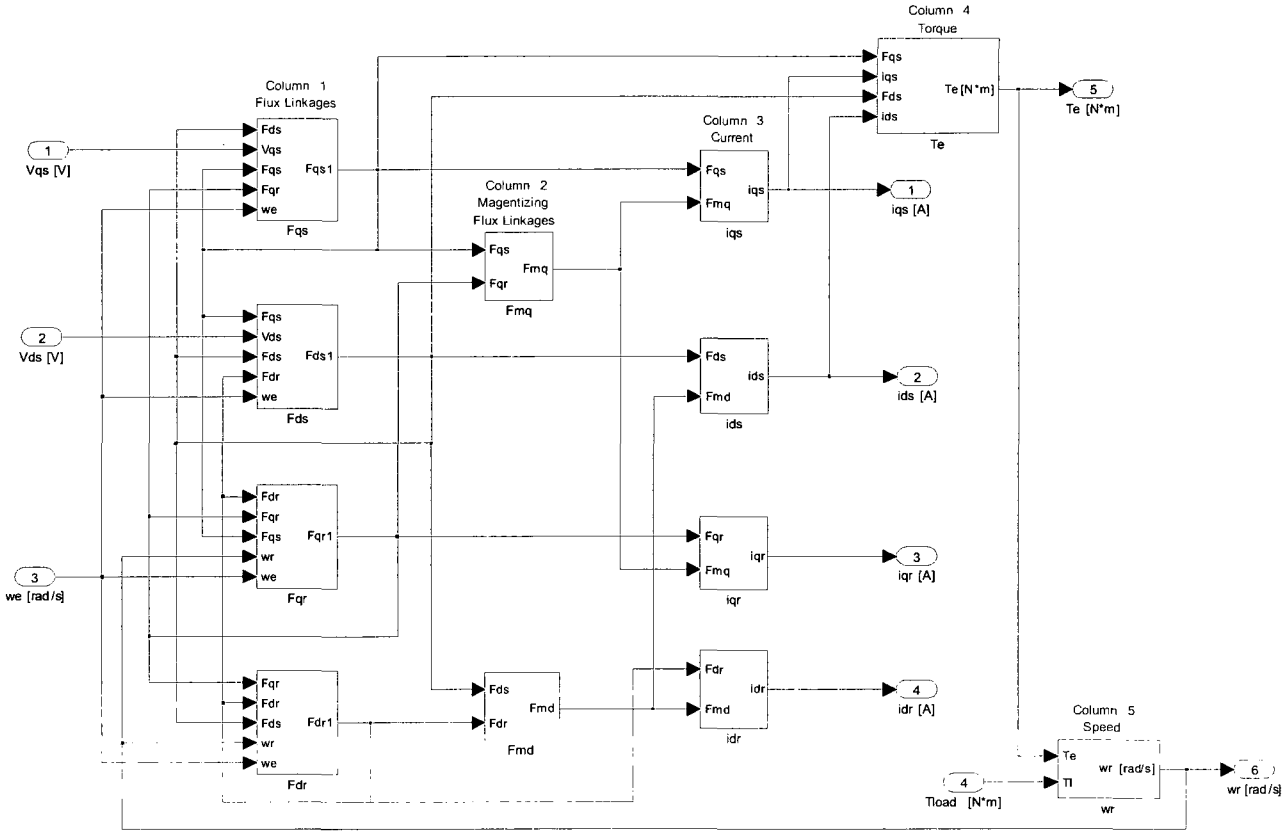

Figure 47: Three-phase AC Induction Machine Dynamic model implementation in Simulink

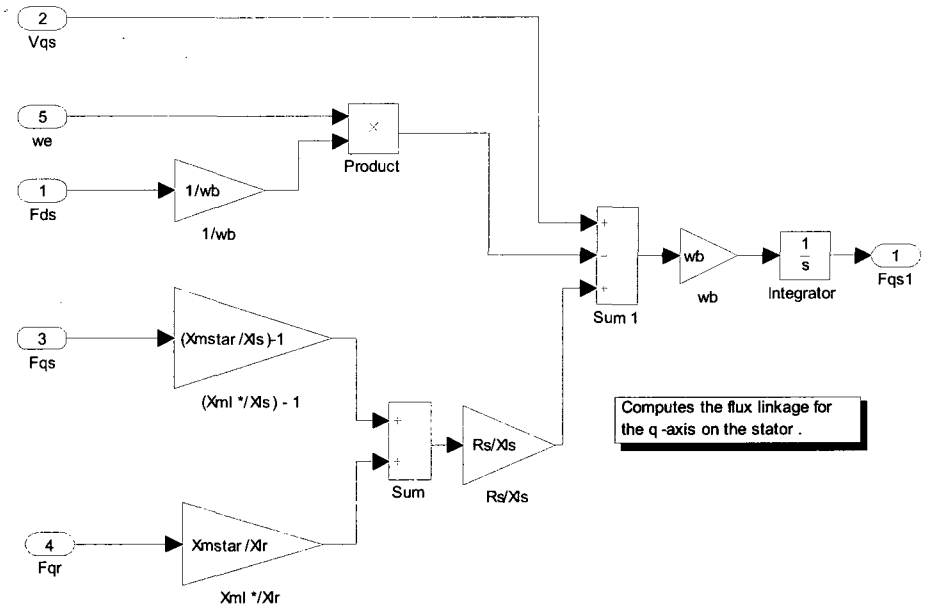

Figure 48: Implementation of F_{qs}, see Equation 3.49

4.2.3 Control System Model

The control system for the motor and drive is based on an indirect vector control scheme. The overall implementation is depicted in Figure 49. The inputs are the commanded rotor angular velocity and the load torque. The outputs are the three-phase currents, electrical torque output, and the feedback rotor angular velocity.

The main objective of vector control is to independently control the developed torque and flux, like a DC motor with separately excited states; see Figure 50. The current is fed back from the induction machine motor block. Slip is computed in an indirect manner via Equation 3.105. The inputs to the controller are the commanded and feedback rotor velocity. The system then controls the velocity with a PI controller, and saturation limits constrain the motor's maximum speed – 377 rad/sec. Thereafter, it is controlled independently with two PI controllers, and saturation limits were set to ±1 A. It should be noted that a PID controller is later added to the overall system to control the position.

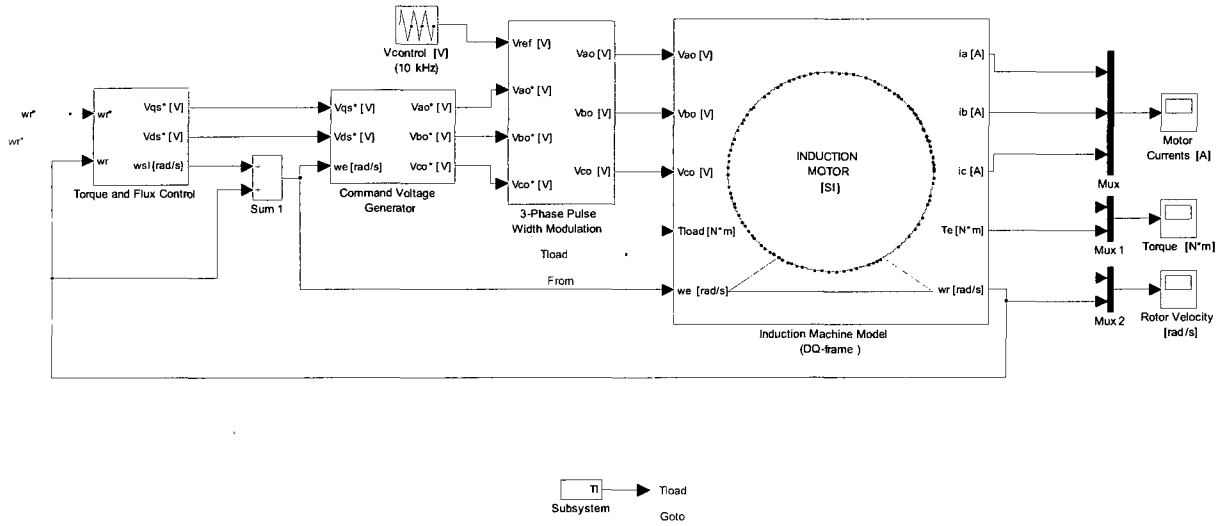

Figure 49: Overall indirect vector control Simulink model

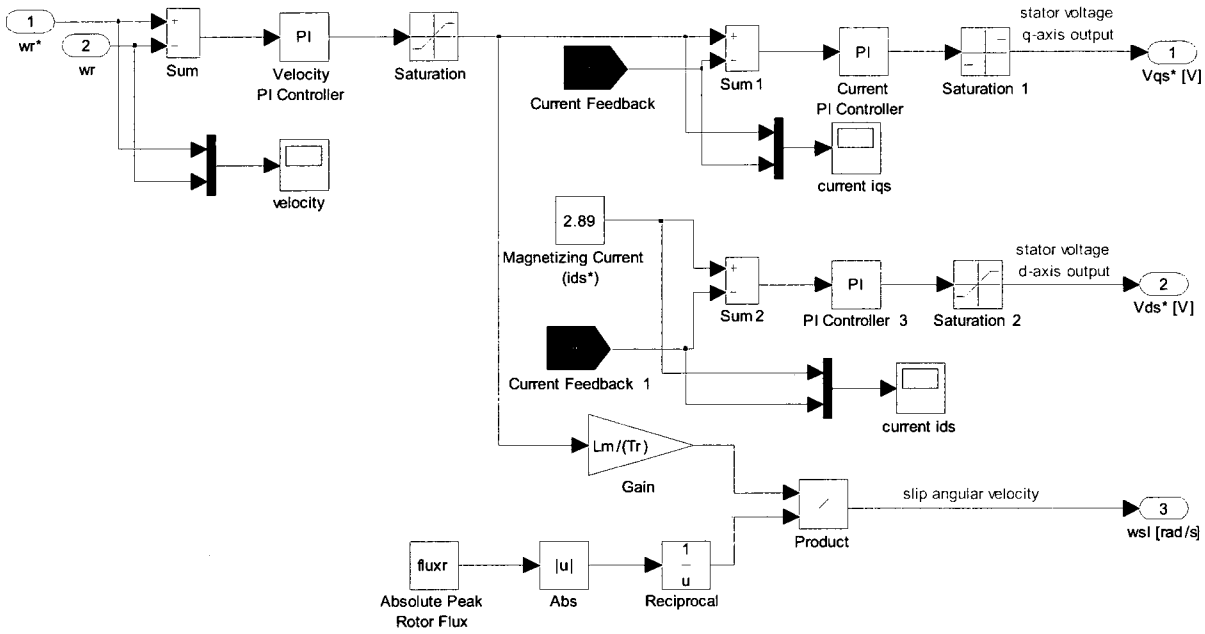

Figure 50: Vector control block in Simulink

The command voltage generator block generates the necessary three-phase voltages to power the motor after it passes through the pulse width modulator. Figure 51 is the Simulink model necessary for that implementation.

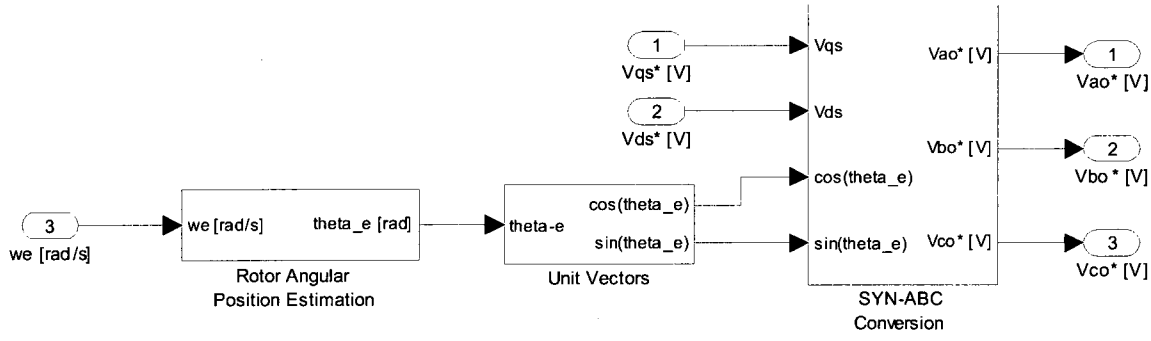

Figure 51: Command voltage generator block in Simulink

The pulse width modulation (PWM) inverter is modeled as a series of switches. The PWM assumes a sine-triangle which works by switching both upper and lower switches on each leg of the inverter as shown in section 3.3.4. The switch frequency was assumed to be 10 kHz with a duty cycle of 50%. For example, V_{ao} is controlled based on the following rules:

$$
\begin{aligned}
&If\ V_{ao}^{*} > \mathrm{V}_{\mathrm{ref}}, \\
&\quad then\ T_{a1}\ on\ \&\ T_{a2}\ off \\
&otherwise \\
&\quad T_{a1}\ off\ \&\ T_{a2}\ on
\end{aligned}
$$

The steps are the same for the other voltages.

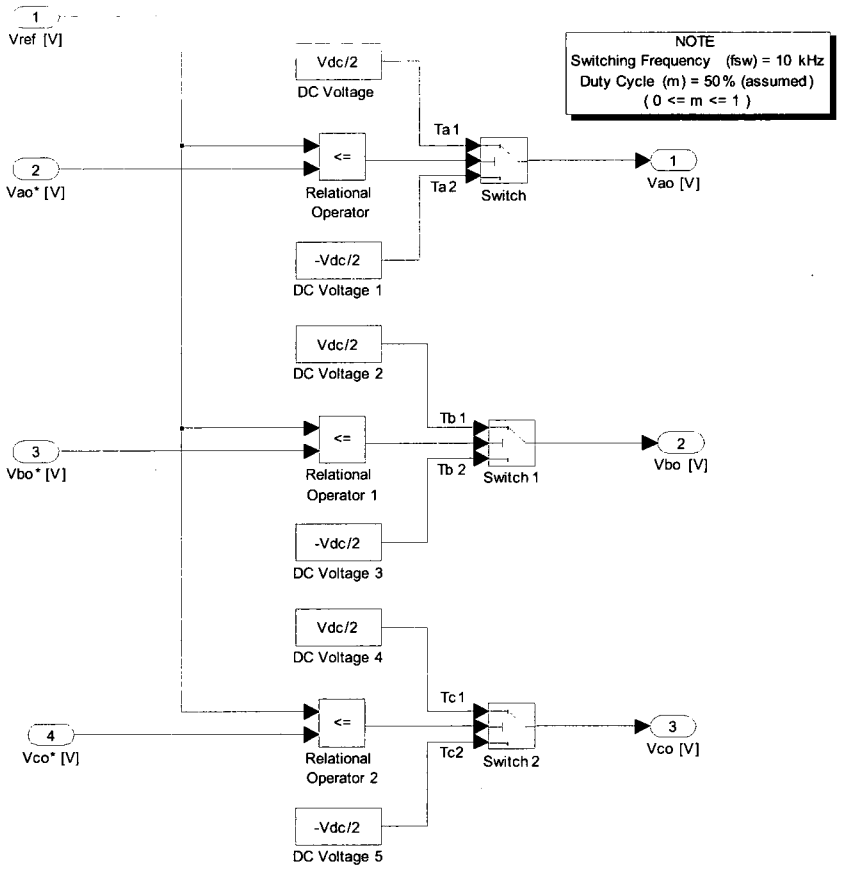

Figure 52: Pulse-width modulation block in Simulink

4.2.4 Compliantly-Coupled Drivetrain Model

The compliantly-coupled drivetrain model was simplified based on a rigid body assumption. Equation 3.122 was used with simple "add" and "multiplication" blocks to compute the torque load. The torque load is determined by the pitching moment from the aerodynamic model.

4.2.5 Sources of Instability in Simulation

There are several sources of instability that can either prevent the simulation from running or produce erroneous results. An obvious source is incorrect wiring which in turn creates positive feedback. The second source is due to an excessive phase lag around the loop. It typically occurs at one frequency and will have a phase lag of 180° which will cause a sign reversal and create positive feedback. However, this alone will not cause instability. The loop gain must also be equal to unity. Loop gain is the sum of the gains of individual blocks. Consequently, no models of the system encoder or the tachometer are represented in the overall simulation because that prevents the loop gain from achieving unity. The third source of instability is caused by phase lag. Typical components such as an integrator will have a -90° phase lag, low-pass filters have -45° phase lag, and a PI controller will have a phase lag between 0° and 90°. The final source of instability is due to margins of stability in a closed loop system. The system becomes unstable when the loop gain is 0 dB and the phase is -180°.

A closer look at the behavior of an integrator will show that the gain decreases as frequency increases, and ultimately the integrator will have a constant phase lag of -90°. See Figure 53 for an example.

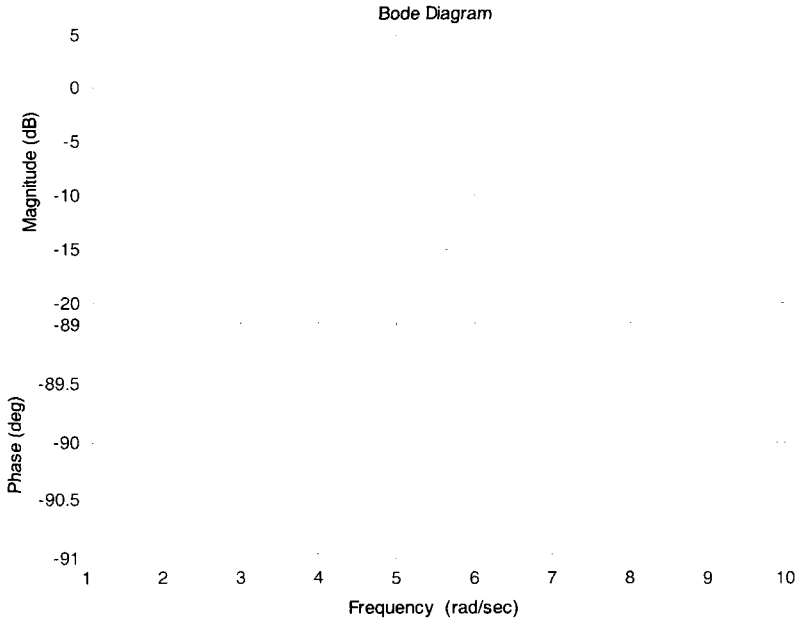

Figure 53: Bode plot of a generic integrator

The PI controller characteristics are shown using a simple Bode plot made for a generic PI controller. The controller was assumed to be a first-order system with a gain of K = 1 and a time constant of $\tau = 2$ [106].

$$G(s) = \frac{K(\tau s + 1)}{\tau s} \tag{4.17}$$

When the system is operating below its break frequency the phase is -90°; the integral term is dominating, and the gain will fall with frequency, as shown in Figure 54. Above the break frequency, the phase lag is 0°, and the proportional gain term is dominating. The gain of the controller is flat with frequency. In transition the phase climbs.

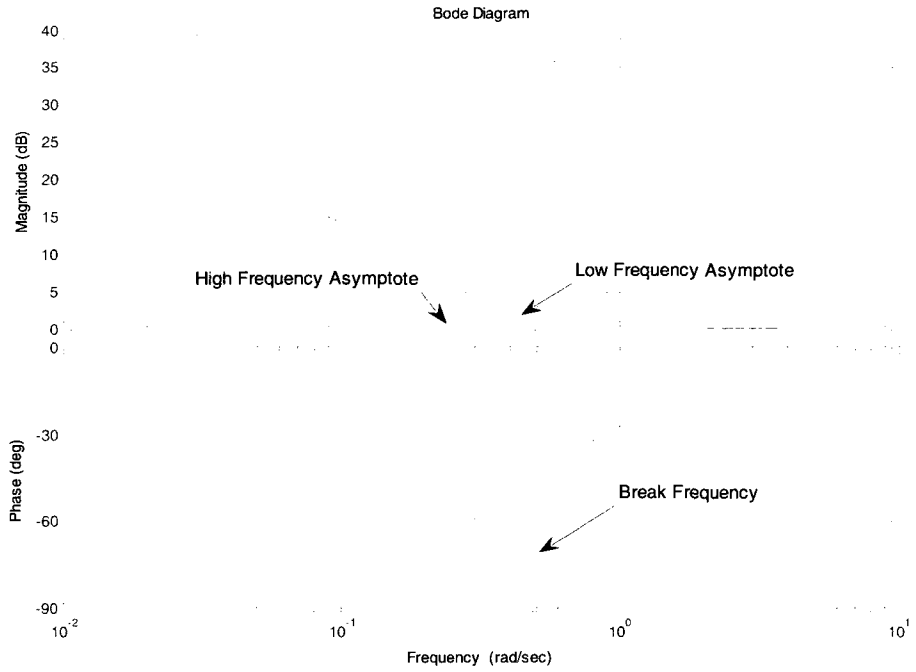

Figure 54: Bode plot of a generic PI controller

Low-pass filters are used primarily to remove noise and resonance from a variety of sources. However, they can cause instability via phase lag at the gain crossover frequency. The low-pass filter is represented by a simple RC circuit, as shown in Figure 55, where R is the resistance and C is the capacitance.

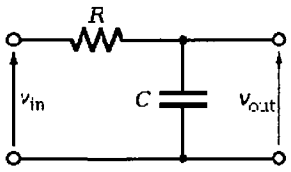

Figure 55: RC circuit

An example response diagram for a generic 45 Hz low-pass filter is shown in Figure 56 where the filter is a first-order transfer function given as:

$$G = \frac{v_{out}}{v_{in}} = \frac{1/RC}{s + 1/RC} \quad . \tag{4.18}$$

This filter allows content to pass below 45 Hz and excludes frequencies higher than 45 Hz. The major issue with using filters is the phase change associated with frequency. It is clear to see that even at low frequency the phase is not 0°, and it changes significantly over the full frequency range. This change in frequency is problematic because it introduces instability into the system. This type of low-pass filter based on an RC circuit design is not very efficient. Also, the filter circuitry is buried within the motor's electronics; therefore, the simple RC circuitry may not accurately represent the true filtering process used. The true representation of the filter is unknown to the author because the manufacturer is not forthcoming with detailed information.

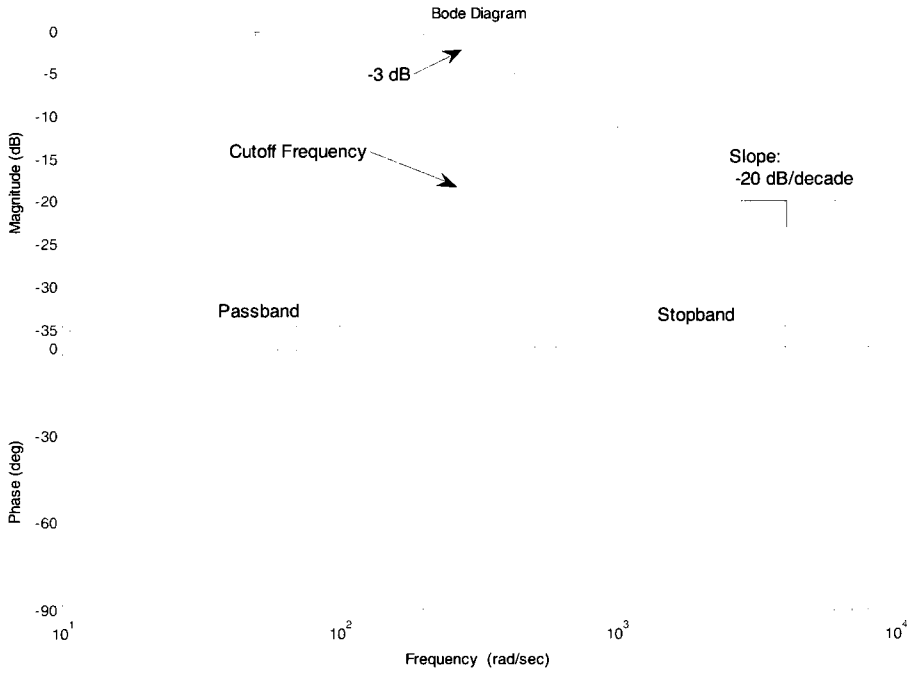

Figure 56: Generic 45 Hz low-pass filter Bode plot

In the actual representative model of the dynamic rig there are two low-pass filters present – 11 Hz low-pass and 5192 Hz low-pass filter. See Figures 57 and 58, respectively. The filters caused instability in the overall system by introducing positive feedback. Consequently, the filters were removed from the full system model.

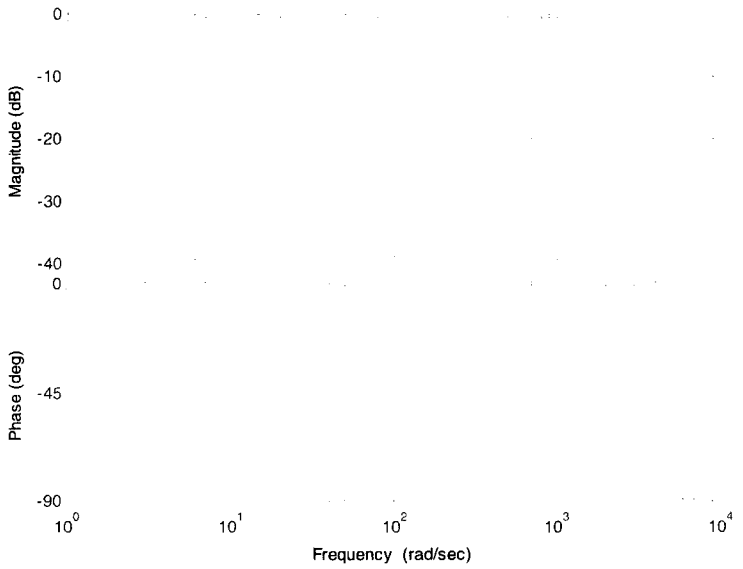

Figure 57: 11 Hz low-pass filter Bode plot

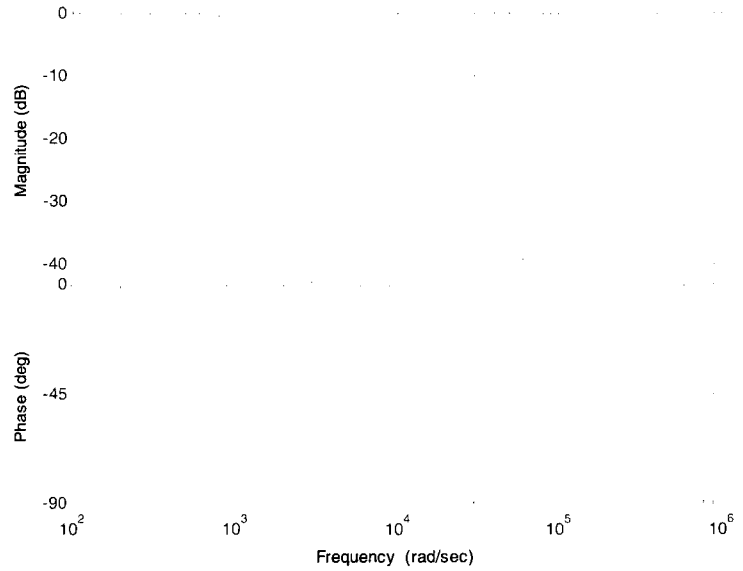

Figure 58: 5192 Hz low-pass filter Bode plot

4.2.6 Overall Computer Model

The overall computer model block diagram is illustrated in Figure 59 showing a small number of components added to the system. Starting from the left side of the figure, an input saturation block is placed after the commanded angular position block to cause saturation on the input, consistent with experimental data for forced oscillation tests. The gear drive was added to amplify the command that the motor would "see." In the physical system the motor "sees" a torque amplification through the gear drive. The PID controller was added for the position control loop. Encoders and tachometers were assumed to have unity gain. The aerodynamic model is located in the "if action subsystem" block. Introduction of aerodynamic forces and moments is delayed by 0.15 sec to allow motor start-up transients and to avoid discontinuities. Backlash is proportional to the angular velocity and is placed ahead of the aerodynamic model. The aerodynamic model is subjected to commanded position and velocity on the other side of the gearbox. Finally, the compliance model uses the total pitching moment and the equivalent damping in order to compute the torque load. The torque load is fed back to the motor. The input reference voltage was assumed to be a triangular waveform operating at 10 kHz – the $V_{control}$ block [120]. Finally, the data were saved to the workspace as matrices, CLdata and CMdata, and "scopes" were added for visual diagnostics.

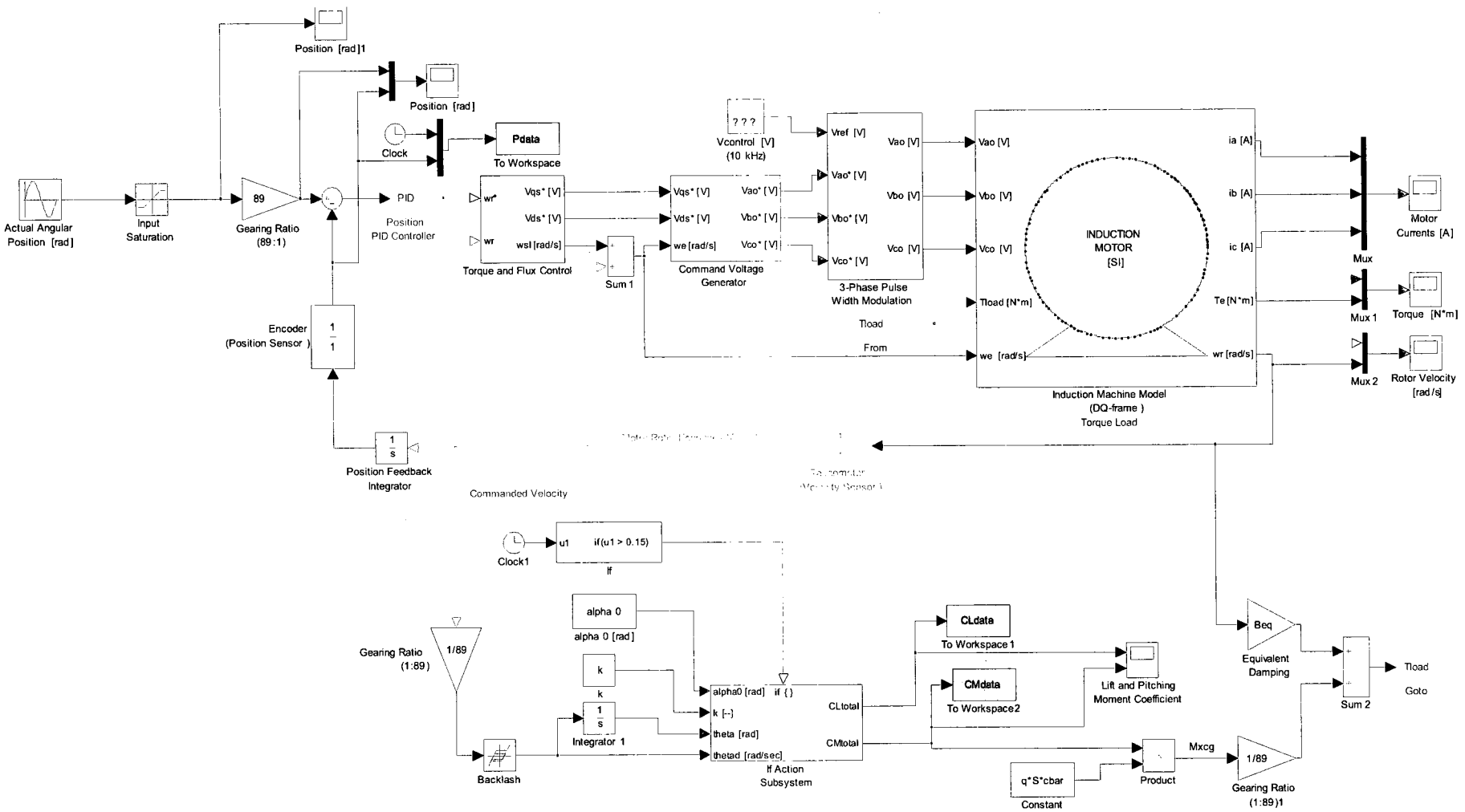

Figure 59: Overall dynamic oscillation simulation in Simulink

4.3 Computer Simulation Model Verification and Validation

When using any computer model, the primary issue is credibility of the simulation model. Every computer simulation must be verified and validated (V&V). There are various definitions for the terminology of verification and validation [121-126]. This study follows the definitions provided by Sargent [126]. Model verification is defined as "ensuring that the computer program of the computerized model and its implementation are correct" [126]. Model validation is defined as "substantiation that a computerized model within its domain of applicability possesses a satisfactory range of accuracy consistent with the intended application of the model" [126].

Figure 60 describes graphically the verification and validation process related to model development. The "problem entity" block is the real system (i.e. forced oscillation dynamic test rig). The "conceptual model" block is the block diagram representation of the real system. The "computerized model" block is the mathematical representation of the real system.

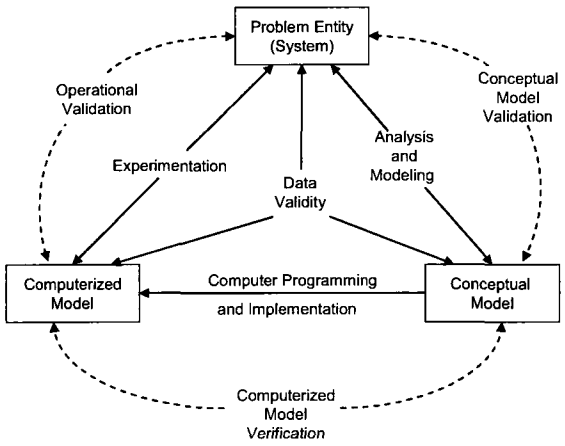

Figure 60: Simplified verification and validation process [126]

The task of conceptual model validation determines if the theories and assumptions of the conceptual model are correct. A complete list of all the theories and assumptions used in the computerized simulation model of the pitch oscillation system is provided in Appendix C. It also includes determining if the model representation of the real system is "reasonable." The computerized model is verified by assuring that the implementation of the conceptual model is correct. The task of operational validity is to determine if the model's output behavior is sufficient. Finally, data validity is defined as "ensuring that the data necessary for model-building, model-evaluation and testing, and conducting the model experiments to solve the problem are adequate and correct" [126].

There are no standard methodologies for V&V. A survey of V&V methodologies varied greatly from application to procedure used, to a combination of techniques; a few detailed examples are provided by [124, 126, and 127]. Verification typically relies on good programming practices, checking intermediate simulation outputs, statistical testing, and animation [124]. Examples of the various validation techniques range from: animation, comparison to other models, degenerate tests, event validity, extreme condition tests, face validity, historical data validation [128-130], rationalism, empiricism, internal validity (i.e. replication of stochastic models), multistage validation [131], operational graphics, sensitivity analysis, predictive validation, traces, and Turing tests [123].

This study uses a combination of techniques for V&V drawn primarily from the work of Kleijnen 1995, Sargent 2007, and Oberkamf et al. 2004 [124, 126, and 127]. The V&V process used in this study is an iterative approach. Some steps require validation before verification; then the computerized model can be validated. For example, the

conceptual model needs to be validated, and then the simulation model can be verified and validated. The verification techniques used to determine if the simulation program performs as intended follow these steps:

1. Proper validation of conceptual model. Validity is determined by:
    a. The theories and assumptions underlying the conceptual model are correct, and
    b. The model representation of the physical system is mathematically correct and "reasonable" for the purposes of the model.
2. Certify that the computerized model reflects the physical system based on the conceptual model. For example, if the actual system is nonlinear, then those nonlinear characteristics must be reflected in the equations of motion underlying the model.
3. Ensure that the simulation is error free and the model has been programmed correctly in the simulation language.
4. Verification of object-oriented software (i.e. Simulink and LabVIEW) systems by determining that the simulation functions *and* the computer model have been programmed and implemented correctly.

The validation technique used to determine whether the computerized model was an accurate representation of the system consisted of using benchmark cases at the component level and then at the whole-system level. The validity of the operational system was determined by exploring the model behavior.

4.3.1 Simulink Model Verification and Validation

The Simulink model of the forced oscillation test rig was verified by ensuring the subsystem models (i.e. AC motor, control system, aerodynamic model, etc.) were programmed correctly and implemented properly. The model was also verified by comparing the conceptual block model and the real representative system with the Simulink model in order to ensure that mistakes have not been made in implementing the model. An input saturation block was added to the overall system to represent the noted position saturation identified in experiments by Kim et al. [10]. The aerodynamic subsystem model was time delayed by a specified amount because of a very large start-up torque transient at the beginning of the simulation which causes the overall system to fail.

Various validation techniques are available and found throughout literature; an excellent survey of popular techniques is available from Sargent [126]. It can also be used in a subjective (i.e. observation) or objective (i.e. some mathematical procedure) evaluation. Typically, a combination of techniques is used. The techniques can be applied to either a submodel and/or an overall model. This study employed a multistage validation approach where the following were carried out: face validity, historical data validity, operational validity, process validity (black- and white-box testing), graphical validity, and comparison to other models validity (with benchmark cases).

Face validity consisted of asking knowledgeable individuals about the system whether the model and/or its behavior are reasonable. For example, Murphy identified mistakes in the aerodynamic coefficient trends and inappropriate magnitudes [4]. The errors were traced back to the original aerodynamic model from Katz and Plotkin,

determined to be an unrealistic representation. The aerodynamic submodel was updated using experimental data for an F-16XL and then verified and validated.

Historical data validation employs available experimental data to build the model, and the data is used to determine whether the model behaves as the physical system does. Experimental data was used to validate the aerodynamic submodel; see Figures 61-64. The experimental NASA data are represented by the lines in the figure, and the aerodynamic submodel predicted result cases are represented by the symbols. Since this data serves as the baseline and measurements will be made as increments from the baseline, the procedure was deemed adequate. Numerical trapezoidal integration was used to determine the coefficients. The procedure can either overestimate or underestimate the true value of the experimental data depending on the sign of the error [132]. The computational code used for validation of the responses is provided in Appendix B.

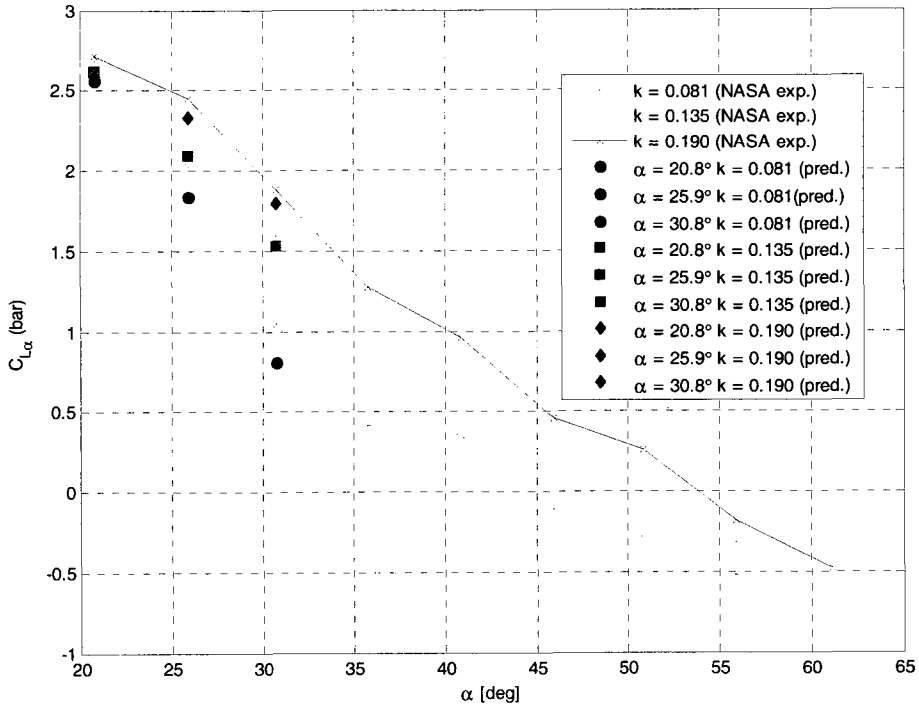

Figure 61: In-phase lift coefficient validation

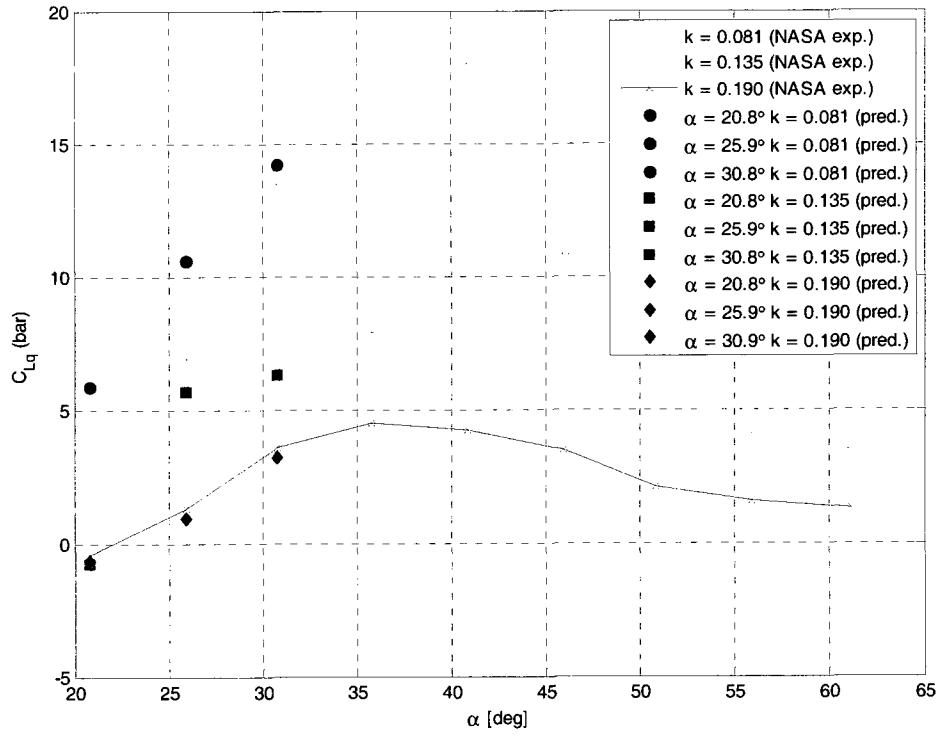

Figure 62: Out-of-phase lift coefficient validation

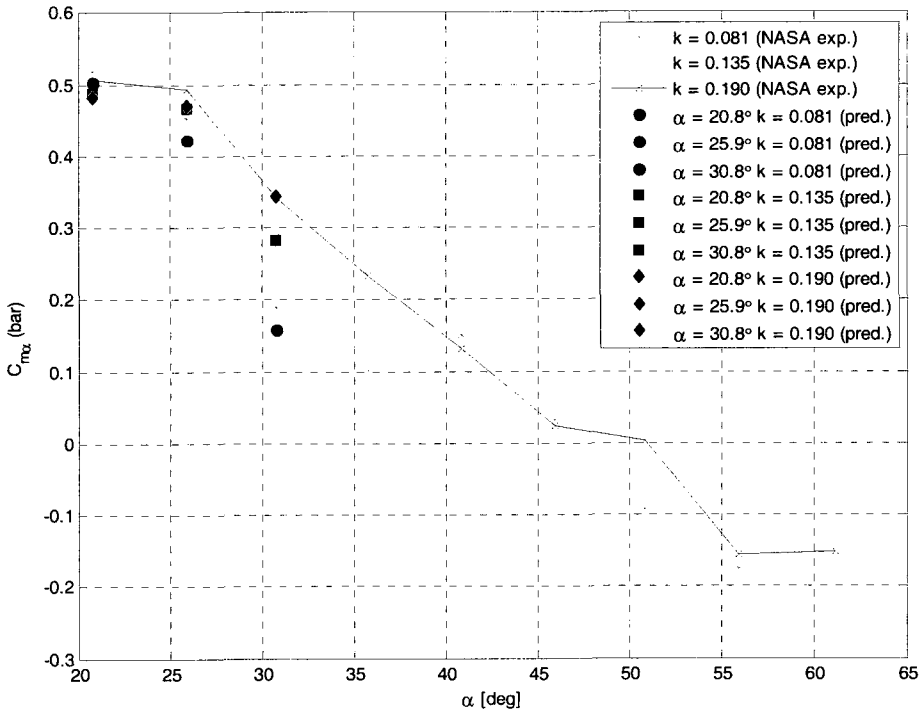

Figure 63: In-phase pitching moment coefficient validation

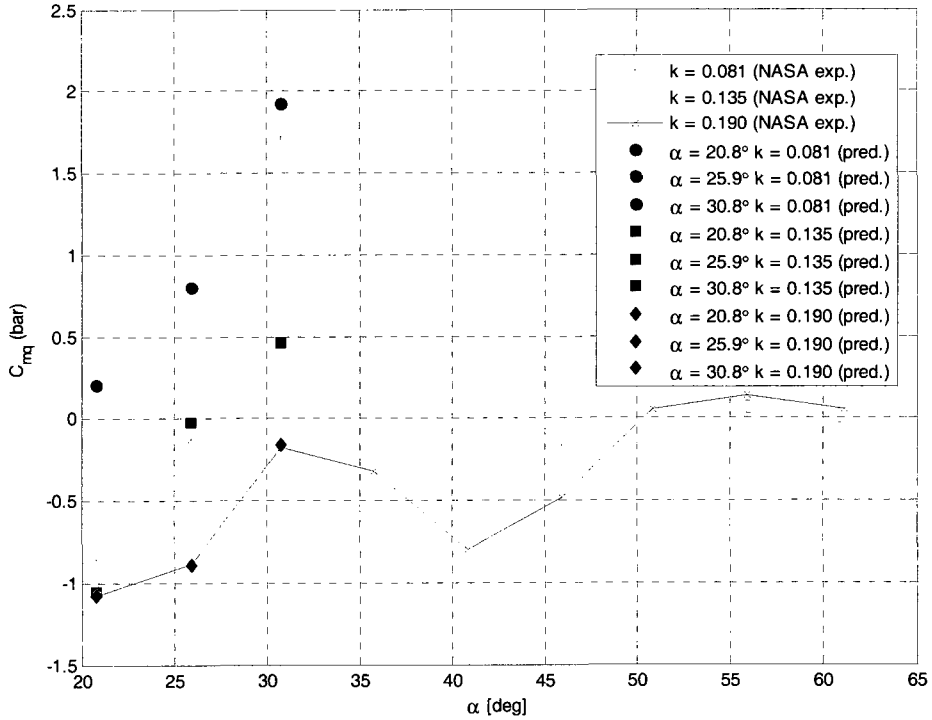

Figure 64: Out-of-phase pitching moment coefficient validation

The AC motor submodel was validated by comparing the submodel to a benchmark case. This type of validation uses various output results of the simulation model and compares it to other validated models. The benchmark case was a 10 Hp motor with results provided by Ozpineci and Tolbert [118]. The current model reproduced the results provided by the benchmark case, as shown in Figure 65.

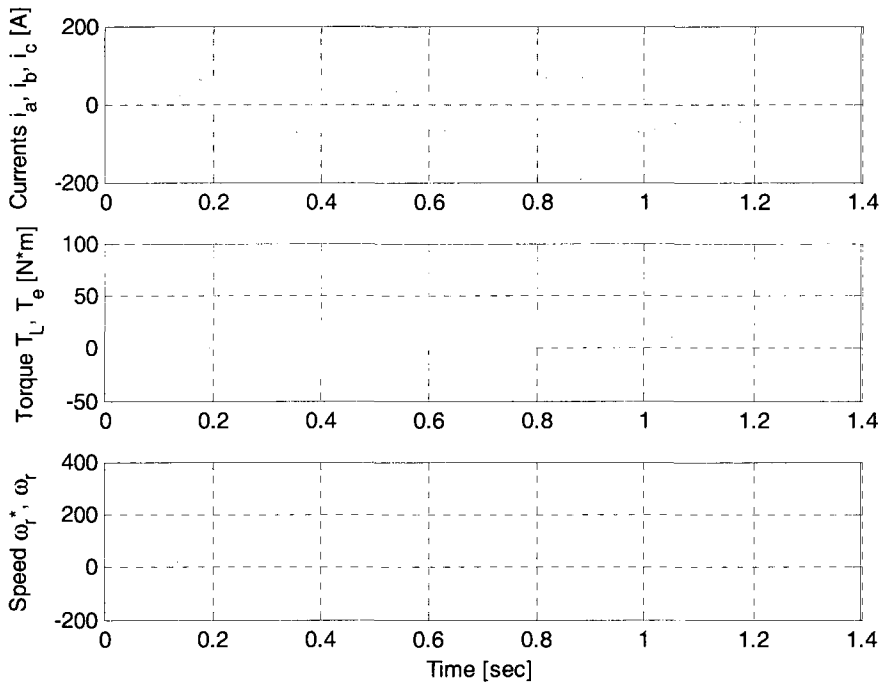

Figure 65: Characteristic behavior of 10 Hp AC motor with specified commanded velocity and load torque (reproduction of article results [118])

The performance of the compliantly-coupled drive train cannot be validated independently because its parameters are dependent on other parameters such as the load torque. The computerized model of the drive train is validated during operational and process validation of the overall system.

Operational and process validation goes hand in hand in this study. Operational validation uses either a subjective or objective approach. The dynamical behavior of the system is displayed visually as the simulation model proceeds through time to ensure dynamic similarity [126]. This study explored the model behavior for various reduced frequencies. It was determined that the model was accurate and operational for a reduced frequency range of 0.081 to 0.1. At higher reduced frequencies, there were problems due to controller gains. An example is provided in Figure 66. It is possible, even likely, that the real system is scheduling gains depending on frequencies. Queries to NASA users of the FOS led to discovery that the microprocessor controller was performing scheduling gains.

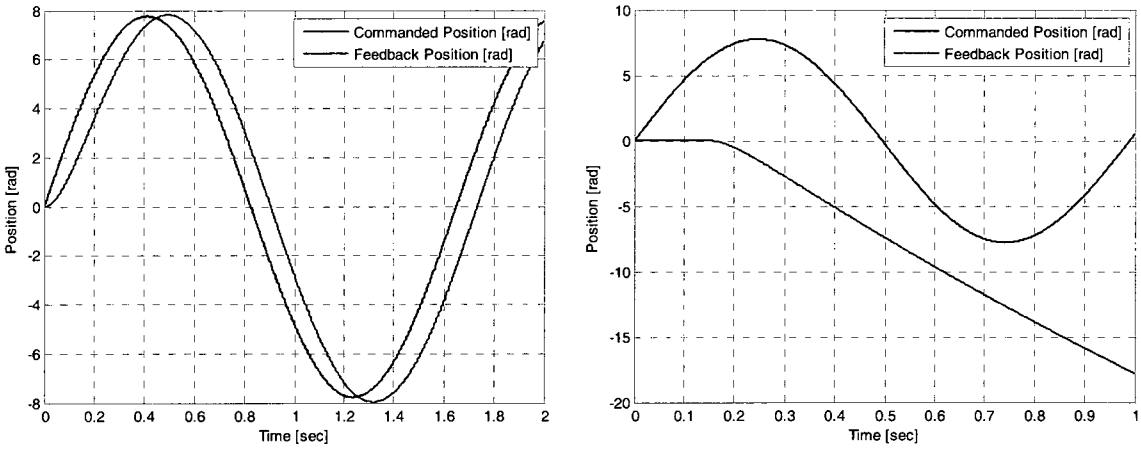

Figure 66: Commanded and feedback position for different reduced frequencies (k = 0.081 left side and k = 0.135 for right side)

Validating the overall computer model is a black-box approach because all of the internal relationships cannot be measured directly. Consequently, validation is based on

prediction and not explanation. This final step was completed by using a design of experiments approach.

4.4 Design of Experiments Approach

4.4.1 Statistical Principles

The foundation of design of experiments is based on the use of statistical principles and regression modeling. The terminology of experimental design is not uniform across disciplines. Factors are defined as controllable experimental variables that are thought to influence the response(s). The response(s) are defined as the outcome or result of an experiment. Responses can be quantitative or qualitative. Statistically designed experiments are efficient in the sense that they are economical in terms of the number of test runs that must be conducted, testing, efficiency. Moreover, individual interaction as well as interaction between factor effects can be evaluated. They allow one to measure the influence of one or several factors on a response. They allow the estimation of the magnitude of experimental error. When experiments are designed without adhering to statistical principles, they usually violate one or more design goals.

The statistical principles are based on a few classical assumptions, residuals are normally and independently distributed (NID(0,σ^2)): (1) normality, (2) independence, and (3) constant variance [133]. The normality assumption assumes that the residuals have a normal distribution centered at zero using a normal probability plot (NPP). If the residual distribution is a normal distribution, then the NPP will resemble a straight line. A moderate departure from the norm does not imply the assumption is no longer valid. However, gross departures can be potentially serious. The independence assumption checks for correlation between the residuals. Independence is determined by plotting the

residuals in time order to detect correlation. Proper randomization of the experiment is necessary to avoid violating the independence assumption. The constant variance assumption assumes that the residuals are structure-less and bounded and not related to any other variable including the predicted response [133]. A simple check is to plot the residuals against the predicted response.

4.4.2 Common Design Problems

When the statistical methodology is not used to design engineering experiments, several common problems occur. Experimental variation can mask factor effects. Questions arise if the factor effect is measuring a true difference in the population. A second problem that occurs is the effect of uncontrolled factors on the response which could compromise the experimental conclusions. Erroneous principles of efficiency lead to unnecessary waste of resources or inconclusive results. Finally, scientific objectives for many-factor experiments may not be achieved with one-factor-at-a-time designs.

4.4.3 2^k Factorial Designs

Factorial designs are the most efficient for experiments with two or more factors. The general model for a two-factor design is

$$y = \beta_0 + \beta_1 x_1 + \beta_2 x_2 + \beta_{12} x_{12} + \ldots + \varepsilon \ . \tag{4.19}$$

A 2^k factorial design is a design with k factors, each at two-levels. The statistical model for a 2k design would include k main effects, two-factor interactions, three-factor interactions, and so forth up to a single k-factor interaction. The general approach to analyzing a factorial design is given by Table 7.

Table 7: Analysis Procedure for a 2^k design [133]

1. Estimate factor effects
2. Form initial model a. If the design is replicated, fit the full model b. If there is no replication, form the model using a normal probability plot of the effects
3. Perform statistical hypothesis testing to identify significant terms in model
4. Refine model – use summary statistics, such as R^2
5. Analyze residuals
6. Interpret results

Estimating the factor effects and examining their signs and magnitudes gives preliminary information regarding which factors and interactions are significant. The analysis of variance (ANOVA) is used to formally test for significance of main effects and interactions; see Table 8. An F-test is used to judge the degree of change in the response due to changing a factor level. The F-test can be thought of as a signal/noise ratio. A factor effect change is compared to random errors. Montgomery has given a detailed analysis of computing the sum of squares, mean square, and F-value [133]. The model is refined generally by removing any non-significant factors from the full model. Finally, the analysis is completed by analyzing the residuals for model adequacy and checking the assumptions. Interpreting the results usually consists of reviewing response surface plots or the resulting regression models.

Table 8: Symbolic Analysis of Variance for a 2^k Design [133]

Source of Variation	Sum of Squares	Degrees of Freedom	Mean Square	F-Value
k main effects				
A	SS_A	1	MS_A	$F_A = MS_A/MS_E$
B	SS_B	1	MS_B	$F_B = MS_B/MS_E$
⋮	⋮	⋮	⋮	⋮
K	SS_K	1	MS_K	$F_K = MS_K/MS_E$
two-factor interactions				
AB	SS_{AB}	1	MS_{AB}	$F_{AB} = MS_{AB}/MS_E$
AC	SS_{AC}	1	MS_{AC}	$F_{AC} = MS_{AC}/MS_E$
⋮	⋮	⋮	⋮	⋮
JK	SS_{JK}	1	MS_{JK}	$F_{JK} = MS_{JK}/MS_E$
three-factor interactions				
ABC	SS_{ABC}	1	MS_{ABC}	$F_{ABC} = MS_{ABC}/MS_E$
ABD	SS_{ABD}	1	MS_{ABD}	$F_{ABD} = MS_{ABD}/MS_E$
⋮	⋮	⋮	⋮	⋮
IJK	SS_{IJK}	1	MS_{IJK}	$F_{IJK} = MS_{IJK}/MS_E$
⋮	⋮	⋮	⋮	⋮
k-factor interaction ABC … K	$SS_{ABC...K}$	1	$MS_{ABC...K}$	$F_{ABC...K} = MS_{ABC...K}/MS_E$
Error	SS_E	$2^k(n-1)$	MS_E	
Total	SS_T	$n2^k-1$		

Center points are usually added to a factorial design that will "provide protection against curvature from second-order effects as well as to provide an independent estimate of error" [133]. Replicated runs for an experimental design are often chosen at the center of the design space because they do not affect estimates in a 2^k design. However, it should be pointed out that replication is not necessary when an experiment under consideration is deterministic (i.e. computational).

4.4.4 2^{k-p} Fractional Factorial Design

As the number of factors increases in an experiment, the number of test runs becomes resource intensive. If it can be assumed that high-order interactions are negligible, then a fractional factorial design can be used to model the main effects and

low-order interactions. The primary use of fractional factorials is for screening experiments. The goal is to identify the significant factors that have large effects out of many potential factors. The use of fractional factorials is based on three key principles [133]: (1) the sparsity of effects principle, (2) the projection property, and (3) sequential experimentation. The sparsity of effects principle is based on the idea that a system is likely to be driven primarily by main effects and low-order interactions [133]. If necessary, the fractional factorial design can be projected into a more robust design in a subset of significant factors [134]. It is also possible to combine subsets of runs of two (or more) fractional factorials to assemble sequentially a larger design to estimate the factor effects and interactions of interest [133].

When using a particular fractional factorial design the effects can be aliased; aliasing refers to correlation of factors in model estimates. Therefore, design resolution becomes important. For *resolution III designs*, no main effects are aliased with any other main effect, but main effects are aliased with two-factor interactions and some two-factor interactions are aliased with each other [133]. An example is the 2^{3-1}_{III} design – a 2^{3-1} fractional factorial with a resolution III design. For *resolution IV designs*, no main effects are aliased with any other main effect or with any other two-factor interactions. However, the two-factor interactions are aliased with each other. An example of a resolution IV design is 2^{4-1}_{IV}. The *resolution V design* has no main effects or two-factor interactions aliased with any other main effect or two-factor interactions, but two-factor interactions are aliased with three-factor interactions [133]. An example of a resolution V design is 2^{5-1}_{V}. The size of the fractional factorial is determined by the highest possible

resolution. The analysis procedure is the same as described in the factorial design section.

4.4.5 Central Composite Designs

Classical central composite designs (CCD) represent the most popular class of second-order designs used in response surface methodology (RSM). It was introduced by Box and Wilson (1951). A graphical representation of a CCD is shown in Figure 67. The CCD design involves F factorial points, $2k$ axial points, and n_c center runs. The distance of the axial points varies from 1.0 to $\sqrt{k}$ [134].

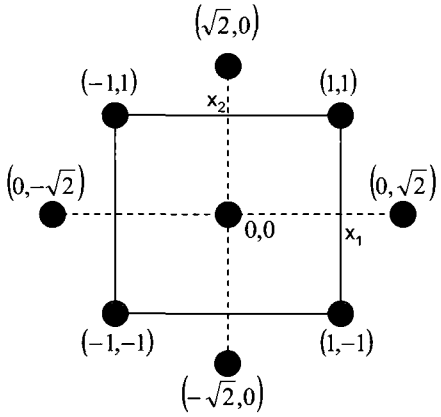

Figure 67: General example of central composite design for k = 2 and $\alpha = \sqrt{2}$ [134]

Central composite designs allow for a second-order model to be fitted to the experimental data; see Equation 4.20.

$$y = \beta_0 + \sum_{i=1}^{k} \beta_i x_i + \sum_{i=1}^{k} \beta_{ii} x_i^2 + \sum \sum_{i \neq j}^{k} \beta_{ij} x_i x_j + \varepsilon \qquad (4.20)$$

The central composite design is popular because of three properties. A CCD can be run sequentially. This is particularly desirable when curvature is present. For

example, a data set can be partitioned into two subsets. The first subset estimates linear and two-factor interaction effects while the second subset estimates curvature effects. CCDs are very efficient. They provide information on the variable effects and overall experimental error in a minimum number of required runs. CCDs are very flexible in that axial points distances can be varied. The flexibility is useful when different experimental regions of interest and regions of operability are being studied.

Generally, CCDs have the desirable property of rotatability. It is important for a second-order design to possess reasonably stable distribution of the scaled prediction variance, $N \operatorname{var}[\hat{y}(x)]/\sigma^2$ [134]. This is a critical property because one will not be sure where in the design space accurate predictions are required. However, there are situations where design variable ranges are restricted. Consequently, examples of a few other types of CCD designs that have been used are: face-centered (FCD), circumscribed, and inscribed [134].

4.4.6 Hybrid Designs

The final design chosen for the study is called an embedded central composite face centered design with a 2^{5-1} fractional factorial with resolution V. The principle of an embedded FCD is illustrated graphically in Figure 68. With more factors, the embedded FCD geometry becomes hypercubes with higher-dimensionality. The extremes of the factor levels are set on the perimeter of the outer box. The nested factor levels are set on the perimeter of the inner box. The design is augmented to include axial points and a center point. This design allows for pure cubic terms to be modeled in addition to the full quadratic model of Equation 4.1. The variance inflation factor (VIF) is used to quantify the degree of correlation between variables in the model [135]. Generally, a VIF less

than 10 is desirable. For this study, the VIF ranged from 1 to 9 depending on whether the term was a first-order, quadratic, or cubic.

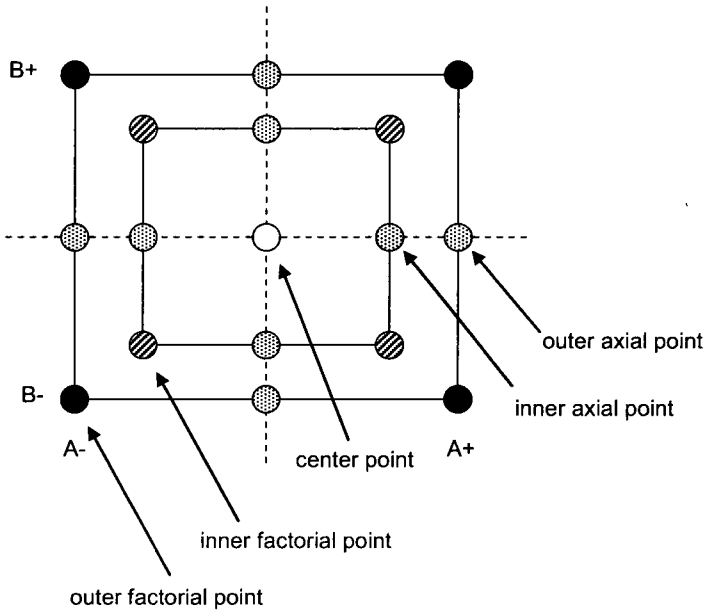

Figure 68: Nested face centered design in two factors [135]

It should be stated that face centered designs are not rotatable. However, it is generally not a priority when the region of interested is cubical [134]. Adding one or two center run points is sufficient to produce reasonable stability in predicted variance.

Table 9: Factor limits

Factor	Units	RSM low (outer)	RSM low (inner)	RSM center	RSM high (inner)	RSM high (outer)
A	$kg*m^2$	0.0001729	0.0002944	0.0004159	0.0005374	0.0006589
B	N-m-s/rad	0.0000000	0.0020140	0.0040280	0.0060420	0.0080560
C	--	0.0810000	0.0857500	0.0905000	0.0952500	0.1000000
D	arcmin	2.0000000	4.0000000	6.0000000	8.0000000	10.0000000
E	rad	0.0809000	0.0856775	0.0840850	0.0856775	0.0872700

Factor Labeling Key:

Label	Factor
A	Jeq (equivalent inertia)
B	Beq (equivalent damping)
C	k (reduced frequency)
D	BL (backlash)
E	IS (input saturation)

The five factors investigated in this study were: equivalent inertia, equivalent damping, reduced frequency, backlash, and input saturation. The output responses were: in-phase lift coefficient, out-of-phase lift coefficient, in-phase pitching moment coefficient, and out-of-phase pitching moment coefficient. The factor limits for the design are specified in Table 9. Equivalent inertia is based on the compliance of the system, assuming a straight sting (for RSM low outer) or a bent sting (for RSM high outer). Equivalent damping is similar; however, it assumes no damping (for RSM low outer) and the compliance damping (for RSM high outer). The reduced frequency range is based on experimental data. The backlash range is based on tabulated information from Winsmith [136]. Finally, the input saturation range is based on observations from experimental data. The inner face center design points were determined by ½ of the distance to the outer face center design points.

The nested face centered design test matrix was analyzed using Design Expert©, commercial software; see Table 10. The simulation was run for each test case. Care

must be taken when analyzing results when using response surface methodology with a deterministic computer simulation.

Table 10: 2^{5-1} nested face centered design test matrix (center run is shown as bold)

Run	Jeq	Beq	k	BL	IS	Run	Jeq	Beq	k	BL	IS
1	0.0006589	0	0.081	10	0.08727	30	0.0002944	0.006042	0.08575	4	0.0824925
2	0.0004159	0.004028	0.0905	6	0.084085	31	0.0005374	0.006042	0.08575	4	0.0856775
3	0.0004159	0.004028	0.0905	10	0.084085	32	0.0002944	0.002014	0.09525	4	0.0824925
4	0.0006589	0.008056	0.1	2	0.0809	33	0.0005374	0.002014	0.09525	4	0.0856775
5	0.0004159	0.004028	0.1	6	0.084085	34	0.0002944	0.006042	0.09525	4	0.0856775
6	0.0004159	0.004028	0.0905	2	0.084085	35	0.0005374	0.006042	0.09525	4	0.0824925
7	0.0006589	0.008056	0.081	10	0.0809	36	0.0002944	0.002014	0.08575	8	0.0824925
8	0.0001729	0	0.1	10	0.08727	37	0.0005374	0.002014	0.08575	8	0.0856775
9	0.0006589	0	0.081	2	0.0809	38	0.0002944	0.006042	0.08575	8	0.0856775
10	0.0006589	0.004028	0.0905	6	0.084085	39	0.0005374	0.006042	0.08575	8	0.0824925
11	0.0001729	0.008056	0.1	10	0.0809	40	0.0002944	0.002014	0.09525	8	0.0856775
12	0.0004159	0	0.0905	6	0.084085	41	0.0005374	0.002014	0.09525	8	0.0824925
13	0.0004159	0.004028	0.081	6	0.084085	42	0.0002944	0.006042	0.09525	8	0.0824925
14	0.0006589	0.008056	0.1	10	0.08727	43	0.0005374	0.006042	0.09525	8	0.0856775
15	0.0006589	0	0.1	10	0.0809	44	0.0002944	0.004028	0.0905	6	0.084085
16	0.0001729	0	0.081	2	0.08727	45	0.0005374	0.004028	0.0905	6	0.084085
17	0.0001729	0.008056	0.081	10	0.08727	46	0.0004159	0.002014	0.0905	6	0.084085
18	0.0001729	0.004028	0.0905	6	0.084085	47	0.0004159	0.006042	0.0905	6	0.084085
19	0.0001729	0	0.081	10	0.0809	48	0.0004159	0.004028	0.08575	6	0.084085
20	0.0001729	0	0.1	2	0.0809	49	0.0004159	0.004028	0.09525	6	0.084085
21	0.0004159	0.004028	0.0905	6	0.08727	50	0.0004159	0.004028	0.0905	4	0.084085
22	0.0006589	0	0.1	2	0.08727	51	0.0004159	0.004028	0.0905	8	0.084085
23	0.0001729	0.008056	0.081	2	0.0809	52	0.0004159	0.004028	0.0905	6	0.0824925
24	0.0004159	0.004028	0.0905	6	0.0809	**53**	**0.0004159**	**0.004028**	**0.0905**	**6**	**0.0856775**
25	0.0006589	0.008056	0.081	2	0.08727						
26	0.0001729	0.008056	0.1	2	0.08727						
27	0.0004159	0.008056	0.0905	6	0.084085						
28	0.0002944	0.002014	0.08575	4	0.0856775						
29	0.0005374	0.002014	0.08575	4	0.0824925						

4.4.7 Statistics and Deterministic Computer Models

RSM has been used successfully with computer simulation models of physical systems. A few examples are Barton (1992, 1994) [137, 138] and Simpson et al. (1997) [139]. The goal of RSM is to build a regression model of the system being modeled by the computer simulation – a regression metamodel. Although RSM is primarily intended for applications with random error, deterministic applications are appropriate and the

analysis is simplified. Care must be taken when using statistics to develop the regression metamodel.

The nature of the computer simulation is represented as an input-output relation,

$$y = f(x) \; . \tag{4.21}$$

Then a metamodel is represented as

$$\hat{y} = g(x) + \varepsilon_{bias} + \varepsilon_{random} \tag{4.23}$$

where g(x) is the metamodel, ε_{bias} is the error of approximation, and ε_{random} is the random error. However, for deterministic models, random error has zero mean and zero variance, so the fitting relationship is

$$\hat{y} = g(x) + \varepsilon_{bias} \; . \tag{4.24}$$

The relationship conflicts with methods of least squares regression [140]. Unless the error of approximation follows the assumptions of $NID(0, \sigma^2)$ then statistical inference from least squares regression are violated. Consequently, Sacks et al. (1989) and Kleijnen (1990) have pointed out that since deterministic computer simulations lack random error [141, 142]:

1. The response surface model adequacy is determined solely by systematic bias.
2. The usual measures of uncertainty derived from least squares residuals have no obvious statistical meaning; deterministic measures of uncertainty exist.
3. The notions of experimental blocking, replication, and randomization are irrelevant.

Several statistical measures such as pure error, F-statistics, and mean squared error for verification of model adequacy have no statistical meaning because they are all

based on random error. Care should be taken when using commercial software because manufacturers employ these types of statistical measures for developing a model. These measures have no statistical meaning since they assume that observations include an error term, which has a mean of zero and a non-zero standard deviation. The ANOVA tables for the responses are provided in Appendix E; although their results have no statistical meaning, the relative size of the coded model terms and sum of squares (SS) contributions may be compared.

4.4.8 Fitting and Validating of Regression Metamodel

For this study, terms in the model were added manually and removed while applied V&V techniques were used to validate the metamodel. The only true way to verify and validate the metamodels is by using coefficients of determination, cross-validation and point prediction methods [143, 140].

The classic coefficient of determination measure is

$$R^2 = \frac{SS_R}{SS_T} = 1 - \frac{SS_E}{SS_T} \tag{4.25}$$

where SS_R is the regression sum of squares, SS_T is the total sum of squares, and SS_E is the error sum of squares. It follows that $0 \le R^2 \le 1$. Values of R^2 that are close to 1 imply that the variability in the response is explained by the regression model [143]. However, caution should be exercised when using R^2. Increasing the number of regression variables always increases R^2 regardless of the value of the contribution of the variable. This does not necessarily mean that the model is an accurate predictor and the model becomes over-fitted. There are several other misconceptions about R^2. The coefficient of determination does not measure the magnitude of the slope of the

regression line. R^2 does not measure the appropriateness of the linear model. For example, R^2 will often be large even though the system is nonlinear.

Consequently, R^2_{adj} is used as an indicator of model adequacy; see Equation 4.6.

$$R^2_{adj} = 1 - \frac{SS_E/(n-p)}{SS_T/(n-1)} \tag{4.26}$$

The adjusted R^2 penalizes the model for adding terms that are not helpful, so it is most useful in evaluating and comparing candidate regression models, particularly when working with deterministic simulations.

Cross validation is useful when collecting new data for validation purposes, but it is not possible. A reasonable procedure is to split the available data into two parts called the estimation data and the prediction data [144]. The estimation data are used to build the regression model, and the prediction data are then used to study the predictive ability of the model [140]. The technique of data splitting is called *cross validation*. One useful statistic that performs cross validation is the prediction error sum of squares (PRESS). The PRESS residuals are defined as $e_{(i)} = y_i - \hat{y}_{(i)}$ where $\hat{y}_{(i)}$ is the predicted value of the i^{th} observed response based on a model fit to the remaining n-1 sample points [140]. Thus, the PRESS statistic is defined as a measure of model quality; see Equation 4.7.

$$\begin{aligned} PRESS &= \sum_{i=1}^{n} \left[y_i - \hat{y}_{(u)} \right]^2 \\ &= \sum_{i=1}^{n} \left(\frac{e_i}{1-h_{ii}} \right)^2 \end{aligned} \tag{4.27}$$

Generally, when using the PRESS statistic, small values of PRESS are desired. Using the PRESS statistic, the predicted R^2 is described as

$$R^2_{pred} = 1 - \frac{PRESS}{SS_T} \quad . \tag{4.28}$$

This statistic gives an indication of the predictive capability of the regression model and a sense of how much variability in new observations the model might be expected to explain [140].

Using the statistics of this section, the regression metamodels, developed from the commercial software package Design Expert, were validated. Results are shown in Table 11 along with the model fit summary statistics in Table 12. It should be noted that the standard deviations and means listed in Table 12 are computed based on the factor limits and not due to variability.

Table 11: Regression Metamodels

In-phase lift coefficient		Out-of-phase lift coefficient		In-phase pitching moment coefficient		Out-of-phase pitching moment coefficient	
$\overline{C}_{L_\alpha}$	=	$\overline{C}_{L_q}$	=	$\overline{C}_{m_\alpha}$	=	$\overline{C}_{m_q}$	=
1.524E+01		-2.006E+02		1.827E+00		-3.473E+01	
-1.815E+02	* Jeq	5.947E+03	* Jeq	-5.969E+01	* Jeq	6.942E+02	* Jeq
-4.905E+01	* Beq	4.812E+02	* Beq	-5.504E+00	* Beq	9.434E+01	* Beq
-1.645E+03	* k	1.630E+04	* k	-1.900E+02	* k	3.112E+03	* k
-1.445E-02	* BL	6.625E-02	* BL	-1.083E-03	* BL	1.696E-02	* BL
8.496E+02	* IS	-6.697E+03	* IS	9.779E+01	* IS	-1.376E+03	* IS
5.978E+03	* Jeq * Beq	-7.649E+04	* Jeq * Beq	8.131E+02	* Jeq * Beq	-1.338E+04	* Jeq * Beq
-1.509E+04	* Jeq * IS	1.283E+05	* Jeq * IS	-1.564E+03	* Jeq * IS	2.614E+04	* Jeq * IS
3.621E+02	* Beq * k	-3.589E+03	* Beq * k	4.071E+01	* Beq * k	-6.955E+02	* Beq * k
-5.075E-01	* Beq * BL	4.999E+00	* Beq * BL	-5.719E-02	* Beq * BL	9.160E-01	* Beq * BL
2.204E-01	* k * BL	-2.052E+00	* k * BL	2.355E-02	* k * BL	-3.993E-01	* k * BL
-6.385E-01	* BL * IS	7.299E+00	* BL * IS	-8.078E-02	* BL * IS	1.327E+00	* BL * IS
3.472E+06	* Jeq^2	-4.065E+07	* Jeq^2	4.605E+05	* Jeq^2	-6.976E+06	* Jeq^2
5.191E+03	* Beq^2	-5.067E+04	* Beq^2	5.637E+02	* Beq^2	-1.002E+04	* Beq^2
1.781E+04	* k^2	-1.766E+05	* k^2	2.057E+03	* k^2	-3.379E+04	* k^2
1.172E-02	* BL^2	-1.235E-01	* BL^2	1.396E-03	* BL^2	-2.284E-02	* BL^2
-4.951E+03	* IS^2	3.922E+04	* IS^2	-5.688E+02	* IS^2	8.053E+03	* IS^2
-2.618E+09	* Jeq^3	3.107E+10	* Jeq^3	-3.481E+08	* Jeq^3	5.310E+09	* Jeq^3
-3.886E+05	* Beq^3	4.003E+06	* Beq^3	-4.263E+04	* Beq^3	7.766E+05	* Beq^3
-6.387E+04	* k^3	6.315E+05	* k^3	-7.360E+03	* k^3	1.211E+05	* k^3
-7.236E-04	* BL^3	7.763E-03	* BL^3	-8.639E-05	* BL^3	1.427E-03	* BL^3

Table 12: Regression metamodel fit summary statistics

In-Phase Lift Coefficient			
Std. Dev.	0.0235	R-Squared	0.8957
Mean	1.1047	Adj R-Squared	0.8305
C.V. %	2.1261	Pred R-Squared	0.7670
PRESS	0.0394	Adeq Precision	14.4567
Out-of-phase Lift Coefficient			
Std. Dev.	0.2294	R-Squared	0.9574
Mean	12.6622	Adj R-Squared	0.9307
C.V. %	1.8119	Pred R-Squared	0.9110
PRESS	3.5140	Adeq Precision	20.9072
In-phase Pitching Moment Coefficient			
Std. Dev.	0.00273	R-Squared	0.9452
Mean	0.20025	Adj R-Squared	0.9109
C.V. %	1.36576	Pred R-Squared	0.8762
PRESS	0.0005407	Adeq Precision	20.2269
Out-of-phase Pitching Moment Coefficient			
Std. Dev.	0.0436	R-Squared	0.9575
Mean	1.5613	Adj R-Squared	0.9310
C.V. %	2.7944	Pred R-Squared	0.9089
PRESS	0.1307	Adeq Precision	20.9245

The final validation procedure is to apply a few confirmation runs using point prediction to test the regression metamodels [140]. A few points within the design space were selected that were not used to build the regression model. The results of the regression metamodel were compared with the simulation results. The percent difference was calculated to provide a measure of prediction for the regression metamodel, compared to the simulation.

The percent difference between the metamodel and simulation ranged from 0.1% to 7%. The difference is due to the system being highly nonlinear. Also, a test case has a factor that is near the edge of the design space; see test case 1 of Table 13.

Table 13: Point prediction results

Test Case # 1				
Factor	**Name**	**Level**	**Low Level**	**High Level**
A	Jeq	0.0005	0.0001729	0.0006589
B	Beq	0.006	0	0.008056
C	k	0.09	0.081	0.1
D	BL	3	2	10
E	IS	0.085	0.0809	0.08727
Response	**Prediction**	**Simulation Result**	**% difference**	
$\overline{C}_{L_\alpha}$	1.0998	1.1498	4.35	
$\overline{C}_{L_q}$	12.8375	12.2544	4.76	
$\overline{C}_{m_\alpha}$	0.2000	0.2059	2.88	
$\overline{C}_{m_q}$	1.6043	1.4874	7.86	
Test Case # 2				
Factor	**Name**	**Level**	**Low Level**	**High Level**
A	Jeq	0.0002	0.0001729	0.0006589
B	Beq	0.003	0	0.008056
C	k	0.09	0.081	0.1
D	BL	9.5	2	10
E	IS	0.081	0.0809	0.08727
Response	**Prediction**	**Simulation Result**	**% difference**	
$\overline{C}_{L_\alpha}$	1.0382	1.0852	4.34	
$\overline{C}_{L_q}$	13.0937	12.5065	4.70	
$\overline{C}_{m_\alpha}$	0.1919	0.1968	2.50	
$\overline{C}_{m_q}$	1.6067	1.5461	3.92	
Test Case # 3				
Factor	**Name**	**Level**	**Low Level**	**High Level**
A	Jeq	0.00055	0.0001729	0.0006589
B	Beq	0.007	0	0.008056
C	k	0.084	0.081	0.1
D	BL	4	2	10
E	IS	0.085	0.0809	0.08727
Response	**Prediction**	**Simulation Result**	**% difference**	
$\overline{C}_{L_\alpha}$	1.0700	0.9977	7.25	
$\overline{C}_{L_q}$	13.4651	14.1205	4.64	
$\overline{C}_{m_\alpha}$	0.1940	0.1850	4.86	
$\overline{C}_{m_q}$	1.7378	1.8441	5.76	

Test Case # 4				
Factor	**Name**	**Level**	**Low Level**	**High Level**
A	Jeq	0.000251711	0.0001729	0.0006589
B	Beq	0.000326595	0	0.008056
C	k	0.086648649	0.081	0.1
D	BL	8.486486486	2	10
E	IS	0.08649527	0.0809	0.08727
Response	**Prediction**	**Simulation Result**	**% difference**	
$\overline{C}_{L_\alpha}$	1.0893	1.0775	1.09	
$\overline{C}_{L_q}$	13.2030	13.3731	1.27	
$\overline{C}_{m_\alpha}$	0.1974	0.1954	0.98	
$\overline{C}_{m_q}$	1.6498	1.6856	2.12	
Test Case # 5				
Factor	**Name**	**Level**	**Low Level**	**High Level**
A	Jeq	0.0002517	0.0001729	0.0006589
B	Beq	0.0003266	0	0.008056
C	k	0.0982	0.081	0.1
D	backlash	6.757	2	10
E	input sat.	0.08348	0.0809	0.08727
Response	**Prediction**	**Simulation Result**	**% difference**	
$\overline{C}_{L_\alpha}$	1.2006	1.1998	0.06	
$\overline{C}_{L_q}$	11.2306	11.2094	0.19	
$\overline{C}_{m_\alpha}$	0.2146	0.2141	0.23	
$\overline{C}_{m_q}$	1.3245	1.2850	3.07	

4.5 Monte Carlo Simulation

One use for Monte Carlo simulation is studying the propagation of uncertainty in a system. The basic procedure is outlined as follows [145]:

1. Determine the pseudo-population or model that represents the true population of interest.
2. Use a sampling procedure to sample from the pseudo-population or distribution.
3. Calculate a value for the statistic of interest and store it.

4. Repeat steps 2 and 3 for M trials, where M is large
5. Use the M values found in step 4 to study the distribution of the statistic.

Two methods were used for the uncertainty analysis – 'indirect' and 'direct' Monte Carlo; see Appendix F. The 'indirect' Monte Carlo simulation procedure is detailed on the flowchart of Figure 69. This method uses Taylor series based sensitivity analysis in conjunction with a Monte Carlo simulation to determine the uncertainty. The sensitivities are computed at a given nominal setting of the factors. The sensitivity matrix is determined analytically using the MATLAB symbolic solver.

$$\left[\begin{array}{cccc} \frac{\partial \overline{C}_{L_\alpha}}{\partial J_{EQ}} & \frac{\partial \overline{C}_{L_\alpha}}{\partial B_{EQ}} & \cdots & \frac{\partial \overline{C}_{L_\alpha}}{\partial IS} \\ \frac{\partial \overline{C}_{L_q}}{\partial J_{EQ}} & \ddots & & \vdots \\ \vdots & & \ddots & \vdots \\ \frac{\partial \overline{C}_{m_q}}{\partial J_{EQ}} & \cdots & \cdots & \frac{\partial \overline{C}_{m_q}}{\partial IS} \end{array}\right]_{J_{EQ_0}, B_{EQ_0} k_0, BL_0, IS_0} \tag{4.29}$$

The procedure then follows by sampling from a pseudo-population with M = 100,000 trials. Uniform distributions were used for δJ_{EQ} and δB_{EQ}, as shown in Figures 70 and 71 respectively. Normal distributions were used for δBL and δIS, as shown in Figures 72 and 73. The distributions have a standard deviation of σ. The standard deviation was computed using the factor limits from Design Expert. No distribution was used for δk since the study assumed it does not have any distribution. Finally, the procedure computes the in-phase and out-of-phase lift and pitching moment coefficients (see Equations 4.10 and 4.11) and concludes with summary statistics, confidence intervals, and histograms as the results. The results are presented in Chapter 5.

$$\delta\overline{C}_{L_\alpha} = \left[\left(\frac{\partial \overline{C}_{L_\alpha}}{\partial J_{EQ}}\delta J_{EQ}\right)^2 + \left(\frac{\partial \overline{C}_{L_\alpha}}{\partial B_{EQ}}\delta B_{EQ}\right)^2 + \cdots + \left(\frac{\partial \overline{C}_{L_\alpha}}{\partial IS}\delta IS\right)^2\right]^{1/2}$$
$$\delta\overline{C}_{L_q} = \cdots \tag{4.30}$$
$$\delta\overline{C}_{m_\alpha} = \cdots$$
$$\delta\overline{C}_{m_q} = \cdots$$

$$\overline{C}_{L_\alpha} = \overline{C}_{L_\alpha}\Big|_0 + \delta\overline{C}_{L_\alpha}$$
$$\overline{C}_{L_q} = \cdots \tag{4.31}$$
$$\overline{C}_{m_\alpha} = \cdots$$
$$\overline{C}_{m_q} = \cdots$$

The 'direct' Monte Carlo method is similar in procedure to the 'indirect' Monte Carlo method. Figure 74 provides a flowchart of the procedure. The 'direct' Monte Carlo method applies a pseudo-population of the factors (Jeq, Beq, BL, and IS). The populations are sampled, and the result is applied to the metamodel regression models. The pseudo-population is provided in Figures 75-78. Again, the distributions have a standard deviation of σ. Also, no distribution was used for the reduced frequency factor. Similarly, the uncertainty analysis concludes with summary statistics, confidence intervals, and histograms as the results. The results are presented in Chapter 5.

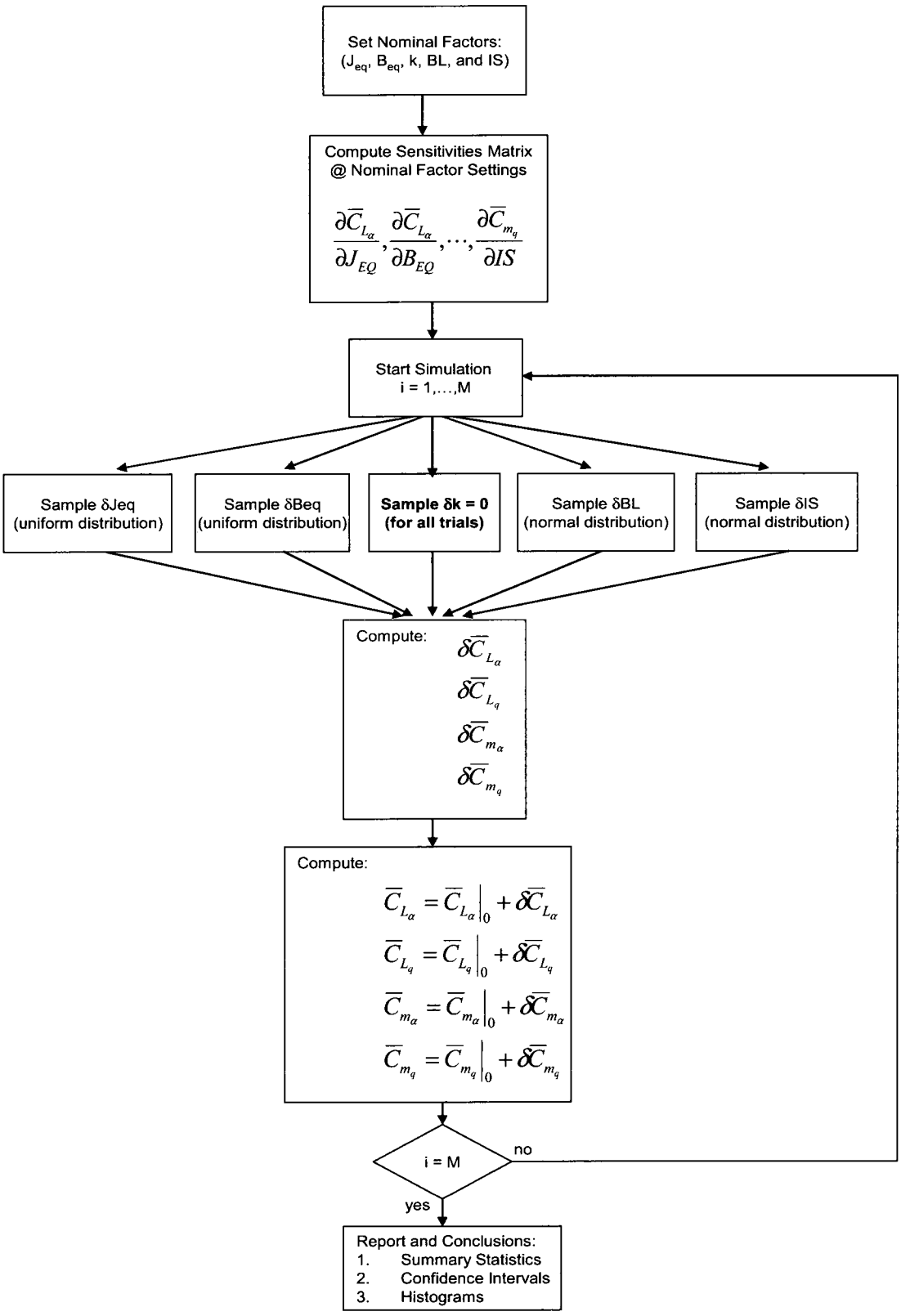

Figure 69: 'Indirect' Monte Carlo Simulation Procedure

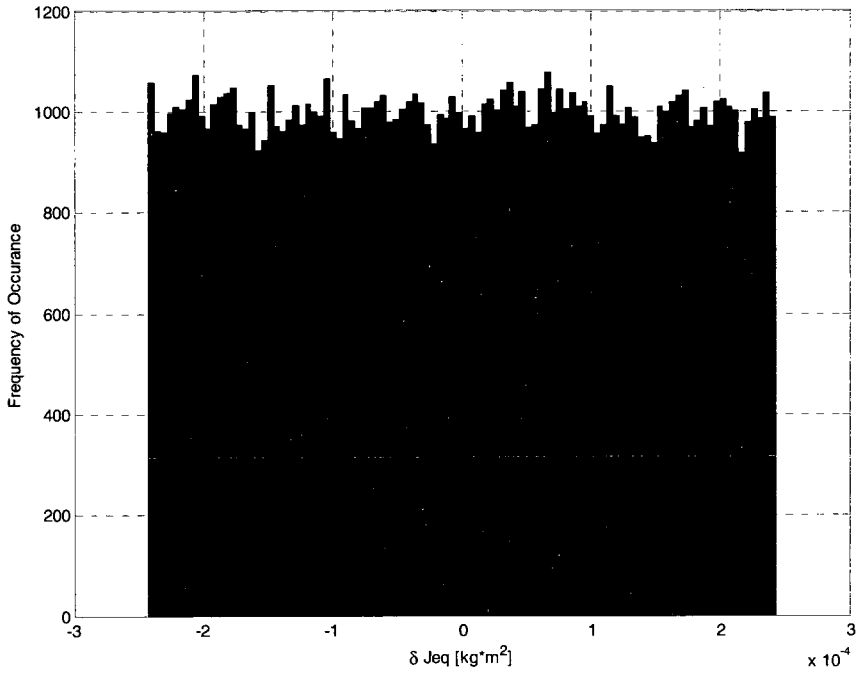

Figure 70: Uniform distribution for incremental equivalent inertia

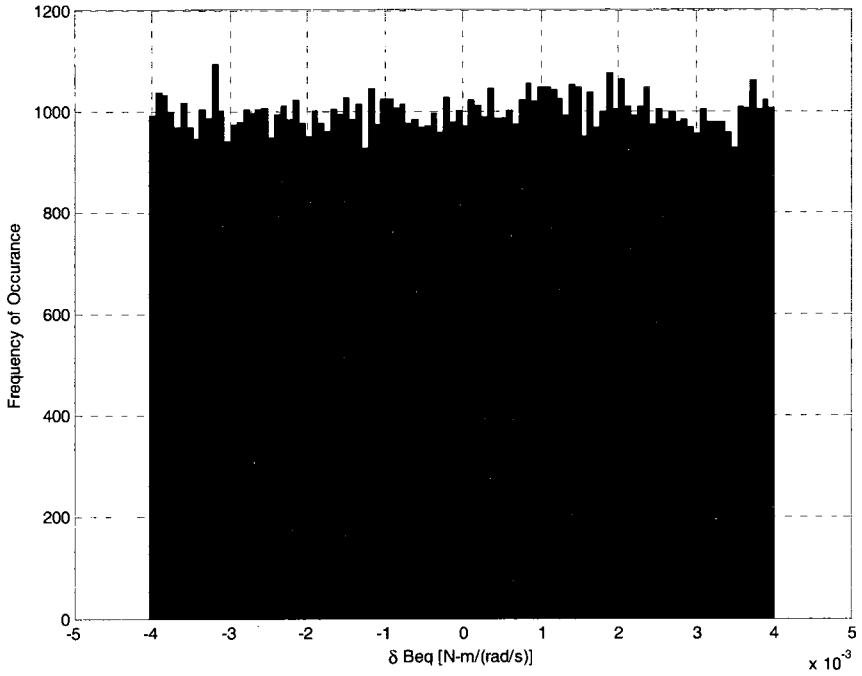

Figure 71: Uniform distribution for incremental equivalent damping

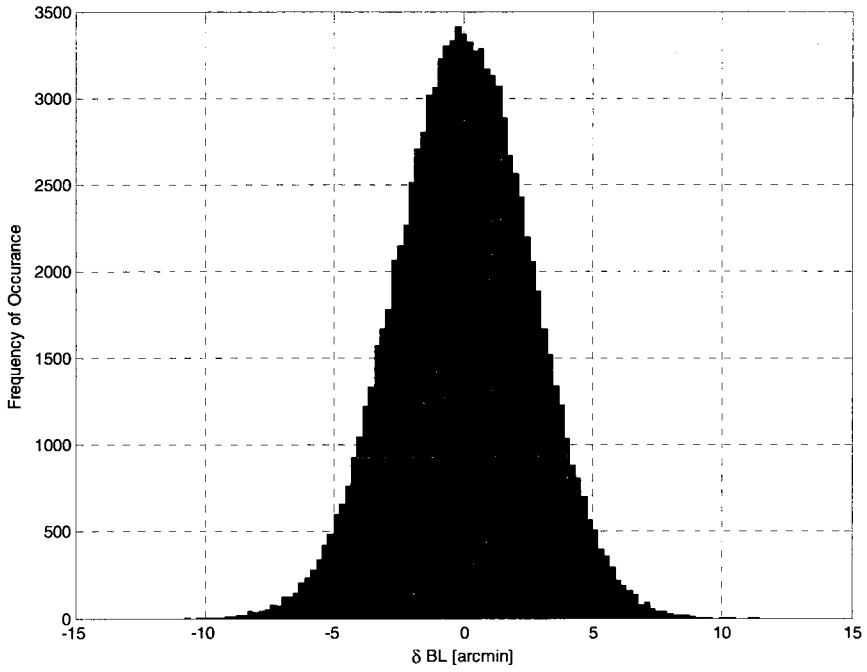

Figure 72: Normal distribution for incremental backlash

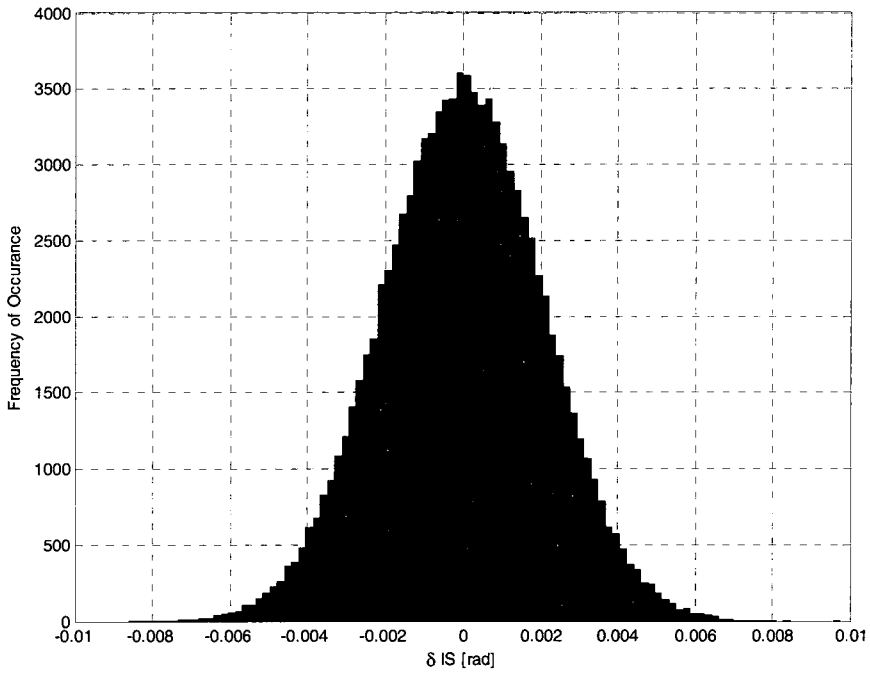

Figure 73: Normal distribution for incremental input saturation

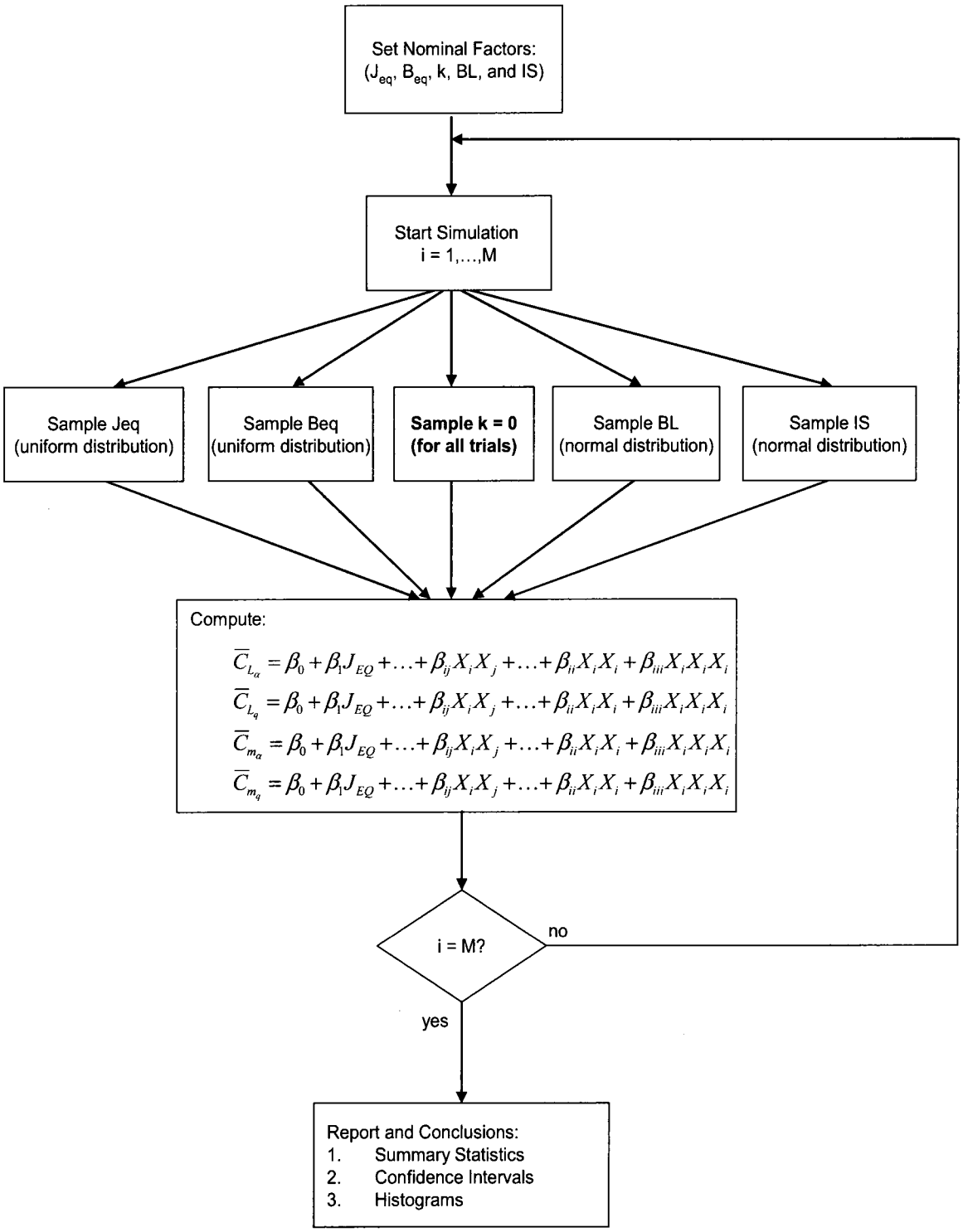

Figure 74: 'Direct' Monte Carlo Simulation Procedure

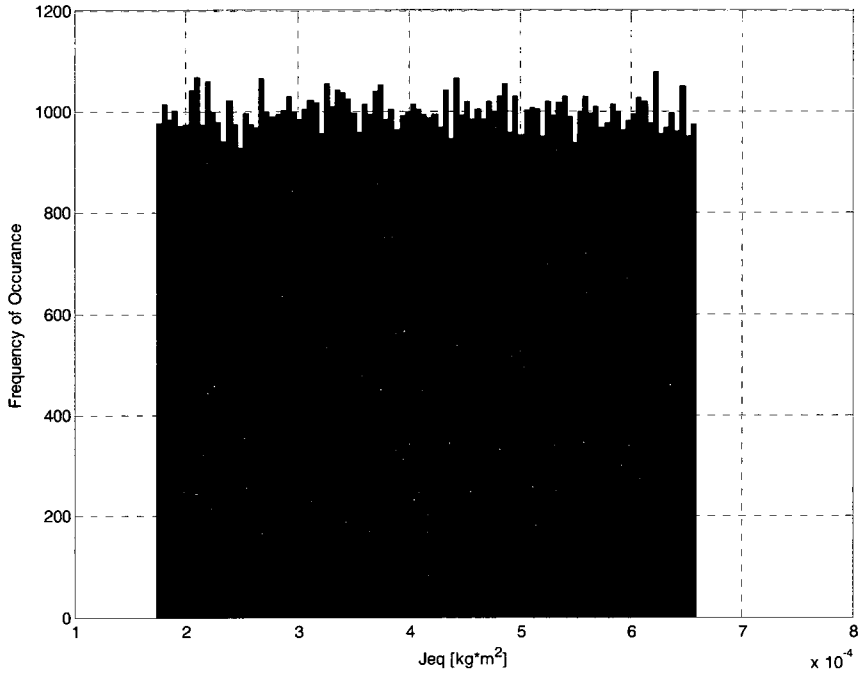

Figure 75: Uniform distribution for equivalent inertia

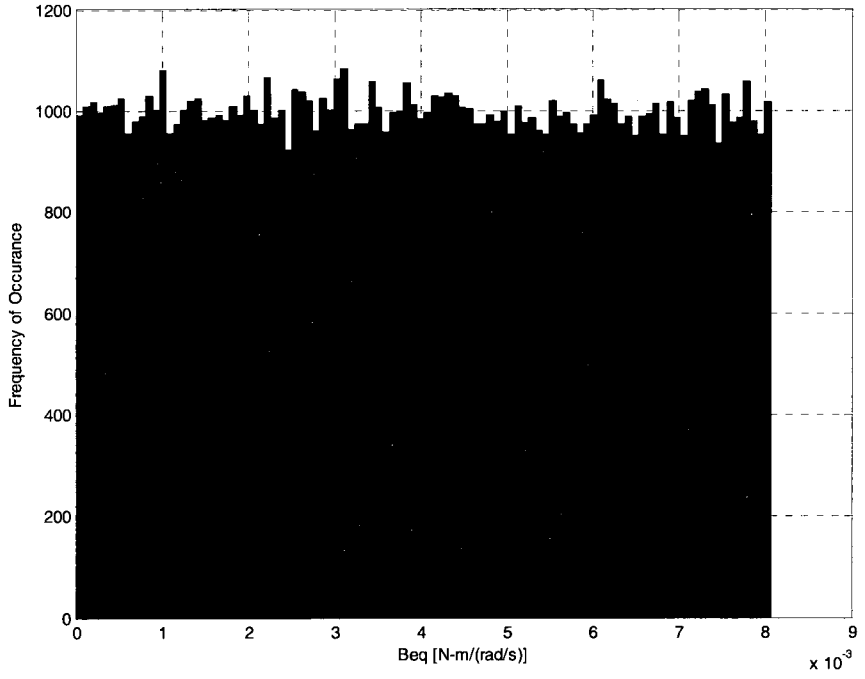

Figure 76: Uniform distribution for equivalent damping

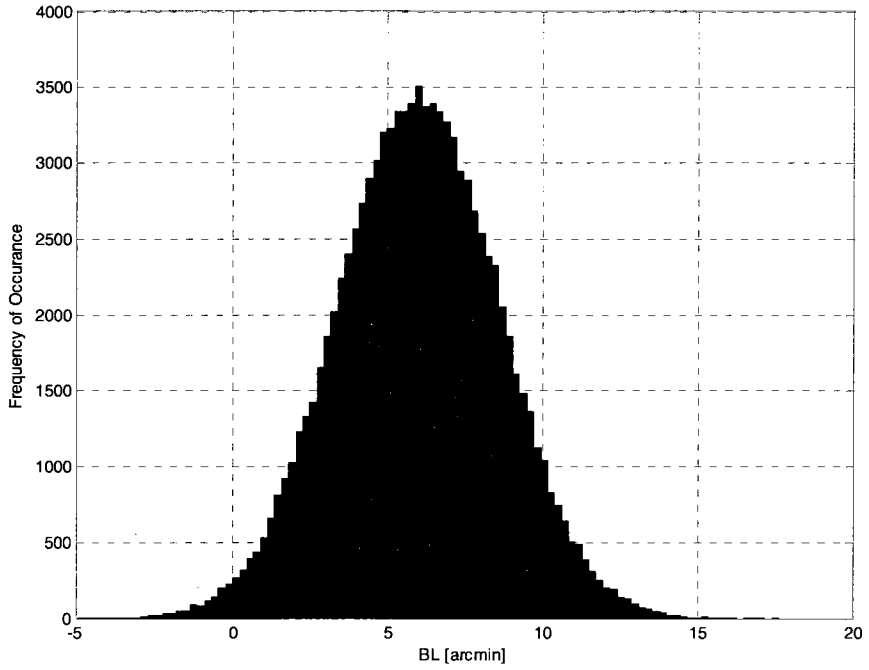

Figure 77: Normal distribution for backlash

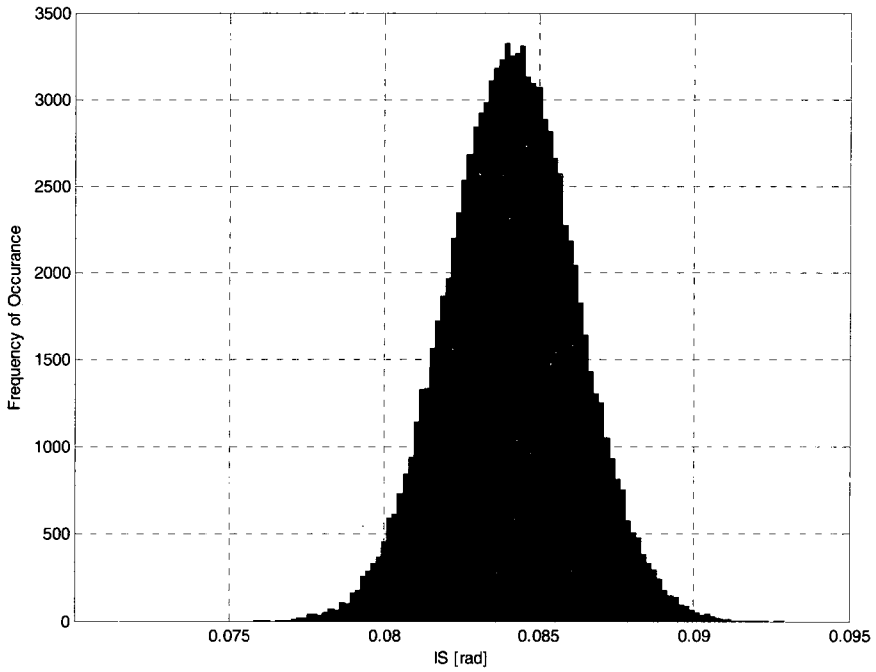

Figure 78: Normal distribution for input saturation

4.6 Summary

This chapter has detailed a modular approach to building a pitch oscillation simulation. Specific details were given about the experimental aerodynamic model used for the simulation. The control system for the three-phase AC motor was developed. The Simulink implementation of the AC motor and drivetrain were described. Various sources of instability prevented the simulation from running properly. The sources and solutions were discussed. The chapter also outlined the procedure used for verifying and validating the Simulink model. Finally, the design of experiments approach used for experimental design and the Monte Carlo methods used for uncertainty analysis were discussed.

CHAPTER 5

RESULTS

5.1 Results

This chapter presents the uncertainty analysis results. Two uncertainty methods were used: (1) indirect (i.e. usage of sensitivities) Monte Carlo method and (2) direct (i.e. use of regression metamodels) Monte Carlo method. Standard summary statistics such as sample mean, sample standard deviation, maximum, minimum, skewness, and coverage intervals are provided. Histograms of the responses are also provided.

Since the distribution of the Monte Carlo results are asymmetric, due to high nonlinearity in the system, calculating the standard deviation and assuming that the central limit theorem applies to obtain the uncertainty will not be appropriate. The coverage interval that provides a 95% level of confidence is shown in Figure 79.

The procedure used is given by [146]:

1. Sort the M Monte Carlo simulation results from lowest value to the highest value.
2. For a 95% coverage interval:

$$r_{low} = result\ number(0.025M) \tag{5.1}$$

$$r_{high} = result\ number(0.975M)\ . \tag{5.2}$$

   If the numbers $0.025M$ and 0.975M are not integers, then add ½ and take the integer part as the result number. The lower limit of the coverage interval is r_{low}, and the higher limit of the coverage interval is r_{high}.

3. For 95% expanded uncertainty limits:

$$U_r^- = r(X_1, X_2, \ldots, X_J) - r_{low} \tag{5.3}$$

$$U_r^+ = r_{high} - r(X_1, X_2, \ldots, X_J) \; . \tag{5.4}$$

4. The interval that contains r_{true} at a 95% level of confidence is then:

$$r - U_r^- \leq r_{true} \leq r + U_r^+ \; . \tag{5.5}$$

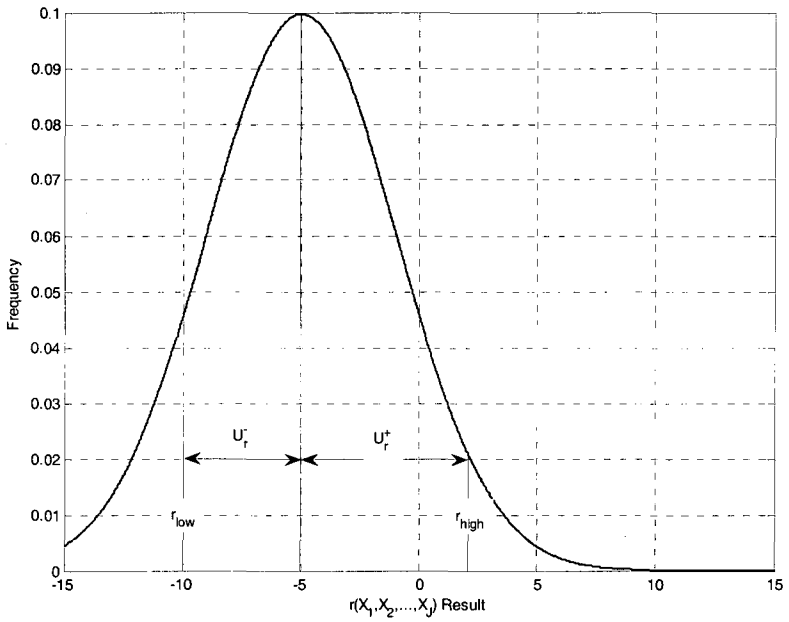

Figure 79: Example probabilistically symmetric coverage interval for 95% level of confidence [146]

Skewness present in a probability distribution results from a nonlinear system. In statistics, skewness is a measure of the asymmetry in a probability distribution; it is also called the third central moment [145]. If a distribution is highly normal, then skewness is zero; see Figure 80 for example. When the extreme values are elongated on the positive side the distribution is said to be positively skewed. On the other hand, if the extreme values are elongated on the negative side the distribution is said to be negatively

skewed. Examples of positively and negatively skewed distributions are shown in Figures 81 and 82, respectively.

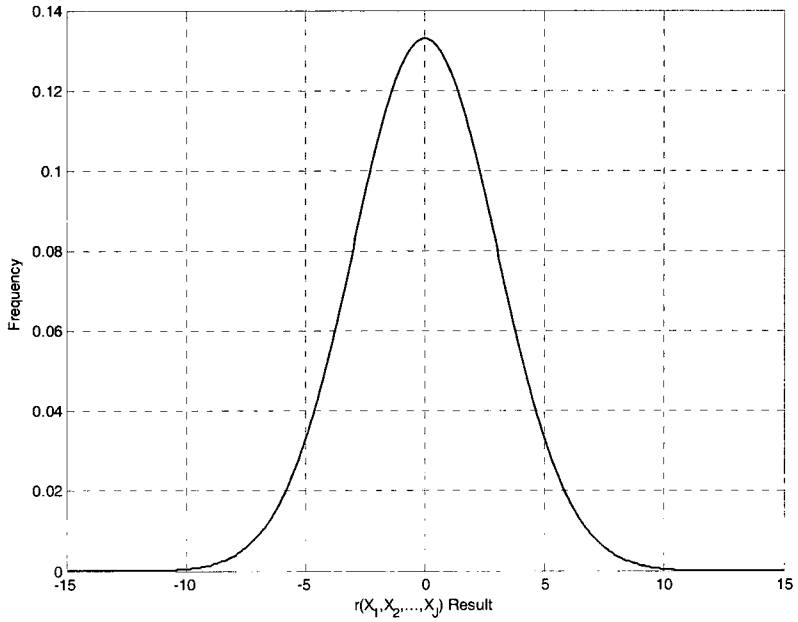

Figure 80: Example of normal distribution

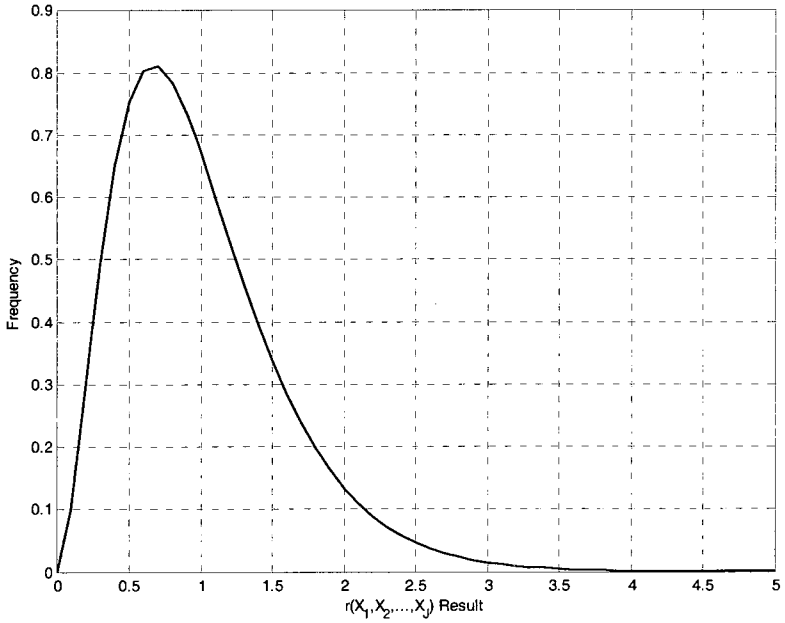

Figure 81: Example of positive skewed distribution

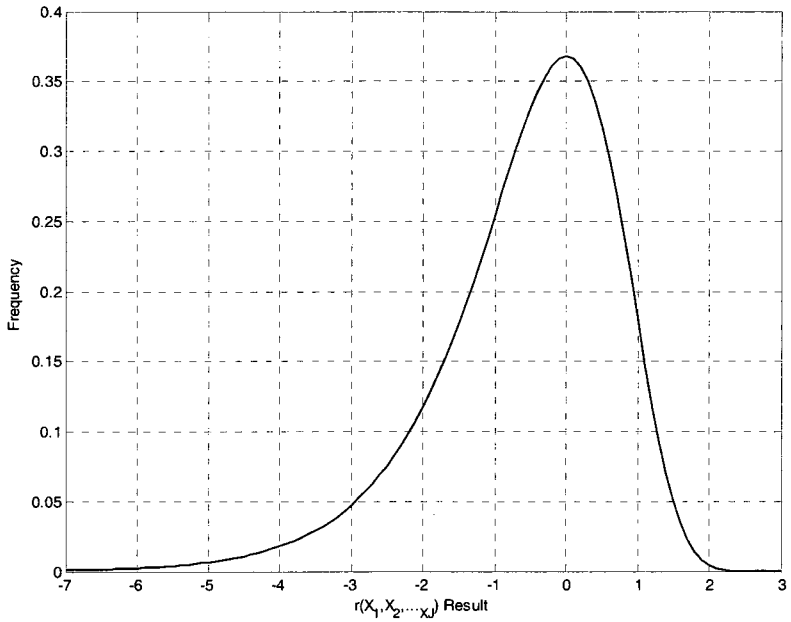

Figure 82: Example of negatively skewed distribution

5.1.1 Indirect Monte Carlo Simulation Results

Five test cases were run using the indirect Monte Carlo method developed in Chapter 4. The first test case represents the ideal factor settings for a test rig operating at a low reduced frequency, summarized in Table 14. The ideal settings were based on reported information from NASA Langley. The equivalent inertia and damping are set at their maximum limit. Backlash is set at its minimum, and input saturation is not present. This test case has factors near the limits of the factor ranges. The summary statistics are provided in Table 15. Figures 83-86 show the histogram of the responses.

Table 14: Factor settings test case #1

Test Case #1		
Factor	Setting	Name
Jeq	0.0006589	Equivalent inertia [kg*m^2]
Beq	0.008056	Equivalent damping [N-m-s/rad]
k	0.081	Reduced frequency [--]
BL	2	Backlash [arcmin]
IS	0.08727	Input saturation [rad]

Table 15: Summary statistics for test case #1

Response	**Mean**	Standard Deviation	Variance	Min	Max	Skewness	$\mathbf{r_{low}}$	$\mathbf{r_{high}}$
$\overline{C}_{L_\alpha}$	**1.1303**	0.0293	0.0009	1.0555	1.31	0.6324	**1.0816**	**1.1967**
$\overline{C}_{L_q}$	**14.7505**	0.2836	0.0805	13.9672	16.4241	0.4476	**14.2512**	**15.3687**
$\overline{C}_{m_\alpha}$	**0.1998**	0.0032	0	0.1912	0.2178	0.5061	**0.1942**	**0.207**
$\overline{C}_{m_q}$	**1.9552**	0.0549	0.003	1.8084	2.2962	0.5702	**1.8614**	**2.0782**

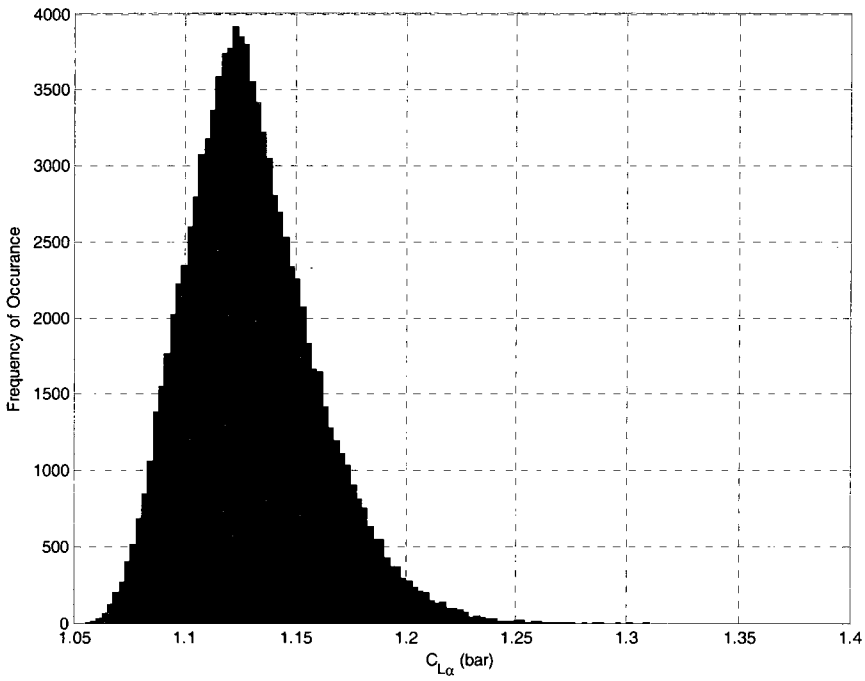

Figure 83: Histogram for in-phase lift coefficient (test case #1)

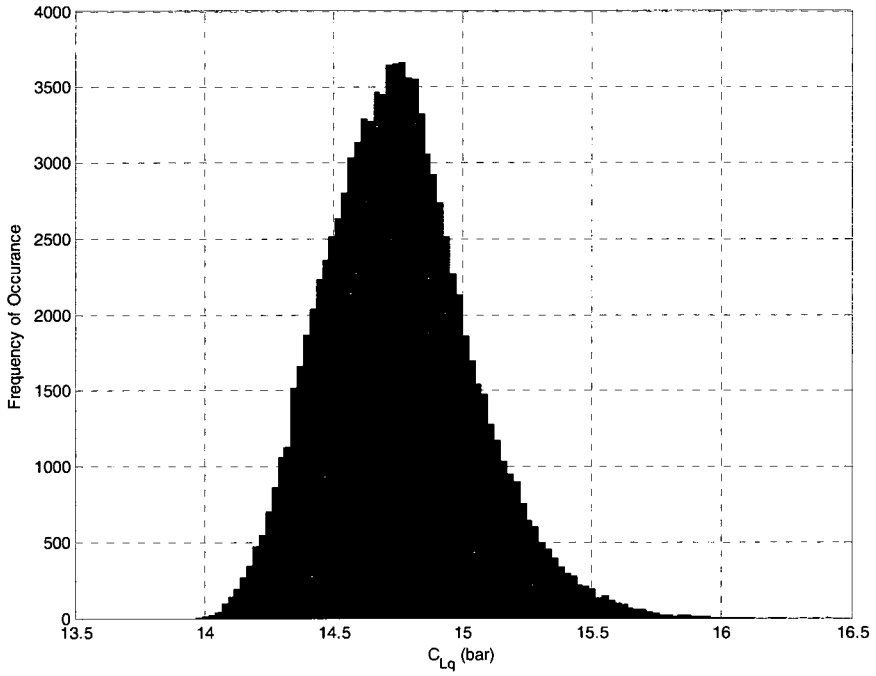

Figure 84: Histogram for out-of-phase lift coefficient (test case #1)

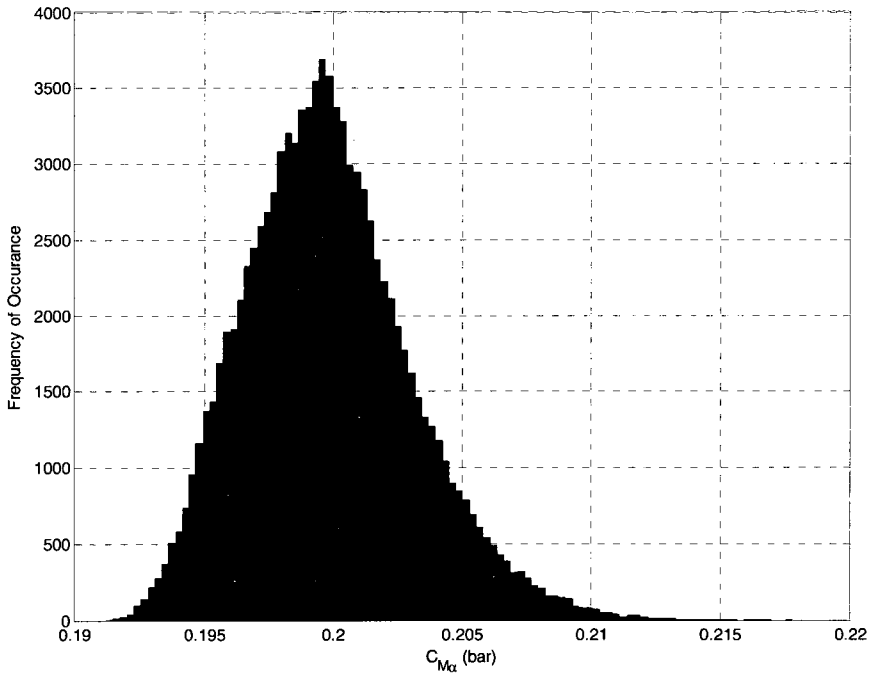

Figure 85: Histogram for in-phase pitching moment coefficient (test case #1)

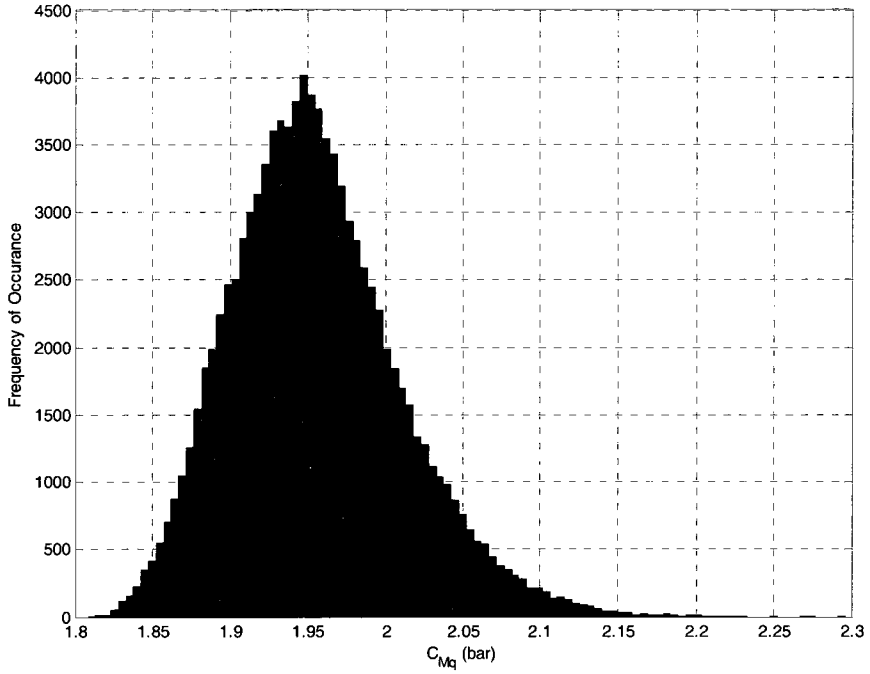

Figure 86: Histogram for out-of-phase pitching moment coefficient (test case #1)

The next test case uses the factors set at the center of the design space; see Table 16. Histograms for test case 2 are shown in Figures 87-90. The summary statistics are provided in Table 17.

Table 16: Factor settings (test case #2)

Test Case #2		
Factor	Setting	Name
Jeq	0.0004159	Equivalent inertia [kg*m^2]
Beq	0.004028	Equivalent damping [N-m-s/rad]
k	0.0905	Reduced frequency [--]
BL	6	Backlash [arcmin]
IS	0.08409	Input saturation [rad]

Table 17: Summary statistics for test case #2

Response	**Mean**	Standard Deviation	Variance	Min	Max	Skewness	$\mathbf{r_{low}}$	$\mathbf{r_{high}}$
$\overline{C}_{L_\alpha}$	**1.1455**	0.0156	0.0002	1.1105	1.253	1.0978	**1.1225**	**1.1842**
$\overline{C}_{L_q}$	**13.0091**	0.1697	0.0288	12.6561	14.1552	1.0998	**12.7585**	**13.4310**
$\overline{C}_{m_\alpha}$	**0.2051**	0.0019	0	0.2008	0.2177	0.9755	**0.2023**	**0.2096**
$\overline{C}_{m_q}$	**1.6223**	0.0312	0.001	1.5583	1.8347	1.1429	**1.5772**	**1.7004**

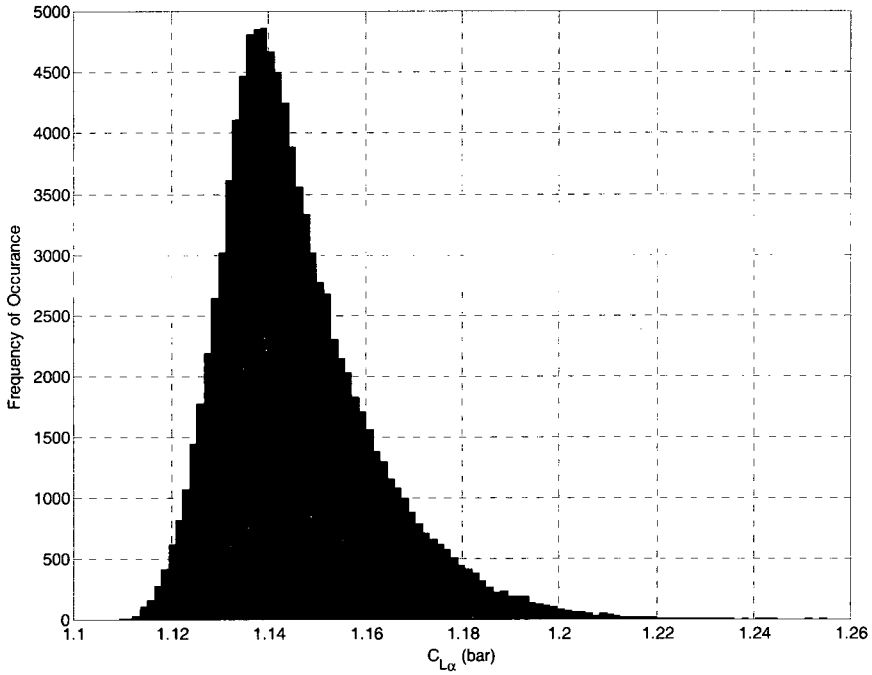

Figure 87: Histogram for in-phase lift coefficient (test case #2)

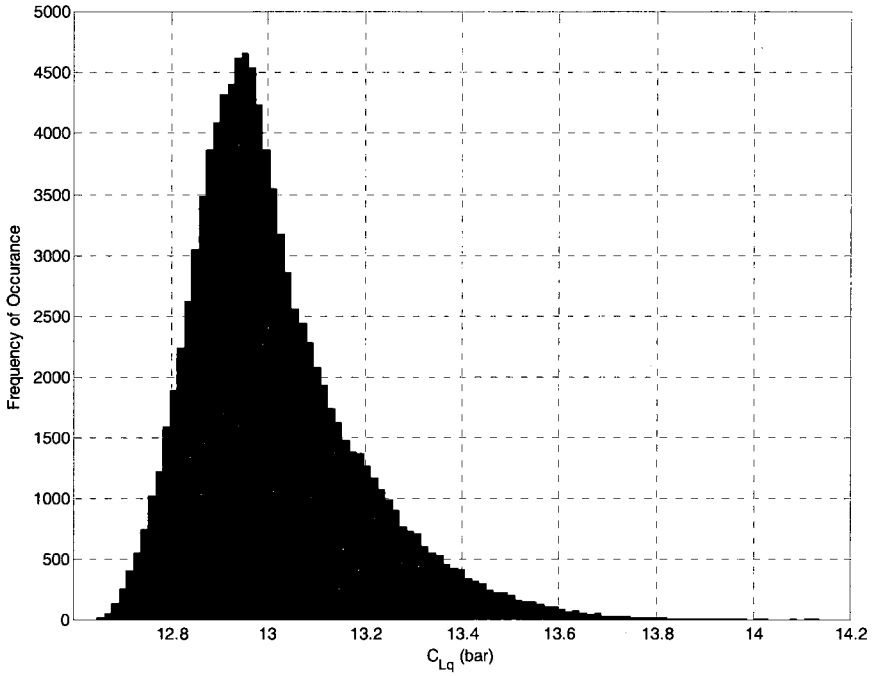

Figure 88: Histogram for out-of-phase lift coefficient (test case #2)

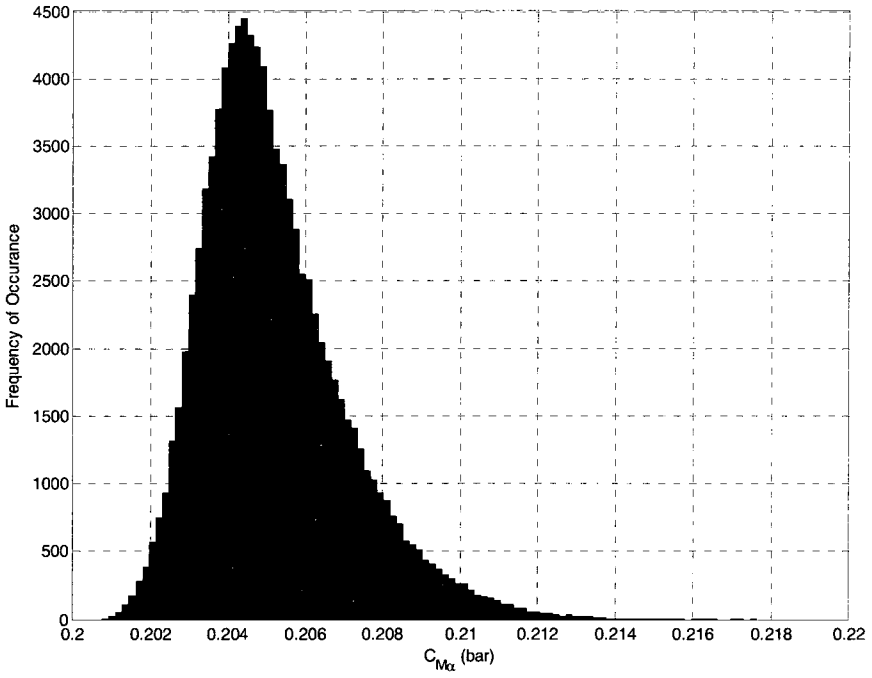

Figure 89: Histogram for in-phase pitching moment coefficient (test case #2)

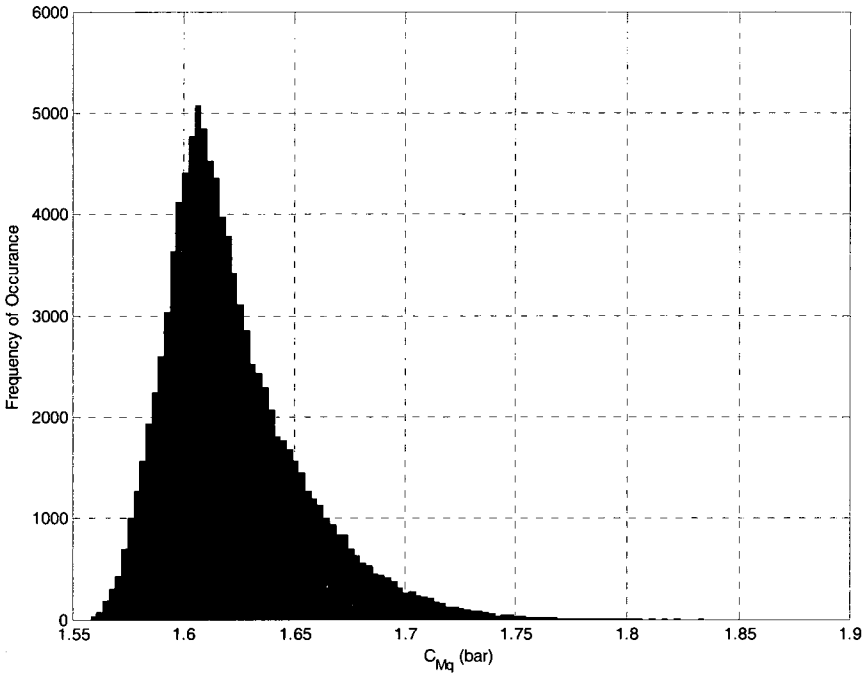

Figure 90: Histogram for out-of-phase pitching moment coefficient (test case #2)

The third test case had factor settings at low levels within the design space; see Table 18. The histogram results of the responses are shown in Figures 91-94. Again, the histogram results are highly skewed due to the nonlinearity of the system. Unlike test case #1, test case #3 assumes that input saturation is significant. Backlash is at a minimum. The equivalent inertia is at the low level of the design space, and the equivalent damping is not present. Also, reduced frequency is at its minimum as well.

Table 18: Factor settings (test case #3)

Test Case #3		
Factor	Setting	Name
Jeq	0.0001729	Equivalent inertia [kg*m^2]
Beq	0	Equivalent damping [N-m-s/rad]
k	0.081	Reduced frequency [--]
BL	2	Backlash [arcmin]
IS	0.0809	Input saturation [rad]

Table 19: Summary statistics for test case #3

Response	**Mean**	Standard Deviation	Variance	Min	Max	Skewness	$\mathbf{r_{low}}$	$\mathbf{r_{high}}$
$\overline{C}_{L_\alpha}$	**1.1434**	0.0451	0.002	1.0361	1.4654	0.9452	**1.0714**	**1.2528**
$\overline{C}_{L_q}$	**14.7088**	0.3482	0.1212	13.734	16.8006	0.3025	**14.0692**	**15.4326**
$\overline{C}_{m_\alpha}$	**0.2008**	0.0055	0	0.1877	0.2389	0.8515	**0.1919**	**0.2138**
$\overline{C}_{m_q}$	**1.9654**	0.0685	0.0047	1.7789	2.4205	0.5433	**1.8436**	**2.1181**

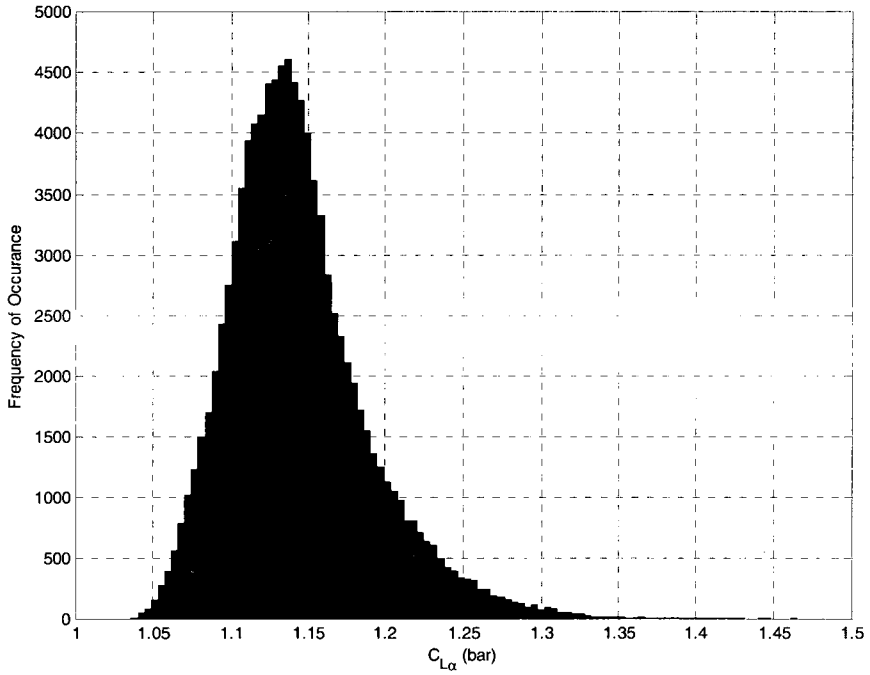

Figure 91: Histogram for in-phase lift coefficient (test case #3)

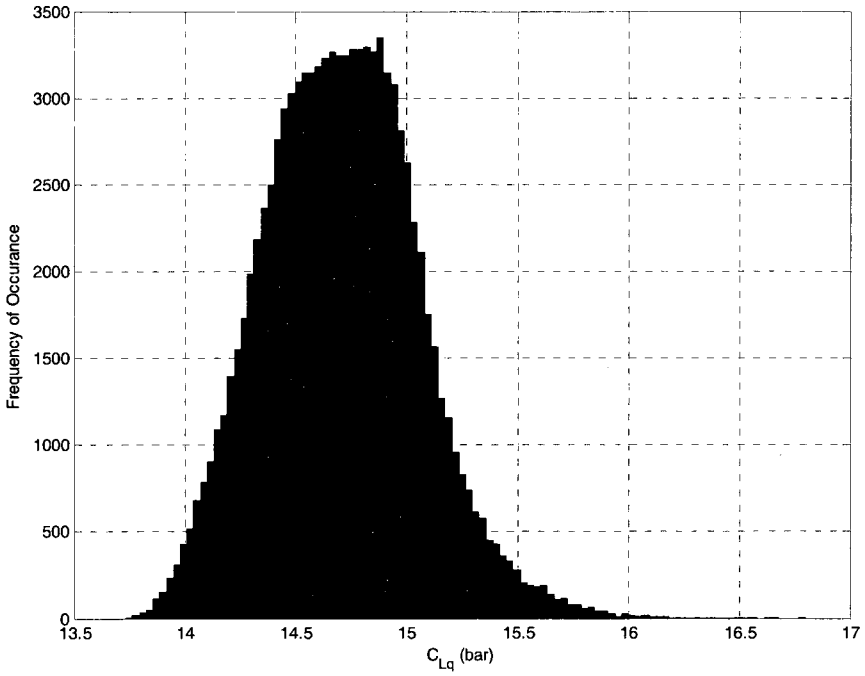

Figure 92: Histogram for out-of-phase lift coefficient (test case #3)

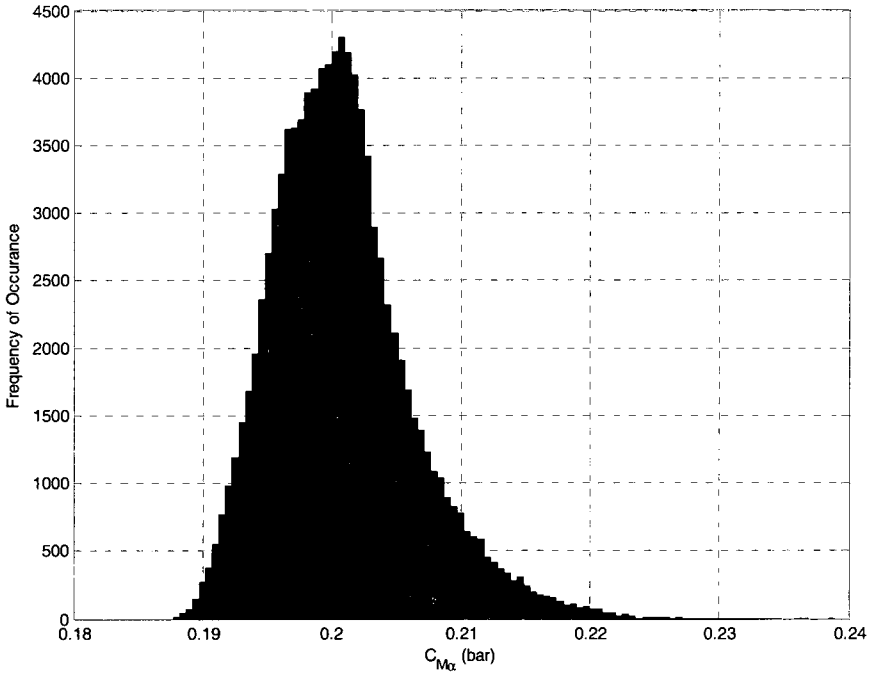

Figure 93: Histogram for in-phase pitching moment coefficient (test case #3)

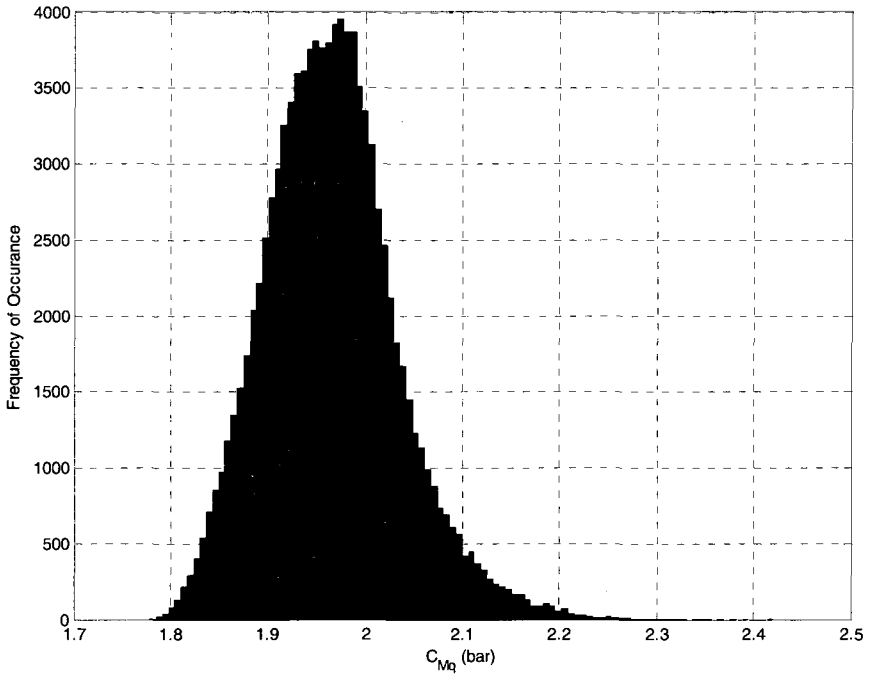

Figure 94: Histogram for out-of-phase pitching moment coefficient (test case #3)

The fourth test case was randomly selected; see Table 20. The equivalent inertia and damping were chosen at the center of the design space. The reduced frequency and backlash were set at their minimum factor settings. The input saturation was set to its significant level (i.e. the low factor level in DOE). The summary statistics are given in Table 21, and histogram results are provided in Figures 95-98.

Table 20: Factor settings (test case #4)

Test Case #4		
Factor	Setting	Name
Jeq	0.0001729	Equivalent inertia [kg*m^2]
Beq	0	Equivalent damping [N-m-s/rad]
k	0.081	Reduced frequency [--]
BL	2	Backlash [arcmin]
IS	0.0809	Input saturation [rad]

Table 21: Summary statistics for test case #4

Response	**Mean**	Standard Deviation	Variance	Min	Max	Skewness	$\mathbf{r_{low}}$	$\mathbf{r_{high}}$
$\overline{C}_{L_\alpha}$	**1.0780**	0.0457	0.0021	0.9983	1.3844	1.1433	**1.0185**	**1.191**
$\overline{C}_{L_q}$	**14.6621**	0.3046	0.0928	14.0535	16.7184	1.0665	**14.2323**	**15.4076**
$\overline{C}_{m_\alpha}$	**0.1925**	0.0055	0	0.1829	0.2297	1.1502	**0.1853**	**0.2062**
$\overline{C}_{m_q}$	**1.9617**	0.0649	0.0042	1.8383	2.3998	1.1034	**1.8731**	**2.1218**

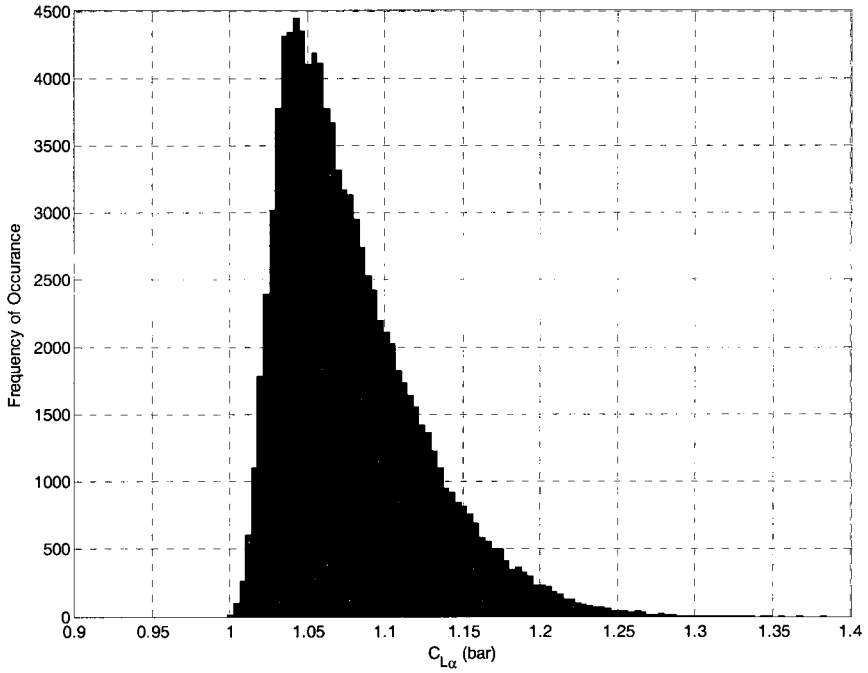

Figure 95: Histogram of in-phase lift coefficient (test case #4)

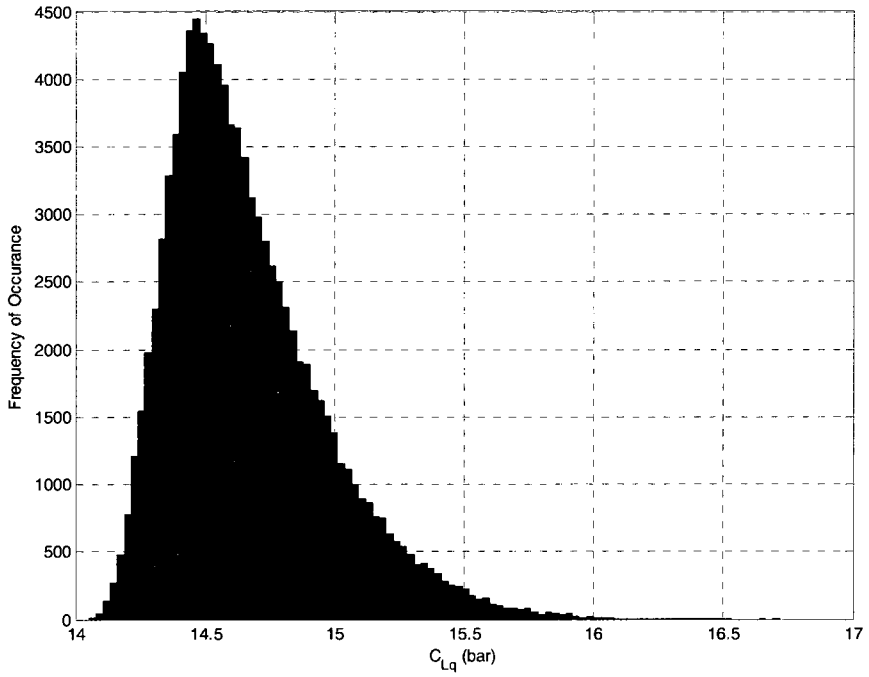

Figure 96: Histogram of out-of-phase lift coefficient (test case #4)

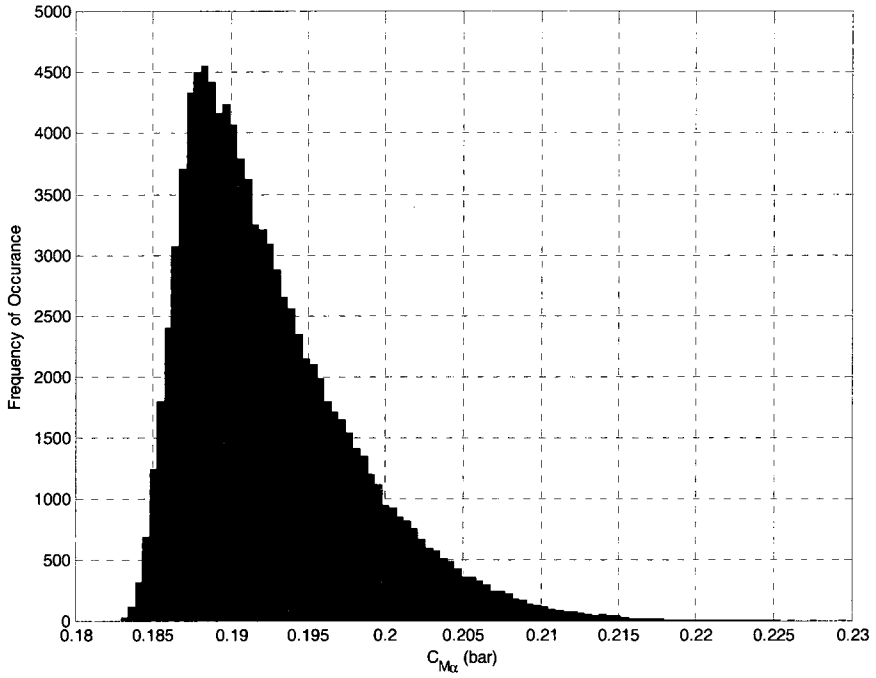

Figure 97: Histogram of in-phase pitching moment coefficient (test case #4)

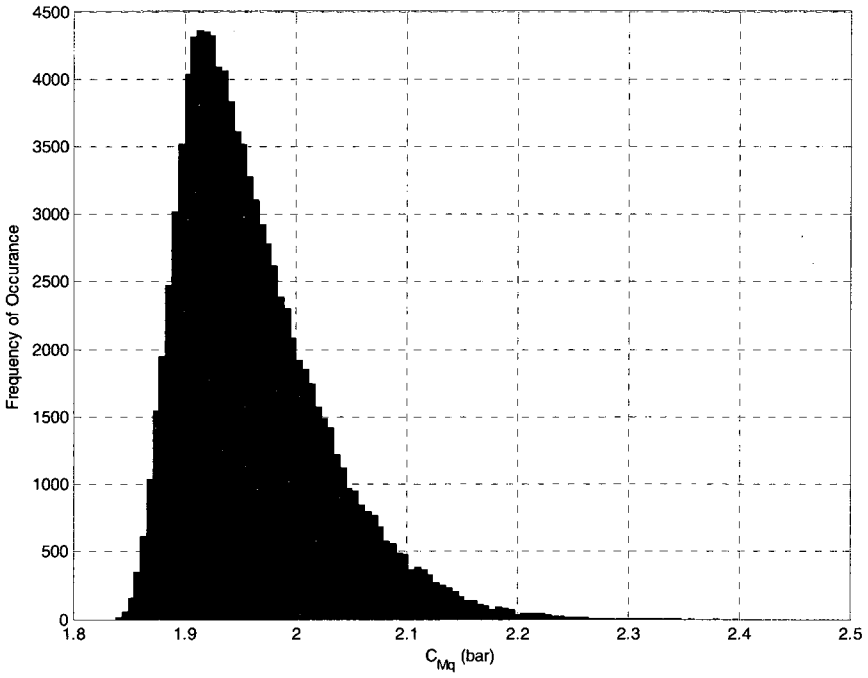

Figure 98: Histogram of out-of-phase pitching moment coefficient (test case #4)

For the final test case, the factor settings were again chosen randomly. The reduced frequency was set to its high factor settings. The equivalent inertia and damping were set high, while the backlash was set to a minimum and input saturation was set at its significant level. Table 22 summarizes the factor settings. Table 23 contains the summary statistics for test case 5. Also, the histogram results of the responses are given in Figures 99-102.

Table 22: Factor settings (test case #5)

Test Case #5		
Factor	Setting	Name
Jeq	0.0006589	Equivalent inertia [kg*m^2]
Beq	0.008056	Equivalent damping [N-m-s/rad]
k	0.1	Reduced frequency [--]
BL	2	Backlash [arcmin]
IS	0.0809	Input saturation [rad]

Table 23: Summary statistics for test case #5

Response	**Mean**	Standard Deviation	Variance	Min	Max	Skewness	$\mathbf{r_{low}}$	$\mathbf{r_{high}}$
$\overline{C}_{L_\alpha}$	**1.2194**	0.041	0.0017	1.1478	1.4905	1.1479	**1.1643**	**1.3211**
$\overline{C}_{L_q}$	**12.1505**	0.2648	0.0701	11.5547	13.897	0.8361	**11.727**	**12.7796**
$\overline{C}_{m_\alpha}$	**0.218**	0.005	0	0.209	0.2511	1.1423	**0.2111**	**0.2303**
$\overline{C}_{m_q}$	**1.4734**	0.0562	0.0032	1.3588	1.8482	1.0338	**1.3899**	**1.6111**

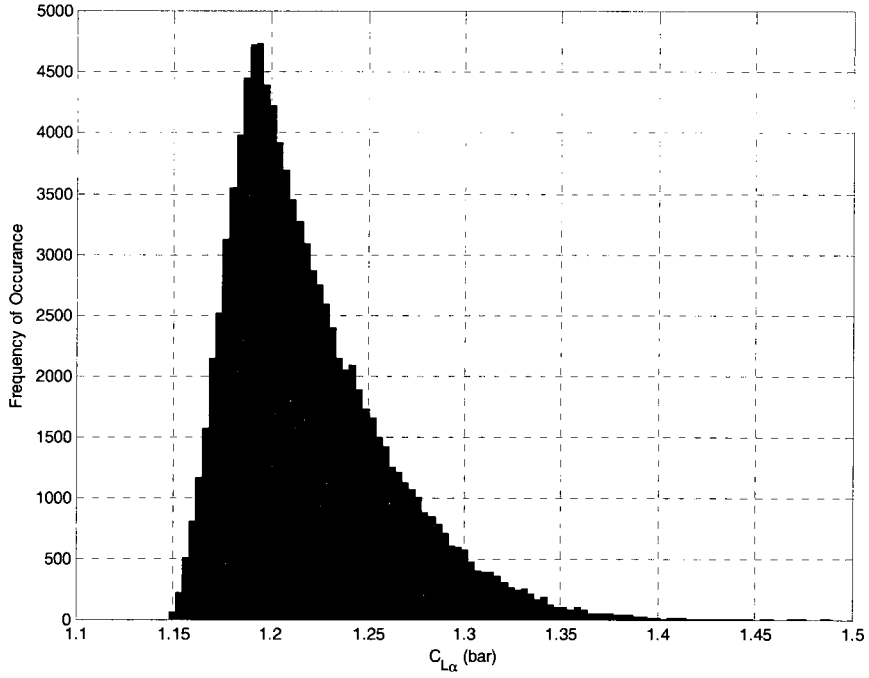

Figure 99: Histogram of in-phase lift coefficient (test case #5)

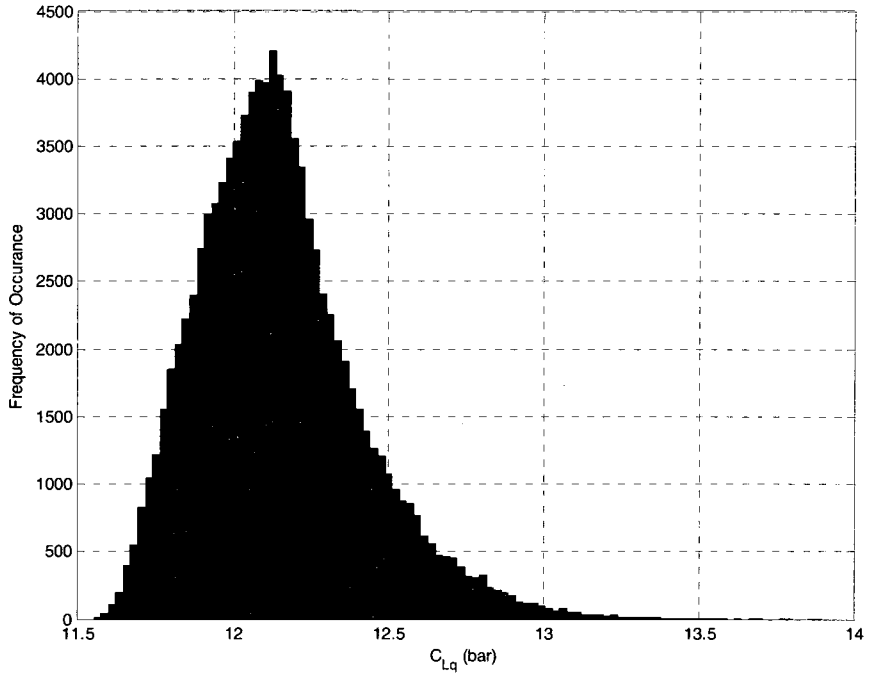

Figure 100: Histogram of out-of-phase lift coefficient (test case #5)

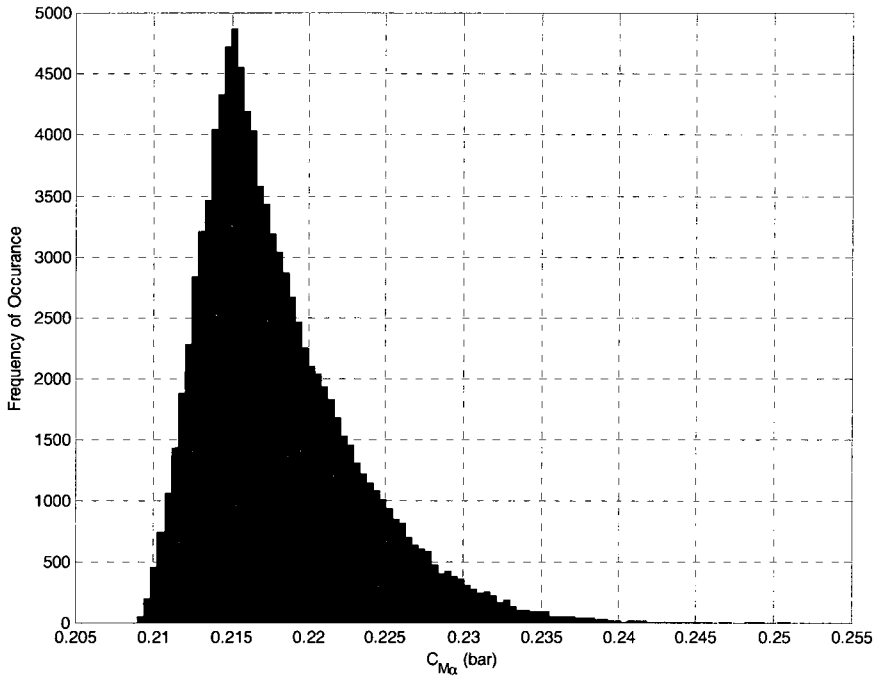

Figure 101: Histogram of in-phase pitching moment coefficient (test case #5)

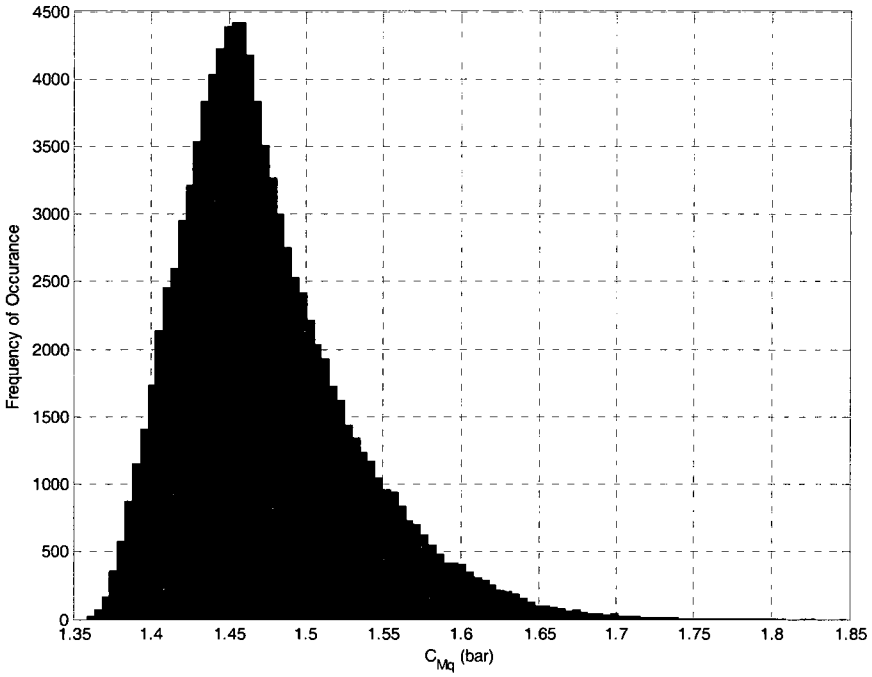

Figure 102: Histogram of out-of-phase pitching moment coefficient (test case #5)

5.1.2 Direct Monte Carlo Simulation Results

The same test cases were used for the direct Monte Carlo method. Factor settings for test cases 1, 2, 3, 4, and 5 are given in Tables 14, 16, 18, 20, and 22 respectively. The direct Monte Carlo method was described in Chapter 4. Test case 1 predicted a larger coverage interval when compared to the indirect Monte Carlo method. The difference may lie in the severity of the skewness in the histogram results. The summary statistics are provided in Table 24. Histograms are shown in Figures 103-106.

Table 24: Summary statistics for test case #1

Response	**Mean**	Standard Deviation	Variance	Min	Max	Skewness	$\mathbf{r_{low}}$	$\mathbf{r_{high}}$
$\overline{C}_{L_\alpha}$	**1.0236**	0.1489	0.0222	0.3206	2.9021	1.4913	**0.7641**	**1.3765**
$\overline{C}_{L_q}$	**14.2235**	1.5691	2.4621	-5.523	20.912	-1.4288	**10.5543**	**16.9851**
$\overline{C}_{m_\alpha}$	**0.1872**	0.0176	0.0003	0.1057	0.4104	1.5251	**0.1567**	**0.2291**
$\overline{C}_{m_q}$	**1.854**	0.2905	0.0844	-1.8044	3.1365	-1.4458	**1.1725**	**2.3632**

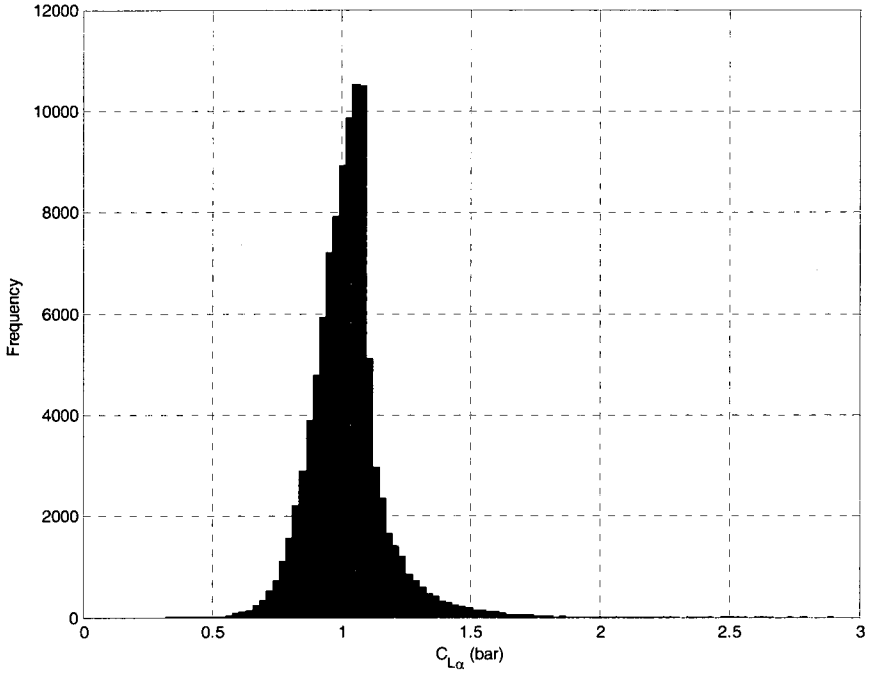

Figure 103: Histogram for in-phase lift coefficient (test case #1)

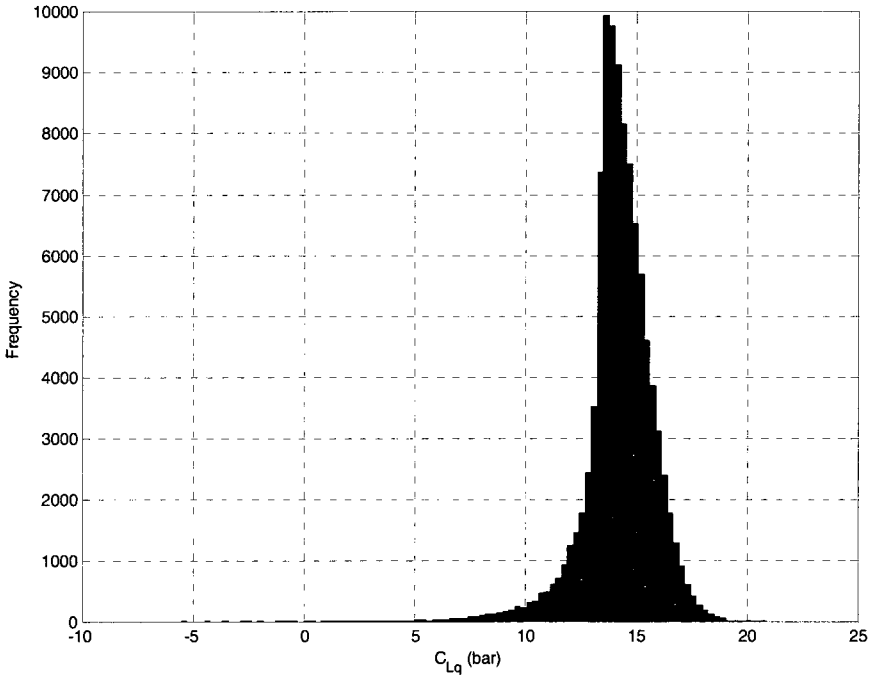

Figure 104: Histograms for out-of-phase lift coefficient (test case #1)

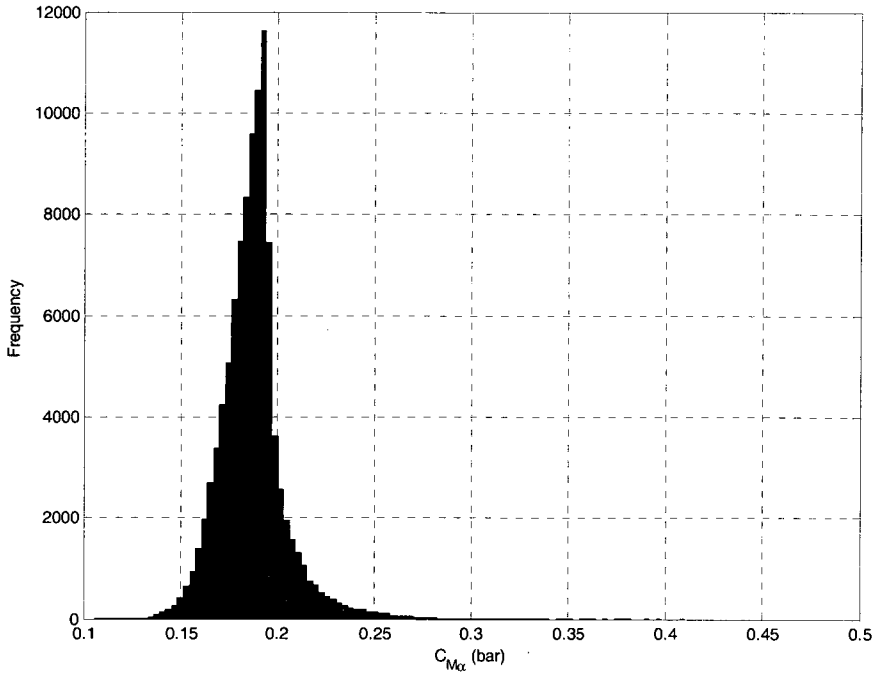

Figure 105: Histograms for in-phase pitching moment coefficient (test case #1)

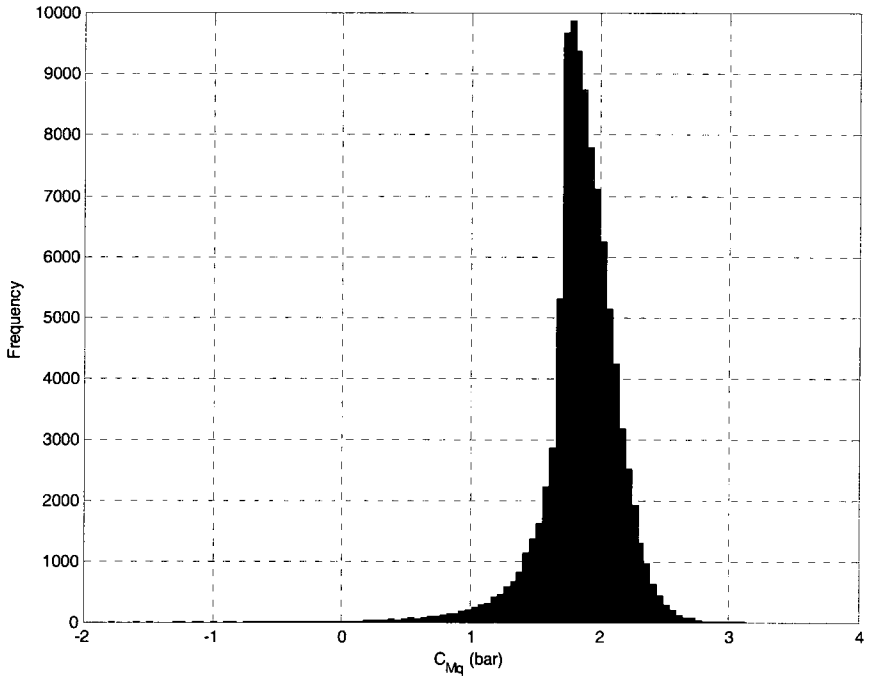

Figure 106: Histograms for out-of-phase pitching moment coefficient (test case #1)

Summary statistics for test case 2 are provided in Table 25. Histograms of the response are shown in Figures 107-110. The difference between the results of 'indirect' and 'direct' Monte Carlo methods is negligible for this case.

Table 25: Summary statistics for test case #2

Response	**Mean**	Standard Deviation	Variance	Min	Max	Skewness	$\mathbf{r_{low}}$	$\mathbf{r_{high}}$
$\overline{C}_{L_\alpha}$	**1.0848**	0.0486	0.0024	0.0169	2.3266	-2.1662	**0.9644**	**1.1387**
$\overline{C}_{L_q}$	**12.8742**	0.4545	0.2066	-0.0239	24.7466	2.7709	**12.3624**	**13.9079**
$\overline{C}_{m_\alpha}$	**0.1978**	0.0059	0	0.07	0.3459	-2.1667	**0.1832**	**0.2042**
$\overline{C}_{m_q}$	**1.5993**	0.0862	0.0074	-0.7977	3.76	2.5609	**1.5027**	**1.8014**

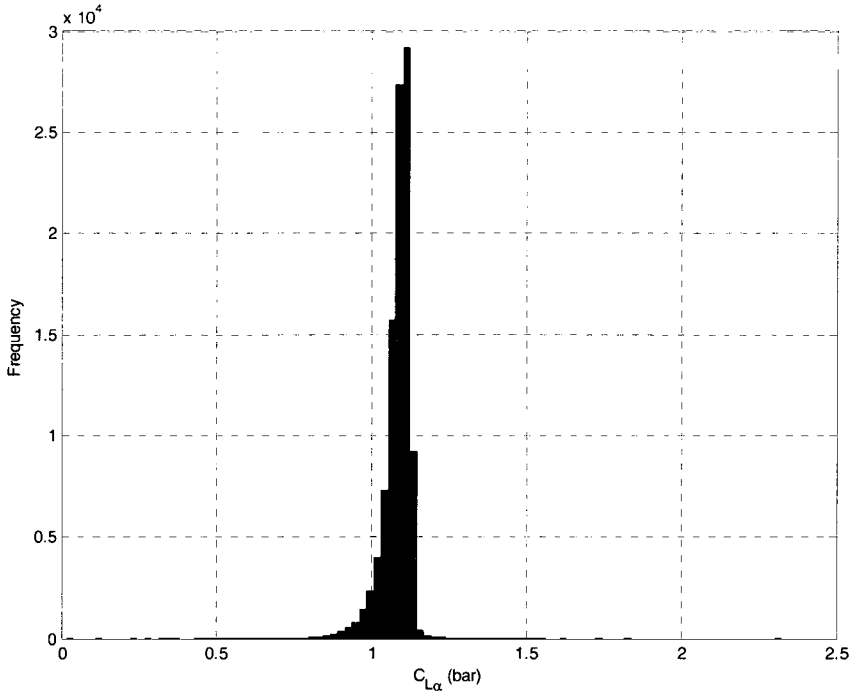

Figure 107: Histogram for in-phase lift coefficient (test case #2)

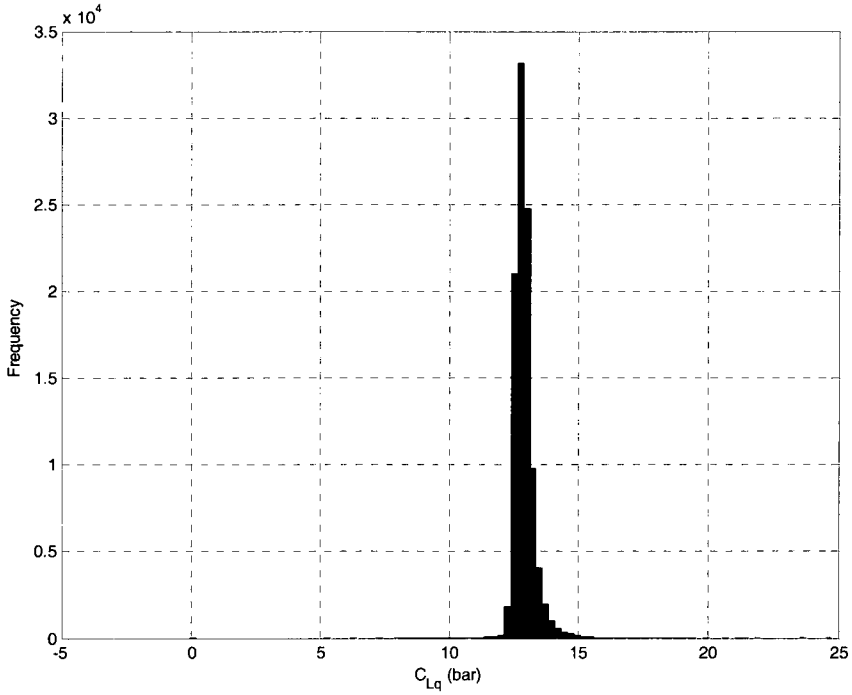

Figure 108: Histogram of out-of-phase lift coefficient (test case #2)

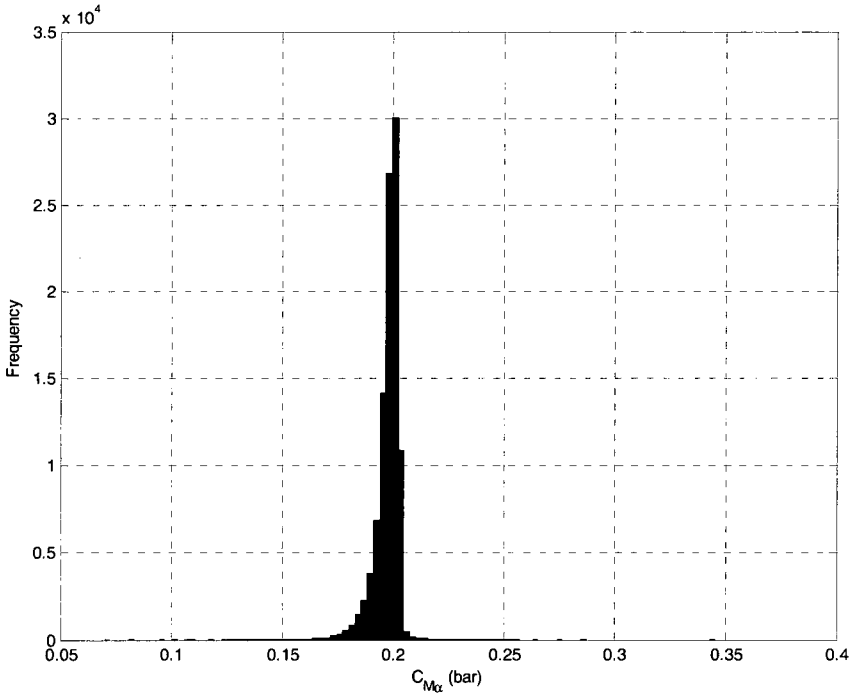

Figure 109: Histogram of in-phase pitching moment coefficient (test case #2)

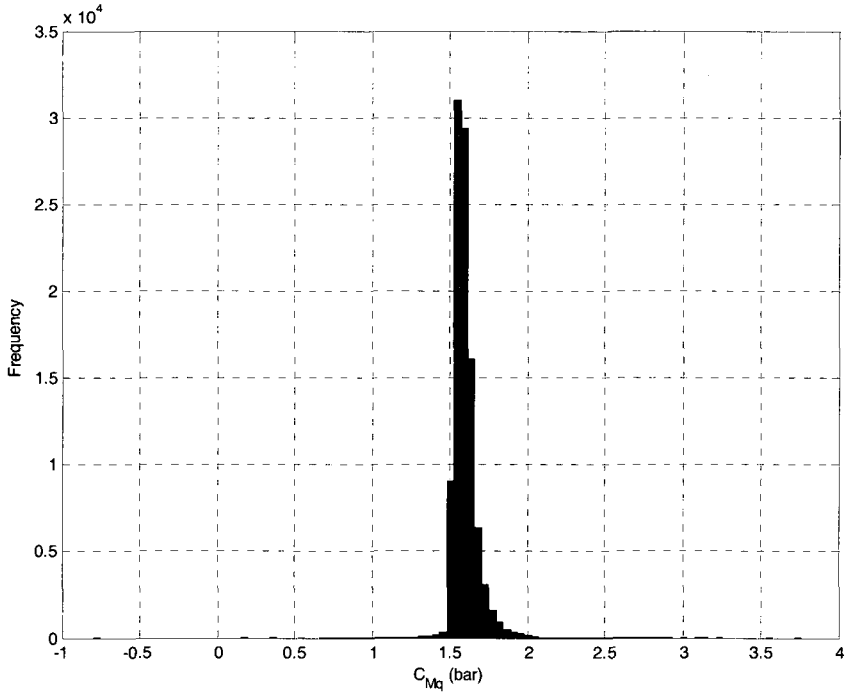

Figure 110: Histogram for out-of-phase pitching moment coefficient (test case #2)

Summary statistics for test case 3 are provided in Table 26. Similarly, the histogram results of the responses are shown in Figures 111-114. Similar to test case 1, the 'direct' Monte Carlo method has a wider confidence interval when compared to the 'indirect' Monte Carlo method, as show in Figures 111-114.

Table 26: Summary statistics for test case 3

Response	**Mean**	Standard Deviation	Variance	Min	Max	Skewness	$\mathbf{r_{low}}$	$\mathbf{r_{high}}$
$\overline{C}_{L_\alpha}$	**1.1281**	0.1743	0.0304	0.1743	3.1974	0.9177	**0.8238**	**1.5077**
$\overline{C}_{L_q}$	**12.5723**	1.6908	2.8589	-9.4857	20.0001	-1.334	**8.7298**	**15.1489**
$\overline{C}_{m_\alpha}$	**0.199**	0.0211	0.0004	0.0873	0.4463	0.911	**0.1624**	**0.2452**
$\overline{C}_{m_q}$	**1.569**	0.3172	0.1006	-2.4906	3.0897	-1.2312	**0.8564**	**2.0756**

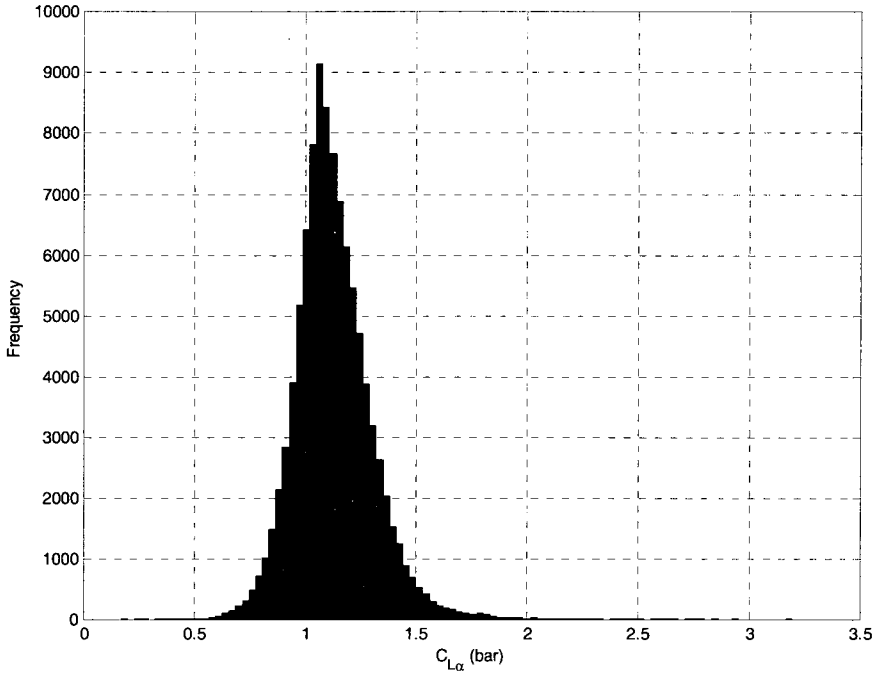

Figure 111: Histogram of in-phase lift coefficient (test case #3)

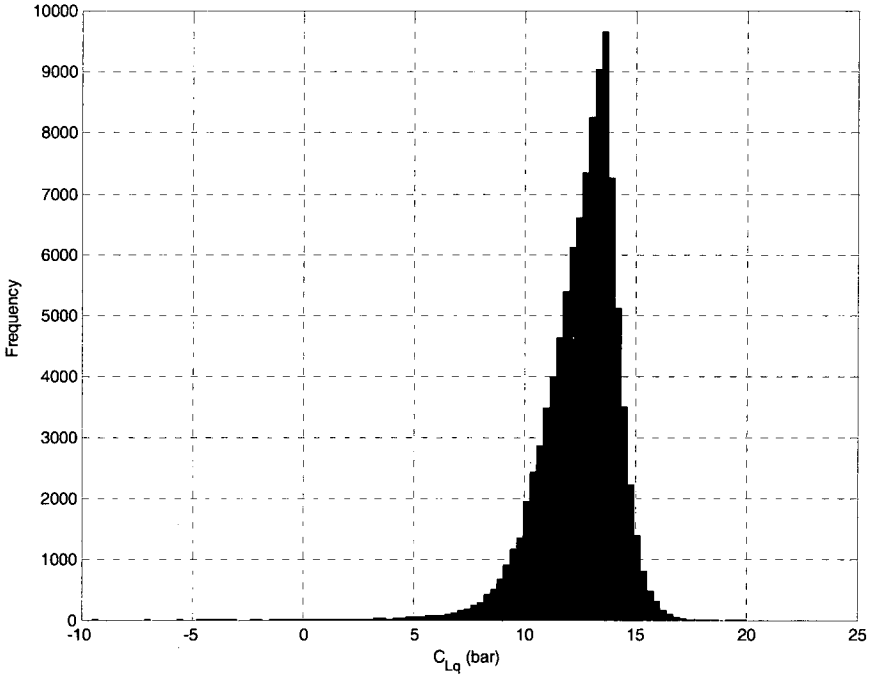

Figure 112: Histogram of out-of-phase lift coefficient (test case #3)

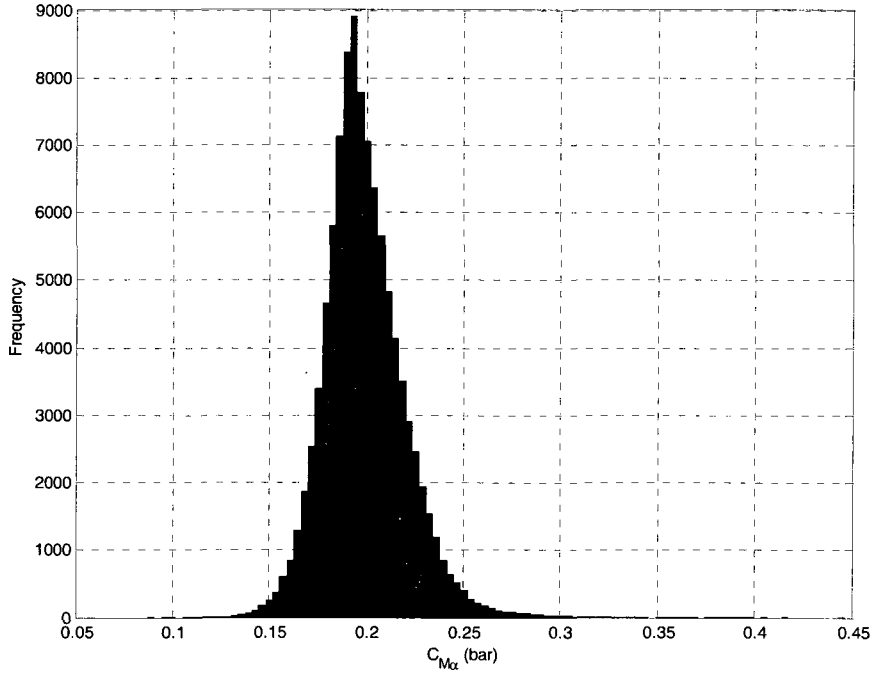

Figure 113: Histograms of in-phase pitching moment coefficient (test case #3)

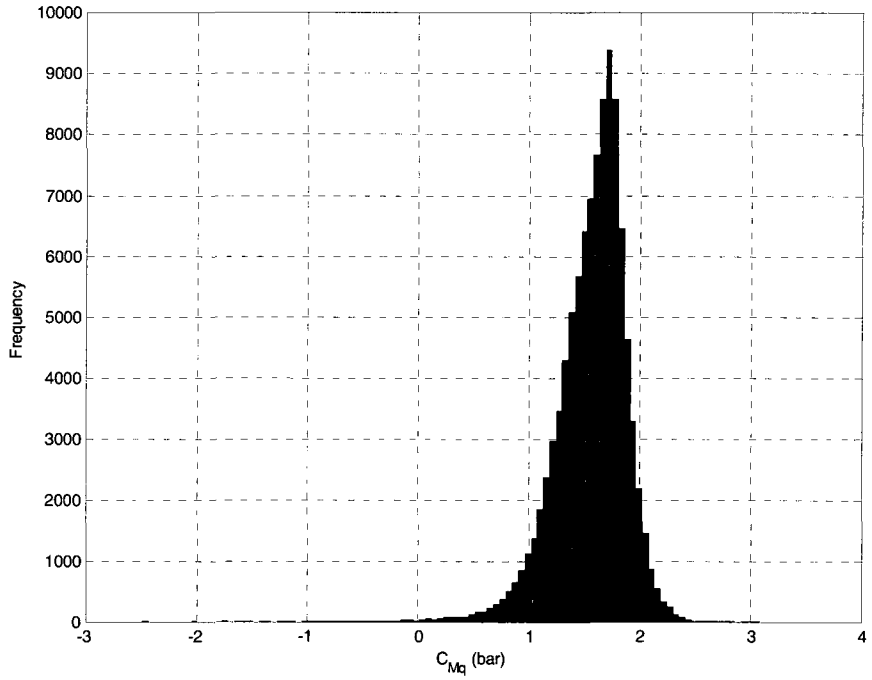

Figure 114: Histogram of out-of-phase pitching moment coefficient (test case #3)

Summary statistics for test case 4 are provided in Table 27. Again, the histograms of the responses are shown in Figures 115-118. The results have a greater confidence interval than the previous results.

Table 27: Summary statistics for test case #4

Response	**Mean**	Standard Deviation	Variance	Min	Max	Skewness	$\mathbf{r_{low}}$	$\mathbf{r_{high}}$
$\overline{C}_{L_\alpha}$	**1.0316**	0.1386	0.0192	0.2509	3.156	1.5625	**0.7786**	**1.3573**
$\overline{C}_{L_q}$	**13.6275**	1.2527	1.5693	-8.2334	19.6584	-2.6923	**10.419**	**15.5613**
$\overline{C}_{m_\alpha}$	**0.187**	0.0165	0.0003	0.095	0.4399	1.5433	**0.1568**	**0.2257**
$\overline{C}_{m_q}$	**1.7617**	0.2415	0.0583	-2.3077	2.9971	-2.354	**1.1576**	**2.1568**

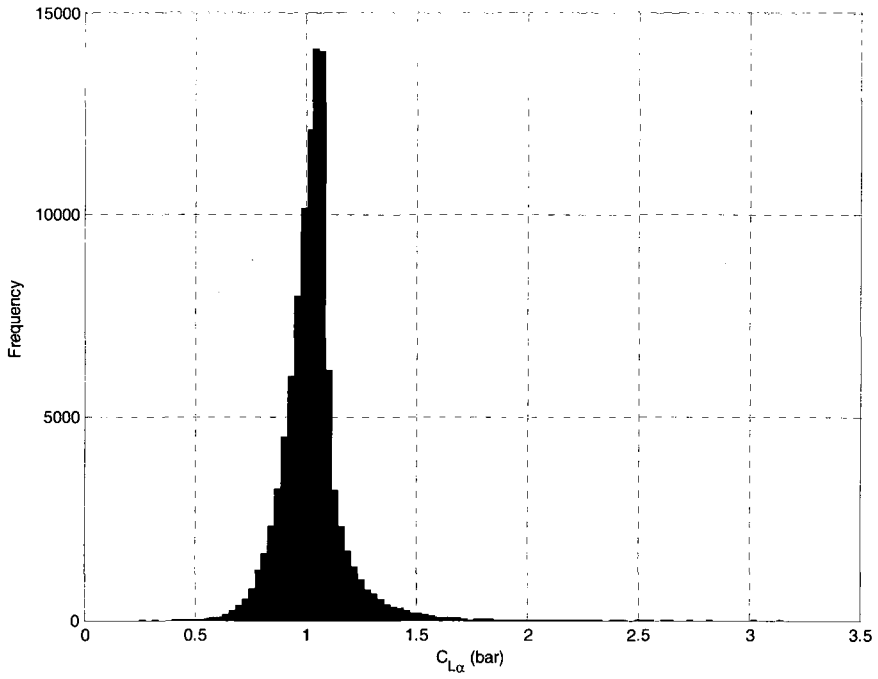

Figure 115: Histogram of in-phase lift coefficient (test case #4)

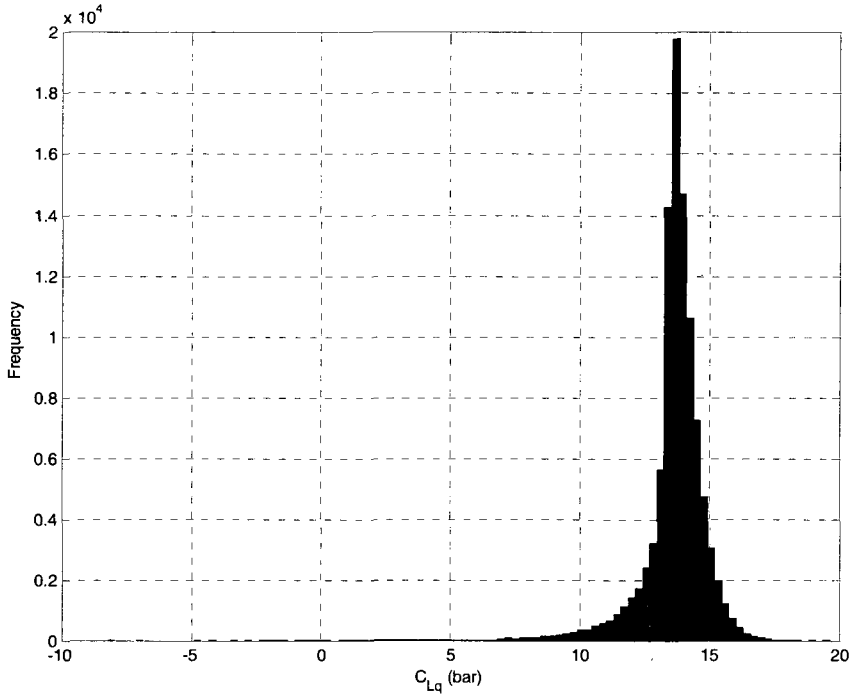

Figure 116: Histograms of out-of-phase lift coefficient (test case #4)

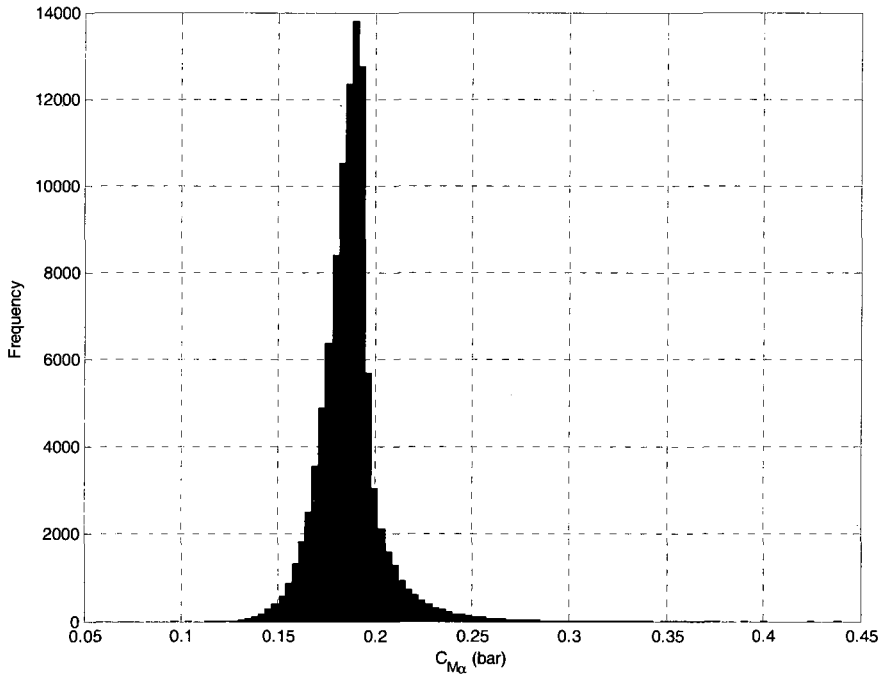

Figure 117: Histogram of in-phase pitching moment coefficient (test case #4)

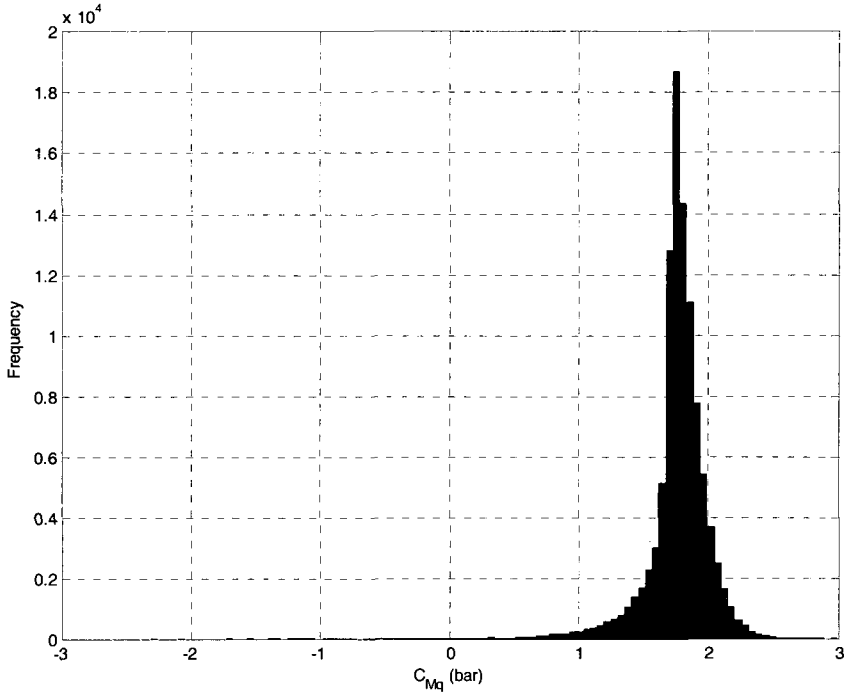

Figure 118: Histogram of out-of-phase pitching moment coefficient (test case #4)

The final test case summary statistics are provided in Table 28. Histograms of the responses are given in Figures 119-122. Again, the confidence intervals are larger than predicted from the 'indirect' Monte Carlo method. This is possibly due to the high skewness.

Table 28: Summary statistics for test case #5

Response	**Mean**	Standard Deviation	Variance	Min	Max	Skewness	$\mathbf{r_{low}}$	$\mathbf{r_{high}}$
$\overline{C}_{L_\alpha}$	**1.1171**	0.1424	0.0203	0.336	3.4103	1.359	**0.8593**	**1.4391**
$\overline{C}_{L_q}$	**11.8193**	1.3883	1.9275	-12.0816	17.5705	-1.8002	**8.5762**	**14.1788**
$\overline{C}_{m_\alpha}$	**0.2051**	0.0174	0.0003	0.1125	0.4789	1.2442	**0.1734**	**0.2438**
$\overline{C}_{m_q}$	**1.4054**	0.259	0.0671	-3.0225	2.6017	-1.7618	**0.8004**	**1.8465**

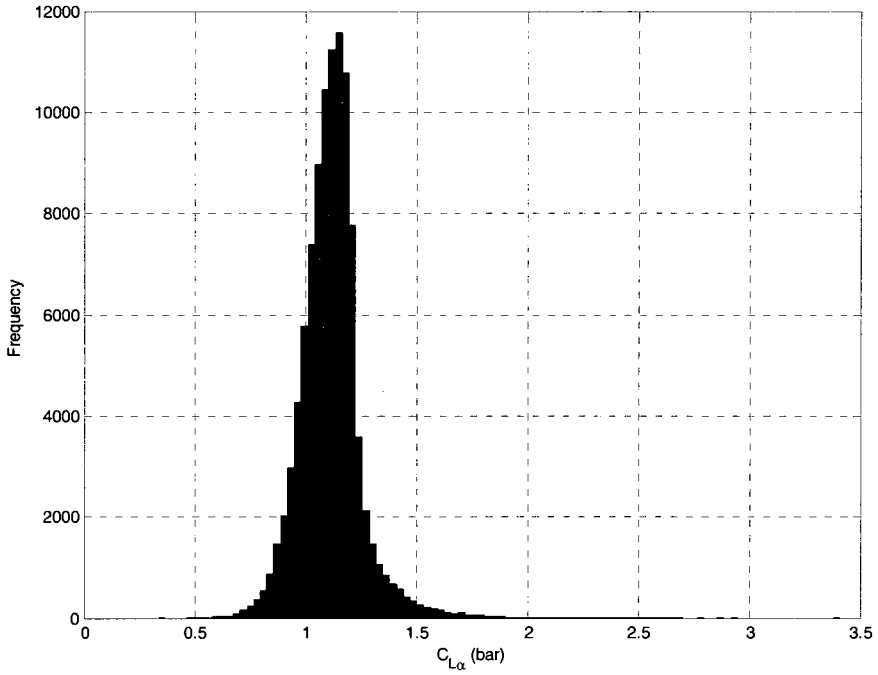

Figure 119: Histogram of in-phase lift coefficient (test case #5)

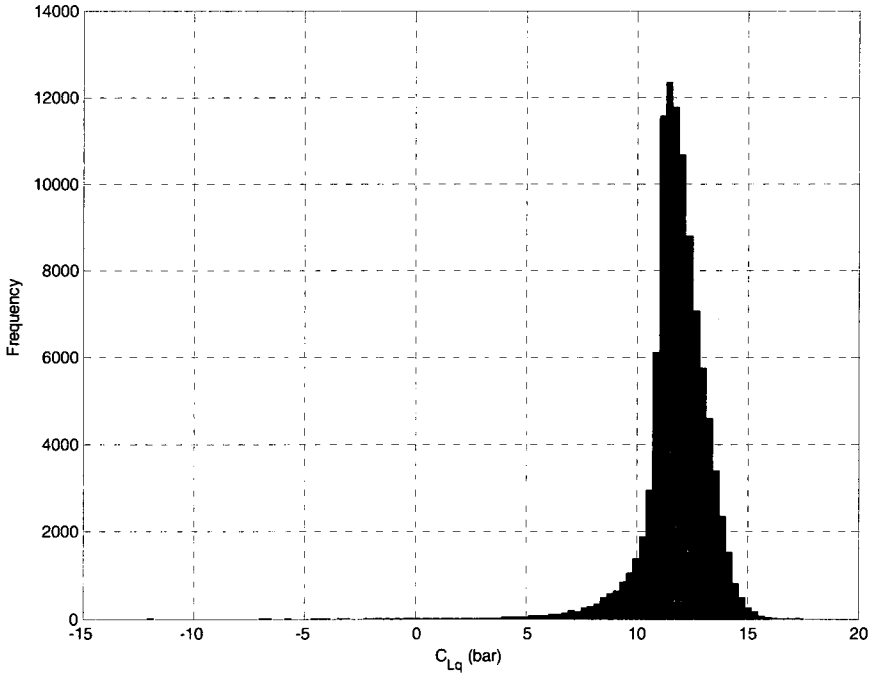

Figure 120: Histogram of out-of-phase lift coefficient (test case #5)

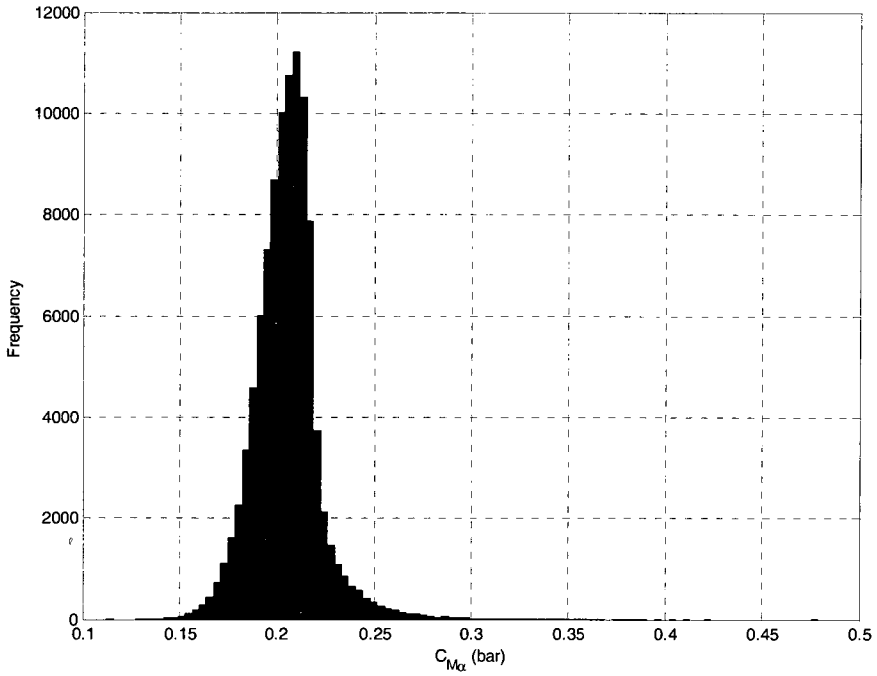

Figure 121: Histogram of in-phase pitching moment coefficient (test case #5)

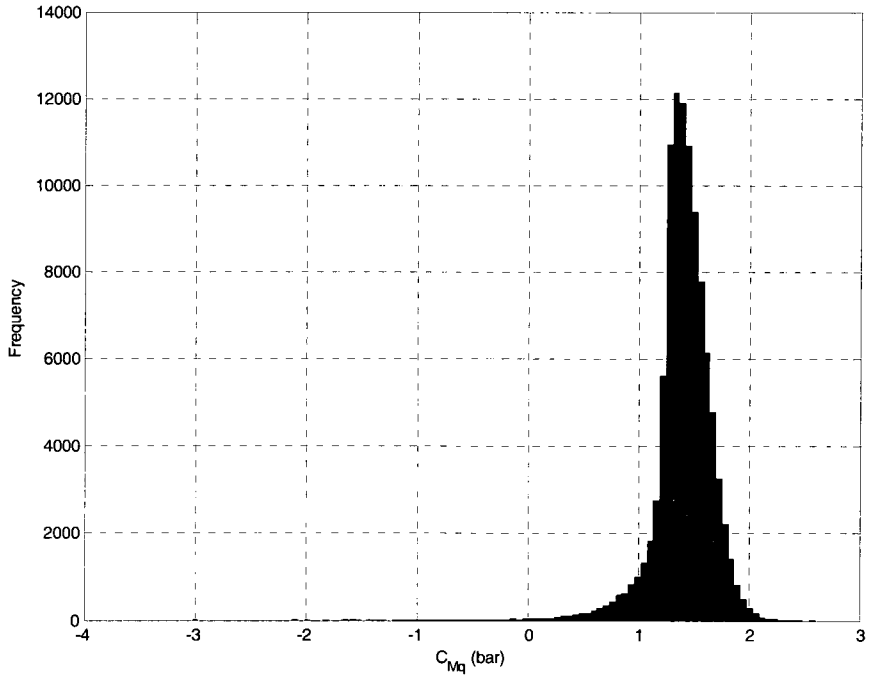

Figure 122: Histogram of out-of-phase pitching moment coefficient (test case #5)

5.2 Discussion

Tables 29 and 30 have summarized the 95% probability confidence intervals for all test cases. Table 29 contains the results from using the 'indirect' Monte Carlo method, and Table 30 contains the results from using the 'direct' Monte Carlo method. Generally, the 'direct' method provided a larger coverage interval compared to the 'indirect' method.

The 'indirect' method used a sensitivity analysis via a Taylor series expansion to determine the uncertainty in a response. Although the method is simple, its use has several drawbacks. Since the sensitivity analysis is based on computing derivatives, numerical differentiation can be difficult for complex functions, or, worse, it can be incorrectly computed. The Taylor series expansion assumes the response is nearly linear over a small range. It will not always be easy to determine whether the approximations involved using this method are acceptable. The 'direct' Monte Carlo method does not suffer from this problem because it can reach an arbitrary level of accuracy. In addition, the method is strictly based on the statistical moments of each parameter and does not directly incorporate the parameter probability distribution(s). One of the major drawbacks is that the method lacks coupled variable effects. The interactions between the distributions are not modeled adequately by changing only one of the model parameters. If an input variable is statistically correlated, one-at-a-time sensitivity analysis does not address such correlations. Attempting to evaluate all the potential combinations of input parameters can be unmanageable. Also, high order estimates may be necessary to adequately address highly skewed distributions.

The 'direct' Monte Carlo method obtains high accuracy by using a sufficiently large number of runs. Sometimes Latin hypercube sampling can be used when the method becomes extremely time consuming. The 'direct' Monte Carlo method can suffer from improper selection of probability distributions either from inadequate data or lack of understanding of the underlying physical process.

The sensitivity analysis base method (i.e. 'indirect' Monte Carlo method) may be used to obtain preliminary answers. However, the 'direct' Monte Carlo method is preferred when error propagation with a complex system is being studied because the method is easily implemented and generally applicable.

The 'indirect' Monte Carlo method predicts that the response variability ranges from approximately 3% to 6% of the mean responses over all test cases. On the other hand, the 'direct' Monte Carlo method predicts that the response variability ranges from approximately 3% to 40% of the mean responses over all test cases.

Table 29: Summary of 95% confidence intervals for all test cases using the 'indirect' Monte Carlo method

Test Case	95% Confidence Interval
#1	$1.0816 \le \overline{C}_{L_\alpha} \le 1.1967$ $14.2512 \le \overline{C}_{L_q} \le 15.3689$ $0.1942 \le \overline{C}_{m_\alpha} \le 0.2070$ $1.8614 \le \overline{C}_{m_q} \le 2.0782$
#2	$1.1225 \le \overline{C}_{L_\alpha} \le 1.1842$ $12.7585 \le \overline{C}_{L_q} \le 13.4310$ $0.2023 \le \overline{C}_{m_\alpha} \le 0.2096$ $1.5772 \le \overline{C}_{m_q} \le 1.7004$
#3	$1.0714 \le \overline{C}_{L_\alpha} \le 1.2526$ $12.7585 \le \overline{C}_{L_q} \le 15.4326$ $0.1919 \le \overline{C}_{m_\alpha} \le 0.2138$ $1.8436 \le \overline{C}_{m_q} \le 2.1181$
#4	$1.0185 \le \overline{C}_{L_\alpha} \le 1.1910$ $14.2323 \le \overline{C}_{L_q} \le 15.4076$ $0.1853 \le \overline{C}_{m_\alpha} \le 0.2062$ $1.8731 \le \overline{C}_{m_q} \le 2.1218$
#5	$1.1643 \le \overline{C}_{L_\alpha} \le 1.3211$ $11.7270 \le \overline{C}_{L_q} \le 12.7796$ $0.2111 \le \overline{C}_{m_\alpha} \le 0.2303$ $1.3899 \le \overline{C}_{m_q} \le 1.6111$

Table 30: Summary of 95% confidence intervals for all test cases using the 'direct' Monte Carlo method

Test Case	95% Confidence Interval
#1	$0.7664 \le \overline{C}_{L_\alpha} \le 1.3756$ $10.5639 \le \overline{C}_{L_q} \le 16.9628$ $0.2290 \le \overline{C}_{m_\alpha} \le 0.3538$ $1.1743 \le \overline{C}_{m_q} \le 2.3590$
#2	$0.9644 \le \overline{C}_{L_\alpha} \le 1.1387$ $12.3625 \le \overline{C}_{L_q} \le 13.9079$ $0.1832 \le \overline{C}_{m_\alpha} \le 0.2042$ $1.5027 \le \overline{C}_{m_q} \le 1.8014$
#3	$0.8238 \le \overline{C}_{L_\alpha} \le 1.5077$ $8.7298 \le \overline{C}_{L_q} \le 15.1489$ $0.1624 \le \overline{C}_{m_\alpha} \le 0.2452$ $0.8564 \le \overline{C}_{m_q} \le 2.0756$
#4	$0.7786 \le \overline{C}_{L_\alpha} \le 1.3573$ $10.4190 \le \overline{C}_{L_q} \le 15.5613$ $0.1568 \le \overline{C}_{m_\alpha} \le 0.2257$ $1.1576 \le \overline{C}_{m_q} \le 2.1568$
#5	$0.8593 \le \overline{C}_{L_\alpha} \le 1.4391$ $8.5762 \le \overline{C}_{L_q} \le 14.1788$ $0.1734 \le \overline{C}_{m_\alpha} \le 0.2438$ $0.8004 \le \overline{C}_{m_q} \le 1.8465$

The most significant finding of the study is that researchers using different test rigs can have, even with the same aircraft model, significantly varied results due only to the differences in system dynamic parameters. Many researchers often assume that bias errors can simply be averaged out or that they are negligible. However, the parameters play a larger role in that the systematic errors interact with the aerodynamics, even with proper calibration of the forced oscillation test rig.

Such large variability shows the bias effects are interacting with the aerodynamics. For example, input saturation causes the dynamic contributions of lift coefficient and pitching moment coefficient to have missing data at the peaks and troughs of the sine wave; an example is shown in Figure 123. This result has also been shown in experimental results; refer to the work of [10]. The poor prediction of the stability derivatives is problematic because the analysis used to compute the in-phase and out-of-phase coefficients assumes that the sine fidelity is high, when in actuality it is not. The analysis used simply solves for the area under the curve to determine the in-phase and out-of-phase coefficients. Therefore, one cause of the poor prediction is due to poor sine fidelity caused by input saturation.

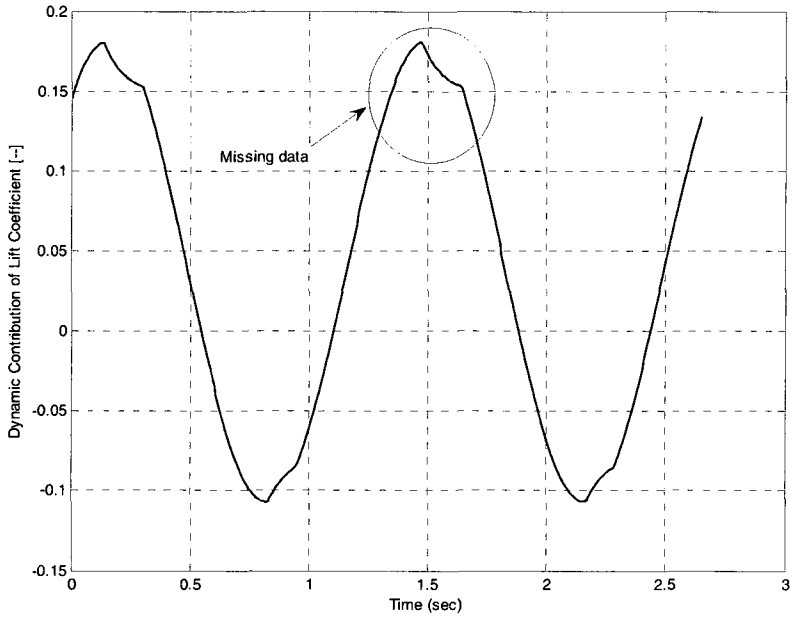

Figure 123: Incomplete sinusoidal waveform of dynamic contribution of lift coefficient

The bias effect of backlash is also highly problematic. Although some backlash is necessary in all geared systems to allow a certain amount of clearance between the components transmitting the motion under the load to avoid interference, wear, and excessive heat generation, it can be particularly challenging if the backlash is large (i.e. 8 arcmin or higher). Backlash is also not important in applications where there is no load reversal or the position after a reversal is not critical. However, forced oscillation wind tunnel testing requires precision positioning with frequent load reversal. Backlash can directly influence the positioning. When the gears are separated the load is no longer under control. Control is only retained on the motor side. When the gears reconnect backlash can introduce a nonlinear vibration that may be on the same order as the aerodynamics one is trying to measure.

Even worse, the coupling effects between the systematic errors make it very difficult to decouple them from the aerodynamic measurement. Referring to Table 31, the coded (i.e. nondimensional) regression metamodels can be used to examine the magnitude of the effects. In Table 31, factors are represented as:

1. A – equivalent inertia,
2. B – equivalent damping,
3. C – reduced frequency,
4. D – backlash, and
5. E – input saturation.

Reduced frequency is the most dominant contributor to the in-phase and out-of-phase components; it is shown in bold in Table 31. This result is expected since the aerodynamic model developed was based on reduced frequency. Interestingly, the coupling effects are about the same order of magnitude. The coupling makes it difficult to determine which systematic error is dominating and should be eliminated. For example, looking at the in-phase pitching moment coefficient the interaction between backlash and input saturation (i.e. D*E) has a larger effect compared to an interaction between equivalent damping and backlash (i.e. B*D). On the other hand, the backlash and input saturation interaction can also have the same order effect as the interaction between equivalent damping and reduced frequency (i.e. B*C). Therefore, no one effect is dominating; however, its overall contributions together are affecting the final result making it difficult to decouple the coupled systematic errors from the aerodynamics.

Table 31: Coded Regression Metamodels

In-Phase Lift Coefficient		Out-of-Phase Lift Coefficient		In-Phase Pitching Moment Coefficient		Out-of-Phase Pitching Moment Coefficient	
$\overline{C}_{L_\alpha}$	=	$\overline{C}_{L_q}$	=	$\overline{C}_{m_\alpha}$	=	$\overline{C}_{m_q}$	=
1.108E+00		1.264E+01		2.005E-01		1.555E+00	
2.525E-02	* A	-3.061E-01	* A	3.524E-03	* A	-5.061E-02	* A
2.443E-02	* B	-2.369E-01	* B	2.585E-03	* B	-4.668E-02	* B
1.140E-01	*** C**	**-1.688E+00**	*** C**	**1.761E-02**	*** C**	**-3.224E-01**	*** C**
4.892E-02	* D	-5.170E-01	* D	5.765E-03	* D	-9.549E-02	* D
2.172E-02	* E	-1.208E-02	* E	3.197E-03	* E	-9.387E-03	* E
5.852E-03	* A * B	-7.487E-02	* A * B	7.959E-04	* A * B	-1.309E-02	* A * B
-1.168E-02	* A * E	9.933E-02	* A * E	-1.210E-03	* A * E	2.023E-02	* A * E
1.386E-02	* B * C	-1.373E-01	* B * C	1.558E-03	* B * C	-2.661E-02	* B * C
-8.176E-03	* B * D	8.054E-02	* B * D	-9.214E-04	* B * D	1.476E-02	* B * D
8.376E-03	* C * D	-7.797E-02	* C * D	8.947E-04	* C * D	-1.517E-02	* C * D
-8.135E-03	* D * E	9.299E-02	* D * E	-1.029E-03	* D * E	1.690E-02	* D * E
1.215E-02	* A^2	-1.112E-01	* A^2	1.544E-03	* A^2	-2.066E-02	* A^2
8.037E-03	* B^2	-3.725E-02	* B^2	7.871E-04	* B^2	-1.030E-02	* B^2
4.221E-02	* C^2	-4.648E-01	* C^2	5.321E-03	* C^2	-8.230E-02	* C^2
-2.091E-02	* D^2	2.596E-01	* D^2	-2.553E-03	* D^2	4.557E-02	* D^2
-5.023E-02	* E^2	3.979E-01	* E^2	-5.770E-03	* E^2	8.170E-02	* E^2
-3.757E-02	* A^3	4.459E-01	* A^3	-4.995E-03	* A^3	7.620E-02	* A^3
-2.540E-02	* B^3	2.616E-01	* B^3	-2.786E-03	* B^3	5.075E-02	* B^3
-5.476E-02	* C^3	5.415E-01	* C^3	-6.311E-03	* C^3	1.038E-01	* C^3
-4.631E-02	* D^3	4.968E-01	* D^3	-5.529E-03	* D^3	9.133E-02	* D^3

CHAPTER 6

CONCLUSIONS AND FUTURE WORK

6.1 Summary

Poor prediction of aircraft stability derivatives is caused by unsteady, nonlinear aerodynamics brought on by high angle-of-attack and/or high angular rate maneuvers. Consequently, researchers have begun to use unsteady nonlinear modeling methodologies and forced oscillation wind tunnel testing in attempts to estimate unsteady, nonlinear stability derivatives. There is no standard methodology for computational modeling currently. The most popular method is, by far, forced oscillation wind tunnel testing. However, wind tunnel testing is not without its problems.

There have been measurement data inconsistencies noted by researchers. The inconsistencies are possibly from low accuracy and non-physical values of parameter estimation. Other sources of error are due to model structure error in the form of measurement bias. Bias errors are a particular concern because the aerodynamic phenomena are occurring below 10 Hz, which can interact with the test rig dynamics. Other sources of error, classical to all wind tunnels, are Reynolds number scaling issues, dynamic scaling issues, and turbulence intensity (transition) effects.

This study used a high fidelity simulation model of a forced oscillation testing apparatus. The NASA Langley 12-ft Wind Tunnel was used as a representative model for developing the simulation model. The simulation was verified and validated. Factors

were chosen based on either experimental data (i.e. input saturation), straight or bent sting characteristics (i.e. inertia and damping), or from the manufacturer's data sheet (i.e. backlash).

After validation, a design of experiments methodology was used to experiment with the model. An embedded fractional factorial 2_V^{5-1}, face-centered design was used. The design was chosen based on the flexibility of the face centered design for building higher order regression metamodels. Third order polynomial regression metamodels were built for the responses: in-phase lift coefficient, out-of-phase lift coefficient, in-phase pitching moment coefficient, and out-of-phase pitching moment coefficient. The metamodel adequacy was judged using R-squared, adjusted R-squared, predicted R-squared, and PRESS statistics. Notions of experimental blocking, replication, and randomization are irrelevant in this study because the simulation is deterministic. Also, usual measures of uncertainty have no obvious statistical meaning (i.e. with an F-statistic). Since no random error was present, the error associated with uncertainty was based on only systematic error.

Finally, the study concluded with an uncertainty analysis using 'indirect' and 'direct' Monte Carlo simulations. The 'indirect' method was based on the classical sensitivity analysis using Taylor series expansion. The method provided results which showed a variability range of 3% to 6% of the responses from their mean. On the other hand, a 'direct' Monte Carlo simulation was based on the method outlined by Coleman & Steele [146]. The 'direct' method predicts larger variability in the responses, approximately 3% to 40%. The 'direct' Monte Carlo method was determined to have the superior results because of several issues with the 'indirect' method. The 'indirect'

Monte Carlo method lacks coupled variable changes which doesn't account for coupling between parameter probability distributions. Higher order estimates may be necessary to adequately address highly skewed distributions.

This study showed variability in the responses in keeping with a system that is highly nonlinear. Responses were highly sensitive to the factors (i.e. J_{eq}, B_{eq}, k, IS, BL). In addition, unfortunately, the nonlinear behavior of the dynamic system and its systematic biases has a coupling effect with the aerodynamics of an aircraft (in this case the F-16XL). While factors may not change over the ranges chosen within one system, it is highly likely that factors differ for different facilities.

6.2 Recommendations

There are a few recommendations that can be made to improve the fidelity of forced oscillation wind tunnel testing based on the simulation results. Although the damping of a system cannot be changed readily or easily, the inertia of the system should be kept as low as possible. For example, the results of this study show that a straight sting will have less of an impact on the dynamics of the system than the bent sting. Backlash is very problematic for the system. Although the specific gear drive used in the representative model uses a low backlash of 2 arcmin, the gear drive should be measured over time because it will not remain the same as that reported by the manufacturer. Backlash is a major issue because it decouples the motor from the drive. When decoupling of the gears occurs the system on the drive side is no longer under control. When the gears are meshed together again it generates a nonlinear vibration. This nonlinear vibration may be on the same order of the aerodynamic measurement. The total amount of coulomb and viscous friction in the system should be measured or

computed as well. The total amount of friction in the system can affect the control system and possibly be one of the sources of input saturation. Input saturation can also be due to manufacturer limitations set within the motor or due to poor control schemes on the position controller. The manufacturer sets actuator limits to prevent the motor from overheating. Even minor amounts of input saturation reduce the magnitude of the response. The position controller scheme should be evaluated and improved if necessary.

6.3 Future Work

As with any study there is always future work identified. The simulation should be updated to include other body axes for roll forced oscillation and yaw forced oscillation testing. Testing of the physical forced oscillation dynamic test rig should be conducted with particular attention paid to investigating the measurable effects of changing sting inertia, gear train backlash and motor control algorithms. This may help further validate or disprove the simulation results. To fully understand the role that a forced oscillation rig plays in the error of stability derivative parameter estimation, a matched simulation and experimental rig, for which all the parameters are known including the motor control method and gains, is essential.

REFERENCES

[1] Bryan, G.H., *Stability in Aviation,* Macmillian, London, 1911.

[2] Nelson, R.C., *Flight Stability and Automatic Control,* 2nd ed., McGraw-Hill, Boston, 1998.

[3] Kyle, H., Lowenburg, M., and Greenwell, D., "Comparative Evaluation of Unsteady Aerodynamic Modeling Approaches," AIAA Paper 2004-5272, Aug. 2004.

[4] Murphy, P.C., Personal communication.

[5] Greewell, D.I., "A Review of Unsteady Aerodynamic Modelling for Flight Dynamics of Maneuverable Aircraft," AIAA Paper 2004-5276, Aug. 2004.

[6] Owens, D.B., Brandon, J.M., Croom, M.A., Fremaux, C.M., Heim, E.H., and Vicroy, D.D., "Overview of Dynamic Test Techniques for Flight Dynamics Research at NASA LaRC (Invited)," AIAA Paper 2006-3146, June. 2006.

[7] Tomek, D.M., Sewall, W.G., Mason, S.E., and Szchur, B.W.A., "The Next Generation of High-Speed Dynamic Stability Wind Tunnel Testing (Invited)," AIAA Paper 2003-3148, June. 2006.

[8] Vicroy, D.D., "Blended-Wing-Body Low-Speed Flight Dynamics: Summary of Ground Tests and Sample Results (Invited)," AIAA Paper 2009-933, Jan. 2009.

[9] Heim, E.H.D., and Brandon, J.M., "Uncertainty-Based Approach for Dynamic Aerodynamic Data Acquisition and Analysis," AIAA Paper 2004-5364, Aug. 2004.

[10] Kim, S., Murphy, P.C., and Klein, V., "Evaluation and Analysis of F-16XL Wind Tunnel Data from Dynamic Tests," AIAA Paper 2003-5396, Aug., 2003.

[11] de Silva, C.W., *Mechatronics: An Integrated Approach*, CRC Press, Boca Raton, 2005.

[12] Freeman, D.C., "Low Subsonic Flight and Force Investigation of a Supersonic Transport Model with a Highly Swept Arrow Wing," NASA-TN-D-3887, June 1967.

[13] Orlik-Ruckemann, K., "Review of Techniques for Determination of Dynamic Stability Parameters in Wind Tunnels," *Dynamic Stability* Parameters, AGARD-LS-114, May 1981.

[14] Grafton, S.B., and Libbey, C.E., "Dynamic Stability Derivatives of a Twin-Jet Fighter Model for Angles of Attack from -10° to 110°," NASA-TN-D-6091, Jan 1971.

[15] Chambers, J.R., and Grafton, S.B., "Static and Dynamic Longitudinal Stability Derivatives of a Powered 1/9-Scale Model of a Tilt-Wing V/STOL Transport," NASA-TN-D-3591, Sept 1966.

[16] Freeman, D.C., Grafton, S.B., and D'Amato, R., "Static and Dynamic Stability Derivatives of a Model of Jet Transport Equipped with External-Flow Jet-Augmented Flaps," NASA-TN-D-5408, Sept 1969.

[17] Grafton, S.B., and Anglin, E.L., "Dynamic Stability Derivatives at Angles-of-Attack from -5° to 90° for a Variable-Sweep Fighter Configuration with Twin Vertical Tails," NASA-TN-D-6909, Oct 1972.

[18] Grafton, S.B., "Low-Speed Wind Tunnel Study of the High-Angle-of-Attack Stability and Control Characteristics of a Cranked-Arrow-Wing Fighter Configuration," NASA-TM-85776, May 1984.

[19] Scherer, M., and Lopez, J., "Progres Realises dans les Techniques de Mesure des Derivees Aerodynamiques en Soufflerie Methode d'Oscillations Forcees," AGARD-CP-17, Sept 1966.

[20] Boyden, R.P., "Effects of Leading-Edge Vortex Flow on the Roll Damping of Slender Wings," *Journal of Aircraft*, Vol. 8, No. 7, 1971.

[21] Burt, G.E., "Forced-Oscillation Test Mechanism for Measuring Dynamic-Stability Derivatives in Roll," *Journal of Aircraft*, Vol. 12, No. 1, 1975.

[22] Burt, G.E., "Dynamic-Stability Measurement Capabilities in the AEDC Wind Tunnels," AGARD-B-2, 1976.

[23] Coulter, S.M., "Description of a New High-Alpha, High-Load, Pitch-Yaw Dynamic Stability Test Mechanism at AEDC," AIAA Paper 80-0451, March 1980.

[24] Decken, J., Schmidt, E., and Schulze, B., "On the Test Procedues of the Derivative Balances used in W. Germany," *AGARD FDP Symposium on Dynamic Stability Parameters*, Paper 6, 1978.

[25] Orlik-Ruckemann, K., "Half- and Full-Model Experiments on Slender Cones at Angles of Attack," *Journal of Spacecraft and Rockets*, Vol. 11, No. 9, Sept 1973.

[26] Davison, P.M., Di Bernardo, M., and Lowenberg, M.H., "Modeling and Control of a Single Degree-of-Freedom Dynamic Wind Tunnel Rig," *European Control Conference*, Cambridge, Sept 2003.

[27] Papageorgiou, G., and Glover, K., "Design, Development, and Control of the HIRM Wind Tunnel Model," *Proceedings of the 38th Conference on Decision and Control*, Arizona, Dec. 1999.

[28] Alemdaroglu, N., Uysal, H., Nackli, Y., and Sahin, T., "Roll Oscillatory Test in a Low Speed Wind Tunnel," AIAA Paper 2003-398, Jan. 2003.

[29] Loeser, T., and Bergmann, A., "Development of the Dynamic Wind Tunnel Testing Capabilities at DNW-NWB," AIAA Paper 2003-453, Jan. 2003.

[30] Rajamurthy, M., "Generation of Comprehensive Longitudinal Aerodynamic Data Using Dynamic Wind-Tunnel Simulation," *Journal of Aircraft*, Vol. 34, No. 1, 1997, pp. 29-33.

[31] Klein, V., Murphy, P.C., Curry, T.J., and Brandon, J.M., "Analysis of Wind Tunnel Longitudinal Static and Oscillatory Data of the F-16XL Aircraft," NASA-TM-97-206276, Dec 1997.

[32] Trieu, B.C., Tyler, T.R., Stewart, B.K., Charnock, J.K., Fisher, D.W., Heim, E.H., Brandon, J., and Grafton, S.B., "Development of a Forced Oscillation System for Measuring Dynamic Derivatives of Fluidic Vehicles," *38th Aerospace Mechanisms Symposium*, Langley Research Center, May 2006, pp. 387-399.

[33] Samardzic, Anastasijevic, Z., and Marinkoviski, D., "Some Experimental Results of Subsonic Derivative Obtained in the T-38 Wind Tunnel by Forced Oscillation," *Scientific Technical Review*, Vol. LVII, No. 3-4, 2007, pp. 83-86.

[34] Davison, P.M., Lowenberg, M.H., and di Bernardo, M., "Experimental Analysis and Modeling of Limit Cycles in a Dynamic Wind-Tunnel Rig," *Journal of Aircraft*, Vol. 40, No. 4, July-Aug 2003, pp. 776-785.

[35] Ahn, S., Choi, K.Y., and Simpson, R.L., "The Design and Development of a Dynamic Plunge-Pitch-Roll Model Mount," AIAA Paper 89-0048, 1989.

[36] Owens, D.B., Capone, F.J., Hall, R.M., Brandon, J.M., and Chambers, J.R., "Transonic Free-to-Roll Analysis of Abrupt Wing Stall on Military Aircraft," *Journal of Aircraft*, Vol. 41, No. 3, 2004, pp. 474-484.

[37] Capone, F.J., Owens, D.B., and Hall, R.M., "Development of a Transonic Free-to-Roll Test Capability," *Journal of Aircraft*, Vol. 41, No. 3, 2004, pp. 456-463.

[38] Balakrishna, S., Niranjana, T., Rajamurthy, M.S., Srinathkumar, S., Rajan, S.R., and Singh, S.K., "Estimation of Aerodynamic Derivatives using Dynamic Wind Tunnel Simulation Techniques," Deutschen Zentrums fur Luft- und Raumfahrt, Mitteilung 93-14, Brunswick, Germany, Dec. 1993, pp. 289-298.

[39] Kyle, H., "An Investigation into the use of a Pendulum Support Rig for Aerodynamic Modeling," Ph.D. Dissertation, Dept. of Aerospace Engineering, Univ. of Bristol, Bristol, UK, 2004.

[40] Bennett, R., Farmer, M., Mohr, R., and Hall, W., "Wind-Tunnel Technique for Determining Stability Derivatives from Cable-Mounted Models," *Journal of Aircraft*, Vol. 15, No. 5, 1978, pp. 304-310.

[41] Magill, J.C., Cataldi, P., Morency, J.R., Hammer, D.X., and Anderson, B.D., "Design of a Wire Suspension System for Dynamic Testing in AEDC 16T," AIAA Paper 2003-0452, Jan. 2003.

[42] Cook, M.V., "On the use of Small Aircraft Models for Dynamic Wind Tunnel Investigation of Stability and Control,"*Transactions of the Institute of Measurement and Control*, Vol. 1, No. 3, 1979, pp. 135-140.

[43] Subke, H., "Test Installations to Investigate the Dynamic Behavior of Aircraft with Scaled Models in Wind Tunnels," *Transactions of the Institute of Measurement and Control*, Vol. 1, No. 3, 1979, pp. 135-140.

[44] Jordan, F.L., and Hahne, D.E., "Wind-Tunnel Static and Free-Flight Investigation of High Angle of Attack Stability and Control Characteristics of a Model of the EA-6B Airplane," NASA-TP-3194, May 1992.

[45] Pedreiro, D., "Development of an Apparatus for Wind Tunnel Dynamic Experiments at High Alpha," NASA-CR-203713, Feb. 1997.

[46] Thompson, J.S., "Oscillatory-Derivative Measurements on Sting-Mounted Wind-Tunnel Models," ARC R&M 3355, July 1962.

[47] Thompson, J.S., "Oscillatory Derivative Measurements on Sting-Mounted Models at RAE, Beford," AGARD-CP-17, Sept. 1966.

[48] Bennett, R., Farmer, M., Mohr, R., and Hall, W., "Wind-Tunnel Technique for Determining Stability Derivatives from Cable-Mounted Models," *Journal of Aircraft*, Vol. 15, No. 5, 1978, pp. 304-310.

[49] Lowenberg, M.H., and Kyle, H., "Development of a Pendulum Support Rig Dynamic Wind Tunnel Apparatus," AIAA Paper 2002-4879, Aug. 2002.

[50] Gatto, A., "Application of a Pendulum Support Test Rig for Aircraft Stability Derivative Estimation," *Journal of Aircraft*, Vol. 46, No. 3, May-June 2009.

[51] Gatto, A., and Lowenberg, M.H., "Evaluation of a Three-Degree-of-Freedom Test Rig for Stability Derivative Estimation," *Journal of Aircraft*, Vol. 43, No. 6, Nov-Dec 2006.

[52] Sen, A., Bhange, N.P., Wahi, P., and Ghosh, A.K., "5-Degree-of-Freedom Dynamic Rig for Wind Tunnel Tests of Aerospace Vehicles," AIAA Paper 2009-5605, Aug. 2009.

[53] Beyers, M.E., "Interpretation of Experimental High-Alpha Aerodynamics – Implications for Flight Prediction," *Journal of Aircraft*, Vol. 32, No. 2, March –April 1995, pp.247-261.

[54] Ericsson, L.E., and Reding, J.P., "Review of Support Interference in Dynamic Tests," *AIAA Journal*, Vol. 21, No. 12, March 1983, pp. 1652-1666.

[55] Taylor, G.S., Gursul, I., and Greenwell, D.I., "Investigation of Support Interference in High-Angle-of-Attack Testing," *Journal of Aircraft*, Vol. 40, No. 1, Jan-Feb. 2003.

[56] Acum, W.E.A., "Interference Effects in Unsteady Experiments," AGARDograph 109, Oct. 1966.

[57] Beyers, M.E., "Unsteady Wind-Tunnel Interference in Aircraft Dynamic Experiments," *Journal of Aircraft*, Vol. 29, No. 6, 1992, pp. 1122-1129.

[58] Beyers, M.E., and Ericsson, L.E., "Ground Facility Interferences on Aircraft Configurations with Separated Flow," *Journal of Aircraft*, Vol. 30, No. 5, 1993, pp. 682-688.

[59] Polhamus, E.C., "A Review of Some Reynolds Number Effects Related to Bodies at High Angles of Attack," NASA-CR-3809, Aug. 1984.

[60] Barlow, J.B., Rae, W.H., and Pope, A., *Low-Speed Wind Tunnel Testing*, John Wiley & Sons, New York, 1999.

[61] Beyers, M.E., "Influence of Support Oscillation in Dynamic Stability Tests," *Journal of Aircraft*, Vol. 25, No. 2, Dec. 1983.

[62] Hanff, E.S., "Direct Forced-Oscillation Techniques for the Determination of Stability Derivatives in the Wind Tunnel,"AGARD-LS-114, 1981.

[63] Ericsson, L.E., "Another Look at High-Alpha Support Interference," AIAA Paper 90-0188, 1990.

[64] Tobak, M., "On the use of Indicial Function Concept in the Analysis of Unsteady Motions of Wings and Wing-Tail Combinations," NACA-1188, 1954.

[65] Tobak, M., and Schiff, L.B., "On the Formulation of the Aerodynamic Characteristics in Aircraft Dynamics," NASA-TR-R-456, Jan. 1976.

[66] Tobak, M., and Schiff, L.B., "The Role of Time-History Effects in the Formulation of the Aerodynamics of Aircraft Dynamics," AGARD-CP-235, May 1978.

[67] Tobak, M., and Schiff, L.B., "Aerodynamic Mathematical Modeling – Basic Concepts," AGARD-LS-114, March 1981.

[68] Tobak, M., and Schiff, L.B., "Some Applications of Aerodynamic Formulations to Problems in Aircraft Dynamics," AGARD-LS-114, March 1981.

[69] Goman, M., and Khrabrov, "State-Space Representation of Aerodynamic Characteristics of an Aircraft at High Angles of Attack," *Journal of Aircraft*, Vol. 31, No. 5, Sept-Oct. 1994, pp. 1109-1115.

[70] Lan, C.E., Li, J., Yau, W., and Brandon, J.M., "Longitudinal and Lateral-Directional Coupling Effects on Nonlinear Unsteady Aerodynamic Modeling from Flight Data," AIAA Paper 2002-4804, Aug. 2002.

[71] Lin, G.F., Songster, T., and Lan, C.E., "Effect of High-Alpha Unsteady Aerodynamics on Longitudinal Dynamics of an F-18 Configuration," AIAA Paper 95-3488CP, Aug. 1995.

[72] Alemdaroglu, N., Iyigun, I., Altun, M., Uysal, H., Quagliotti, F., and Guglieri, G., "Determination of Dynamic Stability Derivatives using Forced Oscillation Technique," AIAA Paper 02-13758, Jan. 2002.

[73] Klein, V., and Noderer, K.D., "Modeling of Aircraft Unsteady Aerodynamic Characteristics – Part 1: Postulated Models," NASA-TM-109120, May 1994.

[74] Klein, V., and Noderer, K.D., "Modeling of Aircraft Unsteady Aerodynamic Characteristics – Part 2: Parameters Estimated from Wind Tunnel Data," NASA-TM-110161, April 1995.

[75] Klein, V., and Murphy, P.C., "Estimation of Aircraft Nonlinear Unsteady Parameters from Wind Tunnel Data," NASA-TM-98-208969, 1998.

[76] Klein, V., and Murphy, P.C., "Estimation of Aircraft Unsteady Aerodynamic Parameters from Dynamic Wind Tunnel Testing," AIAA Paper 2001-4016,

[77] Klein, V., "Modeling of Longitudinal Unsteady Aerodynamics at High Incidence with Account of Wing-Tail Interaction," NASA-CR-1999-209547, Sept. 1999.

[78] Box, G.E.P., and Wilson, K.G., "On the Experimental Attainment of Optimum Conditions," *Journal of the Royal Statistical Society*, B, Vol. 13, 1951, pp. 1-45.

[79] Taguchi, G., and Wu, Y., *Introduction to Off-Line Quality Control*, Central Japan Quality Control Association, Nagoya, Japan, 1980.

[80] Taguchi, G., *System of Experimental Design: Engineering Methods to Optimize Quality and Minimize Cost*, UNIPUB, White Plains, NY, 1987.

[81] Taguchi, G., *Introduction to Quality Engineering*, Asian Productivity Organization, UNIPUB, White Plains, NY, 1987.

[82] DeLoach, R., "Applications of Modern Experiment Design to Wind Tunnel Testing at NASA Langley Research Center," AIAA Paper 98-0713, Jan. 1998a.

[83] DeLoach, R., "Tailoring Wind Tunnel Data Volume Requirements Through the Formal Design of Experiments," AIAA Paper 98-2884, Jan. 1998b.

[84] DeLoach, R., "Improved Quality in Aerospace Testing Through the Modern Design of Experiments," AIAA Paper 2000-0825, Jan. 2000.

[85] DeLoach, R., and Cler, D.L., "Fractional Factorial Experiment Designs to Minimize Configuration Changes in Wind Tunnel Testing," AIAA Paper A02-142129, Jan. 2002.

[86] DeLoach, R., and Berrier, B.L., "Productivity and Quality Enhancements in a Configuration Aerodynamics Test using the Modern Design of Experiments," AIAA Paper 2004-1145, Jan. 2004.

[87] Simpson, J., Landman, D., Giroux, R., Zeisset, M., Hall, B., and Rhew, R., "Calibrating Large Capacity Aerodynamic Force Balances using Response Surface Methods," AIAA Paper 2005-7601, Dec. 2005.

[88] Landman, D., Simpson, J., Mariani, R., Ortiz, F., and Britcher, C., "A High Performance Aircraft Wind Tunnel Test using Response Surface Methodologies," AIAA Paper 2005-7602, Dec. 2005.

[89] Landman, D., Simpson, J., Vicroy, D., and Parker, P., "Efficient Methods for Complex Aircraft Configuration Aerodynamic Characterization using Response Methodologies," AIAA 2006-992, Jan. 2006.

[90] Stevens, B.L., and Lewis, F.L., *Aircraft Control and Simulation*, 2nd ed., John Wiley & Sons, New Jersey, 2003.

[91] Stengel, R.F., *Flight Dynamics*, Princeton University Press, New Jersey, 2004.

[92] Schmidt, L.V., *Introduction to Aircraft Flight Dynamics*, AIAA Education Series, Virginia, 1998.

[93] Etkin, B., *Dynamics of Atmospheric Flight*, Dover Publications, New York, 2005.

[94] Etkin, B., and Reid, L.D., *Dynamics of Flight: Stability and Control*, 3rd ed., John Wiley & Sons, New Jersey, 1996.

[95] Heim, E., Personal Communication.

[96] Paddock, D.A., "Bent Stings for NASA LaRC 12' LSWT," NASA Internal Report – Mechanical Systems Branch, Nov. 2005.

[97] Ohm, D.Y., "Dynamic Model of Induction Motors for Vector Control," *Technical Articles* [online], Drivtech, Inc., http://www.drivetechinc.com/id16.html

[98] Krause, P.C., and Thomas, C.H., "Simulation of Symmetrical Induction Machinery," *IEEE Transactions on Power Apparatus and Systems*, IEEE, Vol. 84, No. 11., Nov. 1965, pp. 1038-1053.

[99] Riaz, M., "Simulation of Electric Machine and Drive Systems using Matlab and Simulink," *University of Minnesota* [online], Dept. of Electrical and Computer Engineering, http://www.ece.umn.edu/users/riaz/

[100] Krause, P.C., Wasynczuk, O., and Sudoff, S.C., *Analysis of Electric Machinery and Drive Systems*, 2nd ed., IEEE-Press, 2002.

[101] Tez, E.S., "A Simple Understand of Field-Orientation for AC Motor Control," *IEEE Colloquium: Vector Control and Direct Torque Control of Induction Motors* [online], http://ieeexplore.ieee.org/stamp/stamp.jsp?arnumber=00496004

[102] Boonchiam, P., "Electrical Drive Notes – Lectures 9-11," *Lecture/Notes*, University of Technology Thanyaburi [online], http://web.en.rmutt.ac.th/ee/psrc

[103] Holtz, J., "Pulsewidth Modulation – A Survey," *IEEE* [online], http://ieeexplore.ieee.org/stamp/stamp.jsp?tp=&arnumber=254685&userType=inst

[104] Callender, A., Hartree, D.R., and Porter, A., "Time-lag in a Control System," *Philosophical Transactions of the Royal Society of London*, Cambridge University Press, London, 1936, pp. 415-444.

[105] Franklin, G.F., Powell, J.D., Emami-Naeini, A., *Feedback Control of Dynamic Systems*, 6th ed., Pearson Hall, New Jersey, 2010.

[106] Johnson, M.A., and Moradi, M.H., ed., *PID Control: New Identification and Design Methods*, Springer, New York, 2005.

[107] Ellis, G., *Control System Design Guide: Using Your Computer to Understand and Diagnose Feedback Controllers*, 3rd ed, Academic Press, New York, 2004.

[108] Astrom, K.J., and Hagglund, T., "PID Control," *Control System Fundamentals*, 1st ed., CRC Press, Florida, 1999, pp. 198-209.

[109] Wilkie, J., Johnson, M., and Katebi, R., *Control Engineering – An Introductory Course*, 1st ed., Palgrave, New York 2002.

[110] Serikitkankul, P., Seki, H., Hikizu, M., and Kamiya, Y., "The Effects of Controller Saturation on Dynamic Characteristics of Commericial Positioning Systems and their Countermeasures," *SICE-ICASE Internation Joint Conference*, Korea, Oct. 2006.

[111] Serikitkankul, P., Seki, H., Hikizu, M., and Kamiya, Y., "Current Limiter Complicates the Dynamic Characteristics of Servo Motor," *Mechatronics for Safety, Security, and Dependability in a New Era*, Elsevier, 2007.

[112] de Marchi, J.A., "Modeling of Dynamic Friction, Impact Backlash, and Elastic Compliance Nonlinearities in Machine Tools, with Applications to Asymmetric Viscous and Kinetic Friction Identification," Ph.D. Dissertation, Resselaer Polytechnic Institute, Dec. 1998.

[113] Craig, K., "Modeling, Analysis, and Control of Compliantly-Coupled Systems," *Mechatronics - Lecture/Notes* [online], Resselaer Polytechnic Institute, http://www.eng.mu.edu/~craigk/mech_notes.htm

[114] Ellis, G., "Cures for Mechanical Resonance in Industrial Servo Systems," Kollmorgen, A Danaher Motion Company [online], http://www.kollmorgen.com/website/common/img/mimetype/pcim2001resonance.pdf

[115] Gopal, M., *Control Systems: Principles and Design*, 2nd ed., McGraw-Hill Higher Education, Boston, 2002.

[116] Carter, W.C., "Mechanical Factors Affecting Electrical Drive Performance," IEEE Transactions on Industry and General Applications, Vol. IGA-5, No. 3, May-June 1969, pp. 282-290.

[117] Litak, G., and Friswell, M.I., "Vibration in Gear Systems," Chaos, Solitons, and Fractals, Pergamon, Vol. 16, 2003, pp. 795-800.

[118] Ozpineci, B., and Tolbert, L.M., "Simulink Implementation of Induction Machine Model – A Modular Approach," *IEEE* [online], 2003, http://power.eecs.utk.edu/pubs/iemdc_2003_im_model_updated.pdf

[119] Katz, J., and Plotkin, A., *Low-Speed Aerodynamics*, 2nd ed., Cambridge Aerospace Series, Cambridge, 2001.

[120] Murphy, J.M.D., and Turnbull, F.G., *Power Electronic Control of AC Motors*, Peragmon Press, Oxford, 1988.

[121] Schlesinger, S., et. al. "Terminology for Model Credibility," *Simulation* [online], Vol. 32, No. 103, 1979, http://sim.sagepub.com/cgi/reprint/32/3/103

[122] Schruben, L.W., "Establishing the credibility of Simulation Models," *Simulation*, Vol. 34, No. 3, 1980.

[123] Law, A.M., *Simulation Modeling and Analysis*, 4th ed., McGraw-Hill, New York, 2006.

[124] Kleijnen, J.P.C., "Statistical Validation of Simulation Models," *European Journal of Operational Research*, Vol. 85, 1995, pp. 21-34.

[125] Sargent, R.G., "Verification and Validation of Simulation Models," *Proceedings of the 2001 Winter Simulation Conference*, IEEE, 2005, pp. 130-143.

[126] Sargent, R.G., "Verification and Validation of Simulation Models," *Proceedings of the 2007 Winter Simulation Conference*, IEEE, 2007, pp. 124-137.

[127] Oberkampf, W.L., Trucano, T.G., and Hirsch, C., "Verification, Validation, and Predictive Capability in Computational Engineering and Physics," *Applied Mechanical Review*, ASME, Vol. 54, No. 5, Sept. 2004, pp. 345-384.

[128] Balci, O., and Sargent, R.G., "Validation of Multivariate Response Simulation Models by using Hoteling's Two-Sample T^2 Test," *Simulation*, Vol. 39, No. 6, 1982a, pp. 185-192.

[129] Balci, O., and Sargent, R.G., "Some Examples of Simulation Model Validation using Hypothesis Testing," *Proceedings of the 1982 Winter Simulation Conference*, IEEE, 1982b, pp. 620-629.

[130] Balci, O., "Verification, Validation, and Accreditation of Simulation Models," *Proceedings of the 1997 Winter Simulation Conference*, IEEE, 1997, pp. 135-141.

[131] Naylor, T.H., and Finger, J.M., "Verification of Computer Simulation Models," *Management Science*, Vol. 14, No. 2, Oct. 1967.

[132] Chapra, S.C., and Canale, R.P., *Numerical Methods for Engineers*, McGraw-Hill, New York, 2001.

[133] Montgomery, D.C., *Design and Analysis of Experiments*, 7th ed., John Wiley & Sons, New Jersey, 2008.

[134] Myers, R.H., and Montgomery, D.C., *Response Surface Methodology: Process and Product Optimization using Designed Experiments*, 2nd ed., Wiley-Interscience Publication, New Jersey, 2002.

[135] Landman, D., Simpson, J., Mariani, R., Ortiz, F., and Britcher, C., "Hybrid Design for Aircraft Wind-Tunnel Testing using Response Surface Methodolgies," *Journal of Aircraft*, Vol. 44, No. 4, July-Aug. 2007.

[136] Data Sheet, "Speed Reducer Backlash" *Peerless-Winsmith Inc* [online], pp. 230-231, www.winsmith.com

[137] Barton, R.R., "Metamodels for Simulation Input-Output Relations," *Proceedings of the 1992 Winter Simulation Conference*, IEEE, 1992, pp. 289-299.

[138] Barton, R.R., "Metamodeling: A State of the Art Review," *Proceedings of the 1994 Winter Simulation Conference*, IEEE, 1994, pp. 237-244.

[139] Simpson, T.W., Peplinski, J.D., Koch, P.N., and Allen J.K., "On the use of Statistics in Design and the Implications for Deterministic Computer Experiments," *1997 ASME Design Engineering Technical Conferences*, Sept. 1997.

[140] Montgomery, D.C., Peck, E.A., and Vining, G.G., *Introduction to Linear Regression Analysis*, 3rd ed., John Wiley & Son, New York, 2001.

[141] Sacks, J., Schiller, S.B., and Welch, W.J., "Designs for Computer Experiments," *Technometrics*, Vol. 31, No. 1, Feb. 1989.

[142] Kleijnen, J.P.C., "Statistics and Deterministic Simulation Models: Why Not?," *Proceedings of the 1990 Winter Simulation Conference*, IEEE, 1990, pp. 344-346.

[143] Kleijnen, J.P.C., "Simulation Experiments in Practice: Statistical Design and Regression Analysis," *Journal of Simulation*, Vol. 2, 2008, pp. 19-27.

[144] Snee, R.D., "Validation of Regression Models: Methods and Examples," *Technometrics*, Vol. 19, No. 4, Nov. 1977, pp. 415-428.

[145] Martinez, W.L., and Martinez, A.R., *Computational Statistics Handbook with Matlab*, 2nd ed., Chapman & Hall, Boca Raton, 2008.

[146] Coleman, H.W., and Steele, W.G., *Experimentation, Validation, and Uncertainty Analysis for Engineers*, 3rd ed., John Wiley & Sons, New York, 2009.

APPENDIX A

EXPERIMENTAL TABULATED DATA FOR F16-XL AIRCRAFT FORCED OSCILLATION WIND TUNNEL TEST

Table 32: Variation of static coefficient due to angle of attack for 10% F16-XL aircraft [4]

PT	ALPHA [deg]	QBAR [psf]	CNORMAL [--]	CAXIAL [--]	CPITCHM [--]	CROLLM [--]	CYAWM [--]	CSIDEF [--]	CLIFT [--]	CDRAG [--]
1	-4	3.9775	-0.1022	0.0281	0.0201	-0.0067	0.0008	0.0012	-0.1	0.0352
2	0	3.9932	0.0535	0.023	0.0242	-0.0061	0	0.0026	0.0535	0.023
3	5	4.0082	0.2612	0.0136	0.0441	-0.007	-0.0007	0.0049	0.259	0.0363
4	10	3.9786	0.5058	0.0027	0.0733	-0.0088	-0.0002	0.0054	0.4977	0.0905
5	15	3.9484	0.7714	-0.0073	0.1107	-0.008	0.0001	0.0075	0.747	0.1926
6	20	3.9424	1.0335	-0.0182	0.153	-0.0089	0.0001	0.0084	0.9774	0.3364
7	22	3.9499	1.1269	-0.0253	0.1685	-0.0092	0.0003	0.0083	1.0544	0.3987
8	24	3.9044	1.2416	-0.0309	0.1858	-0.0093	-0.0002	0.0103	1.1468	0.4767
9	26	3.921	1.3256	-0.0354	0.2009	-0.0098	-0.0008	0.0098	1.207	0.5492
10	28	3.9001	1.3993	-0.0368	0.2161	-0.0098	-0.001	0.0108	1.2528	0.6244
11	30	3.8678	1.448	-0.037	0.2244	-0.01	-0.0004	0.011	1.2726	0.6919
12	32	3.8489	1.4839	-0.0368	0.2256	-0.0077	0.0002	0.0131	1.278	0.7551
13	34	3.8535	1.5012	-0.0365	0.2214	-0.0048	-0.0011	0.0142	1.265	0.8091
14	36	3.8606	1.5046	-0.0366	0.2183	-0.0004	-0.0039	0.0079	1.2388	0.8547
15	38	3.85	1.5115	-0.0377	0.2186	-0.0015	-0.0037	0.0104	1.2143	0.9008
16	40	3.8249	1.4546	-0.0317	0.1995	-0.0028	-0.0019	0.0161	1.1347	0.9107
17	45	3.8498	1.284	-0.0248	0.1867	-0.0034	0.0011	0.0149	0.9255	0.8904
18	50	3.8769	1.2674	-0.03	0.1793	-0.0042	0.0006	0.0096	0.8377	0.9516
19	60	3.8193	1.3642	-0.0439	0.1578	-0.0061	-0.007	0.0024	0.7202	1.1594
20	70	3.7771	1.4411	-0.0504	0.1208	-0.0028	-0.0001	0.0136	0.5403	1.3369
21	80	3.9599	1.4643	-0.0412	0.0594	-0.0026	-0.0052	0.0441	0.295	1.4348

Table 33: In-phase and out-of-phase components of lift coefficient [4]

Component	alpha [deg]	k = 0.081	k = 0.135	k = 0.190	k = 0.237	k = 0.397
$\overline{C}_{L_\alpha}$	20.8	2.7173	2.7262	2.7169	2.6812	2.7182
	25.9	2.0605	2.3022	2.4510	2.4699	2.6217
	30.8	1.0483	1.5909	1.8777	1.9985	2.1274
	35.8	0.4157	1.0925	1.2745	1.4028	1.6543
	40.8	0.3572	0.7653	0.9657	1.0359	1.2423
	45.9	-0.1074	0.3471	0.4584	0.6013	0.9278
	50.8	-0.2827	0.0172	0.2680	0.2907	0.4220
	55.9	-0.5163	-0.3175	-0.1771	-0.0864	0.0863
	61.1	-0.7259	-0.6200	-0.4795	-0.4348	-0.2624
$\overline{C}_{L_q}$	20.8	0.6274	-0.6749	-0.4411	-0.4391	0.1617
	25.9	6.8878	2.8420	1.3282	0.5986	0.4959
	30.8	13.4790	6.8415	3.5802	2.3319	1.0400
	35.8	17.0380	7.8742	4.5156	3.2101	1.4278
	40.8	18.0300	7.8265	4.2304	2.9332	1.4082
	45.9	10.8080	5.3759	3.5004	2.2017	1.2853
	50.8	7.3799	3.6589	2.0937	1.2329	0.6319
	55.9	4.0848	2.6166	1.5641	1.0655	0.2893
	61.1	3.5036	1.7856	1.3260	1.0968	0.2086

Table 34: In-phase and out-of-phase pitching moment coefficient [4]

Component	alpha [deg]	k = 0.081	k = 0.135	k = 0.190	k = 0.237	k = 0.397
$\overline{C}_{m_\alpha}$	20.8	0.5183	0.5096	0.5076	0.5013	0.4656
	25.9	0.4529	0.4775	0.4937	0.4941	0.5023
	30.8	0.1901	0.2764	0.3429	0.3668	0.3865
	35.8	0.1090	0.2378	0.2325	0.2419	0.2278
	40.8	0.1509	0.1682	0.1318	0.1336	0.0124
	45.9	0.0323	0.0706	0.0253	0.0458	-0.0816
	50.8	-0.0921	-0.0733	0.0041	0.0489	0.0633
	55.9	-0.1755	-0.1386	-0.1546	-0.6012	0.1958
	61.1	-0.2081	-0.1714	-0.1520	-0.1195	0.1636
$\overline{C}_{m_q}$	20.8	-0.8553	-1.1161	-1.0749	-1.0589	-1.0527
	25.9	-0.1240	-0.7076	-0.8825	-0.9685	-1.0761
	30.8	1.7197	0.4942	-0.1789	-0.2611	-0.7195
	35.8	2.3630	0.5519	-0.3245	-0.4752	-0.7640
	40.8	1.3537	-0.3968	-0.7955	-0.7878	-0.6640
	45.9	-0.1715	-0.5400	-0.4869	-0.6901	-0.6076
	50.8	0.3532	-0.0418	0.0527	-0.1078	-0.4099
	55.9	0.0235	0.1021	0.1407	0.1023	-0.2927
	61.1	-0.0310	0.0538	0.0567	0.2266	0.0463

APPENDIX B

STATIC AND DYNAMIC COEFFICIENT RESPONSES

MATLAB CODE

STATIC COEFFICIENT RESPONSES

```
%{
FILENAME: NASAdata_static.m

AUTHOR:   Brianne Williams

PURPOSE:  Plots static experimental responses from NASA data (see reference).

REFERENCES: NASA/TM-97-206276

NOTES: none.
%}

clc;
close all;

alpha = [-4 0 5 10 15 20 22 24 26 28 30 32 34 36 38 40 45 50 60 70 80];

% Static effect of angle of attack on lift coefficient
CL = [-0.1 0.0535 0.259 0.4977 0.747 0.9774 1.0543 1.1468 1.207 ...
        1.2529 1.2726 1.278 1.265 1.2388 1.2143 1.1347 0.9255 0.8377 ...
        0.7202 0.5403 0.2950];

figure(1),plot(alpha,CL,'-b','LineWidth',2),grid on,...
    xlabel('\alpha [deg]'),ylabel('Lift Coefficient'),...
    axis auto;

% Static effect of angle of attack on normal-force coefficient
CN = [-0.1022 0.0535 0.2612 0.5058 0.7714 1.0335 1.1269 1.2416 ...
        1.3256 1.3993 1.4480 1.4839 1.5012 1.5046 1.5115 1.4546 ...
        1.284 1.2674 1.3642 1.4411 1.4643];

figure(2),plot(alpha,CN,'-b','LineWidth',2),grid on,...
    xlabel('\alpha [deg]'),ylabel('Normal Force Coefficient'),...
    axis auto;

% Static effect of angle of attack on pitching moment coefficient
CM = [0.0201 0.0242 0.0441 0.0733 0.1107 0.1530 0.1685 0.1858 ...
        0.2009 0.2161 0.2244 0.2256 0.2214 0.2183 0.2186 0.1995 ...
        0.1867 0.1793 0.1578 0.1208 0.0594];

figure(3),plot(alpha,CM,'-b','LineWidth',2),grid on,...
    xlabel('\alpha [deg]'),ylabel('Pitching Moment Coefficient'),...
    axis auto;
```

DYNAMIC COEFFICIENT RESPONSES

```
%{
FILENAME: NASAdata_dynamic.m

AUTHOR:   Brianne Williams

PURPOSE:  Validation of simulation responses. Comparison of experimental
            results with simulation response results.

REFERENCES: NASA/TM-97-206276

NOTES: none.
%}

clc;
clear all;
close all;
format long;

% F16XL Aircraft Geometry
S = 0.557;                          % Wing Area [m^2]
b = 0.988;                          % Wing Span [m]
cbar = 0.753;                       % Mean Aerodynamic Chord [m]
Xcg = 0.558*cbar;                   % Reference Center of Gravity Location [m]
alphaA = 5*pi/180;                  % Oscillating Amplitude [rad]

% Test Conditions
q = 192;                            % Dynamic Pressure [Pa]
rho = 1.225;                        % Density [kg/m^3]
U = sqrt(2*q/rho);                  % Freestream Velocity [m/s]

% Dynamic Results from NASA/TM-97-206276 Tables 5-7 (pg. 22-24)
alpha = [20.8 25.9 30.8 35.8 40.8 45.9 50.8 55.9 61.1];             % angle of
attack [deg]

CLalpha_bar1 = [2.7173 2.0605 1.0483 0.4157 0.3572 -0.1074 -0.2827 -0.5163 -
0.7259];    % k = 0.081
CLalpha_bar2 = [2.7262 2.3022 1.5909 1.0925 0.7653 0.3471 0.0172 -0.3175 -0.6200];
% k = 0.135
CLalpha_bar3 = [2.7169 2.4510 1.8777 1.2745 0.9657 0.4584 0.2680 -0.1771 -0.4795];
% k = 0.190
figure(1),plot(alpha,CLalpha_bar1,'*--
b',alpha,CLalpha_bar2,'+:r',alpha,CLalpha_bar3,'x-k'),...
    xlabel('\alpha [deg]'),ylabel('C_L_\alpha (bar)'),...
    title('In-phase Component of Lift Coefficient'),...
    legend('k = 0.081','k = 0.135','k = 0.190'),grid on;

CLq_bar1 = [0.6274 6.8878 13.4790 17.0380 18.0300 10.8080 7.3799 4.0848 3.5036];
% k = 0.081
CLq_bar2 = [-0.6749 2.8420 6.8415 7.8742 7.8265 5.3759 3.6589 2.6166 1.7856];
% k = 0.135
CLq_bar3 = [-0.4411 1.3282 3.5802 4.5156 4.2304 3.5004 2.0937 1.5641 1.3260];
% k = 0.190
figure(2),plot(alpha,CLq_bar1,'*--b',alpha,CLq_bar2,'+:r',alpha,CLq_bar3,'x-k'),...
    xlabel('\alpha [deg]'),ylabel('C_L_q (bar)'),...
    title('Out-of-phase Component of Lift Coefficient'),...
    legend('k = 0.081','k = 0.135','k = 0.190'),grid on;

CMalpha_bar1 = [0.5183 0.4529 0.1901 0.1090 0.1509 0.0323 -0.0921 -0.1755 -0.2081];
% k = 0.081
CMalpha_bar2 = [0.5096 0.4775 0.2764 0.2378 0.1682 0.0706 -0.0733 -0.1386 -0.1714];
% k = 0.135
CMalpha_bar3 = [0.5076 0.4937 0.3429 0.2325 0.1318 0.0253 0.0041 -0.1546 -0.1520];
% k = 0.190
figure(3),plot(alpha,CMalpha_bar1,'*--
b',alpha,CMalpha_bar2,'+:r',alpha,CMalpha_bar3,'x-k'),...
    xlabel('\alpha [deg]'),ylabel('C_m_\alpha (bar)'),...
    title('In-phase Component of Pitching-Moment Coefficient'),...
    legend('k = 0.081','k = 0.135','k = 0.190'),grid on;

CMq_bar1 = [-0.8553 -0.1240 1.7197 2.3630 1.3537 -0.1715 0.3532 0.0235 -0.0310];
% k = 0.081
CMq_bar2 = [-1.1161 -0.7076 0.4942 0.5519 -0.3968 -0.5400 -0.0418 0.1021 0.0538];
% k = 0.135
```

```
CMq_bar3 = [-1.0749 -0.8825 -0.1789 -0.3245 -0.7955 -0.4869 0.0527 0.1407 0.0567];
% k = 0.190
figure(4),plot(alpha,CMq_bar1,'*--b',alpha,CMq_bar2,'+:r',alpha,CMq_bar3,'x-k'),...
    xlabel('\alpha [deg]'),ylabel('C_m_q (bar)'),...
    title('Out-of-phase Component of Pitching-Moment Coefficient'),...
    legend('k = 0.081','k = 0.135','k = 0.190'),grid on;

alpha0 = [20.8 25.9 30.8];

c1 = load('M065R577.mat');
k = 0.081;
w = 2*pi*0.6;
T = (2*pi)/w;
t = c1.DATA(131:631,1) - c1.DATA(131,1);
tend = max(t);
nc = tend/T;
CLdyn1 = c1.DATA(131:631,10) - mean(c1.DATA(131:631,10));
CMdyn1 = c1.DATA(131:631,6) - mean(c1.DATA(131:631,6));
CLalpha_bar1 = (2/(alphaA*nc*T))*trapz(t,CLdyn1.*sin(w*t));
CLq_bar1 = (2/(alphaA*k*nc*T))*trapz(t,CLdyn1.*cos(w*t));
CMalpha_bar1 = (2/(alphaA*nc*T))*trapz(t,CMdyn1.*sin(w*t));
CMq_bar1 = (2/(alphaA*k*nc*T))*trapz(t,CMdyn1.*cos(w*t));
clear c1;

c2 = load('M065R602.mat');
k = 0.081;
w = 2*pi*0.6;
T = (2*pi)/w;
t = c2.DATA(131:631,1) - c2.DATA(131,1);
tend = max(t);
nc = tend/T;

CLdyn2 = c2.DATA(131:631,10) - mean(c2.DATA(131:631,10));
CMdyn2 = c2.DATA(131:631,6) - mean(c2.DATA(131:631,6));

CLalpha_bar2 = (2/(alphaA*nc*T))*trapz(t,CLdyn2.*sin(w*t));
CLq_bar2 = (2/(alphaA*k*nc*T))*trapz(t,CLdyn2.*cos(w*t));

CMalpha_bar2 = (2/(alphaA*nc*T))*trapz(t,CMdyn2.*sin(w*t));
CMq_bar2 = (2/(alphaA*k*nc*T))*trapz(t,CMdyn2.*cos(w*t));
clear c2;

c3 = load('M065R627.mat');
k = 0.081;
w = 2*pi*0.6;
T = (2*pi)/w;
t = c3.DATA(131:631,1) - c3.DATA(131,1);
tend = max(t);
nc = tend/T;
CLdyn3 = c3.DATA(131:631,10) - mean(c3.DATA(131:631,10));
CMdyn3 = c3.DATA(131:631,6) - mean(c3.DATA(131:631,6));
CLalpha_bar3 = (2/(alphaA*nc*T))*trapz(t,CLdyn3.*sin(w*t));
CLq_bar3 = (2/(alphaA*k*nc*T))*trapz(t,CLdyn3.*cos(w*t));
CMalpha_bar3 = (2/(alphaA*nc*T))*trapz(t,CMdyn3.*sin(w*t));
CMq_bar3 = (2/(alphaA*k*nc*T))*trapz(t,CMdyn3.*cos(w*t));
clear c3;

c4 = load('M065R582.mat');
k = 0.135;
w = 2*pi*1;
T = (2*pi)/w;
t = c4.DATA(58:358,1) - c4.DATA(58,1);
tend = max(t);
nc = tend/T;
CLdyn4 = c4.DATA(58:358,10) - mean(c4.DATA(58:358,10));
CMdyn4 = c4.DATA(58:358,6) - mean(c4.DATA(58:358,6));
CLalpha_bar4 = (2/(alphaA*nc*T))*trapz(t,CLdyn4.*sin(w*t));
CLq_bar4 = (2/(alphaA*k*nc*T))*trapz(t,CLdyn4.*cos(w*t));
CMalpha_bar4 = (2/(alphaA*nc*T))*trapz(t,CMdyn4.*sin(w*t));
CMq_bar4 = (2/(alphaA*k*nc*T))*trapz(t,CMdyn4.*cos(w*t));
clear c4;

c5 = load('M065R607.mat');
k = 0.135;
w = 2*pi*1.00;
T = (2*pi)/w;
t = c5.DATA(63:363,1) - c5.DATA(63,1);
tend = max(t);
nc = tend/T;
```

```
mu = mean(c5.DATA(63:363,6))
CLdyn5 = c5.DATA(63:363,10) - mean(c5.DATA(63:363,10));
CMdyn5 = c5.DATA(63:363,6) - mean(c5.DATA(63:363,6));
figure,plot(t,CMdyn5)
CLalpha_bar5 = (2/(alphaA*nc*T))*trapz(t,CLdyn5.*sin(w*t));
CLq_bar5 = (2/(alphaA*k*nc*T))*trapz(t,CLdyn5.*cos(w*t));
CMalpha_bar5 = (2/(alphaA*nc*T))*trapz(t,CMdyn5.*sin(w*t));
CMq_bar5 = (2/(alphaA*k*nc*T))*trapz(t,CMdyn5.*cos(w*t))
clear c5;

c6 = load('M065R632.mat');
k = 0.135;
w = 2*pi*1;
T = (2*pi)/w;
t = c6.DATA(58:358,1) - c6.DATA(58,1);
tend = max(t);
nc = tend/T;
CLdyn6 = c6.DATA(58:358,10) - mean(c6.DATA(58:358,10));
CMdyn6 = c6.DATA(58:358,6) - mean(c6.DATA(58:358,6));
CLalpha_bar6 = (2/(alphaA*nc*T))*trapz(t,CLdyn6.*sin(w*t));
CLq_bar6 = (2/(alphaA*k*nc*T))*trapz(t,CLdyn6.*cos(w*t));
CMalpha_bar6 = (2/(alphaA*nc*T))*trapz(t,CMdyn6.*sin(w*t));
CMq_bar6 = (2/(alphaA*k*nc*T))*trapz(t,CMdyn6.*cos(w*t));
clear c6;

c7 = load('M065R587.mat');
k = 0.190;
w = 2*pi*1.41;
T = (2*pi)/w;
t = c7.DATA(100:313,1) - c7.DATA(100,1);
tend = max(t);
nc = tend/T;
CLdyn7 = c7.DATA(100:313,10) - mean(c7.DATA(100:313,10));
CMdyn7 = c7.DATA(100:313,6) - mean(c7.DATA(100:313,6));
CLalpha_bar7 = (2/(alphaA*nc*T))*trapz(t,CLdyn7.*sin(w*t));
CLq_bar7 = (2/(alphaA*k*nc*T))*trapz(t,CLdyn7.*cos(w*t));
CMalpha_bar7 = (2/(alphaA*nc*T))*trapz(t,CMdyn7.*sin(w*t));
CMq_bar7 = (2/(alphaA*k*nc*T))*trapz(t,CMdyn7.*cos(w*t));
clear c7;

c8 = load('M065R612.mat');
k = 0.190;
w = 2*pi*1.41;
T = (2*pi)/w;
t = c8.DATA(100:313,1) - c8.DATA(100,1);
tend = max(t);
nc = tend/T;
CLdyn8 = c8.DATA(100:313,10) - mean(c8.DATA(100:313,10));
CMdyn8 = c8.DATA(100:313,6) - mean(c8.DATA(100:313,6));
CLalpha_bar8 = (2/(alphaA*nc*T))*trapz(t,CLdyn8.*sin(w*t));
CLq_bar8 = (2/(alphaA*k*nc*T))*trapz(t,CLdyn8.*cos(w*t));
CMalpha_bar8 = (2/(alphaA*nc*T))*trapz(t,CMdyn8.*sin(w*t));
CMq_bar8 = (2/(alphaA*k*nc*T))*trapz(t,CMdyn8.*cos(w*t));
clear c8;

c9 = load('M065R637.mat');
k = 0.190;
w = 2*pi*1.41;
T = (2*pi)/w;
t = c9.DATA(100:313,1) - c9.DATA(100,1);
tend = max(t);
nc = tend/T;
CLdyn9 = c9.DATA(100:313,10) - mean(c9.DATA(100:313,10));
CMdyn9 = c9.DATA(100:313,6) - mean(c9.DATA(100:313,6));
CLalpha_bar9 = (2/(alphaA*nc*T))*trapz(t,CLdyn9.*sin(w*t));
CLq_bar9 = (2/(alphaA*k*nc*T))*trapz(t,CLdyn9.*cos(w*t));
CMalpha_bar9 = (2/(alphaA*nc*T))*trapz(t,CMdyn9.*sin(w*t));
CMq_bar9 = (2/(alphaA*k*nc*T))*trapz(t,CMdyn9.*cos(w*t));
clear c9;

figure(1),hold on,...
    plot(alpha0(1),CLalpha_bar1,'ob','MarkerFaceColor','b'),...
    plot(alpha0(2),CLalpha_bar2,'ob','MarkerFaceColor','b'),...
    plot(alpha0(3),CLalpha_bar3,'ob','MarkerFaceColor','b'),...
    plot(alpha0(1),CLalpha_bar4,'sr','MarkerFaceColor','r'),...
    plot(alpha0(2),CLalpha_bar5,'sr','MarkerFaceColor','r'),...
    plot(alpha0(3),CLalpha_bar6,'sr','MarkerFaceColor','r'),...
    plot(alpha0(1),CLalpha_bar7,'dk','MarkerFaceColor','k'),...
    plot(alpha0(2),CLalpha_bar8,'dk','MarkerFaceColor','k'),...
```

```
    plot(alpha0(3),CLalpha_bar9,'dk','MarkerFaceColor','k'),...
    hold off;

figure(2),hold on,...
    plot(alpha0(1),CLq_bar1,'ob','MarkerFaceColor','b'),...
    plot(alpha0(2),CLq_bar2,'ob','MarkerFaceColor','b'),...
    plot(alpha0(3),CLq_bar3,'ob','MarkerFaceColor','b'),...
    plot(alpha0(1),CLq_bar4,'sr','MarkerFaceColor','r'),...
    plot(alpha0(2),CLq_bar5,'sr','MarkerFaceColor','r'),...
    plot(alpha0(3),CLq_bar6,'sr','MarkerFaceColor','r'),...
    plot(alpha0(1),CLq_bar7,'dk','MarkerFaceColor','k'),...
    plot(alpha0(2),CLq_bar8,'dk','MarkerFaceColor','k'),...
    plot(alpha0(3),CLq_bar9,'dk','MarkerFaceColor','k'),...
    hold off;

figure(3),hold on,...
    plot(alpha0(1),CMalpha_bar1,'ob','MarkerFaceColor','b'),...
    plot(alpha0(2),CMalpha_bar2,'ob','MarkerFaceColor','b'),...
    plot(alpha0(3),CMalpha_bar3,'ob','MarkerFaceColor','b'),...
    plot(alpha0(1),CMalpha_bar4,'sr','MarkerFaceColor','r'),...
    plot(alpha0(2),CMalpha_bar5,'sr','MarkerFaceColor','r'),...
    plot(alpha0(3),CMalpha_bar6,'sr','MarkerFaceColor','r'),...
    plot(alpha0(1),CMalpha_bar7,'dk','MarkerFaceColor','k'),...
    plot(alpha0(2),CMalpha_bar8,'dk','MarkerFaceColor','k'),...
    plot(alpha0(3),CMalpha_bar9,'dk','MarkerFaceColor','k'),...
    hold off;

figure(4),hold on,...
    plot(alpha0(1),CMq_bar1,'ob','MarkerFaceColor','b'),...
    plot(alpha0(2),CMq_bar2,'ob','MarkerFaceColor','b'),...
    plot(alpha0(3),CMq_bar3,'ob','MarkerFaceColor','b'),...
    plot(alpha0(1),CMq_bar4,'sr','MarkerFaceColor','r'),...
    plot(alpha0(2),CMq_bar5,'sr','MarkerFaceColor','r'),...
    plot(alpha0(3),CMq_bar6,'sr','MarkerFaceColor','r'),...
    plot(alpha0(1),CMq_bar7,'dk','MarkerFaceColor','k'),...
    plot(alpha0(2),CMq_bar8,'dk','MarkerFaceColor','k'),...
    plot(alpha0(3),CMq_bar9,'dk','MarkerFaceColor','k'),...
    hold off;
```

APPENDIX C

LIST OF SIMULATION MODELING ASSUMPTIONS

1. Aerodynamic modeling assumptions:
   a. F-16XL aircraft (10% scale)
   b. Longitudinal motion only (pitch axis)
   c. Freestream velocity is fixed at 17 m/s
   d. Dynamic pressure is fixed at 192 Pa
   e. Reduced frequency ranged from 0.081 to 0.1
   f. Mean angle of attack is fixed at 30°
   g. Oscillation angle of attack is fixed at 5°
   h. Model is based on Taylor series approximation
      i. Makes use of empirical model from F-16XL data
2. Induction machine modeling assumptions:
   a. 3-phase AC motor
   b. Symmetrical machine
   c. Uniform air gap
   d. Balanced
   e. Wye-connected circuitry
   f. Indirect vector control
   g. Fixed stator
3. Motor encoder, tachometer, and filter assumptions:
   a. Unity gain
   b. Adds unnecessary noise
   c. Adds unnecessary phase changes

APPENDIX D

PITCH OSCILLATION SIMULATION BLOCK DIAGRAM

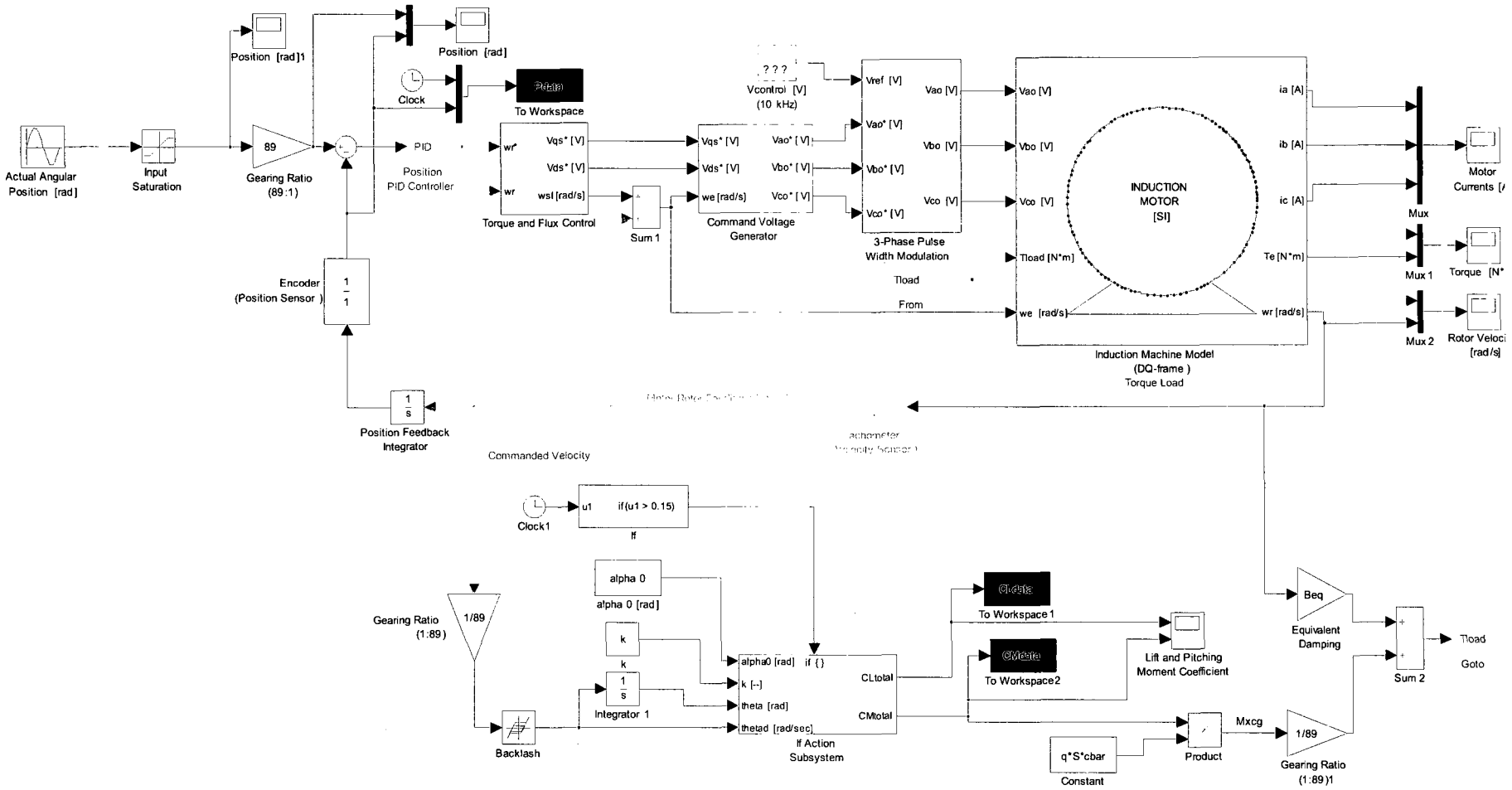

Figure 124: Larger view of pitch oscillation simulation

APPENDX E

PITCH OSCILLATION SIMULATION MATLAB CODE

PROGRAM INFORMATION

PART 1 INITIALIZATION FOR PITCH OSCILLATION SIMULATION 203
DESIGN OF EXPERIMENTS PARAMETERS (TO BE SET BY THE USER) 203
PARAMETERS 204
AERODYNAMIC PARAMETERS 204
MOTOR PARAMETERS 204
MISCELLANEOUS PARAMETERS 205
COMPLIANTLY-COUPLED DRIVE TRAIN PARAMETERS 205
PART 2 RUN SIMULATION AND GET RESULTS 207
PART 3 DATA REDUCTION FOR ONE COMPLETE CYCLE (PRE-PROCESSING) 207
PART 4 COMPUTE DYNAMIC COEFFICIENTS (POST-PROCESSING) 207

```
%{
--------------------------------------------------------------------------
--------------------------------------------------------------------------
    FILENAME:   PITCH_PARAMETERS_AND_RESULTSv2.m

    AUTHOR(s):  Brianne Williams & Drew Landman

    PURPOSE:    Part 1 - set DOE parameters
                Part 2 - initialization for ROS simulation (PITCH ONLY)
                Part 3 - run and save data result from simulation
                Part 4 - take data one cycle from data
                Part 5 - compute the dynamic coefficients

    REFERENCES: N/A

    NOTES:      - Please set simulation configuration parameters in the
                    simulink model and also set the D.O.E parameters
                    before running this m-file.

                *** All units need to be in SI-unit system. ***

                - Unit Conversions:
                    1 m = 3.2808 ft
                    1 N = 0.2248 m
                    1 kg*m^2 = 0.7376 slug*ft^2

    COMMENTS:   N/A

    DATE:       7/29/09 - simplify load as rigid, balance, and sting
                              only damping
                8/11/09 - updated file to include parts 2, 3, & 4
--------------------------------------------------------------------------
--------------------------------------------------------------------------
%}

clc;                        % clear command window screen
clear all;                  % clear all variables from workspace
close all;                  % closes all open figures
format long;                % set output format (15 significant digits)
```

PART 1 INITIALIZATION FOR PITCH OSCILLATION SIMULATION

DESIGN OF EXPERIMENTS PARAMETERS (TO BE SET BY THE USER)

```
% total inertia seen at motor [kg*m^2]
J_param = 1;

% equivalent damping [N*m/(rad/s)]
Beq_param = 1;

% reduced frequency [--]
k_param = -1;
```

```
% backlash [arcmin]
backlash = -1;

% lost motion [rad]
lost_motion = 1;
```

PARAMETERS

AERODYNAMIC PARAMETERS

```
                Wing Geometry (F-16XL 10% Model Scale [Murphy])

S       =   0.557;              % wing area [m^2]
b       =   0.988;              % wing span [m]
cbar    =   0.753;              % mean aerodynamic chord [m]
c       =   1.326;              % root (max) chord [m]
xcg     =   0.558*cbar;         % center of gravity location [m]
alpha0  =   30.8*pi/180;        % angle of attack [rad]
theta0  =   5*pi/180;           % oscillation angle of attack [rad]

%                           Test Conditions
q       =   192;                % dynamic pressure [Pa]
rho     =   1.225;              % freestream density [kg/m^3]
U       =   sqrt(2*q/rho);      % freestream velocity [m/s]

if k_param      == -1           % low test case
    k = 0.081;
elseif k_param  == 1            % high test case
    k = 0.1;
elseif k_param  == 0            % center test case
    k = (0.081 + 0.1)/2;
elseif k_param == 0.5
    k = 0.09525;
elseif k_param == -0.5
    k = 0.08575;
elseif k_param == 2             % point prediction
    k = 0.09820;
elseif k_param == 100
    k = 0.135
else
    error('Wrong selection for reduced frequency, k.');
end

w       =   2*U*k/cbar;         % oscillation frequency [rad/s]
freq    =   w/(2*pi);           % frequency [Hz]
T       =   (2*pi)/w;           % period [sec]
nc      =   1;                  % number of cycles [--]
tFinal  =   round(nc*T);        % simulation stop time [sec]

%{
%               Wing Geometry (70 deg sweep delta wing [Klein])
sweep   =   70*pi/180;          % leading edge sweep [rad]
b       =   0.90;               % trailing edge span of delta wing [m]
cbar    =   0.824;              % mean aerodynamic chord [m]
c       =   (b/2)*tan(sweep);   % root (max) chord [m]
S       =   0.5*b*c;            % wing area [m^2]
xcg     =   0.25*cbar;          % center of gravity location [m]
alpha0  =   0*pi/180;           % initial angle of attack [rad] (not used)
%}
```

MOTOR PARAMETERS

```
Vdc     =   230;                % DC supplied voltage [V]
fsw     =   10e3;               % switching frequency [Hz]
fluxr   =   0.10982;            % absolute peak rotor flux [Wb]
Rr      =   4.89;               % rotor resistance [Ohms]
Rs      =   5.16;               % stator resistance [Ohms]
Lls     =   11.883e-03;         % stator inductance [H]
Llr     =   17.163e-03;         % rotor inductance [H]
Lm      =   38e-03;             % magnetizing inductance [H]
fb      =   60;                 % base frequency [Hz]
p       =   4;                  % number of poles [--]
Ns      =   120*fb/p;           % base synchronous speed [rpm]
```

```
Ls      =   Lls + Llr;          % total leakage inductance [H]
Lr      =   Llr + Lm;           % total rotor inductance [H]
Tr      =   Lr/Rr;              % rotor time constance [sec]
wb      =   2*pi*fb;            % base angular speed [rad/s]
Xls     =   wb*Lls;             % stator impedance [Ohms]
Xlr     =   wb*Llr;             % rotor impedance [Ohms]
Xm      =   wb*Lm;              % magnetizing impedance [Ohms]

% equivalent magnetizing impedance [Ohms]
Xmstar  =   1/(1/Xls + 1/Xm + 1/Xlr);
```

MISCELLANEOUS PARAMETERS

```
c1   =   pi*rho*b^2/4;          % constant for aerodynamic model (lift) [--]
c2   =   pi*rho/4*(b^2/c^2);    % constant for aerodynamic model (moment) [--]
ratio   =   1/89;               % gear ratio [--]

if backlash == -1
    back_width = 0.033*pi/180;
elseif backlash == 1
    back_width = 0.167*pi/180;
elseif backlash == 0
    back_width = (0.033 + 0.167)*pi/180;
elseif backlash == 0.5
    back_width = 0.133*pi/180;
elseif backlash == -0.5
    back_width = 0.067*pi/180;
elseif backlash == 2        % point prediction
    back_width = 6.757/60*pi/180
end

if lost_motion == -1            % value determined from NASA F16XL test case
M065R627
    upper_limit = 4.634*pi/180;
    lower_limit = -4.817*pi/180;
elseif lost_motion == 1         % no motion lost
    upper_limit = inf;
    lower_limit = -inf;
elseif lost_motion == 0
    upper_limit = (5 - ((5-4.634)/2))*pi/180;
    lower_limit = (-5 - ((-5+4.817)/2))*pi/180;
elseif lost_motion == 0.5
    upper_limit = 0.08568;
    lower_limit = -0.08568;
elseif lost_motion == -0.5
    upper_limit = 0.08249;
    lower_limit = -0.08249;
elseif lost_motion == 2     % point prediction
    upper_limit = 0.08348
    lower_limit = -0.08348
end
```

COMPLIANTLY-COUPLED DRIVE TRAIN PARAMETERS

Moment of Inertia Constants

```
Jmotor      =   1.275e-04;      % motor rotor inertia [slug*ft^2]
Jrtangle    =   1.474e-04;      % right angle reducer inertia [slug*ft^2]
Jsumitomo   =   0.981e-04;      % torque reducer inertia [slug*ft^2]
Jos         =   26.855e-04;     % output shaft inertia [slug*ft^2]
Jsmf        =   36.432e-04;     % sting mount flange inertia [slug*ft^2]
Jsting      =   3160e-04;       % bent sting inertia [slug*ft^2]
% Jsting     =   55.891e-04;     % straight sting inertia [slug*ft^2]

%               *** NEEDS TO BE PITCH (DOUBLE CHECK!) ***
Jbal        =   12.164e-04;     % balance roll inertia [slug*ft^2]
% metric side of balance roll inertia [slug*ft^2]
Jbalmetric  =   1e-04;
Jmodel      =   5724e-04;       % model inertia [slug*ft^2]

%   Equivalent inertias required for compliance model
% all inertias on the motor side [slug*ft^2]
J1          =   Jmotor + Jrtangle + Jsumitomo;
% all inertias on the load side [slug*ft^2]
J2          =   Jos + Jsmf + Jsting + Jbalmetric + Jmodel;
```

```
if J_param      ==  -1          % low test case
    J = Jmotor;
    % total motor + load inertia seen at the motor [kg*m^2]
    J           =   J/0.7376;
elseif J_param  ==  1           % high test case
    J = J1 + J2*(ratio^2);
    % total motor + load inertia seen at the motor [kg*m^2]
    J           =   J/0.7376;
elseif J_param  ==  0           % center test case
    J = (Jmotor + (J1 + J2*(ratio^2)))/2;
    % total motor + load inertia seen at the motor [kg*m^2]
    J           =   J/0.7376;
elseif J_param == 0.5
    J = 0.0005374;      % [kg*m^2]
elseif J_param == -0.5
    J = 0.0002944;    % [kg*m^2]
elseif J_param == 2     % point prediction
    J = 0.0002517
else
    error('Wrong selection for equivalent inertia, Jeq');
end

%   Convert inertias to appropriate units
% all inertias on the motor side [kg*m^2]
J1          =   J1/0.7376;
% all inertias on the load side [kg*m^2]
J2          =   J2/0.7376;
% % total motor + load inertia seen at the motor [kg*m^2]
% J           =   J/0.7376;

%               *** DOUBLE CHECK CALCULATION BELOW ***
%                       Balance Constants
% balance spring (stiffness) constant [ft*lb/rad]
Bal_K       =   (1/0.0132*(60/1)*180/pi)*(1/12);    % NEEDS TO BE PITCH!

% balance damping constant [ft*lb/(rad/sec)]
Bal_B       =   0.005*2*sqrt(Bal_K/Jbal);

%                           Sting Constants
Sting_rt    =   1.1/2;              % missing label (Gene?)
Sting_rb    =   1.875/2;            % missing label (Gene?)

% sting spring constant [ft*lb/rad]
Sting_K     =   1/(2*33.108/(3*pi*6.4e6)*...
                    (Sting_rb^2 + Sting_rb*Sting_rt + ...
                    Sting_rt^2)/(Sting_rt*Sting_rb)^3);
% sting damping constant [ft*lb/(rad/sec)]
Sting_B     =   0.005*2*sqrt(Sting_K/Jsting);

%   Convert spring and damping constants to appropriate units
% balance damping constant [N*m/(rad/s)]
Bbal        =   Bal_B/3.2808/0.2248;
% sting damping constant [N*m/(rad/s)]
Bsting      =   Sting_B/3.2808/0.2248;


if Beq_param        ==  -1          % low test case
    Beq = 0;
elseif Beq_param    ==  1           % high test case
    Beq = (Bbal + Bsting)*(ratio^2);
elseif Beq_param    ==  0           % center test case
    Beq = ((Bbal + Bsting)*(ratio^2))/2;
elseif Beq_param == 0.5
    Beq =  0.006042;
elseif Beq_param == -0.5
    Beq = 0.002014;
elseif Beq_param == 2
    Beq = 0.0003266
else
    error('Wrong selection for equivalent damping coefficient, Beq.');
end

%{
    NOTE:   - NOT USED IN SIMPLIFIED SIMULATION MODEL
            - WILL NEED FOR COMPLEX COMPLIANCE MODEL
%}
Kbal        =   Bal_K/3.2808/0.2248;    % balance spring constant [N*m/rad]
Ksting      =   Sting_K/3.2808/0.2248;  % sting spring constant [N*m/rad]
```

PART 2 RUN SIMULATION AND GET RESULTS

```
%{
    NOTE:   MAKE SURE THE CONFIGURATION PARAMETERS IN THE SIMULINK
                FILE IS SET FIRST.
%}
sim('POS_final_ver14',tFinal);            % runs simulink model from m-file

figure(1),plot(Pdata(:,1),Pdata(:,2),'-b','LineWidth',2),grid on,...
    xlabel('time [sec]'),ylabel('Position [rad]');
```

PART 3 DATA REDUCTION FOR ONE COMPLETE CYCLE (PRE-PROCESSING)

```
%{
    DATA TAKING SCHEME:
            1.  Input data from the simulink file.
                    (i.e. lift and moment coefficient)
            2.  A polynomal curve is fitted to the data.
            3.  User selects desired roots from the results.
            4.  Data is taken from selected range, based on the roots,
                    to obtain 1 complete cycle.
            5.  Data is then processed for the dynamic aerodynamic
                    coefficients.

    NOTE: This scheme is only accurate up to 3 significant digits
%}
tol = 1e-2;
disp('Select starting pointing and ending point using mouse cursor');
[pointX,pointY] = ginput(2);

err1            =   abs(Pdata(:,1) - pointX(1));    % error for starting point
err2            =   abs(Pdata(:,1) - pointX(2));    % error for ending point

for n = 1:length(Pdata(:,2))
    if err1(n) <= tol
        startpt = n;
    end
    if err2(n) <= tol
        finalpt = n;
    end
end

startpt
finalpt
%{
% plot check
figure(2),plot(Pdata(startpt:finalpt,1),Pdata(startpt:finalpt,2)),grid on;
%}
```

PART 4 COMPUTE DYNAMIC COEFFICIENTS (POST-PROCESSING)

```
%{

    NOTE:
        Computes the unsteady stability derivatives from the simulation
            results.
%}
% figure(2),plot(Pdata(:,1),CLdata),grid on;

alphaA  =   theta0;                         % oscillation amplitude [rad]
t       =   Pdata(startpt:finalpt,1) - Pdata(startpt,1);    % time vector [sec]
tend    =   max(t);
nc      =   tend/T;

CLstatic    =   mean(CLdata);               % static lift coefficient
CMstatic    =   mean(CMdata);               % static pitching moment coefficient

CLdyn       =   CLdata(startpt:finalpt) - CLstatic;     % dynamic lift coefficient
CMdyn       =   CMdata(startpt:finalpt) - CMstatic;     % dynamic pitching moment
coefficient

figure(1),plot(t,CLdyn),grid on;
```

```
figure(2),plot(t,CMdyn),grid on;

CLalpha_bar     =   (2/(alphaA*nc*T))*trapz(t,CLdyn.*sin(w*t))
CLq_bar     =   (2/(alphaA*k*nc*T))*trapz(t,CLdyn.*cos(w*t))

CMalpha_bar     =   (2/(alphaA*nc*T))*trapz(t,CMdyn.*sin(w*t))
CMq_bar     =   (2/(alphaA*k*nc*T))*trapz(t,CMdyn.*cos(w*t))
```

APPENDIX F

ANOVA RESULTS FOR RESPONSES

RESPONSE – IN-PHASE LIFT COEFFICIENT $\overline{C}_{L_\alpha}$

Table 35: ANOVA table for in-phase lift coefficient

Response 1 CLalpha_bar ANOVA for Response Surface Reduced Cubic Model Analysis of variance table [Partial sum of squares - Type III]					
Source	**Sum of Squares**	**df**	**Mean Square**		
Model	0.15160	20	0.00758		
A-Jeq	0.00159	1	0.00159		
B-Beq	0.00149	1	0.00149		
C-k	0.03241	1	0.03241		
D-BL	0.00596	1	0.00596		
E-IS	0.01061	1	0.01061		
AB	0.00058	1	0.00058		
AE	0.00232	1	0.00232		
BC	0.00326	1	0.00326		
BD	0.00114	1	0.00114		
CD	0.00119	1	0.00119		
DE	0.00113	1	0.00113		
A^2	0.00039	1	0.00039		
B^2	0.00017	1	0.00017		
C^2	0.00467	1	0.00467		
D^2	0.00115	1	0.00115		
E^2	0.00661	1	0.00661		
A^3	0.00286	1	0.00286		
B^3	0.00131	1	0.00131		
C^3	0.00607	1	0.00607		
D^3	0.00434	1	0.00434		
Residual	0.01765	32	0.00055		
Cor Total	0.16925	52			

Table 36: Model adequacy results for in-phase lift coefficient

Std. Dev.	0.0235	R-Squared	0.8957
Mean	1.1047	Adj R-Squared	0.8305
C.V. %	2.1261	Pred R-Squared	0.7670
PRESS	0.0394	Adeq Precision	14.4567

RESPONSE – OUT-OF-PHASE LIFT COEFFICIENT $\overline{C}_{L_q}$

Table 37: ANOVA table for out-of-phase lift coefficient

Response 2 CLq_bar					
ANOVA for Response Surface Reduced Cubic Model					
Analysis of variance table [Partial sum of squares - Type III]					
Source	**Sum of Squares**	**df**	**Mean Square**		
Model	37.8115	20	1.8906		
A-Jeq	0.2336	1	0.2336		
B-Beq	0.1399	1	0.1399		
C-k	7.1022	1	7.1022		
D-BL	0.6663	1	0.6663		
E-IS	0.0033	1	0.0033		
AB	0.0953	1	0.0953		
AE	0.1677	1	0.1677		
BC	0.3207	1	0.3207		
BD	0.1103	1	0.1103		
CD	0.1033	1	0.1033		
DE	0.1470	1	0.1470		
A^2	0.0324	1	0.0324		
B^2	0.0036	1	0.0036		
C^2	0.5661	1	0.5661		
D^2	0.1766	1	0.1766		
E^2	0.4150	1	0.4150		
A^3	0.4026	1	0.4026		
B^3	0.1386	1	0.1386		
C^3	0.5937	1	0.5937		
D^3	0.4998	1	0.4998		
Residual	1.6844	32	0.0526		
Cor Total	39.4959	52			

Table 38: Model adequacy results for out-of-phase lift coefficient

Std. Dev.	0.2294	R-Squared	0.9574
Mean	12.6622	Adj R-Squared	0.9307
C.V. %	1.8119	Pred R-Squared	0.9110
PRESS	3.5140	Adeq Precision	20.9072

RESPONSE – IN-PHASE PITCHING MOMENT COEFFICIENT $\overline{C}_{m_\alpha}$

Table 39: ANOVA table for in-phase pitching moment coefficient

Response 3 CMalpha_bar ANOVA for Response Surface Reduced Cubic Model Analysis of variance table [Partial sum of squares - Type III]					
Source	**Sum of Squares**	**df**	**Mean Square**		
Model	4.1268E-03	20	0.000206		
A-Jeq	3.0946E-05	1	3.09E-05		
B-Beq	1.6649E-05	1	1.66E-05		
C-k	7.7259E-04	1	0.000773		
D-BL	8.2841E-05	1	8.28E-05		
E-IS	2.2994E-04	1	0.00023		
AB	1.0769E-05	1	1.08E-05		
AE	2.4896E-05	1	2.49E-05		
BC	4.1258E-05	1	4.13E-05		
BD	1.4432E-05	1	1.44E-05		
CD	1.3609E-05	1	1.36E-05		
DE	1.8003E-05	1	1.8E-05		
A^2	6.2519E-06	1	6.25E-06		
B^2	1.6235E-06	1	1.62E-06		
C^2	7.4202E-05	1	7.42E-05		
D^2	1.7082E-05	1	1.71E-05		
E^2	8.7242E-05	1	8.72E-05		
A^3	5.0522E-05	1	5.05E-05		
B^3	1.5718E-05	1	1.57E-05		
C^3	8.0642E-05	1	8.06E-05		
D^3	6.1907E-05	1	6.19E-05		
Residual	2.3936E-04	32	7.48E-06		
Cor Total	4.3661E-03	52			

Table 40: Model adequacy results for in-phase pitching moment coefficient

Std. Dev.	0.00273	R-Squared	0.9452
Mean	0.20025	Adj R-Squared	0.9109
C.V. %	1.36576	Pred R-Squared	0.8762
PRESS	0.0005407	Adeq Precision	20.2269

RESPONSE – OUT-OF-PHASE PITCHING MOMENT COEFFICIENT $\overline{C}_{m_q}$

Table 41: ANOVA table for out-of-phase pitching moment coefficient

Response	**4**	**CMq_bar**			
ANOVA for Response Surface Reduced Cubic Model					
Analysis of variance table [Partial sum of squares - Type III]					
Source	**Sum of Squares**	**df**	**Mean Square**		
Model	1.3732E+00	20	0.068661		
A-Jeq	6.3838E-03	1	0.006384		
B-Beq	5.4304E-03	1	0.00543		
C-k	2.5905E-01	1	0.25905		
D-BL	2.2725E-02	1	0.022725		
E-IS	1.9828E-03	1	0.001983		
AB	2.9139E-03	1	0.002914		
AE	6.9594E-03	1	0.006959		
BC	1.2042E-02	1	0.012042		
BD	3.7028E-03	1	0.003703		
CD	3.9133E-03	1	0.003913		
DE	4.8571E-03	1	0.004857		
A^2	1.1187E-03	1	0.001119		
B^2	2.7803E-04	1	0.000278		
C^2	1.7750E-02	1	0.01775		
D^2	5.4419E-03	1	0.005442		
E^2	1.7492E-02	1	0.017492		
A^3	1.1758E-02	1	0.011758		
B^3	5.2159E-03	1	0.005216		
C^3	2.1826E-02	1	0.021826		
D^3	1.6892E-02	1	0.016892		
Residual	6.0917E-02	32	0.001904		
Cor Total	1.43413861	52			

Table 42: Model adequacy results for out-of-phase pitching moment coefficient

Std. Dev.	0.0436	R-Squared	0.9575
Mean	1.5613	Adj R-Squared	0.9310
C.V. %	2.7944	Pred R-Squared	0.9089
PRESS	0.1307	Adeq Precision	20.9245

APPENDIX G

MONTE CARLO SIMULATIONS

```
%{
    FILENAME:   MCMv5_indirect.m

    AUTHOR:     Brianne Y. Williams

    PURPOSE:    Performs Monte Carlo method simulation on indirect
                    computation of the absolute sensitivity coefficient and
                    respective derivatives.
                Monte Carlo (indirect method)

    REFERENCE:  Coleman, H.W., and Steele, W.G., "Experimentation, Validation,
                    and Uncertainty Analysis for Engineers" 3rd edition.

    NOTE:       1) For extreme cases where the Monte Carlo distribution is
                    highly skewed, the asymmetric uncertainty limits will
                    be more appropriate to provide a given level of
                    confidence for the uncertainty estimate. (pg 81)

                2) Calculating the standard deviation and assuming that the
                    central limit theorem applies to obtain the uncertainty
                    will not necessarily be appropriate on the degree of
                    asymmetry
%}
clc;
clear all;
close all;

%   ... Set nominal values

test_case = 5;

if test_case == 1
    Jeq = 0.000658900;          % equivalent inertia [kg*m^2]       A = +1.0
    Beq = 0.00805600;           % equivalent damping [Nms/rad]      B = +1.0
    k   = 0.081;                % reduced frequency [--]            C = -1.0    ***
fixed factor ***
    BL  = 2.00000;              % backlash [arcmin]                 D = -1.0
    IS  = 0.08727;              % input saturation [rad]            E = +1.0

elseif test_case == 2
    Jeq = 0.000415900;          % A = 0.0
    Beq = 0.00402800;           % B = 0.0
    k = 0.0905000;              % C = 0.0
    BL = 6.00000;               % D = 0.0
    IS = 0.0840850;             % E = 0.0

elseif test_case == 3
    Jeq = 0.000172900;          % A = -1.0
    Beq = 0.000000;             % B = -1.0
    k = 0.0810000;              % C = -1.0
    BL = 2.00000;               % D = -1.0
    IS = 0.0809000;             % E = -1.0

elseif test_case == 4
    Jeq = 0.000415900;          % A = 0.0
    Beq = 0.00402800;           % B = 0.0
    k = 0.0810000;              % C = -1.0
    BL = 2.00000;               % D = -1.0
    IS = 0.0809000;             % E = -1.0

elseif test_case == 5
    Jeq = 0.000658900;          % A = +1.0
    Beq = 0.00805600;           % B = +1.0
    k   = 0.100000;             % C = +1.0
    BL = 2.00000;               % D = -1.0
    IS = 0.0809000;             % E = -1.0

end

[Z0,S] = sensitivity_coeff2(Jeq,Beq,k,BL,IS);

n = 100000;                 % number of samples

%   ... Uniform distribution for equivalent inertia
Jeq_low = 0.000172900;                          % [kg*m^2]
Jeq_high = 0.000658900;                         % [kg*m^2]

dJeq = Jeq_low + ((Jeq_high - Jeq_low).*rand(n,1));
```

```
dJeq = mean(dJeq) - dJeq;


figure(1),hist(dJeq,100),grid on,...
    xlabel('\delta Jeq [kg*m^2]'),ylabel('Frequency of Occurance'),...
    title('Uniform Distribution for Equivalent Inertia');


%   ... Uniform distribution for equivalent damping
Beq_low = 0;                                    % [N-m/(rad/s)]
Beq_high = 0.00805600;                          % [N-m/(rad/s)]
Beq_mean = mean([Beq_high,Beq_low]);            % [N-m/(rad/s)]

dBeq = Beq_low + ((Beq_high - Beq_low).*rand(n,1));
dBeq = mean(dBeq) - dBeq;


figure(2),hist(dBeq,100),grid on,...
    xlabel('\delta Beq [N-m/(rad/s)]'),ylabel('Frequency of Occurance'),...
    title('Uniform Distribution for Equivalent Damping');


%   ... No distribution for reduced frequency
dk = zeros(n,1);

%   Normal distribution for backlash
BL_low = 2;                                     % [arcmin]
BL_high = 10;                                   % [arcmin]
muBL = mean([BL_high,BL_low]);                  % [arcmin]
sdBL = 2.60623;                                 % std (from design expert) [arcmin]

dBL = muBL + (randn(n,1)*sdBL);
dBL = mean(dBL) - dBL;


figure(3),hist(dBL,100),grid on,...
    xlabel('\delta BL [arcmin]'),ylabel('Frequency of Occurance'),...
    title('Normal Distribution for Backlash');


%   ... Normal distribution for input saturation
IS_low = 0.0809000;                             % [rad]
IS_high = 0.0872700;                            % [rad]
muIS = mean([IS_high,IS_low]);                  % [rad]
sdIS = 0.00207521;                              % std (from design expert) [rad]

dIS =  muIS + (randn(n,1)*sdIS);
dIS = mean(dIS) - dIS;


figure(4),hist(dIS,100),grid on,...
    xlabel('\delta IS [rad]'),ylabel('Frequency of Occurance'),...
    title('Normal Distribution for Input Saturation');


%   ... Monte Carlo Simulation
dCLabar = sqrt((S(1,1)^2*dJeq.^2) + (S(1,2)^2*dBeq.^2) + (S(1,3)^2*dk.^2) + ...
    (S(1,4)^2*dBL.^2) + (S(1,5)^2*dIS.^2));

dCLqbar = sqrt((S(2,1)^2*dJeq.^2) + (S(2,2)^2*dBeq.^2) + (S(2,3)^2*dk.^2) + ...
    (S(2,4)^2*dBL.^2) + (S(2,5)^2*dIS.^2));

dCMabar = sqrt((S(3,1)^2*dJeq.^2) + (S(3,2)^2*dBeq.^2) + (S(3,3)^2*dk.^2) + ...
    (S(3,4)^2*dBL.^2) + (S(3,5)^2*dIS.^2));

dCMqbar = sqrt((S(4,1)^2*dJeq.^2) + (S(4,2)^2*dBeq.^2) + (S(4,3)^2*dk.^2) + ...
    (S(4,4)^2*dBL.^2) + (S(4,5)^2*dIS.^2));

% Distribution output is added to the nominal
CLabar = Z0(1) + dCLabar;
CLqbar = Z0(2) + dCLqbar;
CMabar = Z0(3) + dCMabar;
CMqbar = Z0(4) + dCMqbar;

%   ... Histogram Plots
figure(6),hist(CLabar,100),grid on,...
    xlabel('C_L_\alpha (bar)'),ylabel('Frequency of Occurance');

figure(7),hist(CLqbar,100),grid on,...
```

```
    xlabel('C_L_q (bar)'),ylabel('Frequency of Occurance');

figure(8),hist(CMabar,100),grid on,...
    xlabel('C_M_\alpha (bar)'),ylabel('Frequency of Occurance');

figure(9),hist(CMqbar,100),grid on,...
    xlabel('C_M_q (bar)'),ylabel('Frequency of Occurance');

% ... Summary Statistics and Coverage Intervals
%   In-phase lift coefficient
CLa_mean    = mean(CLabar);
CLa_std     = std(CLabar);
CLa_var     = var(CLabar);
CLa_max     = max(CLabar);
CLa_min     = min(CLabar);
CLa_skew    = skewness(CLabar);
CLa_kurt    = kurtosis(CLabar);
%   Coverage interval for CLalpha (bar)
CLa_sort    = sort(CLabar,'ascend');
CLa_rlow    = CLa_sort(0.025*n);
CLa_rhigh   = CLa_sort(0.975*n);
CLa_range   = range(CLabar);

%   Out-of-phase lift coefficient
CLq_mean    = mean(CLqbar);
CLq_std     = std(CLqbar);
CLq_var     = var(CLqbar);
CLq_max     = max(CLqbar);
CLq_min     = min(CLqbar);
CLq_skew    = skewness(CLqbar);
CLq_kurt    = kurtosis(CLqbar);
%   Coverage interval for CLq (bar)
CLq_sort    = sort(CLqbar,'ascend');
CLq_rlow    = CLq_sort(0.025*n);
CLq_rhigh   = CLq_sort(0.975*n);
CLq_range   = range(CLqbar);

%   In-phase pitching moment coefficient
CMa_mean    = mean(CMabar);
CMa_std     = std(CMabar);
CMa_var     = var(CMabar);
CMa_max     = max(CMabar);
CMa_min     = min(CMabar);
CMa_skew    = skewness(CMabar);
CMa_kurt    = kurtosis(CMabar);
%   Coverage interval for CMalpha (bar)
CMa_sort    = sort(CMabar,'ascend');
CMa_rlow    = CMa_sort(0.025*n);
CMa_rhigh   = CMa_sort(0.975*n);
CMa_range   = range(CMabar);

%   Out-of-phase pitching moment coefficient
CMq_mean    = mean(CMqbar);
CMq_std     = std(CMqbar);
CMq_var     = var(CMqbar);
CMq_max     = max(CMqbar);
CMq_min     = min(CMqbar);
CMq_skew    = skewness(CMqbar);
CMq_kurt    = kurtosis(CMqbar);
%   Coverage interval for CMq (bar)
CMq_sort    = sort(CMqbar,'ascend');
CMq_rlow    = CMq_sort(0.025*n);
CMq_rhigh   = CMq_sort(0.975*n);
CMq_range   = range(CMqbar);

summary_statistics = ...

[CLa_mean,CLa_std,CLa_var,CLa_min,CLa_max,CLa_skew,CLa_kurt,CLa_rlow,CLa_rhigh,CLa_
range;

CLq_mean,CLq_std,CLq_var,CLq_min,CLq_max,CLq_skew,CLq_kurt,CLq_rlow,CLq_rhigh,CLq_r
ange;

CMa_mean,CMa_std,CMa_var,CMa_min,CMa_max,CMa_skew,CMa_kurt,CMa_rlow,CMa_rhigh,CMa_r
ange;

CMq_mean,CMq_std,CMq_var,CMq_min,CMq_max,CMq_skew,CMq_kurt,CMq_rlow,CMq_rhigh,CMq_r
ange];
```

```
%{
    FILENAME:   MCMv6_direct.m

    AUTHOR:     Brianne Y. Williams

    PURPOSE:    Performs Monte Carlo method simulation on direct regression
                    model (from Design Expert).
                Monte Carlo (direct method)

    REFERENCE:  Coleman, H.W., and Steele, W.G., "Experimentation, Validation,
                    and Uncertainty Analysis for Engineers" 3rd edition.

    NOTE:       1) For extreme cases where the Monte Carlo distribution is
                    highly skewed, the asymmetric uncertainty limits will
                    be more appropriate to provide a given level of
                    confidence for the uncertainty estimate. (pg 81)

                2) Calculating the standard deviation and assuming that the
                    central limit theorem applies to obtain the uncertainty
                    will not necessarily be appropriate on the degree of
                    asymmetry
%}
clc;
clear all;
close all;

test_case = 5;

%   ... Set nominal values
if test_case == 1
    Jeq0 = 0.000658900;         % equivalent inertia [kg*m^2]       A = +1.0
    Beq0 = 0.00805600;          % equivalent damping [Nms/rad]      B = +1.0
    k0   = 0.081;               % reduced frequency [--]            C = -1.0
*** fixed factor ***
    BL0  = 2.00000;             % backlash [arcmin]                 D = -1.0
    IS0  = 0.08727;             % input saturation [rad]            E = +1.0

elseif test_case == 2
    Jeq0 = 0.000415900;         % A = 0.0
    Beq0 = 0.00402800;          % B = 0.0
    k0 = 0.0905000;             % C = 0.0
    BL0 = 6.00000;              % D = 0.0
    IS0 = 0.0840850;            % E = 0.0

elseif test_case == 3
    Jeq0 = 0.000172900;         % A = -1.0
    Beq0 = 0.000000;            % B = -1.0
    k0 = 0.0810000;             % C = -1.0
    BL0 = 2.00000;              % D = -1.0
    IS0 = 0.0809000;            % E = -1.0

elseif test_case == 4
    Jeq0 = 0.000415900;         % A = 0.0
    Beq0 = 0.00402800;          % B = 0.0
    k0 = 0.0810000;             % C = -1.0
    BL0 = 2.00000;              % D = -1.0
    IS0 = 0.0809000;            % E = -1.0

elseif test_case == 5
    Jeq0 = 0.000658900;         % A = +1.0
    Beq0 = 0.00805600;          % B = +1.0
    k0   = 0.100000;            % C = +1.0
    BL0 = 2.00000;              % D = -1.0
    IS0 = 0.0809000;            % E = -1.0

end

n = 100000;                 % number of samples

%   ... Uniform distribution for equivalent inertia
Jeq_low = 0.000172900;                          % [kg*m^2]
Jeq_high = 0.000658900;                         % [kg*m^2]

dJeq = Jeq_low + ((Jeq_high - Jeq_low).*rand(n,1));
dJeq = mean(dJeq) - dJeq;

%   ... Uniform distribution for equivalent damping
Beq_low = 0;                                    % [N-m/(rad/s)]
Beq_high = 0.00805600;                          % [N-m/(rad/s)]
```

```
Beq_mean = mean([Beq_high,Beq_low]);            % [N-m/(rad/s)]

dBeq = Beq_low + ((Beq_high - Beq_low).*rand(n,1));
dBeq = mean(dBeq) - dBeq;

%   ... No distribution for reduced frequency
dk = zeros(n,1);

%   ... Normal distribution for backlash
BL_low = 2;                                     % [arcmin]
BL_high = 10;                                   % [arcmin]
muBL = mean([BL_high,BL_low]);                  % [arcmin]
sdBL = 2.60623;                                 % std (from design expert) [arcmin]

dBL = muBL + (randn(n,1)*sdBL);
dBL = mean(dBL) - dBL;

%   ... Normal distribution for input saturation
IS_low = 0.0809000;                             % [rad]
IS_high = 0.0872700;                            % [rad]
muIS = mean([IS_high,IS_low]);                  % [rad]
sdIS = 0.00207521;                              % std (from design expert) [rad]

dIS =  muIS + (randn(n,1)*sdIS);
dIS = mean(dIS) - dIS;

%   ... Monte Carlo input distribution for each input factor
Jeq = Jeq0 + dJeq;
Beq = Beq0 + dBeq;
k = k0 + dk;
BL = BL0 + dBL;
IS = IS0 + dIS;


figure(1),hist(Jeq,100),grid on,...
    xlabel('Jeq [kg*m^2]'),ylabel('Frequency of Occurance'),...
    title('Uniform Distribution for Equivalent Inertia');

figure(2),hist(Beq,100),grid on,...
    xlabel('Beq [N-m/(rad/s)]'),ylabel('Frequency of Occurance'),...
    title('Uniform Distribution for Equivalent Damping');

figure(3),hist(BL,100),grid on,...
    xlabel('BL [arcmin]'),ylabel('Frequency of Occurance'),...
    title('Normal Distribution for Backlash');

figure(4),hist(IS,100),grid on,...
    xlabel('IS [rad]'),ylabel('Frequency of Occurance'),...
    title('Normal Distribution for Input Saturation');


%   .... Monte Carlo simulation (direct) method
CLabar = 15.24237555 + ...          % In-phase lift coefficient regression
-181.4547712 * Jeq + ...
-49.04939791 * Beq + ...
-1644.883794 * k + ...
-0.01445232      * BL + ...
849.5947162      * IS + ...
5978.4137        * Jeq.*Beq  + ...
-15085.95095 * Jeq.*IS + ...
362.0822832      * Beq.*k + ...
-0.507463123 * Beq.*BL + ...
0.220413651      * k.*BL + ...
-0.638542716 * BL.*IS + ...
3472467.826      * Jeq.^2 + ...
5191.116119      * Beq.^2 + ...
17809.68319      * k.^2 + ...
0.011718675      * BL.^2 + ...
-4951.365718 * IS.^2 + ...
-2618135863      * Jeq.^3 + ...
-388593.7143 * Beq.^3 + ...
-63874.59632 * k.^3 + ...
-0.000723644 * BL.^3;

CLqbar    = ...                     % Out-of-phase lift coeff. regression
-200.5918986 + ...
5947.141961      * Jeq + ...
481.1658016      * Beq + ...
16298.74358      * k + ...
```

```
0.066249836      * BL + ...
-6697.404238 * IS + ...
-76492.13389 * Jeq.*Beq + ...
128340.3868      * Jeq.*IS + ...
-3589.056778 * Beq.*k + ...
4.99884654       * Beq.*BL + ...
-2.05173152      * k.*BL + ...
7.298762801      * BL.*IS + ...
-40652560.58 * Jeq.^2 + ...
-50671.95304 * Beq.^2 + ...
-176614.5487 * k.^2 + ...
-0.12350422      * BL.^2 + ...
39224.84529      * IS.^2 + ...
31073217728      * Jeq.^3 + ...
4003306.897      * Beq.^3 + ...
631546.1898      * k.^3 + ...
0.007762681      * BL.^3;


CMabar    = ...                % In-phase pitching moment coeff. regression
1.826643706     + ...
-59.69274106 * Jeq + ...
-5.503595299 * Beq + ...
-189.9722455 * k + ...
-0.001082872 * BL + ...
97.78536612      * IS + ...
813.1471009      * Jeq.* Beq + ...
-1563.598629 * Jeq.* IS + ...
40.71132419      * Beq.* k + ...
-0.057186246 * Beq.* BL + ...
0.023545512      * k.* BL + ...
-0.08077536      * BL.* IS + ...
460483.8665      * Jeq.^2 + ...
563.6564637      * Beq.^2 + ...
2057.289215      * k.^2 + ...
0.001395507      * BL.^2 + ...
-568.7501238 * IS.^2 + ...
-348102903.4 * Jeq.^3 + ...
-42630.50891 * Beq.^3 + ...
-7360.338942 * k.^3 + ...
-8.63927E-05 * BL.^3;


CMqbar    = ...                % Out-of-phase pitching moment coeff. regression
-34.72586026 + ...
694.1627312      * Jeq + ...
94.33615494      * Beq + ...
3111.517426      * k + ...
0.016958641      * BL + ...
-1376.124566 * IS + ...
-13375.62027 * Jeq.* Beq + ...
26142.47848      * Jeq.* IS + ...
-695.5185108 * Beq.* k + ...
0.915988304      * Beq.* BL + ...
-0.399267416 * k.* BL + ...
1.326769162      * BL.* IS + ...
-6975790.877 * Jeq.^2 + ...
-10018.92125 * Beq.^2 + ...
-33787.10834 * k.^2 + ...
-0.022839277 * BL.^2 + ...
8053.421672      * IS.^2 + ...
5310496432       * Jeq.^3 + ...
776573.5802      * Beq.^3 + ...
121087.4646      * k.^3 + ...
0.001427068      * BL.^3;

% ... Histogram Results

figure,hist(CLabar,100),xlabel('C_L_\alpha (bar)'),ylabel('Frequency'),grid on;
figure,hist(CLqbar,100),xlabel('C_L_q (bar)'),ylabel('Frequency'),grid on;
figure,hist(CMabar,100),xlabel('C_M_\alpha (bar)'),ylabel('Frequency'),grid on;
figure,hist(CMqbar,100),xlabel('C_M_q (bar)'),ylabel('Frequency'),grid on;

% ... Summary Statistics and Coverage Intervals
%   In-phase lift coefficient
CLa_mean    = mean(CLabar);
CLa_std     = std(CLabar);
CLa_var     = var(CLabar);
CLa_max     = max(CLabar);
```

```
CLa_min     = min(CLabar);
CLa_skew    = skewness(CLabar);
CLa_kurt    = kurtosis(CLabar);
%   Coverage interval for CLalpha (bar)
CLa_sort    = sort(CLabar,'ascend');
CLa_rlow    = CLa_sort(0.025*n);
CLa_rhigh   = CLa_sort(0.975*n);
CLa_range   = range(CLabar);

%   Out-of-phase lift coefficient
CLq_mean    = mean(CLqbar);
CLq_std     = std(CLqbar);
CLq_var     = var(CLqbar);
CLq_max     = max(CLqbar);
CLq_min     = min(CLqbar);
CLq_skew    = skewness(CLqbar);
CLq_kurt    = kurtosis(CLqbar);
%   Coverage interval for CLq (bar)
CLq_sort    = sort(CLqbar,'ascend');
CLq_rlow    = CLq_sort(0.025*n);
CLq_rhigh   = CLq_sort(0.975*n);
CLq_range   = range(CLqbar);

%   In-phase pitching moment coefficient
CMa_mean    = mean(CMabar);
CMa_std     = std(CMabar);
CMa_var     = var(CMabar);
CMa_max     = max(CMabar);
CMa_min     = min(CMabar);
CMa_skew    = skewness(CMabar);
CMa_kurt    = kurtosis(CMabar);
%   Coverage interval for CMalpha (bar)
CMa_sort    = sort(CMabar,'ascend');
CMa_rlow    = CMa_sort(0.025*n);
CMa_rhigh   = CMa_sort(0.975*n);
CMa_range   = range(CMabar);

%   Out-of-phase pitching moment coefficient
CMq_mean    = mean(CMqbar);
CMq_std     = std(CMqbar);
CMq_var     = var(CMqbar);
CMq_max     = max(CMqbar);
CMq_min     = min(CMqbar);
CMq_skew    = skewness(CMqbar);
CMq_kurt    = kurtosis(CMqbar);
%   Coverage interval for CMq (bar)
CMq_sort    = sort(CMqbar,'ascend');
CMq_rlow    = CMq_sort(0.025*n);
CMq_rhigh   = CMq_sort(0.975*n);
CMq_range   = range(CMqbar);

summary_statistics = ...

[CLa_mean,CLa_std,CLa_var,CLa_min,CLa_max,CLa_skew,CLa_kurt,CLa_rlow,CLa_rhigh,CLa_
range;

CLq_mean,CLq_std,CLq_var,CLq_min,CLq_max,CLq_skew,CLq_kurt,CLq_rlow,CLq_rhigh,CLq_r
ange;

CMa_mean,CMa_std,CMa_var,CMa_min,CMa_max,CMa_skew,CMa_kurt,CMa_rlow,CMa_rhigh,CMa_r
ange;

CMq_mean,CMq_std,CMq_var,CMq_min,CMq_max,CMq_skew,CMq_kurt,CMq_rlow,CMq_rhigh,CMq_r
ange];
```

```
%                    Sensitivity Derivative Coefficients
function [Z0,S] = sensitivity_coeff2(Jeqfact,Beqfact,kfact,BLfact,ISfact)
%{
    FILENAME:   sensitivity_coeff2.m

    AUTHOR:     Brianne Y. Williams

    PURPOSE:    The function computes the senstivity derivative coefficients
                at the nominal settings. Regression metamodels are put
                into symbolic form and Matlab computes the sensitivity
                derivatives symbolically. The final solution is computed
                at the nominal values using subs().

    INPUTS:     Jeqfact,Beqfact,kfact, ...  => actual factor values

    OUTPUTS:    Z0  - mean value at nominal setting computed using
                      the regression metamodels
                S   - sensitivity derivative coefficient matrix using
                      the actual factors at nominal settings

    DATE:       2/15/10
%}

syms CLabar CLqbar CMabar CMqbar
syms Jeq Beq k BL IS

%      Regression Metamodel (Actual)
% Actual Metamodels

CLabar    = ...
15.24237555       + ...
-181.4547712 * Jeq + ...
-49.04939791 * Beq + ...
-1644.883794 * k + ...
-0.01445232       * BL + ...
849.5947162       * IS + ...
5978.4137         * Jeq * Beq + ...
-15085.95095 * Jeq * IS + ...
362.0822832       * Beq * k + ...
-0.507463123 * Beq * BL + ...
0.220413651       * k * BL + ...
-0.638542716 * BL * IS + ...
3472467.826       * Jeq^2 + ...
5191.116119       * Beq^2 + ...
17809.68319       * k^2 + ...
0.011718675       * BL^2 + ...
-4951.365718 * IS^2 + ...
-2618135863       * Jeq^3 + ...
-388593.7143 * Beq^3 + ...
-63874.59632 * k^3 + ...
-0.000723644 * BL^3;


CLqbar    = ...
-200.5918986 + ...
5947.141961       * Jeq + ...
481.1658016       * Beq + ...
16298.74358       * k + ...
0.066249836       * BL + ...
-6697.404238 * IS + ...
-76492.13389 * Jeq * Beq + ...
128340.3868       * Jeq * IS + ...
-3589.056778 * Beq * k + ...
4.99884654        * Beq * BL + ...
-2.05173152       * k * BL + ...
7.298762801       * BL * IS + ...
-40652560.58 * Jeq^2 + ...
-50671.95304 * Beq^2 + ...
-176614.5487 * k^2 + ...
-0.12350422       * BL^2 + ...
39224.84529       * IS^2 + ...
31073217728       * Jeq^3 + ...
4003306.897       * Beq^3 + ...
631546.1898       * k^3 + ...
0.007762681       * BL^3;


CMabar    = ...
1.826643706      + ...
```

```
-59.69274106 * Jeq + ...
-5.503595299 * Beq + ...
-189.9722455 * k + ...
-0.001082872 * BL + ...
97.78536612      * IS + ...
813.1471009      * Jeq * Beq + ...
-1563.598629 * Jeq * IS + ...
40.71132419      * Beq * k + ...
-0.057186246 * Beq * BL + ...
0.023545512      * k * BL + ...
-0.08077536      * BL * IS + ...
460483.8665      * Jeq^2 + ...
563.6564637      * Beq^2 + ...
2057.289215      * k^2 + ...
0.001395507      * BL^2 + ...
-568.7501238 * IS^2 + ...
-348102903.4 * Jeq^3 + ...
-42630.50891 * Beq^3 + ...
-7360.338942 * k^3 + ...
-8.63927E-05 * BL^3;

CMqbar    = ...
-34.72586026 + ...
694.1627312      * Jeq + ...
94.33615494      * Beq + ...
3111.517426      * k + ...
0.016958641      * BL + ...
-1376.124566 * IS + ...
-13375.62027 * Jeq * Beq + ...
26142.47848      * Jeq * IS + ...
-695.5185108 * Beq * k + ...
0.915988304      * Beq * BL + ...
-0.399267416 * k * BL + ...
1.326769162      * BL * IS + ...
-6975790.877 * Jeq^2 + ...
-10018.92125 * Beq^2 + ...
-33787.10834 * k^2 + ...
-0.022839277 * BL^2 + ...
8053.421672      * IS^2 + ...
5310496432       * Jeq^3 + ...
776573.5802      * Beq^3 + ...
121087.4646      * k^3 + ...
0.001427068      * BL^3;

% First-order Sensitivity Analysis
% Sensitivity derivative coefficients using actual regression metamodel
dCLabardA = diff(CLabar,Jeq);           % dCLalpha_bar/dJeq
dCLabardB = diff(CLabar,Beq);           % dCLalpha_bar/dBeq
dCLabardC = diff(CLabar,k);             % dCLalpha_bar/dk
dCLabardD = diff(CLabar,BL);            % dCLalpha_bar/dBL
dCLabardE = diff(CLabar,IS);            % dCLalpha_bar/dIS

dCLqbardA = diff(CLqbar,Jeq);           % dCLq_bar/dJeq
dCLqbardB = diff(CLqbar,Beq);           % dCLq_bar/dBeq
dCLqbardC = diff(CLqbar,k);             % dCLq_bar/dk
dCLqbardD = diff(CLqbar,BL);            % dCLq_bar/dBL
dCLqbardE = diff(CLqbar,IS);            % dCLq_bar/dIS

dCMabardA = diff(CMabar,Jeq);           % dCMalpha_bar/dJeq
dCMabardB = diff(CMabar,Beq);           % dCMalpha_bar/dBeq
dCMabardC = diff(CMabar,k);             % dCMalpha_bar/dk
dCMabardD = diff(CMabar,BL);            % dCMalpha_bar/dBL
dCMabardE = diff(CMabar,IS);            % dCMalpha_bar/dIS

dCMqbardA = diff(CMqbar,Jeq);           % dCMq_bar/dJeq
dCMqbardB = diff(CMqbar,Beq);           % dCMq_bar/dBeq
dCMqbardC = diff(CMqbar,k);             % dCMq_bar/dk
dCMqbardD = diff(CMqbar,BL);            % dCMq_bar/dBL
dCMqbardE = diff(CMqbar,IS);            % dCMq_bar/dIS

% Sets the nominal conditions for coded and actual factors
Jeq = Jeqfact;
Beq = Beqfact;
k = kfact;
BL = BLfact;
IS = ISfact;

% Computes the mean value at nominal settings:
Z0  = [subs(CLabar);
```

```
        subs(CLqbar);
        subs(CMabar);
        subs(CMqbar)];

S   =
[subs(dCLabardA),subs(dCLabardB),subs(dCLabardC),subs(dCLabardD),subs(dCLabardE);

subs(dCLqbardA),subs(dCLqbardB),subs(dCLqbardC),subs(dCLqbardD),subs(dCLqbardE);

subs(dCMabardA),subs(dCMabardB),subs(dCMabardC),subs(dCMabardD),subs(dCMabardE);

subs(dCMqbardA),subs(dCMqbardB),subs(dCMqbardC),subs(dCMqbardD),subs(dCMqbardE)];
end
```

VITA

Brianne Y. Williams

Department of Aerospace Engineering

Old Dominion University

Norfolk, Virginia 23539

Brianne Williams was born in Washington, DC and raised in Hyattsville, MD. After finishing high school in 2000, she attended West Virginia University, graduating with a Bachelor's of Science in Aerospace Engineering in 2004. She received a Master's of Science in Aerospace Engineering from Old Dominion University in May 2007 and a Ph.D. in Aerospace Engineering from Old Dominion University in August 2010. Brianne has accepted a full-time position at The Aerospace Corporation located in Los Angeles, California.